Universität Hamburg

DER FORSCHUNG | DER LEHRE | DER BILDUNG

# Determination of the Jet Energy Resolution and Measurements of Jet Substructure and the Top Quark Mass in Decays of Boosted Top Quarks at CMS

DISSERTATION

zur Erlangung des Doktorgrades
an der Fakultät für Mathematik, Informatik und Naturwissenschaften
Fachbereich Physik
der Universität Hamburg

vorgelegt von

**Alexander Maximilian Paasch**

Hamburg
2024

| | |
|---|---|
| Gutacher/innen der Dissertation: | Prof. Dr. Johannes Haller<br>PD Dr. Roman Kogler |
| Zusammensetzung der Prüfungskommision: | Prof. Dr. Johannes Haller<br>PD Dr. Roman Kogler<br>Prof. Dr. Gudrid Moortgat-Pick<br>Prof. Dr. Christian Schwanenberger<br>Prof. Dr. Jochen Liske |
| Vorsitzende/r der Prüfungskommission: | Prof. Dr. Jochen Liske |
| Datum der Disputation: | 15.10.2024 |
| Vorsitzender des Fach-Promotionsausschusses Physik: | Prof. Dr. Markus Drescher |
| Leiter des Fachbereichs Physik: | Prof. Dr. Wolfgang J. Parak |
| Dekan der Fakultät MIN: | Prof. Dr.-Ing. Norbert Ritter |

# Abstract

This thesis presents two analyses using data recorded by the CMS detector in proton-proton collisions at the LHC. First, a determination of the jet transverse momentum resolution scale factors is performed, followed by the measurement of the jet mass in hadronic decays of boosted top quarks and by an extraction of the top quark mass.

The first analysis determines the jet transverse momentum resolution scale factors for data collected during the LHC Run 2 and Run 3 data-taking periods. The width of the jet energy response is calibrated in simulation to match the width in data, exploiting the transverse momentum balance in QCD dijet events. In this thesis, this method has been extended to cover a jet transverse momentum from 200 GeV to 2000 GeV. A modified correction method for additional jet activity is introduced, refining the uncertainty treatment and the reliability of the calibration. The compatibility of simulation to data is studied, particularly in low transverse momentum ranges which are constrained due to the additional jet activity. The final calibration for data collected at a center-of-mass energy of $\sqrt{s} = 13\,\text{TeV}$ has been performed, covering the years 2016, 2017, and 2018, corresponding to an integrated luminosity of $138\,\text{fb}^{-1}$. Moreover, the first calibrations for data collected at 13.6 TeV is presented for 2022 and 2023 corresponding to $62\,\text{fb}^{-1}$.

The second analysis presents the measurement of the differential $\text{t}\bar{\text{t}}$ production cross section as a function of the jet mass in decays of boosted top quarks, using data collected at 13 TeV corresponding to $138\,\text{fb}^{-1}$. At high momenta, the decay products of top quarks are highly Lorentz boosted and can be reconstructed within a single jet, which require a detailed understanding of the jet substructure. The reconstruction of the hadronic top quark decay in a single jet provides the opportunity to explore new energy regimes. Moreover, the jet mass distribution can be compared to analytic calculations, allowing for the extraction of the top quark mass in a well-defined mass scheme. In this work, the focus is set on the dominant uncertainties of an earlier analysis result, the calibration of the jet mass scale and the modeling of the final state radiation. The uncertainty of the jet mass scale is constrained by calibrating the jet mass scale to the reconstructed W boson mass. A refined modeling of the final state radiation is introduced, based on the $N$-subjettiness. This reduces the uncertainty of the jet mass scale by a factor of three and minimizes the final state radiation modeling uncertainty, making it a negligible source of uncertainties. The jet mass is unfolded to particle level and used to extract the top quark mass with $173.06 \pm 0.84\,\text{GeV}$.

# Zusammenfassung

Diese Arbeit präsentiert zwei Messungen mit Datensätzen, die mit dem CMS-Detektor am LHC in Proton-Proton-Kollisionen aufgezeichnet wurden. Zunächst wird die Messung von Skalenfaktoren für die Auflösung des Transversalimpulses von Jets durchgeführt, gefolgt von der Messung der Jet-Masse in hadronischen Zerfällen von hochenergetischen Top-Quarks und der Bestimmung der Top-Quark-Masse.

In der ersten Analyse werden die Skalenfaktoren für die Jet-Energieauflösung für LHC Run 2 und Run 3-Daten gemessen. Die Breite der Verteilung der Response-Funktion wird in Zweijetereignissen in Simulationen kalibriert, sodass sie mit der Breite in den Daten übereinstimmt. Hierfür wird das Gleichgewicht des Transversalimpulses in solchen Ereignissen ausgenutzt. Diese Methode wurde auf einen Transversalimpulsesbereich von 200 GeV bis 2000 GeV erweitert. Eine verfeinerte Korrekturmethode für zusätzliche Abstrahlung verbessert die Unsicherheit und Zuverlässigkeit der Kalibrierung. Die Kompatibilität der Simulationen mit den Daten wird untersucht, insbesondere in Regionen mit niedrigem Transversalimpuls, die durch die zusätzliche Jet-Aktivität eingeschränkt sind. Die endgültige Kalibrierung wird für LHC Run 2-Daten in 2016, 2017 und 2018 mit einer integrierten Luminosität von $138\,\mathrm{fb}^{-1}$ durchgeführt. Außerdem wird die erste Kalibrierung für LHC Run 3-Daten in 2022 und 2023 mit $62\,\mathrm{fb}^{-1}$ vorgestellt.

Die zweite Analyse präsentiert die Messung des differentiellen $\mathrm{t\bar{t}}$-Produktionsquerschnitts als Funktion der Jet-Masse in Zerfällen von hochenergetischen Top-Quarks, unter Verwendung von Daten, die während des LHC Run 2 gesammelt wurden mit $138\,\mathrm{fb}^{-1}$. Bei hohen Transversalimpulsen haben die Zerfallsprodukte von Top-Quarks einen hohen Lorentz-Faktor und können in einem einzigen Jet rekonstruiert werden. Diese Rekonstruktionen von hadronischen Zerfällen von Top-Quarks ermöglicht die Erforschung neuer Energiebereiche. Zudem kann die Jetmassenverteilung mit Berechnungen verglichen werden um die Masse des Top-Quarks in einem eindeutigen Massenschema zu bestimmen. Der Schwerpunkt liegt auf den vorherrschenden Unsicherheiten in einem früheren Analyseergebnis, der Kalibrierung der Jet-Massenskala und der Modellierung der Endzustandsabstrahlung. Die Unsicherheit der Jet-Massenskala wird durch die Kalibrierung auf die rekonstruierte W-Bosonen-Masse eingegrenzt. Es wird eine verfeinerte Modellierung der Endzustandsabstrahlung eingeführt, die auf der $N$-Subjettiness basiert. Dadurch wird die Unsicherheit der Jet-Massenskala um den Faktor drei reduziert und die Modellierungsunsicherheit der Endzustandsabstrahlung zu einer vernachlässigbaren Quelle von Unsicherheiten minimiert. Die Jet-Masse in Daten wird entfaltet und zur Bestimmung der Masse des Top-Quarks verwendet und ergibt $173.06 \pm 0.84\,\mathrm{GeV}$.

# List of own contributions

## Calibration of the jet energy resolution

I performed the calibration of the jet energy resolution and provided the data-to-simulation scale factors (JER SFs) from QCD dijet events to the CMS Collaboration. This included studies of the transverse momentum imbalance method for increasing center-of-mass energies and luminosity. I measured the JER SFs for the Run 3 data-taking periods in 2022 and 2023, and prepared the final reconstruction iteration for the full Run 2. I regularly presented this work at CMS working group meetings and was the primary author of the Detector Performance (DP) note in Ref. [1]. My work also contributed to the DP Note in Ref. [2] and the forthcoming publication in Ref. [3]. The determination of the JER SFs is presented in Chapter 6. Furthermore, I was responsible for setting up the workflow in a new framework [4], significantly accelerating the overall calibration process.
This work was supervised by Dr. Daniel Savoiu and Dr. Andrea Malara. I also supervised Yannick Fischer, a PhD student, in measuring the JER SFs for future iterations and in conducting additional studies on complementary methods.

## Measurement of the jet mass

I am one of the primary analysts of the CMS measurement of the jet mass in decays of boosted top quarks. My responsibilities included the calibration of the jet mass scale and the modeling of the final state radiation. This involved proper statistical treatment and studies to ensure independence of the several measurement regions in the same phase space. The measurements are build upon first studies performed in Ref. [5] with significant extensions to perform the measurement of the jet mass and the top quark mass. In addition, I performed the measurement of the electron trigger scale factors for the electron channel in 2016, 2017, and 2018.
I presented this work in CMS internal meetings and contributed to the publication process, including the presentation of the approval talks. The measurement is described in Chapter 7 of this thesis and the results are published in Ref. [6]. Furthermore, I am the primary author of the proceedings for the EPS conference in 2023 in Ref. [7]. I presented the measurement at the following conferences:

- QCD@LHC 2022 - Title: “Measurement of the top mass with boosted jets”. This talk included additional results from the ATLAS Collaboration in that field. The presentation is available in Ref. [8].

- 14th International Workshop on Boosted Object Phenomenology, Reconstruction, and Searches in HEP (BOOST) - Title: “Measurement of the jet mass distribution of boosted top quarks and the top quark mass with CMS”. The presentation is available in Ref. [9].

- 42nd International Conference on High Energy Physics (ICHEP) - Title: “Measurements of the top-quark mass from boosted jets at CMS”. This talk included results from the single most precise top quark mass measurement from the CMS Collaboration so far. The presentation is available in Ref. [10].

In the scope of this measurement I supervised one Master’s Thesis [11]. Moreover, I contributed to a new unfolding setup based on a machine learning approach conducted in Ref. [12, 13] by participating in the conceptional work and pre-processing the input features in the simulated samples. The results are currently in preparation for a publication in Ref. [14]. Both analyses are summarized in Section 7.9.
This work was supervised by Dr. Dennis Schwarz, the primary author of the previous analysis and responsible for the unfolding setup in Chapter 7.

In this thesis, the large language model from OpenAI, ChatGPT [15], has been used for proof-reading.

# Contents


**1 Introduction** **1**

**2 Theoretical Background** **5**

2.1 The Standard Model of Particle Physics . . . . . 5

2.1.1 Particle Content of the Standard Model . . . . . 5

2.1.2 From Quantum Fields to Particles . . . . . 6

2.1.3 Quantum Electrodynamics . . . . . 7

2.1.4 Quantum Chromo Dynamics . . . . . 8

2.1.5 Weak Interaction . . . . . 9

2.1.6 Electroweak Interaction . . . . . 11

2.1.7 Electroweak Symmetry Breaking . . . . . 12

2.1.8 Shortcomings of the Standard Model . . . . . 13

2.2 Physics of Proton-Proton Collisions . . . . . 14

2.3 Event Simulation . . . . . 17

2.4 Top Quark . . . . . 18

2.4.1 Top Quarks at the LHC . . . . . 18

2.4.2 Top Quark Mass . . . . . 20

**3 Experimental Setup** **25**

3.1 Large Hadron Collider . . . . . 25

3.2 The Compact Muon Solenoid Detector . . . . . 27

3.2.1 The Coordinate System . . . . . 27

3.2.2 The Tracking System . . . . . 28

3.2.3 The Calorimeter System . . . . . 30

3.2.4 The Solenoid . . . . . 33

3.2.5 The Muon System . . . . . 34

3.2.6 The Trigger System . . . . . 34

**4 Object Reconstruction and Calibration** **37**

4.1 Particle Flow Algorithm . . . . . 37

4.1.1 Muon Identification . . . . . 39

4.1.2 Electron Identification . . . 40
4.2 Jet Clustering Algorithms . . . 40
4.2.1 Iterative Clustering . . . 40
4.2.2 XCone Algorithm . . . 42
4.2.3 Pileup Mitigation Techniques . . . 43
4.3 Identification of b Jets . . . 45
4.4 Jet Calibration . . . 47
4.4.1 Pileup Offset Calibration . . . 48
4.4.2 Simulated Response Corrections . . . 50
4.4.3 Residual Corrections . . . 51
4.4.4 Additional XCone Corrections . . . 52
4.5 Missing Transverse Momentum . . . 54

**5 Jet Substructure at the LHC 55**
5.1 Jet Mass . . . 55
5.2 N-subjettiness . . . 58
5.3 Jet Grooming Techniques . . . 60
5.4 Jet Substructure Measurements at the LHC . . . 61
5.4.1 Jet Mass Measurements . . . 62
5.4.2 *N*-subjettiness Measurements . . . 68

**6 Jet Transverse Momentum Resolution Measurement 71**
6.1 Underlying Structure of the Jet Response . . . 72
6.1.1 Transverse Momentum Imbalance Method . . . 73
6.2 Data and Simulations . . . 75
6.3 Event Selection . . . 77
6.3.1 Treatment of Prescaled Triggers . . . 78
6.4 Scale Factor Determination . . . 81
6.4.1 Measurement of the Asymmetry . . . 81
6.4.2 Alpha Extrapolation . . . 81
6.4.3 Particle Level Imbalance . . . 84
6.4.4 Data-to-Simulation Scale Factors . . . 85
6.4.5 Transverse Momentum Dependence . . . 86
6.5 Systematic Uncertainties . . . 87
6.5.1 Total Systematic Uncertainty . . . 89
6.6 Results . . . 90
6.7 Smearing Procedure in Simulation . . . 91
6.7.1 Scaling Method . . . 91
6.7.2 Stochastic Smearing . . . 91
6.8 Towards Larger Jet Activity . . . 92

6.8.1 Limitations of Transverse Momentum Imbalance . . . . . 92
6.8.2 Missing Transverse Momentum Projection Fraction . . . . . 96
6.9 Complementary Methods . . . . . 98

**7 Measurement of the Jet Mass and Top Quark Mass** **99**
7.1 Analysis Strategy . . . . . 100
7.2 Data and Simulations . . . . . 101
7.3 Event Selection and Reconstruction . . . . . 102
7.3.1 Particle Level . . . . . 102
7.3.2 Detector Level Selection . . . . . 103
7.4 Calibration of the Jet Mass Scale . . . . . 110
7.4.1 Jet Flavor Dependence . . . . . 116
7.4.2 Testing for a bias on $m_{\text{top}}$ . . . . . 117
7.5 Performance at Detector Level . . . . . 119
7.6 Modeling of the Final State Radiation . . . . . 121
7.6.1 Stability against $m_{\text{jet}}$ and $p_{\text{T}}^{\text{jet}}$ . . . . . 125
7.7 Differential Cross Section Measurement . . . . . 126
7.7.1 Unfolding . . . . . 127
7.7.2 Uncertainties . . . . . 129
7.7.3 Results . . . . . 134
7.8 Top Quark Mass Measurement . . . . . 136
7.9 Advancing Measurement Techniques . . . . . 142
7.9.1 Optimizing the High-$p_{\text{T}}$ Reconstruction . . . . . 143
7.9.2 Event-Based Unfolding . . . . . 145

**8 Summary** **149**

**A Electron Trigger Scale Factors** **151**

# Chapter 1

# Introduction

The fundamental building blocks of matter are described by the Standard Model of particle physics (SM). It is one of the most precisely tested theories in science, describing three of the four fundamental forces. Despite numerous experiments confirming SM predictions with high precision, it remains an incomplete theory, unable to account for several observed phenomena. Therefore, many experiments seek to precisely measure SM parameters to uncover potential deviations from this theory, hinting at new physics.
The Large Hadron Collider (LHC), the world's largest and most powerful particle collider, achieves a center-of-mass energy of $\sqrt{s} = 13.6\,\text{TeV}$. Those energy regimes enable the search for new physics, including particles not yet described by the SM. Additionally, the LHC allows for unprecedented precision in measuring SM parameters. The top quark, the heaviest known particle, is of special interest for studies of the SM. Due to its high mass, it plays a crucial role in the electroweak sector and is an essential parameter within the dynamics of particle physics. To probe new physics, to measure elusive SM parameters, such as the Higgs self-coupling, or to perform precision tests of known parameters like the top quark mass, it is crucial to have well-calibrated experiments and accurately measured objects. High-energy proton-proton (pp) collisions at the LHC present numerous challenges for precise measurements. During each bunch crossing, multiple interactions between their constituents occur, resulting in the simultaneous measurements of multiple processes. Additionally, radiation of gluons and quarks complicate the reconstruction of the final states from the physics processes of interest. This complexity particularly affects the reconstruction of jets, which are collimated sprays of hadrons originating from color-carrying particles. Jets are present in many final states and are thus crucial for analyses at the LHC. Miscalibration of jets can lead to momentum imbalances in a process and inaccuracies in the measurement of missing energy. Future data-taking periods at the LHC will encounter even harsher conditions, necessitating meticulous calibrations of physics objects to correct for such effects. Therefore, a profound understanding and accurate calibration of jets are essential to enhance the measurement precision. The calibration of jets at the Compact Muon Solenoid (CMS) detector involves determining the jet response, which is a measure of the deviation of the measured momentum from the true value. The width of the jet response,

referred to as jet energy resolution (JER), is of particular interest in this thesis. The JER in simulation is typically better than in data, necessitating corrections to match the JER in data. A well-established method for this calibration exploits the particle-level $p_{\mathrm{T}}$ imbalance in events consisting of two back-to-back jets. However, this method becomes less effective under increasingly challenging conditions. In this thesis, the possibilities for JER measurements using the transverse momentum imbalance method are explored as a preparation for Run 3 of the LHC and the final calibration in Run 2. Data-taking periods with an integrated luminosity of about $138\,\mathrm{fb}^{-1}$ at $\sqrt{s} = 13\,\mathrm{TeV}$ and $62\,\mathrm{fb}^{-1}$ at 13.6 TeV are analyzed.

At high momenta, the decay products of heavy-flavor particles are highly Lorentz-boosted and can be reconstructed within a single large-radius jet, opening up novel possibilities in jet substructure measurements. Jet substructure measurements are of great importance for analyses targeting decays of heavy-flavor particles, as they allow for the identification of the particle that initiates the jet. For instance, the mass of jets that reconstruct the full hadronic decay of boosted top quarks is sensitive to the top quark mass. Moreover, the jet mass distribution can be derived from analytic calculations, offering the measurement of the top quark mass in a well-defined mass scheme [16]. However, energy regions in which the calculations are performed are not yet experimentally accessible at the LHC and the extraction of the top quark mass still relies on simulations. Modeling the evolution of jets is complicated by non-perturbative effects such as hadronization, color reconnection, and contributions from the underlying event. Simulations address these effects using free parameters from theory, known as tunes. These tunes are subject of many analyses, aiming to refine the set of parameters in event generators to resemble data more closely. Moreover, measurements involving the jet mass often encounter large uncertainties due to jet calibrations. Traditional calibrations are based on the transverse momenta of the jets, but the jet mass is introduced as an additional free parameter that is not typically covered. Dedicated studies on the W boson mass are frequently used for specific calibrations. In the scope of this thesis a measurement of the differential $\mathrm{t\bar{t}}$ cross section as a function of the jet mass and the extraction of the top quark mass is performed. This measurement has been performed previously with up to $36.5\,\mathrm{fb}^{-1}$ by the CMS Collaboration [17, 18]. With the latest iteration of the jet mass measurement [18], the largest uncertainties have been identified with the calibration of the jet mass scale (JMS) and the modeling of the final state radiation (FSR). In this thesis, the measurement is extended to a dataset corresponding to $138\,\mathrm{fb}^{-1}$ collected in the years 2016 to 2018. The JMS is calibrated using hadronic W boson decays, which are independent of the top quark mass and can be reconstructed from the hadronic top quark decay. Additionally, parton shower models are studied, exploiting the dependence of the $N$-subjettiness ratio $\tau_{32}$ on the FSR scale. Detector effects are corrected using the unfolding setup from the previous analysis [18]. The top quark mass is extracted from the unfolded normalized distribution. Results of this measurement have been published in Ref. [6].

This thesis is organized as follows. Chapter 2 provides a description of the mathematical foundations of the SM relevant to this thesis and discusses properties of the top quark. In Chapter 3,

the experimental setup is outlined, including the LHC complex and the CMS detector. Techniques for event reconstruction and calibration are summarized in Chapter 4. An overview of current jet substructure measurements, with an emphasis on the reconstruction of heavy-object decays within a single jet is presented in Chapter 5. The JER measurements performed in this thesis are discussed in Chapter 6. The measurement of the differential $\mathrm{t\bar{t}}$ production cross section as a function of jet mass and the extraction of the top quark mass is elaborated on in Chapter 7. Emphasis is set on the calibration of the JMS and the modeling of the FSR in simulations, which are key points in this thesis. A summary of the results obtained in this thesis is given in Chapter 8.

# Chapter 2

# Theoretical Background

Our knowledge of particle physics is described by the Standard Model of particle physics (SM). It covers all particles observed so far and describes their interaction with each other in a great energy range. In order to test the boundaries and the internal structure of the theory and search for new physics, high-energy collider experiments are utilized, such as the LHC, a proton-proton (pp) collider. This chapter gives an overview of the mathematical description of the SM in Section 2.1. The mechanics of proton-proton collisions are described in Section 2.2 and event generators used in high energy physics in Section 2.3. The top quark, a particle of key interest in this thesis, is discussed in Section 2.4. This chapter is based on Ref. [19, 20, 21, 22] if not stated otherwise.

## 2.1 The Standard Model of Particle Physics

The SM is one of the most precisely tested theories in modern physics and describes various observed phenomena. It describes our current knowledge of known matter and three of the four fundamental interactions. These interactions are the electromagnetic (EM), the weak and the strong interaction. The underlying structure of the SM is based on the symmetry group $\mathrm{SU(3)_C \times SU(2)_L \times U(1)_Y}$ . The spontaneous symmetry breaking to incorporate massive gauge bosons into the theory is introduced through the Brout-Englert-Higgs mechanism in the electroweak sector with the symmetry group $\mathrm{SU(2)_L \times U(1)_Y}$. An overview of all particles described by the SM and their properties is shown in Figure 2.1.

### 2.1.1 Particle Content of the Standard Model

Fermions are spin-$\frac{1}{2}$ particles classified into quarks ($q$) and leptons ($\ell$). Quarks carry a color charge and are therefore subject to the strong interaction, while leptons are colorless. Leptons include the electron ($e$), muon ($\mu$), and tau ($\tau$), each of which carry an elementary charge of -1. For each lepton flavor, a corresponding neutrino ($\nu$) exists that carries no electrical charge and interacts solely via the weak force. Despite being postulated as massless, measurements

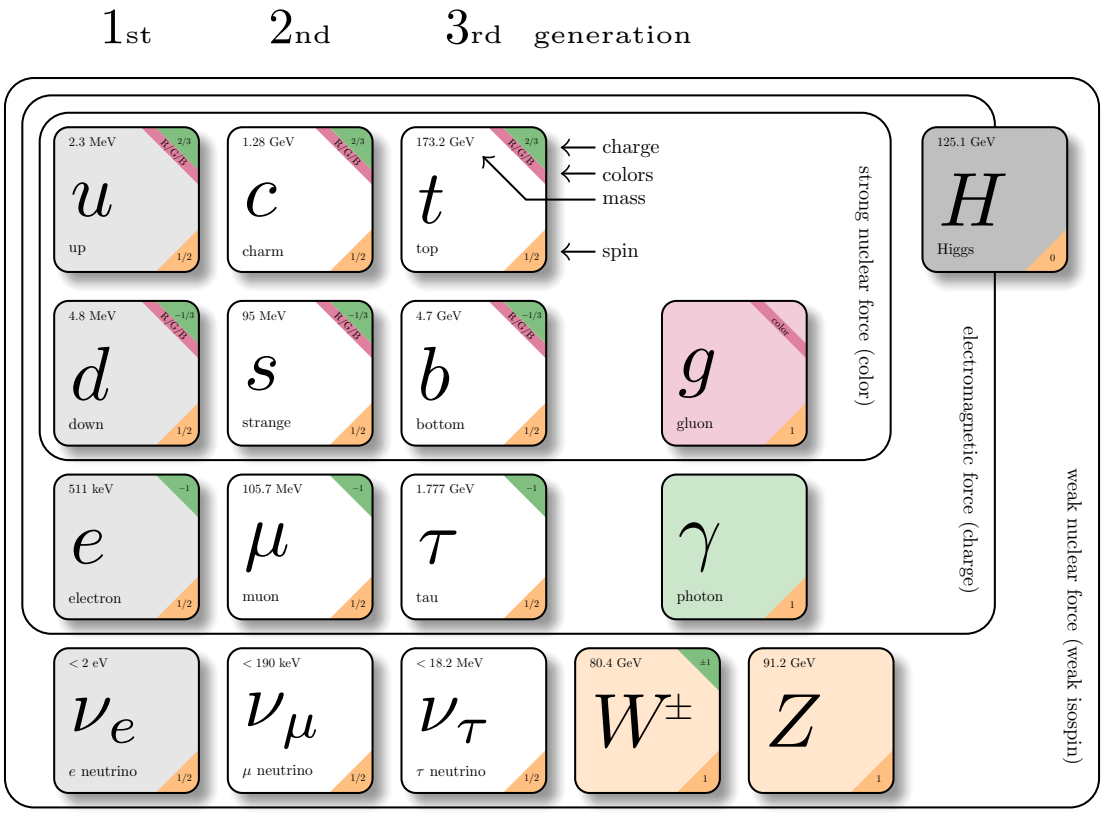


**Figure 2.1:** Overview of particles described by the SM. The defining properties of each particle and the corresponding interactions it takes part in are shown. Adapted from Ref. [23].

of neutrino oscillations [24, 25] indicate that neutrinos have a mass. Up and down-type quarks carry an electrical charge of $+\frac{2}{3}$ and $-\frac{1}{3}$, respectively. All leptons also carry an isospin and are further divided into three generations, consisting of two fermions each. The masses of particles are increasing for higher generations. A generation of the leptons consist of a lepton $\ell$ and the corresponding neutrino $\nu_\ell$. Quarks are classified into up and down-type quarks.
Interaction between two fermionic fields are described by exchanging a gauge boson. These gauge bosons carry a spin of $S = 1$. Each type of gauge boson corresponds to one of the three forces described by the SM, namely the EM- (photon), weak- (W and Z boson) and the strong interaction (gluon). A more detailed description and a mathematical foundation of the mechanism of the SM are described in the following sections. With the discovery of the spin-0 massive Higgs boson, a scalar boson, in the year 2012 by the ATLAS [26] and CMS [27] Collaborations, all particles postulated by the SM have been observed.

### 2.1.2 From Quantum Fields to Particles

Quantum field theory (QFT) characterizes the quantum mechanical behavior of particles in a relativistic framework, ensuring the preservation of Lorentz invariance, unitarity, and locality.

Instead of describing particles with wave characteristics as in the first quantization, QFT postulates particles to be quantized excitations of underlying quantum fields. In terms of fermions, the Dirac spinor, denoted as $\psi(x)$, is utilized to describes spin-$\frac{1}{2}$ particles. The dynamics of a free fermion can be expressed via the corresponding Lagrangian density

$$\mathscr{L}_{\mathrm{D}} = \bar{\psi}\left(i\gamma^{\mu}\partial_{\mu} - m\right)\psi, \tag{2.1}$$

with $\gamma^{\mu}$ symbolizing the gamma matrices and $m$ representing the mass of the fermion.
Maintaining causality, one of the most fundamental principles in physics, necessitates invariance of the Lagrangian under a local transformation. This requires the Lagrangian to remain unchanged under local transformation of space-time parameters, such as the four momentum of the particle $x$. The invariance can be established by postulating a vector field, also referred to as gauge field, as discussed in the upcoming sections. Gauge bosons, the mediators of the fundamental forces described by the SM, are identified as the excitations of these gauge fields.
The characterization of each fundamental force is obtained through the utilization of distinct symmetry groups. The choice of symmetry groups for the corresponding interactions is based on the behavior observed in experiments. Noether's Theorem, a fundamental principle connecting symmetries and conservation laws, postulates that each symmetry group evokes a specific neutral current. These currents are identified with the charges of the various interactions. Consequently, all (anti)particles involved in these interactions must possess the appropriated (anti)charge.

### 2.1.3 Quantum Electrodynamics

Quantum Electrodynamics (QED) is one of the earliest developed QFTs and lays the foundation for the understanding for the upcoming attempts to describe fundamental forces via symmetry groups. It describes the EM interaction between two fermions by exchanging a massless photon.
QED is build upon the symmetry group U(1) with the local gauge transformation

$$\psi \rightarrow \psi' = e^{iq\alpha(x)}\psi, \tag{2.2}$$

with the phase $\alpha$ depending on the four-momentum $x$. Thus, the U(1) invokes a scalar and real phase shift of the fermionic field. The electric charge $q$ of the particle refers to the conserved current of QED. The kinetic term $\bar{\psi}i\gamma^{\mu}\partial_{\mu}\psi$ is not invariant under the gauge transformation in Equation 2.2. As stated in Section 2.1.2, the invariance can be ensured by introducing a gauge field. Those fields are proposed by adding a complex term to the partial derivative $\partial_{\mu}$, to form the gauge-covariant derivative $D_{\mu}$. In terms of the U(1) symmetry group, the gauge-covariant derivative is introduced with

$$\partial_\mu \rightarrow D_\mu = \partial_\mu + iqA_\mu(x), \tag{2.3}$$

where $A_\mu(x)$ is a gauge field. In order to preserve the invariance under a local gauge transformation, the newly introduced gauge field must transform via $A_\mu(x) \rightarrow A_\mu(x) - \frac{1}{q}\partial_\mu\alpha(x)$. Since the U(1) symmetry group is an Abelian group, meaning that the elements commute, the photon has no electrical charge and does not self-interact. The replacement of the derivative $\partial_\mu$ with the covariant derivative $D_\mu$ leads to the Lagrangian density for QED

$$\mathscr{L}_{\text{QED}} = \bar{\Psi}i\gamma^\mu\partial_\mu\Psi - m\bar{\Psi}\Psi - q\bar{\Psi}\gamma^\mu\Psi A_\mu(x) - \frac{1}{4}F_{\mu\nu}F^{\mu\nu}. \tag{2.4}$$

The first two terms are identical to the Dirac Lagrangian density in Equation 2.1. The third term contains the newly introduced gauge field and its coupling to the fermionic field. Considering the local gauge transformations in Equation 2.2, only the addition of an external force that interacts with the fermionic field, ensured the invariance of such. This additional gauge field can be interpreted as a photon field. The last term represents the kinematics of the photon field, with the field strength tensor $F_{\mu\nu} = \partial_\mu A_\nu - \partial_\nu A_\mu$.
The coupling strength of the EM interaction, $\alpha_{\text{EM}} = e^2/4\pi$, depends on the momentum transfer $q^2$ duringan interaction. Dependencies of free parameters in the SM on $q^2$, such as $\alpha_{\text{EM}}$, can be described using perturbative theory. The solutions to the equations of motions derived from the SM Lagrangian are expanded in terms of the coupling constants. The dependence on $q^2$ can be determined by considering only a certain number of higher-order processes in the perturbative expansion series. At leading order (LO), only processes involving two vertices with the coupling $\sqrt{\alpha}$ are considered, while next-to-leading order (NLO) calculations include a third vertex. Loop corrections to the propagator are addressed in higher-order processes, which involve at least four vertices. Specifically, in terms of $\alpha_{\text{EM}}$ at LO, e.g. for infinitesimal momentum transfers, the effective strength reads $\alpha_{\text{EM}}(q^2 \rightarrow 0) \approx 1/137$ [28]. For increasing energy scales and thus requiring to consider higher-order processes in the perturbative expansion series, the effective strength of $\alpha_{\text{EM}}$ also increases. At the energy scale at the Z boson mass the strength is measured with $\alpha_{\text{EM}}(M_{\text{Z}}) \approx 1/129$ [29].

### 2.1.4 Quantum Chromo Dynamics

Quantum Chromodynamics (QCD) offers a comprehensive framework for understanding the dynamics of the strong interaction. The nature of the strong force exhibits a more complex behavior than the EM interaction and can be described in terms of the symmetry group $\text{SU(3)}_{\text{C}}$. Here, the subscript $C$ indicates the color charge, the conserved current in QCD. The group's dimension $N_{\text{C}} = 3$ denotes the degrees of freedom associated with the color charge, commonly referred to as blue, green and red. As a consequence, the fermionic field in QCD is constructed

by the inclusion of color states represented by

$$\psi_{\mathrm{q}} = \begin{pmatrix} \psi_b \\ \psi_g \\ \psi_r \end{pmatrix}. \tag{2.5}$$

In contrast to QED, where local transformations solely induce phase transitions, QCD transformations necessitate rotations within the color space. In general, these rotations are induced by $N$-dimensional generators. The required number of generators for an SU($N$) symmetry group is given by $N^2 - 1$. Consequently, for $\mathrm{SU(3)_C}$, eight generators are necessary, which can be represented by the eight Gell-Mann (GM) Matrices $T^{\mathrm{a}}$ with $a \in \{1 \dots 8\}$, which are $3 \times 3$ Hermitian matrices. Corresponding to the eight generators, eight unique and massless gluon fields are introduced in QCD. Within a non-Abelian groups, such as $\mathrm{SU(3)_C}$, vector-fields also convey the conserved current, enabling gluon self-coupling. This leads to the conclusion that each gluon field represents a superposition of color and anti-color states. The Lagrangian is similar to Equation 2.4, but also comprising the six quarks and the gluon field strength tensor

$$G_{\mu\nu,a} = \partial_\mu G^a_\nu - \partial_\nu G^a_\mu - g_S f^{abc} G^b_\mu G^c_\nu. \tag{2.6}$$

Here, the last term indicates the gluon self-interaction with the constant structure $f^{abc}$ and the coupling of the strong interaction $g_S$.

Similar to QED, the coupling strength of QCD $\alpha_{\mathrm{S}}$, depends on the energy scale of an interaction, i.e. the momentum transfer $q^2$ of two particles. At the Z boson mass scale, the coupling strength has been measured with $\alpha_{\mathrm{S}}(M_Z^2) = 0.1179 \pm 0.0009$ [30] and decreases logarithmically with increasing energy and decreasing length scale. This phenomenon leads to asymptotic freedom, implying that quarks behave almost as free particles at high energies, equivalent to small length scales. Consequently, the field density of the gluon field between two separated colored particles increases with the distance, due to the self-interaction of gluons. For sufficiently large energies, the creation of a new quark-antiquark ($\mathrm{q\bar{q}}$) pair is favored. For that reason, quarks will ultimately form color-neutral bound states called hadrons, further classified into mesons ($\mathrm{q\bar{q}'}$ pairs) or baryons (three quarks). The formation of hadrons is also referred to as hadronization. The phenomenon that colored particles cannot be measured in isolated states but are invariably detected in color-neutral bounded states is also known as color confinement. Furthermore, the increase in the strong coupling strength for small energy scales ($q \approx 1\,\mathrm{GeV}$) means that perturbation theory is no longer applicable. Consequently, the hadronization cannot be described by analytical calculations but need to be simulated based on phenomenological models.

### 2.1.5 Weak Interaction

The weak interaction is represented by the $\mathrm{SU(2)_L}$ symmetry group, with the weak isospin $I$ as the conserved current. Invariance of the Lagrangian requires the introduction of three vector

fields $W^{1,2,3}$.

The Wu experiment [31] demonstrated for the first time that the weak interaction violates parity conversation, indicating that it does not behave symmetrically under spatial reflections. The results of this experiment showed that left and right handed particles are not treated equally in CC interactions. Here, left and right handed referrers to the helicity, the projection of the spin of the particles onto its momentum. The behavior can be described in terms of the chirality, a fundamental quantum mechanic property, introducing two different states for fermions. These states are also denoted as left ('L') and right ('R') handed. For massless particles, which consequently travel with the speed of light, the chirality corresponds to the helicity. It turns out that the CC solely couples to left (right) handed (anti) fermions.

Left-handed particles form doublets in the isospin space. For the lepton sector, these doublets consist of a charged lepton $\ell$ and the corresponding electrically neutral neutrino $\nu_\ell$ and are grouped as follows:

$$\begin{pmatrix} \nu_e \\ e \end{pmatrix}_{\mathrm{L}}, \begin{pmatrix} \nu_\mu \\ \mu \end{pmatrix}_{\mathrm{L}}, \begin{pmatrix} \nu_\tau \\ \tau \end{pmatrix}_{\mathrm{L}}. \tag{2.7}$$

Quarks are arranged similarly into up- and down-type quarks with

$$\begin{pmatrix} u \\ d' \end{pmatrix}_L, \begin{pmatrix} c \\ s' \end{pmatrix}_L, \begin{pmatrix} t \\ b' \end{pmatrix}_L. \tag{2.8}$$

Up- and down-type quarks carry an electrical charge of $Q = +\frac{2}{3}$ and $-\frac{1}{3}$, respectively. Both, neutrinos ($\nu_e$,$\nu_\mu$,$\nu_\tau$) and the up-type quarks (*up*, *charm*, $top$) carry a weak isospin of $T_3 = +\frac{1}{2}$. For charged leptons ($e$,$\mu$,$\tau$) and the down-type quarks (*down*, *strange*, $bottom$) the weak isospin is $T_3 = -\frac{1}{2}$. Two out of the three vector fields $W^{1,2,3}$ couple to particles with opposite $T_3$. Consequently, these two vector fields $W^{1,2}$ must carry an isospin of $T_3 = \pm 1$ and an electric charge of $Q = \pm 1$. In the quark sector, it has been observed that the CC couples to up- and down-type quarks from different generations. This can be explained due to the difference of the mass state (d,s,b) and the flavor state (d',s',c') of quarks. The CC couples to the latter. The connection of both states is made via the unitary matrix Cabibbo-Kobayashi-Maskawa (CKM) matrix

$$\begin{pmatrix} d' \\ s' \\ b' \end{pmatrix} = \begin{pmatrix} V_{ud} & V_{us} & V_{ub} \\ V_{cd} & V_{cs} & V_{cb} \\ V_{td} & V_{ts} & V_{tb} \end{pmatrix} \begin{pmatrix} d \\ s \\ b \end{pmatrix}. \tag{2.9}$$

The transition probability of both states are given by the squared matrix element $|V_{\mathrm{ij}}|^2$ between two quarks $i$ and $j$. The values have been measured by several experiments and a combined fit yields [30]

$$\begin{pmatrix} V_{ud} & V_{us} & V_{ub} \\ V_{cd} & V_{cs} & V_{cb} \\ V_{td} & V_{ts} & V_{tb} \end{pmatrix} = \begin{pmatrix} 0.9737 \pm 0.0003 & 0.2243 \pm 0.0008 & 0.0038 \pm 0.0002 \\ 0.221 \pm 0.004 & 0.975 \pm 0.006 & 0.0408 \pm 0.0014 \\ 0.0086 \pm 0.0002 & 0.0415 \pm 0.0009 & 1.014 \pm 0.029 \end{pmatrix}. \quad (2.10)$$

The rare CP violation within the SM due to the weak interaction is caused by a complex phase included in the CKM matrix. The third vector field $W^3$ exclusively couples to particles with the same isospin and hence carries no isospin and no electrical charge. Flavor changing neutral currents have not yet been observed and are not described by the SM Lagrangian.

### 2.1.6 Electroweak Interaction

Up to this point, all interactions mentioned are described separately with distinct symmetry groups. As discussed previously, the coupling strength of each interaction is scale dependent. It is assumed that all three interactions unify at the Planck scale with $10^{19}$ GeV, each having the same coupling strength. Hence, it is plausible to consider all interactions not as separated theories, but as one, the so-called grand unification theory. The first milestone is accomplished by unifying the QED and weak interaction into the Electroweak Interaction (EWI).
The underlying symmetry group is $\mathrm{SU(2)_L \times U(1)_Y}$. The subscript now indicates the hypercharge $\mathrm{Y} = 2(Q - T_3)$ and combines the conserved currents of QED and the weak interaction. In total, four vector fields are required to implement gauge invariance. These vector fields consists of two charged ones $W_\mu^{1,2}$ and as well as two neutral ones $W_\mu^3$ and $B_\mu$. The gauge bosons from the weak interaction ($W^\pm$, $Z^0$) as well as the QED ($\gamma$) are constructed via a linear combination of these vector fields. For the charged gauge bosons the combination reads

$$\mathrm{W}^\pm = \frac{1}{\sqrt{2}} \left( W_\mu^1 \mp i W_\mu^2 \right), \quad (2.11)$$

while neutral bosons are constructed via

$$\begin{pmatrix} A_\mu \\ Z_\mu \end{pmatrix} = \begin{pmatrix} \cos\theta_W & \sin\theta_W \\ -\sin\theta_W & \cos\theta_W \end{pmatrix} \begin{pmatrix} B_\mu \\ W_\mu^3 \end{pmatrix}. \quad (2.12)$$

The Weinberg angle $\Theta_W$ combines the electromagnetic ($\alpha_{\mathrm{EM}}$) and weak ($\alpha_{\mathrm{W}}$) coupling strength with $\alpha_{\mathrm{W}} = \alpha_{\mathrm{EM}} / \sin^2 \Theta_W$.
While the force carriers of the QCD (*gluons*) and QED (*photon*) are massless, the $W^\pm$ and $Z^0$ bosons have in fact masses of $M_{\mathrm{W}} = 80.4\,\mathrm{GeV}$ and $M_{\mathrm{Z}} = 90.2\,\mathrm{GeV}$ [30]. These masses directly cause the compatibly small coupling strength and short range of the weak interaction.
Up to this point, gauge bosons have been considered massless to preserve local gauge transformation. The observation of massive gauge bosons directly contradicts this requirements, but can be resolved by the mechanism of electroweak symmetry breaking.

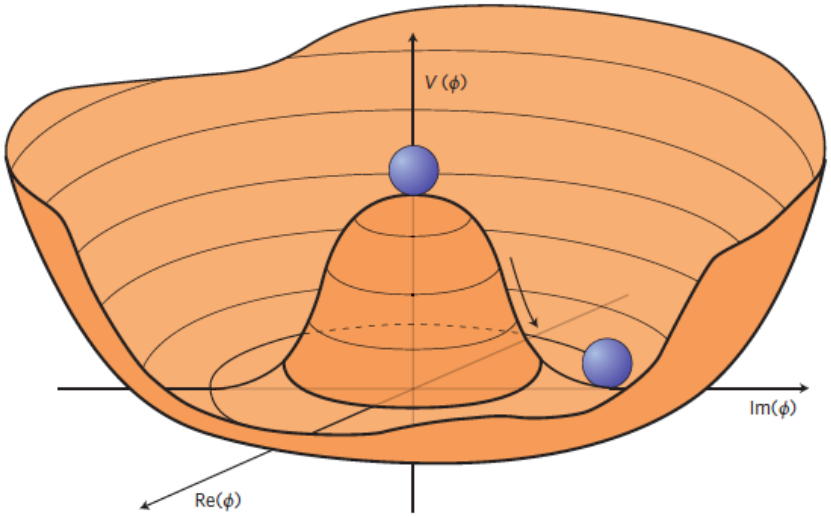


**Figure 2.2:** Potential of the Higgs field introduced in scope of the electroweak symmetry breaking. The ground state no longer assumes a single value but consists of infinite degenerated local minima. Taken from Ref. [32].

### 2.1.7 Electroweak Symmetry Breaking

Electroweak symmetry breaking allows to include massive gauge bosons into the framework of the SM without violating local gauge invariance. A complex scalar field doublet with hypercharge $Y = 1$ and isospin $T_3 = +\frac{1}{3}$ is postulated with

$$\phi = \begin{pmatrix} \phi^+ \\ \phi^0 \end{pmatrix} = \begin{pmatrix} \phi_1 + i\phi_2 \\ \phi_3 + i\phi_4 \end{pmatrix}. \tag{2.13}$$

The Lagrangian of this field reads

$$\mathscr{L}_{\mathrm{H}} = \left(D_\mu \phi\right)^\dagger \left(D^\mu \phi\right) - V\left(\phi\right). \tag{2.14}$$

Here, the covariant derivative is taken from the EWI facilitating the interaction of the complex field with the vector boson fields. The Higgs potential $V\left(\phi\right)$ is postulated with

$$V(\phi) = \mu^2|\phi|^2 + \lambda|\phi|^4, \tag{2.15}$$

where $\mu$ and $\lambda$ are real parameters, steering the shape of the potential. In case of $\mu^2 < 0$, i.e. that $\mu \in \mathbb{C}$, the ground state is not defined by a single value anymore but assembles from infinite degenerated local minima, inducing spontaneous electroweak symmetry breaking.
This leads to the so-called Mexican hat potential visualized in Figure 2.2 with the vacuum expectation value (VEV) $v = \sqrt{-\mu^2/\lambda} \approx 246\,\mathrm{GeV}$ [30]. Expanding the Higgs field around the minimum leads to

$$\phi = \frac{1}{\sqrt{2}} \begin{pmatrix} 0 \\ v + H(x) \end{pmatrix}, \tag{2.16}$$

where the excitation $H(x)$ can be interpreted as the Higgs boson, a scalar particle with a mass $M_{\mathrm{H}} = \sqrt{-2\mu^2}$. The inclusion of the Lagrange density $\mathscr{L}$ under the assumption of $V(\phi)$ manifests into terms including the Higgs self-coupling and the interaction of the weak gauge bosons with the higgs field. The latter introduces the masses of the weak gauge bosons with

$$M_W = \frac{1}{2} v g_{\mathrm{W}} \tag{2.17}$$

and

$$M_Z = \frac{1}{2} v \sqrt{g_{\mathrm{W}}^2 + g'^2}, \tag{2.18}$$

with $g' = e/\cos\theta_W$ as the coupling of the gauge interaction underlying $\mathrm{U(1)_Y}$. Introducing the electroweak symmetry breaking now allows for the description of massive gauge bosons.
Nevertheless, not only gauge bosons couple to the Higgs field but so do fermions. Introducing chirality for fermions also leads to the loss of invariance of the mass term of fermions under $\mathrm{SU(2)_L} \times \mathrm{U(1)_Y}$ transformation, since left- and right-handed particles transform differently. Again, the coupling to the Higgs field via the Yukawa coupling $y_f$ introduces the fermion masses with

$$m_f = \frac{v}{\sqrt{2}} y_f. \tag{2.19}$$

The Yukawa couplings $y_f$ are not predicted by the SM and remain free parameters, which have to be measured experimentally.

### 2.1.8 Shortcomings of the Standard Model

The previous sections described the SM and its description of fermions and their interactions with each other. The discovery of the Higgs boson and the very precise measurements of many parameters of the SM prove the solid description of our matter based on the SM. However, many observations are not covered by the SM and structural limitations within its framework lead to the necessity of further expansion of the theory.
Currently, there is no quantum theory of gravity and thus the gravitational force cannot yet be unified with the SM. One of the most prominent observational incompleteness is the absence of a quantum theory of gravity and thus the gravitational force cannot yet be unified with the SM. So far, gravity is well described within the framework of General Relativity and has been extensively tested over the last century. Nonetheless, there are no theories that successfully describe gravity in terms of quantum fields. Some initial approaches are able to describe gravity as an effective field theory [33], but those violate unitarity at the Planck scale, $\Lambda_{\mathrm{P}} \sim 10^{10}\,\mathrm{GeV}$.
Furthermore, the known matter described by the SM does not conform the behavior of cosmological observation, such as the rotational speed of galaxies, gravitational lensing measurement or microwave background experiments. Observation of the bullet cluster [34] provides strong

evidence for additional matter in the universe, not yet observed. This type of matter is expected to not interact via the strong or EM force but only via the weak force and gravity. The SM does not provide a suitable candidate providing these properties. Similarly, the presence of dark energy, a greater energy density in the vacuum as expected leading to an accelerated expansion of the universe, is not predicted by the SM. Another prominent phenomenon is the matter-antimatter asymmetry. Our universe mainly consists of matter, implying a different behavior of particles and antiparticles. Theories addressing these unknown interactions postulate new particles not covered by the SM. Furthermore, masses of the neutrinos and the mechanism of neutrino oscillation is also not part of the SM.
While the above are more general observations not explained by the SM, several experiments measured parameters of the SM that show a deviation in comparison to the predicted values. Such measurements are the anomalous magnetic dipole moment of muons with a deviation of $5\sigma$ [35] from the SM, the violation of the lepton flavor universality [36, 37] or the W boson mass measurement from CDF [38], claiming a $7\sigma$ deviation from the SM. While the results give hints for new physics, there are great efforts to confirm these results or rule out systematic errors. Nonetheless, these results also lead to the necessity to refine the description of the SM. For instance, precision measurements of the mass of the W boson, the top quark and the higgs boson give insights into the stability of the vacuum [39] and thus are essential for the understanding of the theory.
Furthermore, the internal structure of the SM often gives rise to discussions. For instance, it remains impossible to derive the masses of fermions from first principles and these masses must be determined experimentally. Additionally, the mass of the Higgs boson is substantially influenced by loop corrections, primarily due to the top quark and the electroweak bosons. If the SM is presumed valid up to the Planck scale, these loop corrections would predict a Higgs mass far exceeding the observed value of approximately $\sim 125\,\text{GeV}$. This discrepancy is known as the fine-tuning problem of the Higgs mass [40], which implies that the loop corrections must almost exactly cancel each other out to a large degree. This behavior is generally considered to be unnatural. To that end, theories beyond the SM introduce new particles that naturally cancel these loop correction effects.

## 2.2 Physics of Proton-Proton Collisions

The analyses presented in this thesis are based on data collected by the CMS experiment located at the LHC, a pp collider. Therefore, a detailed understanding of the kinematics of pp collisions is important to make predictions for the observed data.
The proton is not an elementary particle but a complex assembly of quarks and gluons, historically referred to as partons. These partons are categorized into *valence quarks*, *sea quarks* and gluons. The valence quarks, comprising two up quarks and one down quark, define the properties of the proton, such as the electric charge ($Q = +1$). These quarks constantly inter-

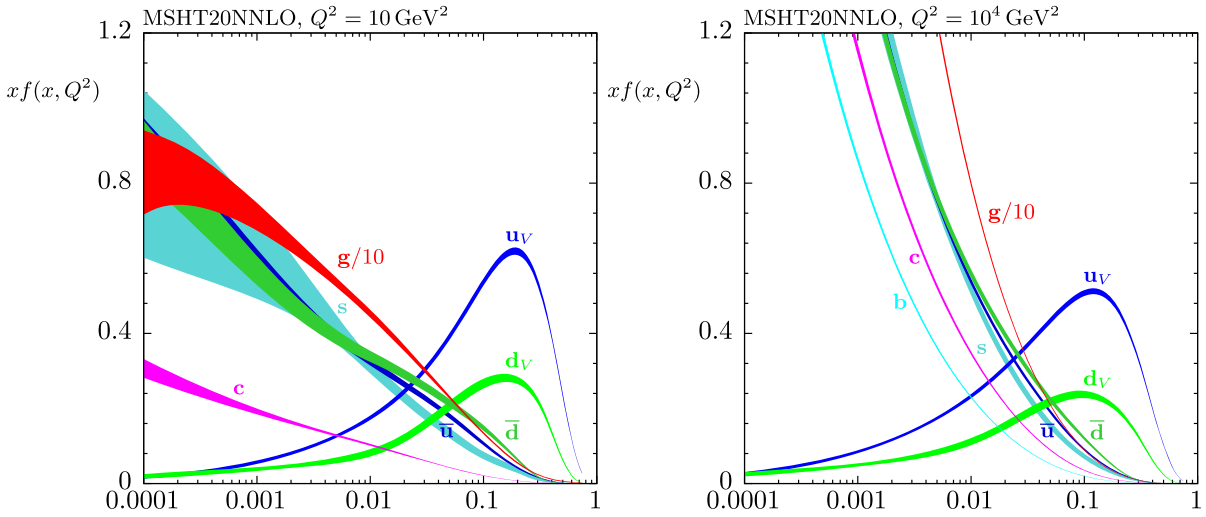


**Figure 2.3:** Parton distribution function as a function of the Bjorken $x$ of the proton for NNLO at $q^2 = 10\,\mathrm{GeV}$ (left) and $1000\,\mathrm{GeV}$ (right). The thickness of the bands corresponds to 68 % confidence-interval. Taken from Ref. [43].

acting with each other by mediating gluons. Simultaneously, the gluon fields within the proton, give rise to quark-antiquark pairs originating from vacuum fluctuations, also referred to as sea quarks.

The momentum of the proton is shared among all its partons, with the Bjorken $x$ defining the momentum fraction of a parton. The probability to encounter a specific parton type within the proton is described by the parton distribution function (PDF), a function of the Bjorken $x$ and the energy scale $Q^2$. While these PDFs cannot be determined from analytic calculations, the scale dependency can be predicted by the DGLAP evolution equations [41, 42]. Thus, the PDF functions are empirically parameterized on $x$ at low scales $q_0^2$ in simulation and compared to data. Predictions for higher scales $q^2 > q_0^2$ can be then calculated with the DGLAP equations. The measurement can be conducted in a variety of initial and final states such as in fixed target experiments, deep inelastic scattering ($\ell$-hadron collisions) or hard scattering processes from hadron colliders like the LHC. Measurements for the MSHT20 PDFs [43] are depicted in Figure 2.3 for $q^2 = 10\,\mathrm{GeV}$ (left) and $1000\,\mathrm{GeV}$.

The internal structure comes with many challenges in simulating the hard scattering processes. While the initial momenta of the protons are well known, the momentum fractions of the partons are not. For a collision of two opposing protons in $z$ direction, as occurs at the LHC, the final state particles are often Lorentz-boosted in the laboratory system, due to the different momenta of the interacting partons. While the momentum of the initial state particles is unknown in flight direction, the transverse component ($x$ and $y$ direction) vanishes in good approximation and is equal in the laboratory and center-of-mass system. As a consequence, the combined transverse momentum $p_\mathrm{T} = \sqrt{p_\mathrm{x}^2 + p_\mathrm{y}^2}$ of all final state particles must also vanishes.

In order to predict the final state of one process, the knowledge of the cross section $\sigma$, a measure of how likely a process occurs, is crucial. Due to the internal structure of protons, the

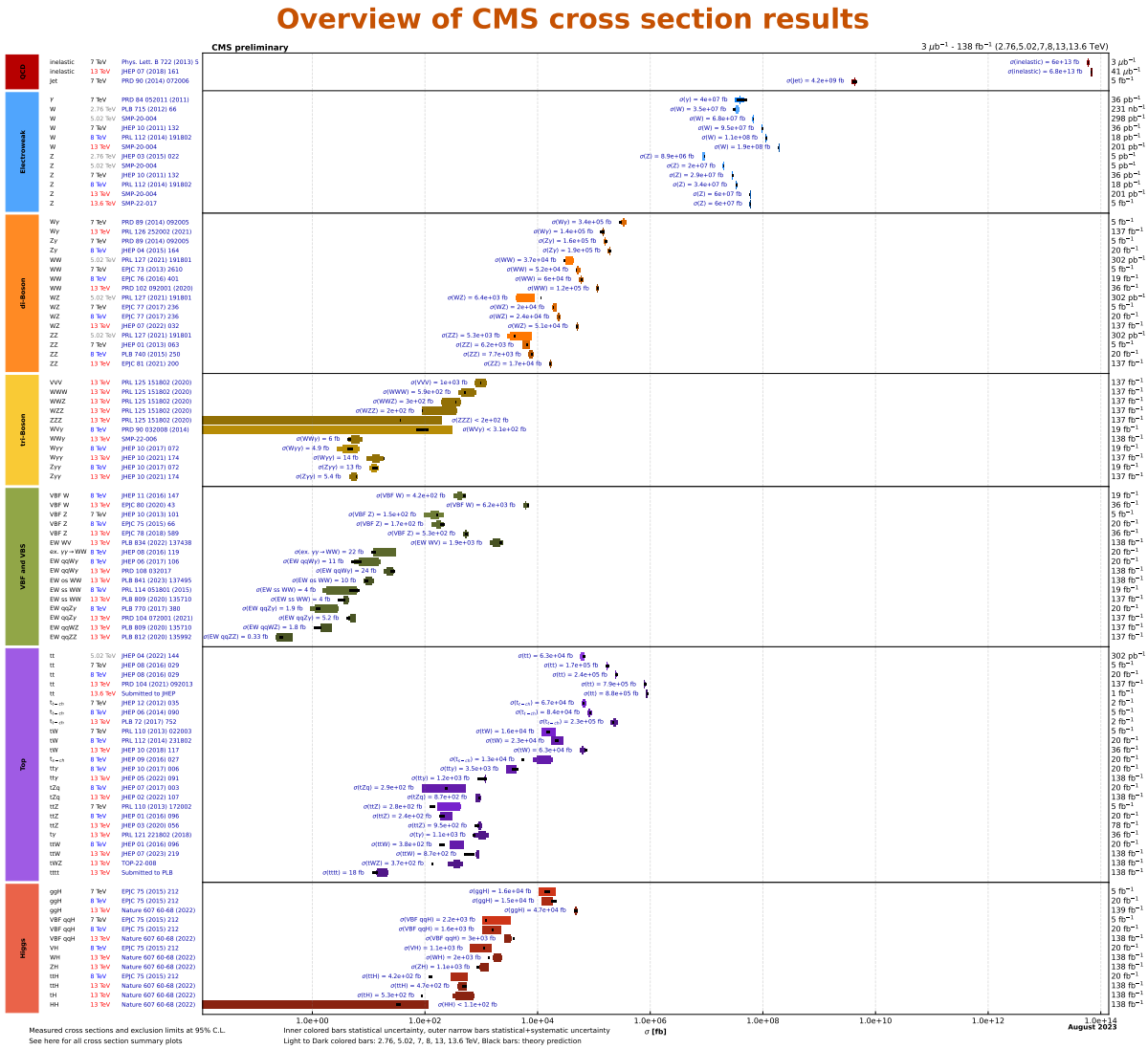


**Figure 2.4:** Summary of predicted cross sections for several Standard Model processes (black bars) measured by the CMS Collaboration (colored bars). The measurements are performed for center-of-mass energies of $\sqrt{s} = 7$, 8, 13 and 13.6 TeV. Taken from Ref. [46].

cross section of a specific process depends on the knowledge of all PDFs $f_i(x, Q^2)$ for a parton type $i$. Based on the factorization theorem [44, 45], the cross section can be calculated for hard scattering processes. To that end, the cross section $\sigma_{ij\to X}$ involving two parton types $i$ and $j$ is convoluted with the corresponding PDFs $f_i$ and $f_j$ with

$$\sigma_{\mathrm{pp}\to\mathrm{X}} = \sum_{i,j} \int\int \mathrm{d}x_1 \mathrm{d}x_2 f_i(x_1, Q^2) f_j(x_2, Q^2) \sigma_{ij\to\mathrm{X}}(x_1, x_2, Q^2). \tag{2.20}$$

Predictions of the cross sections for several SM processes are summarized in Figure 2.4 and compared to measurements with the CMS detector. All cross section measurements, covering a range over ten orders of magnitudes, are in good agreement with the predictions from the SM.

Multiple partons may interact in one pp collision. While all partons originate from the same

proton they induce different processes, also referred to as *underlying event* (UE). Usually, pp collisions are invoked by colliding bunches of protons. Similar to the UE, multiple interactions of protons can occur during one bunch crossing, which is referred to as *pileup*.

## 2.3 Event Simulation

Understanding data collected from particle physics experiments demands a comprehensive knowledge of the underlying physics. Theoretical predictions, based on models derived from first principle, are the most relevant models to give a profound understanding of the components from data. These predictions are derived from analytic calculations from first principles and are rather specific in terms of the phase space and variable of interest. Furthermore, analytic calculations are not able to account for the uncertainties induced by the detector itself. These include various forms of randomness and systematic deviations. Nevertheless, data is inevitably collected with these uncertainties without direct access to the unaltered physical event. Thus, a comparison of calculations to data need a sophisticated methodology to correct data for these detector effects. For unraveling the underlying physics of collected data, event simulations are utilized to obtain all required information about the different stages of a process. Additionally, simulations can be compared to data across any accessible phase space and give insights into the contributing processes. Simulations of hard-scattering process are obtained with Monte Carlo (MC) methods, which are based on probability theory. These simulations incorporate the theoretical framework outlined in the previous sections. All intermediate stages, from the pp collision up to the detector, are simulated in consecutive steps.
First, the matrix element (ME) of the process of interest is calculated and convoluted with the PDFs from the proton. Commonly used software tool kits are MADGRAPH [47, 48], POWHEG [49, 50, 51, 52] and PYTHIA [53]. These tools provide the kinematics of all particles from the hard-scattering process, referred to as parton level. Subsequently, unique features based on QCD properties are simulated with tools such as PYTHIA and HERWIG [54]. The modeling of *parton showers*, describing the splitting of quarks and gluons, is performed down to energies of $\mathcal{O}(1\,\mathrm{GeV})$, which still allows pertubative calculations. Additionally, the formation of color-neutral bound states is simulated by hadronization models. These models are determined phenomenologically and the input parameters are constrained with dedicated measurements in data. This step also includes simulation of the UE, the effect of additional parton-parton interactions in the same pp collision. Furthermore, the emission of inital state radiation (ISR) and FSR is simulated in this step of the event generation. The simulation chain highly depends on free parameters from theory, where a set of parameters is referred to as tune [55, 56]. For instance, the amount of radiation is steered with the strength of the strong coupling $\alpha_\mathrm{S}(m_\mathrm{Z})$. Matching between the ME and PS simulation, i.e. the removal of duplicate jets, is performed using specific procedures. For example in POWHEG, the impact of high-$p_\mathrm{T}$ radiation is controlled by matching the matrix elements and the parton showers using the $h_\mathrm{damp}$ parameter. Finally,

all stable particles are passed through a detailed simulation of the CMS detector implemented in GEANT4 [57, 58]. At his stage, signals in the detector are simulated for each event and reconstructed with the same algorithms as the data to allow one-to-one comparisons. Contribution from pileup, simulated in a separated iteration, or detector effects such as the detector responses are included in this step. A comparison between simulation and data necessitates a comprehensive understanding of simulations itself.

## 2.4 Top Quark

The top quark stands out as the most massive elementary particle discovered so far. It takes a prominent role in the SM because of a Yukawa coupling close to unity, resulting in its large mass. Precise measurements of top quark properties, such as its mass, allow precision tests of the SM, unravel the stability characteristics of our universe, and allow for searches of small deviations from the SM from new physics effects.
The top quark was discovered in 1995 at the Tevatron (Fermilab, Chicago) by the two experiments CDF [59] and DØ [60]. Since then, numerous measurements have confirmed these findings, with current mass measurements achieving precisions below the 1 GeV level. Two recent measurements by the ATLAS and CMS Collaboration have determined the top quark mass with $m_{\text{top}} = 174.41 \pm 0.81\,\text{GeV}$ [61] and $m_{\text{top}} = 171.77 \pm 0.37\,\text{GeV}$ [62], respectively. The latter represents the most precise single measurement of the top quark mass to date.

### 2.4.1 Top Quarks at the LHC

At the LHC, top quarks are dominantly produced in top and anti-top pairs ($\text{t}\bar{\text{t}}$). For a center-of-mass energy of $\sqrt{s} = 13\,\text{TeV}$, the cross section has been measured [64] to

$$\sigma_{\text{t}\bar{\text{t}}} = 791 \pm 25\,\text{pb}. \tag{2.21}$$

This result is in good agreement with predictions from next-to-NLO (NNLO) QCD calculations obtained with MATRIX [65] and the numerical calculation with TOP++2.0 [66].
The production channels are shown in Figure 2.5 and are either induced through the quark-antiquark ($\text{q}\bar{\text{q}}$) annihilation or the gluon-gluon fusion. In order to produce $\text{t}\bar{\text{t}}$ events, the energy transfer of two colliding partons must be $q^2 \geq 2m_{\text{top}}$. At the Tevatron, a $\text{p}\bar{\text{p}}$ collider with a center-of-mass energy of $\sqrt{s} = 1.8\,\text{TeV}$, it is most likely for valence quarks to reach such energies (see Figure 2.3). Hence, the dominant production channel is the $\text{q}\bar{\text{q}}$ annihilation. Due to the higher center-of-mass energy of $\sqrt{s} = 13\,\text{TeV}$ at the LHC, the momentum fraction of the colliding particles can be much lower to produce $\text{t}\bar{\text{t}}$ events. Therefore, the contribution from gluon-gluon fusion significantly increases, making it the dominant production channel. It is also possible to produce single top quarks in the final state. Those processes, however, are only possible via the weak interaction and therefore have a much smaller branching fraction in comparison to the $\text{t}\bar{\text{t}}$

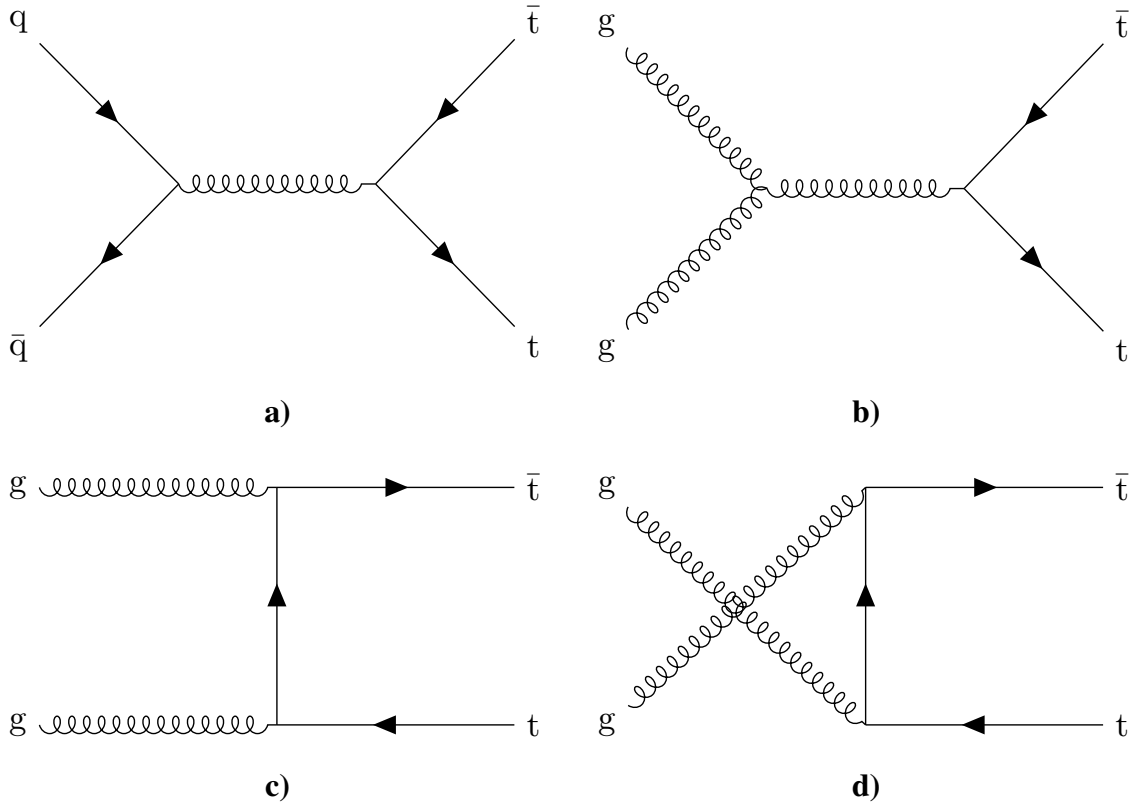


**Figure 2.5:** Feynman diagrams for leading-order $t\bar{t}$-production in a proton-proton collision. These events can arise from quark-antiquark annihilation (a) or gluon-gluon fusion in the s-channel (b), t-channel (c) or u-channel (d). Created with TikZ [63].

process.

A unique feature of the top quark is its short lifetime such that it decays before it forms top-flavored hadrons or $t\bar{t}$-quarkonium-bound states. The time scale of the hadronization exceeds the lifetime of the top quark with $\tau_{\text{top}} \approx 5 \cdot 10^{-25}$ s [30]. For that reason, the bare top quark becomes accessible by analysing its decay products, which is not possible for other color charged particles. The top quark almost exclusively decays into a b quark by emitting a W boson as it can be seen in the CKM matrix in Equation 2.10. The W boson further decays either hadronically into a quark anti-quark pair ($W \rightarrow q\bar{q}'$), or leptonically into a lepton and the corresponding anti-neutrino ($W \rightarrow \ell\bar{\nu}_\ell$). The additional degrees of freedom due to the color charge for quarks lead to branching fraction of 67 %[30] for the hadronic decay channel. Three $t\bar{t}$ decay channels are considered covering all combinations of the two W boson decays; the *all-hadronic* and *dilepton* channel, where both W bosons decay hadronically or leptonically, respectively, and the *lepton+jets* ($\ell$+jets) channel, where one W boson decays hadronically and the other leptonically. The all-hadronic and $\ell$+jets channel have similar branching fractions with 45 % and 44 %, while the dilepton channel only occurs in 11 % of all cases.

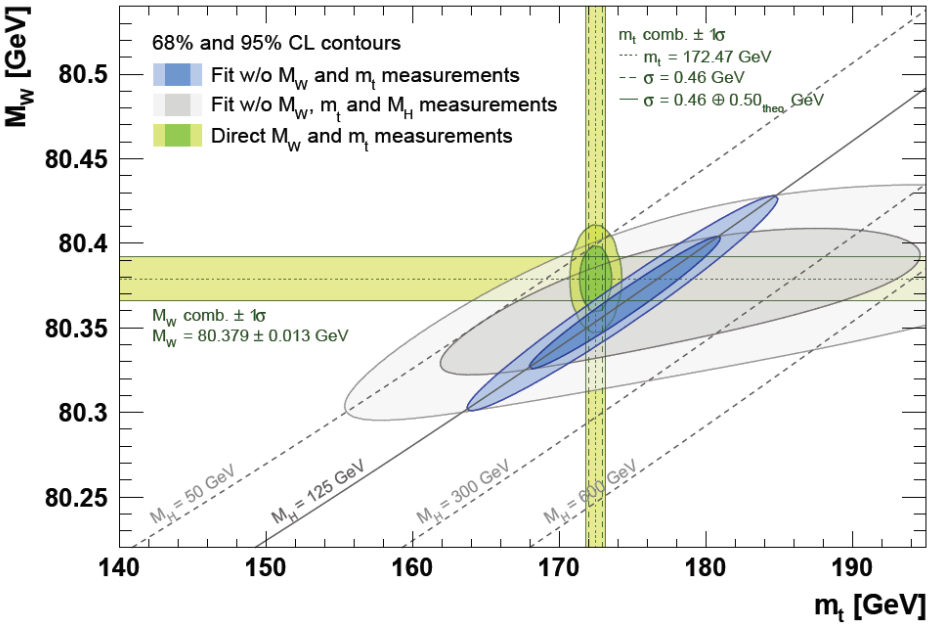


**Figure 2.6:** Electroweak global fit in the $m_t$-$m_W$-plane. Direct measurements of both masses are represented by the green bands. The most consistent regions of $m_H$ are represented by the blue and grey areas, including and excluding direct measurements, respectively. Taken from Ref. [68].

### 2.4.2 Top Quark Mass

The top quark mass $m_{top}$ is of special interest for consistency checks of the SM. Due to the large coupling of the top quark to the Higgs field, it takes a prominent role in the electroweak sector. For instance, the top quark appears in quantum loop corrections that contribute to the masses of the Z boson, W boson or the higgs boson. Hence, it indirectly impacts parameters such as the weak mixing angle. Before the discovery of the top quark, the possible range of its mass could be constrained with electroweak fits [67] that uses measured parameters such as the Z boson mass. Furthermore, the Gfitter group has performed such fits that combine $m_{top}$, $m_W$ and $m_H$ to validate the SM [68]. The overlapping ellipses in Figure 2.6 demonstrate the self-consistency of the SM, as the measured masses align well with the predictions of the fit. In the SM, the masses of fundamental particles are free parameters in the Lagrangian. Observations of free parameters cannot be directly identified with the definition in the Lagrangian, as those parameters highly depend on the renormalization scheme. The concept of renormalization is utilized to counteract divergences in the calculation induced in higher order loop corrections. A comprehensive overview of top quark mass definitions and measurements can be found in Ref. [69].

The top quark mass is commonly described in several schemes, such as the *pole mass*, $m_{top}^{pole}$, the mass from the *MSR* scheme, $m_{top}^{MSR}$, or from the *minimal subtraction*, $\overline{MS}$ scheme $m_{top}^{\overline{MS}}$. These schemes differ by the energy scales of the self-corrections considered in the calculations. In case of $m_{top}^{pole}$, all self-corrections are absorbed in the definition of the top quark mass, and

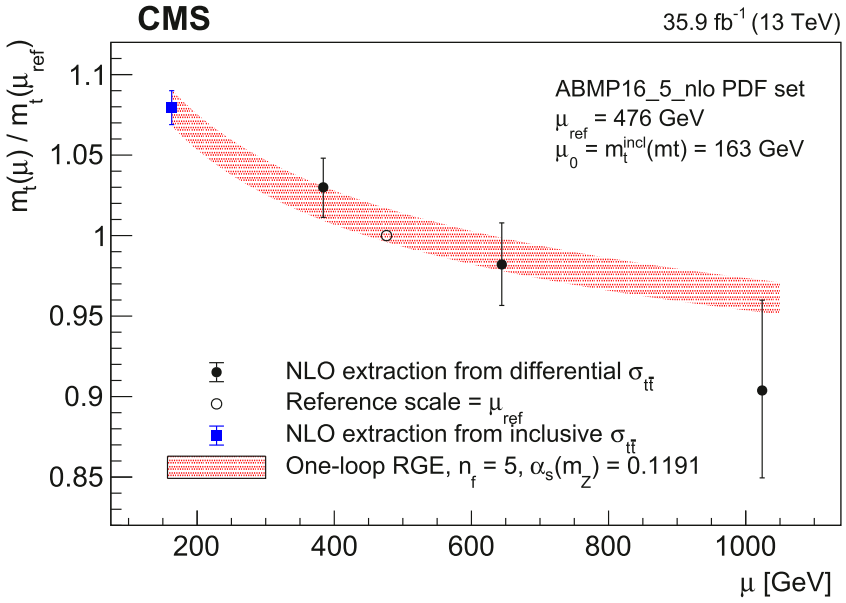


**Figure 2.7:** Dependency of $m_{\text{top}}^{\overline{\text{MS}}}$ on the scale $\mu$, measured from differential $\text{t}\bar{\text{t}}$ production cross section as a function of the invariant mass of the $\text{t}\bar{\text{t}}$ system. The obtained values are in good agreement with renormalization group equations (RGE). Taken from Ref. [70].

thus can be interpreted as the mass of the top quark as a free particle. In the $\overline{\text{MS}}$ scheme, a mass is introduced that depends on the renormalization scale $\mu$. Similar approaches have been discussed in terms of the strong coupling $\alpha_{\text{S}}$ in Section 2.1.2. Here, only corrections above a scale of $\mu > m_{\text{top}}$ are considered for the mass definition. That way, it is independent of non-perturbative effects, which arise for low energy scales in QCD and cannot be calculated analytically. This mass is often referred to as short-distance mass or running mass of the top quark. An analysis from the CMS Collaboration [70] investigated the running top quark mass for the first time. Here, $m_{\text{top}}^{\overline{\text{MS}}}$ is extracted from the differential cross section $\text{d}\sigma_{\text{t}\bar{\text{t}}}/\text{d}m_{\text{t}\bar{\text{t}}}$, with the invariant mass of the $\text{t}\bar{\text{t}}$ system, $m_{\text{t}\bar{\text{t}}}$. The dependence of $m_{\text{top}}^{\overline{\text{MS}}}$ on the renormalization scale $\mu$ is shown in Figure 2.7 and is in good agreement with SM predictions. The MSR scheme defines a scale-dependent short distance mass, $m_{\text{top}}^{\text{MSR}}$, via a momentum scale $R < m_{\text{top}}$. For the limit $R \to 0$, the MSR mass $m_{\text{top}}^{\text{MSR}}$ converts into $m_{\text{top}}^{\text{pole}}$ and acts as an interpolation between $m_{\text{top}}^{\text{pole}}$ and $m_{\text{top}}^{\overline{\text{MS}}}$. It is possible to convert the masses from the different renormalization schemes into each other with a precision of the order of a few tens of MeV.

Measurements of $m_{\text{top}}$ are performed by constructing observables in data sensitive to $m_{\text{top}}$ and compare those to prediticions with different $m_{\text{top}}$ hypotheses. These predictions are either obtained from event generators or analytic calculations from first principles.

In direct measurements, observables sensitive to $m_{\text{top}}$ are constructed from the four-momentum of the top quark decay products at the detector level and hence depend on the parton shower and hadronization models. However, these mechanisms are not calculable from pertubative QCD [71]. Consequently, the observable itself is not derivable from analytic calculations and data can only be compared to simulation. Top quark masses extracted from event generators

are often referred to as Monte Carlo mass $m_{\text{top}}^{\text{MC}}$. This mass definition comes with several ambiguities due to the used models for QCD effects such as the parton shower. Translating $m_{\text{top}}^{\text{MC}}$ to any of the mass schemes from first principles give rise to an additional uncertainty of 0.5 GeV to 1 GeV [72]. Recent studies conducted by the ATLAS Collaboration have calculated an additional uncertainty arising from this translation of $\mathcal{O}(400\,\text{MeV})$ [73].
An alternative approach to extract $m_{\text{top}}$ is through inclusive cross section measurements, accessing $m_{\text{top}}$ from a well-defined renormalization scheme. These measurements are generally sensitive to various sources of uncertainties that cannot be constrained while measuring $m_{\text{top}}$. For instance, the total $\text{t}\bar{\text{t}}$ cross section depends not only on $m_{\text{top}}$ but also on $\alpha_s(m_Z^2)$. A simultaneous measurement of both parameters is not feasible, as variations in one can compensate for changes in the other. While $m_{\text{top}}$ can be determined from the inclusive cross section by fixing $\alpha_s(m_Z^2)$, this approach results in larger uncertainties. This sensitivity to multiple parameters can be mitigated with differential cross section measurements, which examine top quark production as a function of different kinematic variables. In this approach, the top quark is treated as a stable particle and hence predictions do not depend on parton shower or hadronization models and can be calculated from pertubative QCD. Overall, these measurements offer a greater sensitivity to $m_{\text{top}}$ compared to the inclusive cross section. A summary of the measurements of the top quark mass can be seen in Figure 2.8 for direct measurements (upper) and cross section measurements (lower). While direct measurements are yet more precise, measurements from the pole mass become comparable and reach a precision of the sub-GeV benchmark.
The measurement presented in Chapter 7 is such a differential cross section measurement, aiming for the extraction of $m_{\text{top}}$ from analytic calculations.

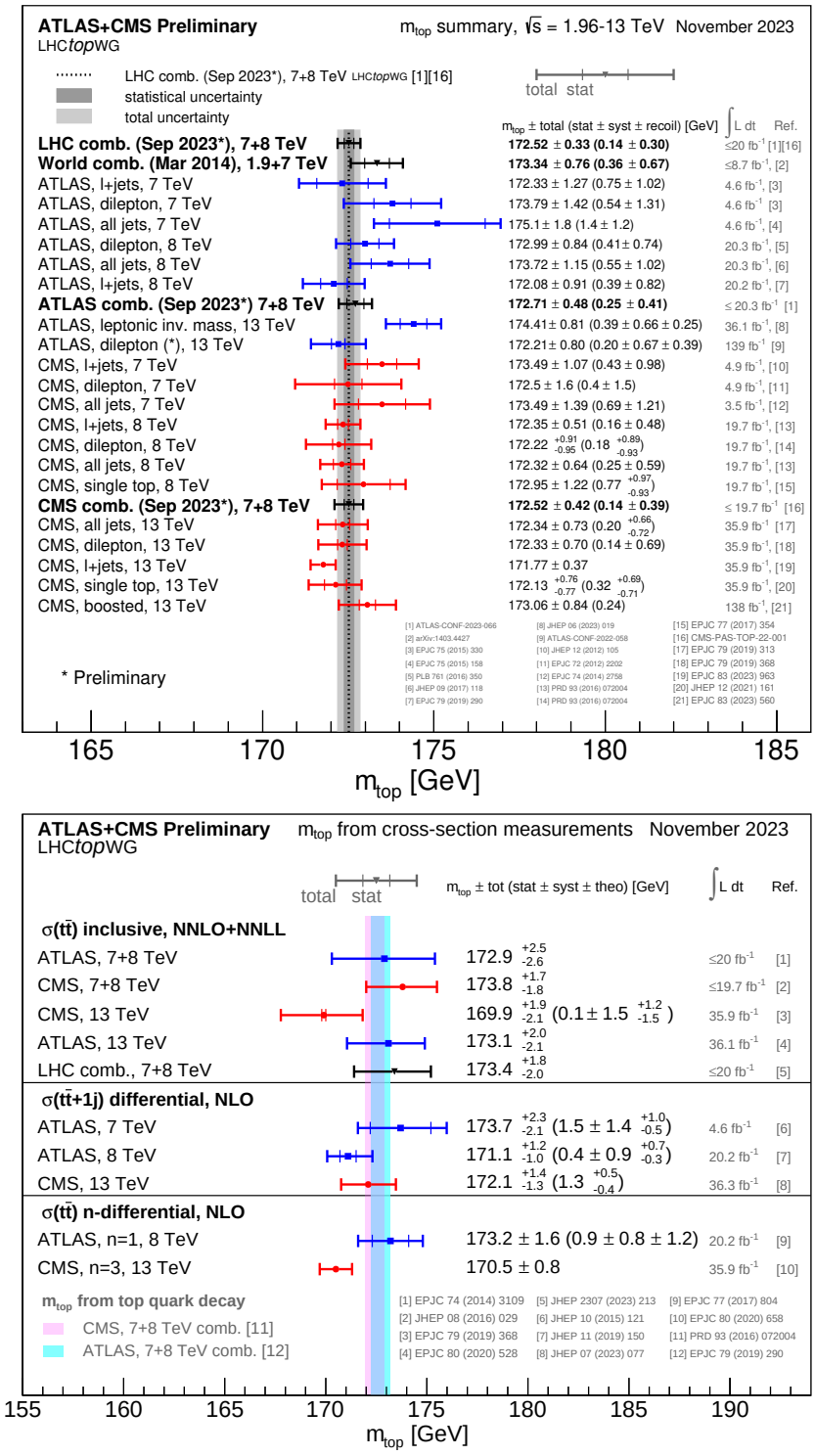


**Figure 2.8:** Summary of top quark mass measurements from the ATLAS and CMS Collaboration. Direct measurements (upper) use Monte Carlo simulations to extract the top quark mass. The top quark pole mass is usually obtained from differential cross section measurements (lower), resulting in an extraction of a well-defined mass. Taken from Ref. [74].

# Chapter 3

# Experimental Setup

The analyses presented in this thesis have been conducted with data recorded by the Compact Muon Solenoid (CMS) detector at the Large Hadron Collider (LHC) [75]. This chapter provides an overview of the overall LHC complex in Section 3.1 as well as a description of the CMS detector in Section 3.2.

## 3.1 Large Hadron Collider

The LHC is the largest circular particle collider built so far. Located at CERN in Switzerland and France, the LHC features a circumferences of 27 km. Designed primarily as a proton-proton (pp) collider, it is also designed to collide heavy ions.
Inside the LHC, the protons revolve in bunches, each containing about $\mathcal{O}(10^{11})$ protons. The bunches are bend onto a curved trajectory by dipole magnets and the beam focus is adjusted by quadrupole and higher-order magnets. Before injected into the LHC ring, protons are accelerated through several pre-accelerators, which were previously main accelerator rings before the LHC was operational. First, protons are obtained by removing electrons from hydrogen atoms utilizing an electric field. After the ionization of the Hydrogen atom, the proton source is accelerated with the *Linear Accelerator 2* (LINAC2), before injected into the first circular accelerator the *Proton Synchrotron Booster*, followed by the *Proton Synchrotron*. Finally, after reaching an energy of 450 MeV in the *Super Proton Synchrotron*, the protons are injected into the LHC. An overview of the LHC complex, including all main experiments and the pre-accelerators, is shown in Figure 3.1. Four main experiments are built around the interaction points: A Toroidal LHC Apparatus (ATLAS) [76], CMS [77], A Large Ion Collider Experiment (ALICE) [78] and the LHC beauty (LHCb) [79]. While the two largest experiments, ATLAS and CMS, are multi-purpose detectors to investigate a wide range of phenomena, ALICE and LHCb are specialized for more specific processes. LHCb focuses on b quark physics and ALICE is specialized for heavy ion collisions.
An important characteristic of colliders is the instantaneous luminosity

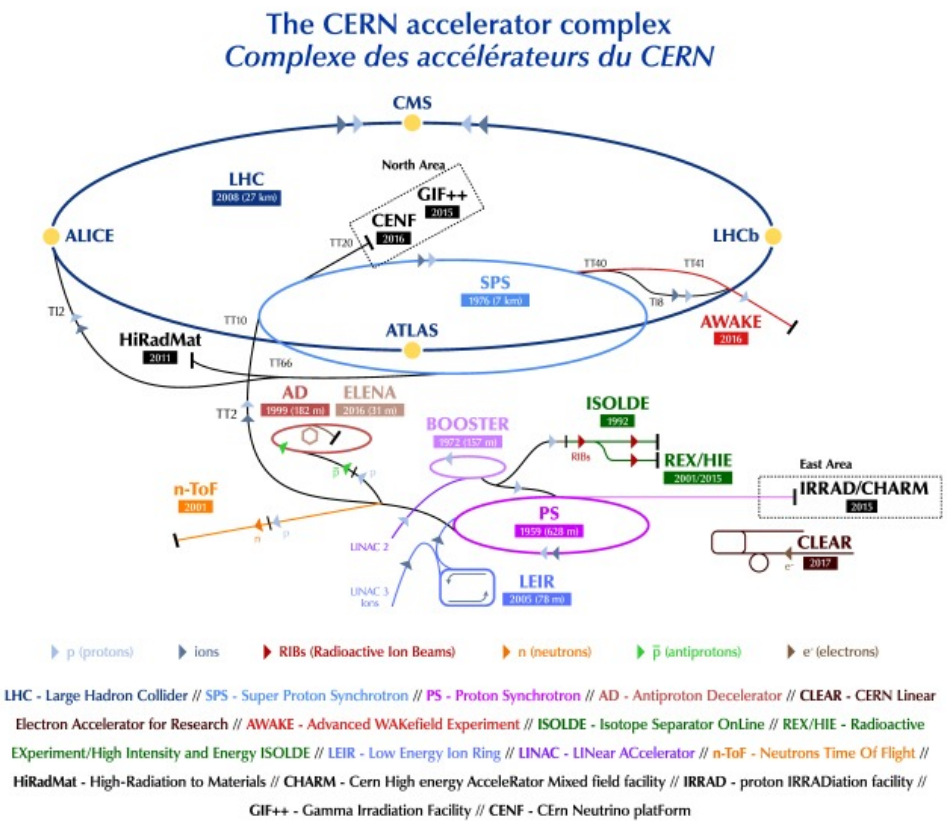


**Figure 3.1:** Overview of the accelerator complex of the LHC. Taken from Ref. [80].

$$\mathscr{L} = \frac{N_{\mathrm{B}} \cdot f \cdot N_1 \cdot N_2}{4\pi \cdot \sigma_x \cdot \sigma_y}, \tag{3.1}$$

with the number of bunches $N_{\mathrm{B}}$, $f$ the revolution frequency with 11 kHz, the number of protons $N$ in each colliding bunch and the their spread $\sigma_x$ and $\sigma_y$ in $x$ and $y$ direction, respectively, perpendicular to the beam axis in $z$ direction. The LHC is designed to operate at $\mathscr{L} = 10^{34}\,\mathrm{cm}^{-2}\mathrm{s}^{-1}$. The size of the datasets is expressed in terms of the *integrated luminosity* $\mathscr{L}_{\mathrm{int}} = \int \mathscr{L} dt$. In combination with the cross section $\sigma$ of a certain process, the expected number of events is determined with $N = \sigma \mathscr{L}_{\mathrm{int}}$.

The center-of-mass energy for the second data taking period (Run 2), including the years 2016 to 2018, reached $\sqrt{s} = 13\,\mathrm{TeV}$. For the third data taking period (Run 3), which started in the year 2022, the energy was increased to 13.6 TeV. In order to increase the luminosity for the upcoming phases of the LHC, several upgrades are made, such as the replacement of LINAC2 with the more advanced LINAC4 [81]. After its last year of data taking in Run 3, the LHC will be upgraded to the High Luminosity LHC (HL-LHC) [82] with $\sqrt{s} = 14\,\mathrm{TeV}$. It is expected that the integrated luminosity is increased by a factor of 10 to $\mathscr{L} = 4000\ \mathrm{fb}^{-1}$ by the end of the data-taking period of the HL-LHC. The timeline of the LHC runs, including the plans for the HL-LHC is shown in Figure. 3.2.

Data used in this thesis is mainly collected during Run 2 data taking period including the years


**Figure 3.2:** Timeline of the LHC data-taking periods up to the year 2040. Taken from Ref. [83].

2016 to 2018. Furthermore, first calibrations were performed with data from Run 3 from the years 2022 and 2023.

## 3.2 The Compact Muon Solenoid Detector

The CMS detector consists of multiple subdetectors, which measures the momentum and energy of a variety of particles. It has a cylindrical form with a length and width of 21.6 m and 14.6 m, respectively and weights 14 000 t, enclosing the collision point. The subdetectors are installed in concentric layers around each other in the following order: the inner tracker, the electromagnetic calorimeter, the hadronic calorimeter, the solenoid and the muon chambers. The superconducting solenoid induces a magnetic field of 4 T and bents the trajectories of electrically charged particles. The CMS detector is further divided into the barrel region and the endcaps, which are aligned parallel and vertical with respect to the beam axis, respectively. The endcaps adjoin both ends of the barrel part. In order to measure events with large pseudorapidity, a third division of the detector is installed to cover events close to the beam line. An overview of CMS detector and its subdetectors is shown in Figure 3.3. The information in this chapter is based on Ref. [77, 84] if not stated otherwise.

### 3.2.1 The Coordinate System

The CMS detector utilizes a right-handed Cartesian coordinate system with its origin at the collision point. The $z$-axis runs counterclockwise along the beam axis, the $x$-axis points towards the center of the LHC ring, and the $y$-axis points upwards. A spherical coordinate system

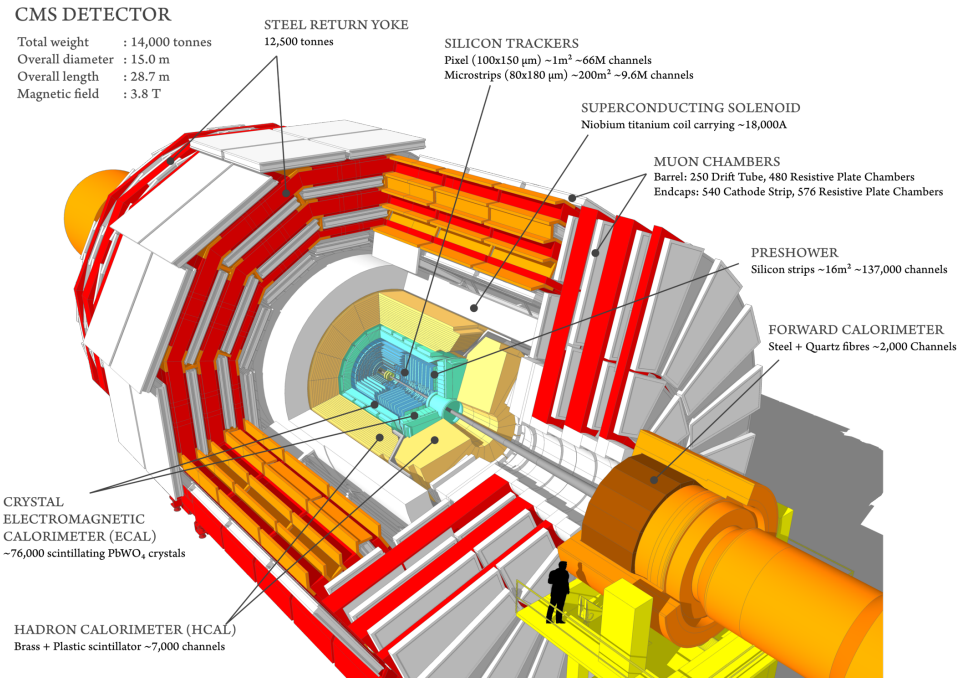


**Figure 3.3:** Illustration of the CMS detector showing the insight of the detector. Each subdetector is indicated by a short description. Taken from Ref. [85].

is preferred, due to the cylindrical form of the detector. In this system, the radial distance $r$ is measured from the collision point, the azimuthal angle $\phi$ represents the rotation in the $x$-$y$-plane, and the polar angle $\theta$ indicates the distance to the beam axis. Due to the internal structure of the proton, the momentum of the initial state in the $z$-direction is unknown. Thus, all coordinates must be invariant under Lorentz-transformations along the $z$-axis. Because differences in $\theta$ do not satisfy these requirements and thus the pseudorapidity $\eta$ is used instead with

$$\eta = -\ln\left(\tan\frac{\theta}{2}\right). \tag{3.2}$$

The pseudorapidity can take any value from zero ($x$-$y$-plane) to infinity ($z$-direction). Differences in $\eta$ are Lorentz-invariant and for relativistic particles, $\eta$ approximates the rapidity $y$. The angular distance of two objects can be calculated via

$$\Delta R = \sqrt{(\Delta\phi)^2 + (\Delta\eta)^2}, \tag{3.3}$$

which is also Lorentz invariant.

### 3.2.2 The Tracking System

The tracking system, is the innermost component of the CMS detector. It plays a crucial role in the identification of particle trajectories and the reconstruction of collision points (vertices). It exploits the ionization process of charged particles and hence neutral particles are not detectable in this part of the CMS detector. It has a length of 5.8 m, a diameter of 2.5 m and it

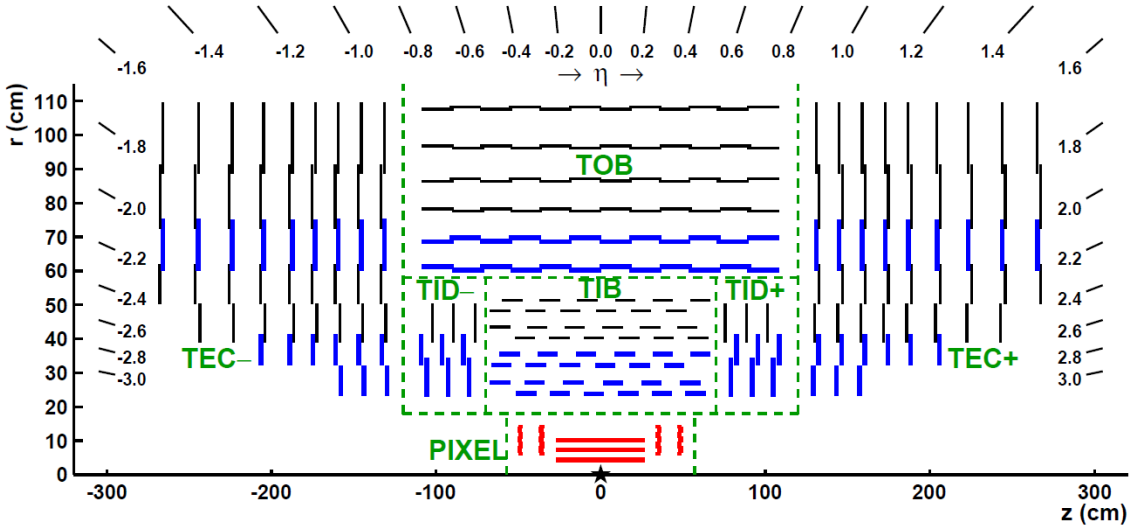


**Figure 3.4:** An overview of the tracker system at the CMS detector in the $r$-$z$ plane before the pixel-detector upgrade. The center of the detector is indicated with a black star and the PIXEL detector in red. Strip modules for a 3D and 2D hit position reconstruction are indicated by blue and black lines, respectively. Taken from Ref. [86].

covers a range of $|\eta| < 2.5$. The tracking system is divided into several subcomponents, which utilize two different silicon detectors, silicon pixels and stripes. Silicon is a material highly suitable to detect numerous particles within a compact area due to its fast response and good spatial resolution. The subcomponents of the tracking system are the *pixel detector* (PIXEL), *tracker inner barrel* (TIB), *tracker outer barrel* (TOB), *tracker inner disks* (TID) and the *tracker endcaps* (TEC). An overview of the tracker system is shown in Figure 3.4.

Until 2016, the PIXEL detector consisted of three silicon detector layers in the barrel (BPix) region with a radial distance of $r = 4.4$, 7.3 and 10.2 cm and two layers in the endcaps (FPix) with $r = 34.5$ and 46.5 cm. An upgrade of the PIXEL detector [87] was implemented during the data taking break between 2016 and 2017. This enhancement introduced an additional layer to both, the barrel and endcap section, expanding them to four and three layers, respectively. The radial distances were modified to $r = 6.8$, 10.2, 16.0 and 43.0 cm, and $r = 29.1$, 39.6 and 51.6 cm for the barrel and endcap section, respectively. These adjustments have significantly improved the track reconstruction and the secondary vertices identification, crucial for identifying jets from heavy quarks. The latter is possible because the innermost layer of the PIXEL now is located even closer to the beam axis.

Other subcomponents of the tracker system surround the PIXEL detector and consists of silicon stripes. The inner detectors, TIB and TID, feature four and three layers, respectively, with a strip thickness of 320 µm and pitches ranging from 80 µm to 141 µm. The TIB covers $|z| < 65$ cm, while the TID spans over $65 < |z| < 110$ cm. The outer detectors, TOB and TEC, utilize a thickness of 500 µm, with pitches of 122 µm and 183 µm. The TOB, comprising 6 layers, extends over $|z| < 118$ cm, and the TEC consists of nine discs covering $124 < |z| < 282$ cm.

The tracker system achieves a hit resolution in $x$ and $y$ direction up to 10 µm, allowing a precise

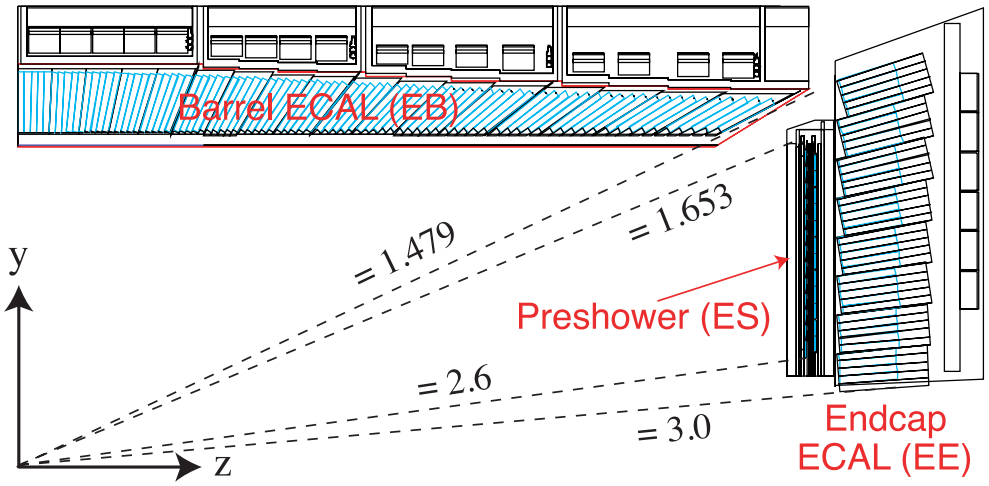


**Figure 3.5:** Schematic overview of the the electromagnetic calorimeter (ECAL). Shown is the coverage in the pseudorapidity $\eta$ for each subcomponent, namely the Barrel ECAL (EB), the preshower detector (ES), and the endcap ECAL (EE) Taken from Ref. [77].

tracking of particles. The measurement of the momentum of charged particles is based on the curvature of their trajectories within the magnetic field. A higher momentum results in less curvature and thus leads to a reduction in the resolution.

### 3.2.3 The Calorimeter System

The calorimeter system is used to measure the energy of the particles. It is installed around the tracking system of the CMS detector. Two types of calorimeter are employed at the CMS detector, the electromagnetic (ECAL) and the hadronic calorimeter (HCAL). Both calorimeter operate with the same underlying principle. Incoming particles initiate a parton shower within the calorimeter material, generating low-energy particles. These particles are absorbed by scintillating material, which in turn emits photons. The emitted photons are subsequently measured using photomultiplier tubes. The energy of the energy deposit of the incoming particle can be then reconstructed from the cumulative intensity of the measured photons. The energy resolution $\sigma_{\mathrm{E}}$ of the calorimeters can be parameterized with

$$\frac{\sigma_{\mathrm{E}}}{E[\mathrm{GeV}]} = \frac{N}{E[\mathrm{GeV}]} \oplus \frac{S}{\sqrt{E[\mathrm{GeV}]}} \oplus C. \tag{3.4}$$

Here, $N$ represents the stochastic term accounting for fluctuations in the parton showers, $S$ the noise term consisting of the electronic and pileup noise and the constant term $C$, including inhomogeneties, miscalibrations and undetected energy leakage. In contrast to the tracker system, the precision of the calorimeters increases with more energetic particles. However, the precision of the energy measurement for high energetic particles is limited by the effects comprised in the constant term. Therefore, a properly calibrated calorimeter is necessary for an improved performance in high energy regions. Neutral particles such as the photons or neutral hadrons can only be measured in this part of the detector.

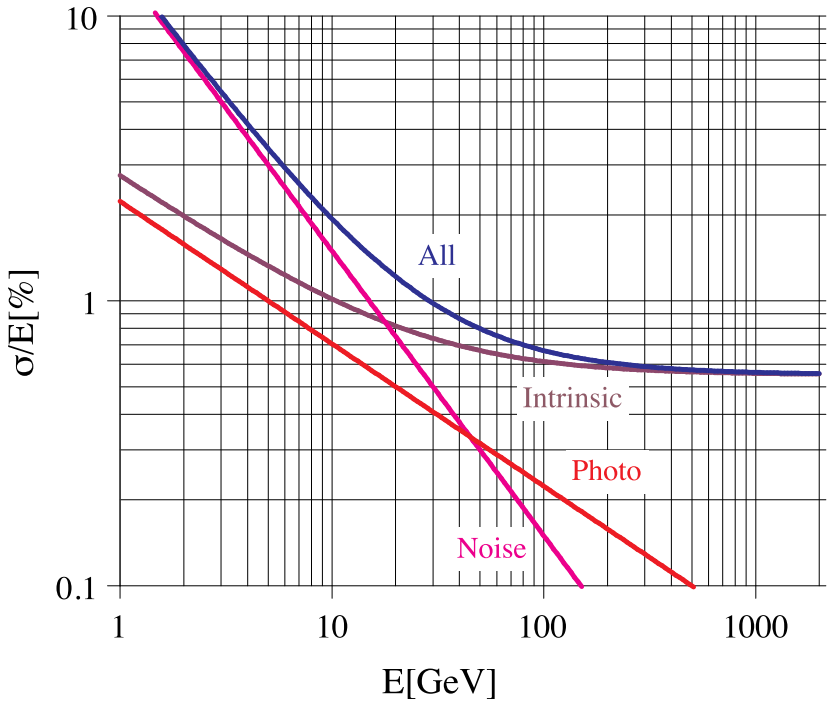


**Figure 3.6:** Energy resolution of the electromagnetic calorimeter (ECAL, blue) for photons and electrons. Shown are the different contributions from the *Noise*, *stochastic* (Photo) and *constant* (intrinsic) term. Taken from Ref. [88].

## The Electromagnetic Calorimeter

The ECAL is designed to detect Higgs decay into two photons ($H \rightarrow \gamma\gamma$), putting requirements for the energy and spatial resolution involving high granularity. It is a homogeneous calorimeter that surrounds the tracker system and is divided into the barrel (EB) and the endcap (EE) region, as shown in Figure 3.5. Homogeneous calorimeters consist of a high-density material, which acts both as the absorber and scintillator. In case of the ECAL, scintillating lead-tungstate ($PbWO_4$) crystals are used. About 80 % of the scintillation is emitted within the time interval of 25 ns. Furthermore, the material has a short radiation length of $X_0 = 0.89\,\text{cm}$ and a Molière radius of 2.2 cm. The former defines the distance at which an incoming electron loses 1/e of its initial energy, and the latter defines the transverse expansion of electromagnetic showers.
The primary purpose of the ECAL is to fully measure the energy of photons and electrons (positrons). Photons and electrons induce showers in the detector material via photon pair production ($\gamma \rightarrow e^+e^-$) or Bremsstrahlung ($e^\pm \rightarrow \gamma e^\pm$), respectively. Other particles, such as hadrons and muons, can also deposit energy in the ECAL. While muons generally pass through the detector with minimal interaction, hadrons typically induce showers. However, the depth of the ECAL is insufficient for hadrons to deposit the majority of their energy.
The crystals are designed with a length of 25.8 $X_0$ (230 mm), such that electrons and photons fully deposit their energy in the calorimeter. The crystals have a cross section of 22 $\text{mm}^2$ facing towards the beam axis and increases to 26 $\text{mm}^2$, facing outwards of the detector. the range extends up to $|\eta| = 3.0$, where the EB covers $|\eta| < 1.479$ and the EE $1.479 < |\eta| < 3.0$. In

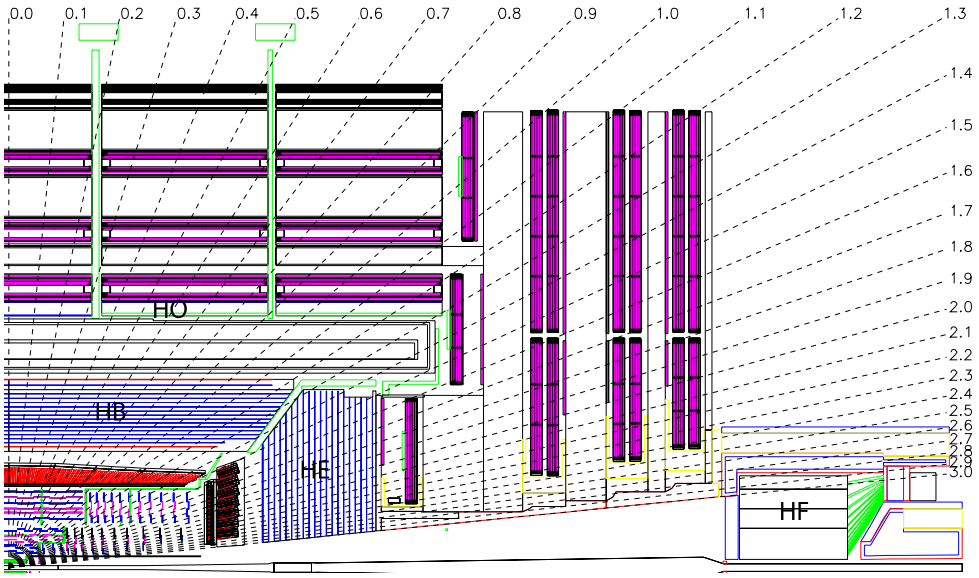


**Figure 3.7:** Layout of the hadronic calorimeter at the CMS detector in comparison to the tracker and the electromagnetic calorimeter. Shown are the components hadron outer (HO), hadron barrel (HB), hadron endcap (HE) and the hadron forward (HF). Taken from Ref. [84].

front of the endcaps additional preshower detectors are installed to identify the photon direction and resolve high energetic photons from $\pi^0$ decays ($\pi^0 \to \gamma\gamma$).
Homogeneous calorimeters lack the information of segmentation in the radial direction, but in exchange, the energy resolution improves significantly. The energy resolution for electrons and photons in the ECAL has bin measured with $N = 12$ %, $S = 2.8$ %, and $C = 0.3$ % [77] (see Equation 3.4). Each contribution is depicted in Figure 3.6.

## The Hadronic Calorimeter

The HCAL, displayed in Figure 3.7, encloses the ECAL and reaches beyond the solenoid (see Section 3.2.4). Its purpose is to measure the energy of neutral and charged hadrons. It is a sampling calorimeter constructed from alternating layers of dense brass plates and a plastic scintillator. The brass layers, acting as an absorber, induce particle showers by converting the energy of passing hadrons. The soft particles in the showers excite the scintillators to scintillate light. The total depth of the barrel part is 11.8 $\lambda_n$, where $\lambda_n$ is the nuclear interaction length, equivalent to the radiation length. The barrel part is installed in a distance of $1.77 < r < 2.95\,\text{m}$ to the $z$-axis and captures a pseudorapidity range up to $|\eta| = 1.3$. The endcaps increasing the coverage with $1.3 < |\eta| < 3.0$. Additionally, the HCAL features a calorimeter in the forward region (HF) positioned at $z = \pm 11.1\,\text{m}$, extending its reach to $3.0 < |\eta| < 5.2$. Measuring the energy of particles that are not covered by the central but the HF region, improves the resolution of the missing transverse momentum. Moreover, processes, such as the Higgs boson production via vector boson fusion, typically feature two highly forward jets, which can be detected with the HF. In contrast, due to the lack of tracking information in this region, there is a reduction in

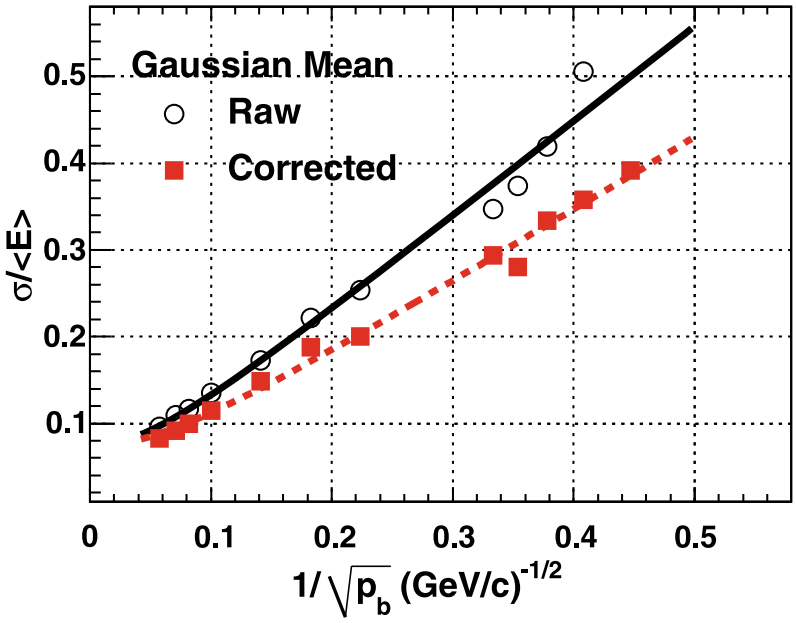


**Figure 3.8:** Energy resolution in the combination of the ECAL and HCAL for pion test beams in dependence of the beam momentum $p_{\mathrm{b}}$. The measurement is performed for pions before (black circles) and after (red squares) corrections for differences in the subdetectors of the ECAL and HCAL. Taken from Ref. [89].

the efficiency of jet reconstruction. The extended structure beyond the solenoid (HO) captures showers that may not be fully absorbed by the inner sections of the calorimeter.
Generally, the energy resolution of the HCAL is inferior to that of the ECAL, because the parton showers are not directly induced in the scintillating material. However, the HCAL contains information from each longitudinal segment, enhancing the reconstruction of jets. The energy resolution for the combined ECAL and HCAL system has been measured in test beams predominantly consisting of pions [89]. Figure 3.8 shows the measurement of the energy resolution, which can be approximated by the stochastic term. The individual contributions are $S = 111.5\ \%$ and $C = 8.6\ \%$, while the noise term $N$ is negligible.

### 3.2.4 The Solenoid

A key feature of the CMS detector is the superconducting solenoid magnet, which encloses the tracker system and both calorimeters. The solenoid is 12.9 m long and has an inner radius of 5.9 m. The magnet is designed to induce a homogeneous magnetic field of $B = 3.8\,\mathrm{T}$ inside the detector. The compact design of the CMS detector requires a high magnetic field to sufficiently bend the trajectory of charged particles with high momenta to ensure a precise measurement of the momenta. Outside the solenoid, iron yokes return the magnetic field ensuring a compact magnetic circuit. The trajectory of charged particles passing the solenoid magnet bent in the opposite direction, enabling an improved reconstruction.

### 3.2.5 The Muon System

The outermost component of the CMS detector is the muon chamber. Its design is motivated by significant discoveries such as the decay of the Higgs boson into four muons ($H \to ZZ \to 4\ell$). Muons are the only particles in the SM, except neutrinos that pass through the preceding detectors with minimal energy loss, allowing them to be reconstructed with a low misidentification rate. An overview of the muon system is shown in Figure 3.9. It consists of multiple independent layers, embedded in the iron return yokes as detailed in Section. 3.2.4.
The muon system employs three different types of gaseous detectors: the drift tubes (DTs), cathode strip chambers (CSCs) and resistive plate chambers (RPCs). All three detector types operate on a similar principle: a passing muon ionizes the gas and induces an electron avalanche. DTs convert these electrons into an electrical signal using a positively-charged wire within the gas volume. CSCs, comprising multiple positively-charged wires and perpendicular negatively-charged stripes, measure the electron avalanche and the gas ions simultaneously, allowing a two-position coordinate measurement. RPCs are gaseous parallel plate detectors that offer a time resolution at the order of a few nanoseconds and adequate spatial resolution, providing a fast read-out for the trigger system (see Section 3.2.6).
In the barrel part, the muon system features four layers covering a range of $|\eta| < 1.2$. The endcap region encounters a higher particle flux and a non-uniform magnetic field. Therefore, CSCs are used due to their fast response time, fine segmentation, and radiation resistance. The endcaps extend the coverage to $0.9 < |\eta| < 2.4$, while additional RPCs are installed up to $|\eta| = 1.6$.
As a preparation for the HL-LHC, the complementary *gas electron multipliers* (GEM) detectors [90] have been installed close to the beam axis during the second long shutdown of the LHC (see Figure3.2). These detectors adapt to the harsher conditions of the LHC for increasing luminosity and center-of-mass energies, enhancing muon detection in the endcaps for a range of $1.6 < |\eta| < 2.4$.

### 3.2.6 The Trigger System

The designed instantaneous luminosity of the LHC with $\mathscr{L} = 10^{34}\,\mathrm{cm}^{-2}\,\mathrm{s}^{-1}$ is achieved with a bunch crossing rate of 40 MHz, resulting in $\mathscr{O}(10^9)$ pp collisions per second. Given that each event requires about 1 MB of storage, the enormous volume of data collected by the CMS detector is impossible to store and process with current computer systems. Therefore, CMS employs a two-tiered trigger system to reduce the event rate by a factor of $10^7$, consisting of the *Level-1* (L1) [92] trigger and the *high-level* trigger (HLT) [93].
The L1 trigger decides whether an event is potentially interesting or not. While the full event information recorded by CMS is stored in a pipelined memory up to 3.2 µs, the L1 trigger level uses a coarsely segmented data from the calorimeters and the muon system. At the stage of the L1 trigger, several potential trigger objects are identified such as lepton or jet candidates

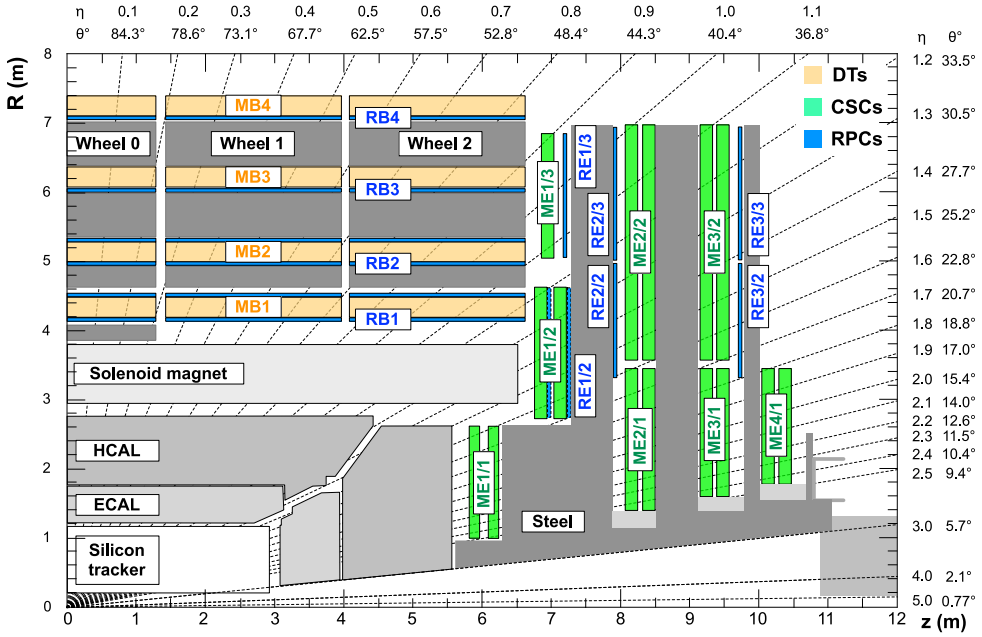


**Figure 3.9:** Layout of the muon system used at the CMS detector in comparison to the tracker and the calorimeters. It uses three types of gaseous detectors, namely the drift tubes (DTs, yellow), cathod strip chambers (CSCs, green) and the resistive plate chamber (RPCs, blue). Taken from Ref. [91].

as well as event based observable such as the missing transverse momentum or the sum of the transverse momentum from all jets above a certain $p_T$ threshold. Electrons and photons cannot be distinguished at this stage of the trigger due to the lack of tracker information. The outcome of the evaluations of each trigger object are consolidated in the global trigger, which determines whether an event is discarded or passed on to the HLT.

The HLT trigger is software-based and has full access to the full event information measured. Thus, it can operate with more complex algorithms similar to offline reconstructions. Although the processing at this level is simplified to meet time and memory constraints, the HLT allows a more sophisticated event selection. This refined filtering reduces the event rate down to $\mathcal{O}(100\ \text{Hz})$, a manageable rate for storage and detailed offline analyses. Several HLT *paths*, a set of filters to select certain events, are merged in the HLT *menu*, equivalent to global L1 trigger. Unlink the L1 trigger system, the structure of the HLT system allows for flexible updates and enhancements.

In instances where the trigger rate is excessively high leading to an overused trigger bandwidth, responsible trigger objects (L1) or paths (HLT) can be scaled down using a *prescale* factor. Those factors are commonly adjusted to the Luminosity profile of the LHC. This approach ensures that only a predefined fraction of events passing the trigger conditions is recorded, effectively managing the event rate.

# Chapter 4

# Object Reconstruction and Calibration

Physics objects are reconstructed from the raw inputs of the subdetectors. The CMS Collaboration employs the Particle-Flow (PF) algorithm [94], which is detailed in Section 4.1. Here, further criteria to identify and categorize particle candidates such as the muon or electron are discussed. Jet clustering algorithms utilized to cluster PF candidates into single objects are discussed in Section 4.2. An summary of the identification of heavy-flavor jets is provided in Section 4.3, followed by a comprehensive overview of the jet calibration workflow at the CMS detector. Lastly, the reconstruction of the missing transverse momentum (MET), an essential property of an event, is covered in Section 4.5.

## 4.1 Particle Flow Algorithm

Object reconstruction at the CMS detector is based on the PF algorithm [94], which aims at identifying particle candidates such as photons, electrons, muons, and charged- and neutral hadrons. The trajectory of different types of particles and their signature in the primary subdetector is displayed in Figure. 4.1. First, the signals in each subdetector are combined and referred to as PF elements. Then, multiple elements can be linked with each other to form PF blocks.

Track reconstruction utilizes a combinatorial track finder based on Kalman Filtering, starting from a track seed that is adjusted with each new tracker layer considered in the algorithm. A detailed description of the iterative application can be found in Ref. [95]. The set of all possible tracks, from the hits in the inner tacker and the muon system, is obtained through multiple iterations of the track finder approach. In each successive step, the hits associated with an identified track are removed from the input list and the quality criteria for track seeds, such as the requirement for hits in the PIXEL detector are loosened. Initially, well-defined tracks from prompt charged particles with high momenta are reconstructed, followed by challenging cases are addressed involving hits that cannot be assigned unambiguously to a track. This approach results in high efficiency and purity in the track reconstruction.

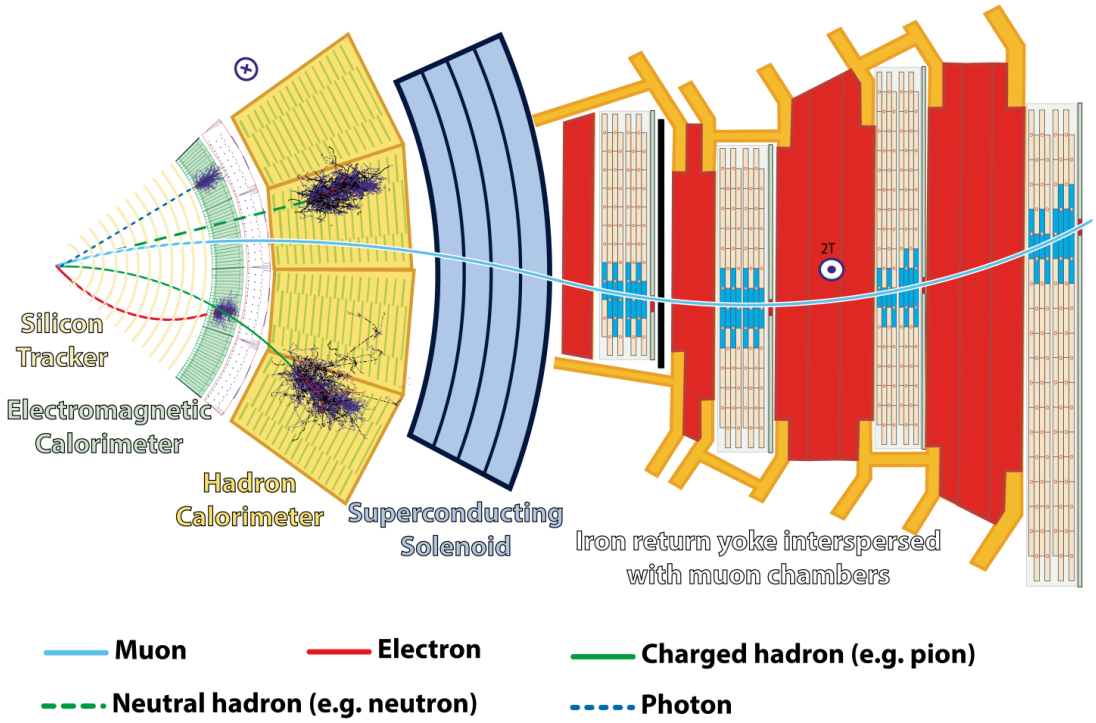


**Figure 4.1:** Slice from the front view of the detector. Shown are the tracks and signals in the subdetectors for each particle from the Standard Model measurable by the CMS detector. Taken from Ref. [96].

The calorimeter clustering algorithm aims at identifying energy deposits from stable neutral and charged particles, estimating the direction of neutral particles, separate neutral from charged particles, and reconstruct photons emitted via Bremsstrahlung from electrons. Energy deposits from all particles in the calorimeter are encapsulated in clusters through an iterative procedure. Seeds are first identified as cells with local energy maxima exceeding a certain threshold. Adjacent cells with energies above twice the noise level are then clustered into these seeds, forming topological clusters. In the endcaps, additional criteria based on transverse energy $E_{\mathrm{T}}$ are applied to account for the higher noise levels with increasing $\theta$. The clustering is performed for each calorimeter system separately, distinguishing between the barrel and endcap region, as well as the preshower detector. In the HF detector, each cell is treated as an individual cluster.
Particles typically induce signals in multiple subdetectors. To reconstruct particles from these signals, a linking algorithm connects the PF elements from different subdetectors to form PF blocks. First, the track from the last hit in the outermost layer of the inner tracker is extrapolated towards the calorimeter systems. If the track lies within the cluster area considering its uncertainties, they are linked. In case multiple HCAL clusters are linked to one track or multiple tracks a linked to one ECAL cluster, only the track with the smallest distance is accepted. Photons from Bremsstrahlung are identified by extrapolating the track's tangent at each point to the ECAL and linking clusters within the tangential area. A dedicated conversion finder [97] also accounts for photon conversion ($\gamma \rightarrow e^{+}e^{-}$) in the inner tacker. Particles can simultaneously induce signals in more then one calorimeter subsystem, like in the ECAL and HCAL or

the ECAL and preshowers. Thus, clusters are linked together if the cluster of the more granular calorimeter (preshower/ECAL) is within the boundaries of the cluster in the less granular calorimeter (ECAL/HCAL).
Based on the PF blocks, particle candidates can be identified and reconstructed. First, muon candidates are solely reconstructed from tracks in the inner tacker and the muon system. Electrons and charged hadrons are reconstructed from clusters linked with one track. Trackless clusters in the ECAL and HCAL are associated with photons and neutral hadrons, respectively. In case of linked clusters from the ECAL and HCAL, one aims to avoid that the energy deposit is not compatible from showers induced by hadrons. This is achieved by also considering tracker information and the deposit energy fraction in the calorimeters.
The primary vertices (PV) for each collision are located along the beam axis. They are ordered by the quadratic sum of the $p_{\mathrm{T}}$ of their tracks with $\sum p_{\mathrm{T}}^2$. The vertex with the highest sum is associated with the hard-scatter vertex and the others are called pileup vertices. Only vertices with at least two assigned tracks are considered.

### 4.1.1 Muon Identification

A detailed description of the muon identification at CMS can be found in Ref. [98] and is briefly summarized in this section. In total, three different types of muons are identified depending on track features and the used information. *Standalone muons* are solely reconstructed from hits in the muon system. A track is classified as a *tracker muon*, if a track from the inner tracker is linked with at least one hit in the muon chambers. Lastly, a *Global muon* is defined when standalone muons are matched with tracks in the inner tracker. Combining tracks from both the muon system and the tracker significantly enhances momentum resolution and reduces the misdentification, particularly concerning cosmic muons, which do not originate from the process within the collision.
Reconstructed muon candidates must pass certain selection and identification criteria. The different selections vary in efficiency and misidentification rates and are referred to as working points (WP). The different strengths of the chosen WP depends on the usage of muons within an analysis. In the scope of this thesis, exactly one lepton $\ell$ is required, which is either a muon or an electron, to identify hadronic top quark decays. To ensure reliable muon detection in an event, the tight WP [98] is utilized, which ensures stringent requirements to minimize the misidentification rate. The tight ID imposes the following requirements; the muon candidates must be reconstructed as a global muon, the global-muon track fit must satisfy $\chi^2/\mathrm{ndof} < 10$, the track must have at least one hit in both the PIXEL and muon chambers, the transverse impact parameter must be $d_{\mathrm{xy}}$<2 mm and the longitudinal distance of the track with respect to the PV is $d_{\mathrm{z}} < 5$ mm. These stringent criteria ensure that the tight ID has the lowest misidentification rate of all WPs, despite having a lower efficiency ($\sim 97$ %) compared to other muon identification methods. Furthermore, an isolation criterion is applied to distinguish prompt muons from those

of decays within a jet, which is evaluated based on the energy deposits within a geometrical cone ($R = 0.4$) with respect to the muon $p_{\mathrm{T}}$.

### 4.1.2 Electron Identification

The reconstruction of electrons considers signals from the inner tracker and the electromagnetic calorimeter. A detailed description can be found in Ref. [99]. Two primary methods are employed for the electron identification; the cut-based electron ID, using sequential selections steps, and a multivariate selection based on a boosted decision tree (BDT) [100]. The criteria consider the shape of the shower in $\eta$-direction, the ratio of the energy deposits in the ECAL and HCAL from the track matched to the electron, the difference $|1/E - 1/p|$ for the track momentum $p$ and the cluster energy $E$, the distance of the electron to the PV in transverse and $z$-direction ($d_0$ and $d_z$), the distance in $\eta$ and $\phi$ between the ECAL supercluster and the track, at most one missing track in the tracker and the electron must pass a conversion veto. The latter aims at rejecting electrons from photon conversion.
The requirements vary depending on the WPs, which correspond to different selection efficiencies. As motivated in the previous section, this analysis uses a tight electron ID with an efficiency of $\sim 70$ %. Furthermore, the analysis presented in Chapter 7 incorporates isolated and non-isolated electrons.

## 4.2 Jet Clustering Algorithms

The definition of jets is ambiguous because there is no unique way to identify hadrons originating from one specific color-charged particle. Therefore, several jet clustering algorithms exist to combine the measured charged and neutral particles, along with photons, into a single object. Each approach offers different properties and possibilities for analyses in high-energy physics. Commonly used algorithms are designed to be infrared and collinear (IRC) safe, ensuring robustness against the emission of soft gluon radiation and particle splitting, respectively. Collinear safety ensures that the outcome of the jet clustering process remains unchanged whether a single particle or two particles with the same combined four-momentum are considered. The main jet clustering algorithms used in this thesis are the iterative anti-$k_{\mathrm{T}}$ [101] (Section 4.2.1) and the exclusive XCone [102] (Section 4.2.2) jet clustering algorithms. They are implemented using the FASTJET software package [103].

### 4.2.1 Iterative Clustering

Iterative jet clustering algorithms gradually cluster particle candidates, also referred to as pseudojets, into jets. By the end of the algorithm, each pseudojet in the input list is merged into one jet. The ordering of the clustering is based on the metric

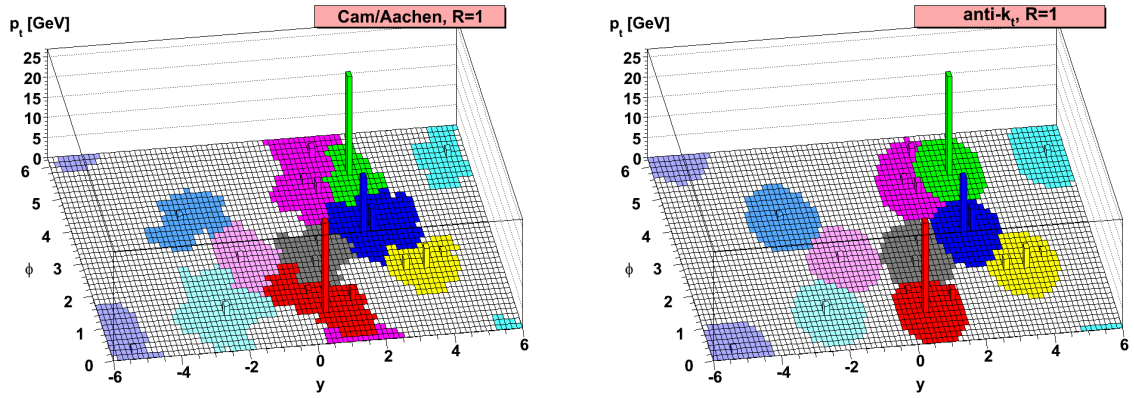


**Figure 4.2:** Shape of the jet areas for Cambridge/Aachen (left) and the anti-$k_T$ (right) jets in the $\eta$-$\phi$-plane. The transverse momenta $p_T$ of the particles inside the jets are indicated by height of the vertical bars. Taken from Ref. [101].

$$d_{iB} = p_{T,i}^{2n} \tag{4.1}$$

and the effective distance of two pseudojets $i$ and $j$ with

$$d_{ij} = \min(p_{T,i}^{2n}, p_{T,j}^{2n}) \frac{\Delta R_{ij}^2}{R^2}. \tag{4.2}$$

Here, $p_{T,i}$ is the transverse momentum of the pseudojets, $\Delta R_{ij}$ the angular distance between two pseudojets, and $R$ the distance parameter that defines the jet radius. The behavior of the clustering is highly dependent on $n$, which weights the contribution from the momentum of the pseudojets. The four-momenta of two pseudojets are added if $d_{ij} < d_{iB}$, forming a new pseudojet for the next iteration. This procedure is continued until $d_{iB} < d_{ij}$, finalizing the current jet, or until all particles are assigned to one jet. The different types of jet clustering algorithms are characterized by the parameter $n$. The Cambridge/Aachen (CA) algorithm [104, 105] sets $n = 0$, thereby removing the dependence on the $p_T$ relying solely on the angular distance of the pseudojets. Without the $p_T$ dependence, pseudojets are considered more uniformly, simplifying analyses focused on jet substructure variables (see Chapter 5). The $k_T$ algorithm [106, 107] utilizes $n = 1$, clustering low-energy pseudojets first. This approach aims to invert QCD splitting processes by favoring pseudojets with soft and collinear momenta. Although both algorithms ensure IRC safety, soft radiation causes irregularities in the shape edges of the jet by definition. This feature becomes negligible with the anti-$k_T$ [101] algorithm, which uses $n = -1$ to cluster high-$p_T$ particles first. As a result, the shape of the final jet is less sensitive to additional soft radiation. All clustering algorithms differ in terms of the jet shape and the treatment of close-by jets. Figure 4.2 displays the resulting jet areas for the CA (left) and anti-$k_T$ (right) jet algorithm. For the anti-$k_T$ algorithm, $d_{iB}$ is also referred to as distance to the beam axis B. When one high-$p_T$ pseudojets has no additional hard pseudojet in close proximity ($2R < \Delta_{ij}$), it will form a perfectly conical jet by accumulating all soft particles within the cone radius. If two high-$p_T$

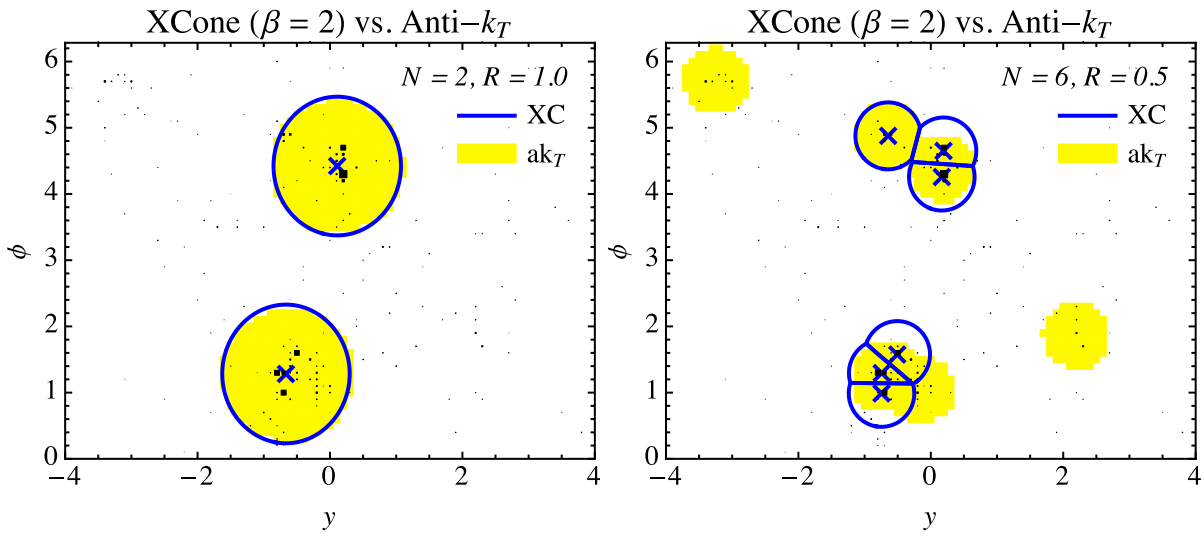


**Figure 4.3:** Comparison of the jet area from XCone (blue lines) and anti-$k_{\mathrm{T}}$ (yellow areas) jets for two large radius jets with $R = 1$ (left) and six small radius jets with $R = 0.5$ (right). Taken from Ref. [102].

pseudojets are nearby ($R < \Delta_{ij} < 2R$), neither of them will form perfect circular jet cones but are divided by a straight line for $p_{\mathrm{T,i}} = p_{\mathrm{T,j}}$ or form crescent moon shapes for $p_{\mathrm{T,i}} \gg p_{\mathrm{T,j}}$. In general, the softer particles favor the pseudojet with the greater $p_{\mathrm{T}}$. If two high-$p_{\mathrm{T}}$ pseudojets are clustered into a single jet ($\Delta_{ij} < R$), the shape becomes more deformed.
Analyses at the CMS Collaboration commonly use the anti-$k_{\mathrm{T}}$ algorithm with a cone radius of $R = 0.4$ (AK4 jets) or $R = 0.8$ (AK8 jets) for high-energetic particle decays.

### 4.2.2 XCone Algorithm

Unlike iterative jet clustering algorithms, which do not predetermine the final number of jets, exclusive jet algorithms are designed to produce a predefined number of jets $N$. XCone [102], additionally employs geometric cones to define jet shapes. The cone radius is specified by a distance parameter $R$, analogous to the one from iterative clustering algorithms.
The jet axes are chosen by minimizing the $N$-jettiness [108], which is a measure of how compatible an event is with counting $N$ jets (see Section 5.2). It is defined as

$$\widetilde{\tau}_{\mathrm{N}} = \sum_{\mathrm{i}} \min\{\rho_{\mathrm{jet}}(p_{\mathrm{i}}, n_1), \ldots, \rho_{\mathrm{jet}}(p_{\mathrm{i}}, n_{\mathrm{N}}), \rho_{\mathrm{beam}}(p_{\mathrm{i}})\}, \tag{4.3}$$

where the sum runs over all particles $i$ considered in the algorithm with the four-momenta $p_i$. The distances of the $i$-th particle to the $A$-th axis $n_A$ and the beam axis are given by $\rho_{\mathrm{jet}}(p_{\mathrm{i}}, n_A)$ and $\rho_{\mathrm{beam}}(p_{\mathrm{i}})$, respectively. These distances can be defined using a conical geometric measure with various metrics. The proposed standard for measurements at the LHC sets

$$\begin{aligned} \rho_{\text{jet}}(p_{\text{i}}, n_A) &= \frac{2\cosh y_A}{R^2} n_A \cdot p_i \quad \text{and} \\ \rho_{\text{beam}}(p_{\text{i}}) &= p_{\text{T},i}, \end{aligned} \tag{4.4}$$

where $y_A$ is the rapidity of the $A$-th axis. This definition ensures that minimizing $\widetilde{\tau}_N$ also minimizes the unclustered $p_{\text{T}}$. The conical measure refines the jet axis, aiming for conical jet shapes. To increase the computational efficiency, a generalized $k_{\text{T}}$ clustering algorithm is used to find jet seeds close to a minimum of $\widetilde{\tau}_N$. The $k_{\text{T}}$ algorithm is configured to behave similarly to the $N$-jettiness metric in Equation 4.4, while also maintaining IRC safety. These axes are then refined once by minimizing $\tau_N$. For this, all particles within a partition, as defined by the metrics in Equation 4.4, are added to the corresponding axis. Subsequently, each particle within the distance $R$ from a final jet axis is clustered to that jet. For isolated jets, the jet area takes on a circular shape. However, for nearby jets ($\Delta_{ij} < R$), particles are assigned to the nearest jet axis, resulting in areas separated by a straight line.

XCone is particularly efficient in high-energy processes where final state particles have a small angular distance, such as in decays of high-energetic top quarks. While iterative algorithms require additional strategies, XCone is capable of handling these scenarios. The advantages are illustrated in Figure 4.3, where simulated $\text{t}\bar{\text{t}}$ events are clustered using the XCone and the anti-$k_{\text{T}}$ algorithm. For two large radius jets ($R = 1$), each reconstructing the entire top quark decay, both algorithms give a similar result. The difference becomes significant for six smaller radius ($R = 0.5$) jets, targeting the individual decay products of the top quark. While the XCone algorithm is able to distinctly identify these closely spaced jets, the anti-$k_{\text{T}}$ algorithm tends to merge them. Therefore, XCone is particularly suited for analyses aiming for high-energetic $\text{t}\bar{\text{t}}$ events, effectively preserving detailed information about the decay products.

### 4.2.3 Pileup Mitigation Techniques

For each bunch crossing, multiple pp interactions can occur, depending on the instantaneous luminosity, referred to as pileup. Interactions from pileup lead to additional particles measured in the detector, affecting the reconstruction and the measurement of the process of interest. Especially in case of the jet clustering and reconstruction, it is crucial to reduce the contribution from pileup to improve the resolution of such algorithms. The pileup profiles measured by the CMS detector for Run 2 and Run 3 are shown in Figure 4.4. Contributions from pileup for Run 3 are larger compared to Run 2 and will further increase for the HL-LHC. In this thesis, two approaches to mitigate the impact from pileup commonly used by the CMS Collaboration are used, namely the *charged hadron subtraction* (CHS) [94, 110] and the *pileup per particle identification* (PUPPI) [111]. These algorithms identify particles originating from pileup vertices (see Section 4.1), and remove them or suppress their contribution to the reconstructed observable.

The CHS algorithm aims to reduce the contribution from charged hadrons not originating from

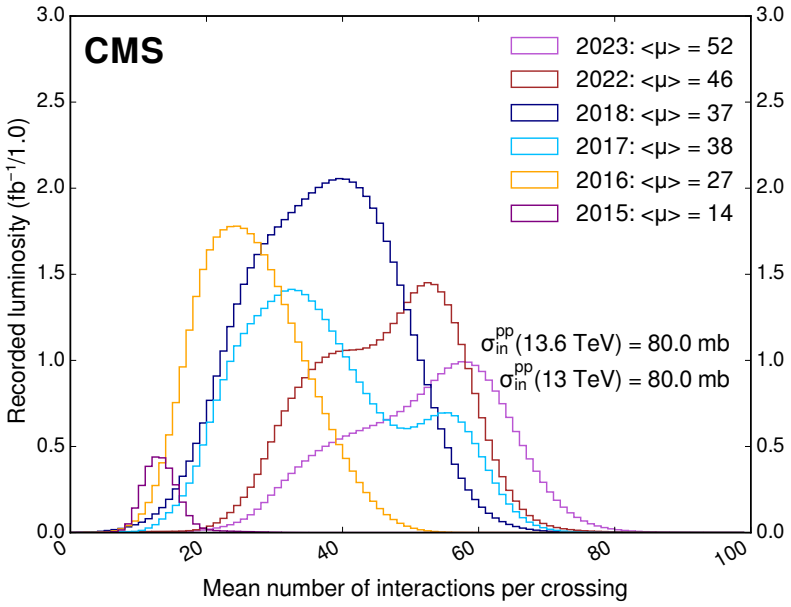


**Figure 4.4:** Mean number of the interactions per bunch crossing for the Run 2 and Run 3 data-taking periods with a center-of-mass energy of $\sqrt{s} = 13\,\text{TeV}$ and 13.6 TeV, respectively. Taken from Ref. [109].

the PV. Based on the tracks of charged hadrons, they can either be assigned to the PV or to the pileup vertex. Particles that can be unambiguously assigned to a pileup vertex are removed from the input list for jet clustering algorithms. Particles that are not used in a vertex fit and neutral particles are kept. Since the CHS algorithm relies on tracker information, it only covers a range up to $|\eta| = 2.5$, the coverage of the tracking system of the CMS detector. Jets clustered with particles based on the CHS algorithm are called CHS jets. To account for neutral particles from pileup, dedicated jet-area based corrections are employed (see Section 4.4.1). Furthermore, jets produced from pileup collisions can be identified based on the jet shape and other properties, summarized in the *pileup jet IDs* [112].

A complementary approach, referred to as PUPPI, additionally addresses neutral particles. In this method, the four-momenta of particles are rescaled with a weight in the range $w \in [0,1]$, which corresponds to the probability that a particle is associated with a pileup vertex ($w = 0$) or the hard-scattering process ($w = 1$). The weight is determined by the properties of nearby particles relative to the particle under consideration and is calculated as

$$\alpha_i = \log \sum_{j \neq i, \Delta R_{ij} < R_0} \left( \frac{p_{\text{T},j}}{\Delta R_{ij}} \right), \tag{4.5}$$

where the sum runs over all particles $j$ within a distance $R_0 = 0.4$ from the particle of interest. Ensuring that dominantly the particles from the PV contribute to $\alpha_i$, for $|\eta_j| < 2.5$ only charged particles from the PV and for $|\eta_j| > 2.5$ all reconstructed particles are considered. The latter ensures that high energetic particles are favored. Charged particles not associated with any vertex are kept based on their $p_\text{T}$, $\eta$ and distance to the PV in $z$-direction [113].

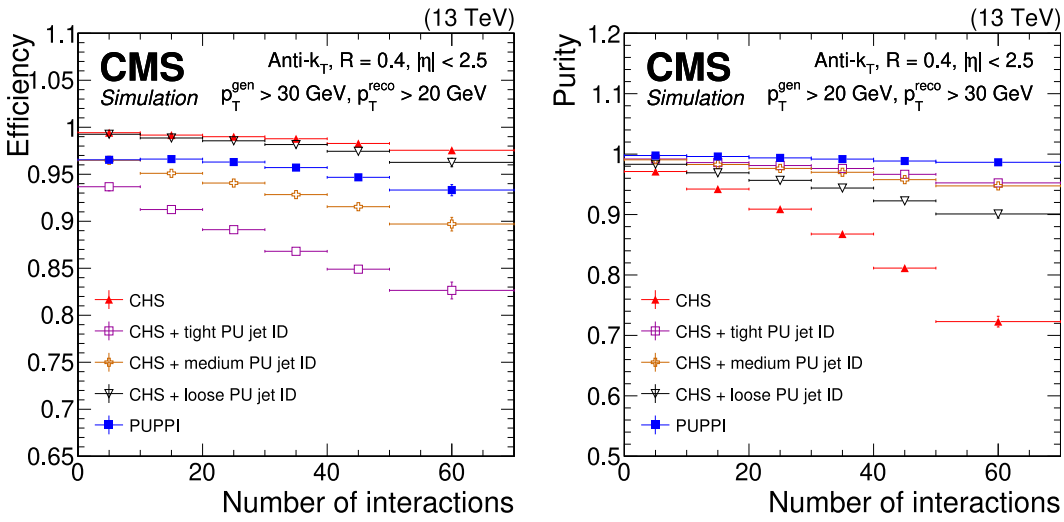


**Figure 4.5:** Efficiency (left) and purity (right) as the function of the number of interactions for the different pileup mitigation techniques (PUPPI and CHS). Taken from Ref. [114].

Jets clustered with the anti-$k_T$ algorithm with $R = 0.4$ and particles from the CHS and PUPPI algorithm are referred to as AK4CHS and AK4Puppi jets, respectively. The efficiency and purity for both algorithms are summarized in Figure 4.5. While PUPPI shows a few percent lower efficiency with respect to CHS, it outperforms in terms of purity, also considering a combination of CHS jet and pileup jets.

## 4.3 Identification of b Jets

Jets originating from b and c quarks (heavy-flavor jets) can be identified based on their properties, allowing to distinguish them from jets arising from gluons or u, d and s quarks (light-flavor jets). One of the main features utilized to identify heavy-flavor jets is the relatively long lifetime of b hadrons with $\sim 1.5\,\text{ps}$ [30]. While the b quark cannot decay into the much heavier top quark, the transition probability to other generations is suppressed as it can be seen in the CKM matrix in Equation 2.10. For that reason, the b quark forms a B hadron with nearby quarks, which can travel several millimeters inside the detector before initiating a jet, as illustrated in Figure 4.6. This flight distance leads to a separated secondary vertex (SV) displaced from the PV of the hard-scattering process. A similar argument applies to jets originating from c quarks, although the distance is generally not as large as it is for b quarks.
The CMS Collaboration has developed several b-tagging algorithms, exploiting properties such as the flight distance to identify heavy-flavor jets. The taggers provide discriminate scores in the range [0,1] that can be interpreted as the probability that a jet arises from a heavy-flavor hadron. Two commonly used algorithms are the DeepCSV [115, 116] and the DeepJet [116, 117] algorithm. Both employ a deep neural network that use several input variables based on the SV and the tracks associated with the SV. Particularly useful for identifying heavy-

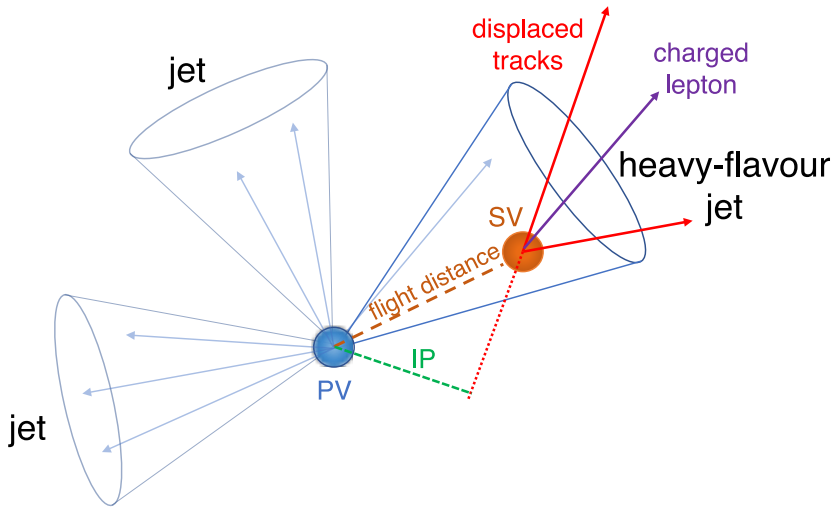


**Figure 4.6:** Illustration of heavy-flavor jets, highlighting the displacement of the jet's origin from the primary vertex (PV). The jet's origin can be identified as a secondary vertex (SV) with an impact parameter (IP). Taken from Ref. [115].

flavor jets are the displacement of the SV relative to the PV and the mass of the SV, which is related to the mass of the heavy-flavored hadron. Furthermore, the correlation of the input features with the jet $p_T$ and $\eta$ are considered to improve the performance of the taggers. In earlier algorithms, the classification was limited to b-flavored jets (b jets). Now, the usage of DNNs allows to further classification of jets initiated by c quarks or light-flavored quarks and gluons. The DeepJet algorithm extends the set of input variables to various features of the jet constituents. A more complex DNN architecture is employed to handle the larger set of input variables. The performance of both taggers are shown in Figure 4.7 (left), where the DeepJet algorithm outperforms the DeepCSV algorithm. This thesis uses the DeepJet algorithm with a misidentification ratio of 0.1 %, corresponding to an efficiency of 80 %, derived from $t\bar{t}$ events for AK4 jets with $p_T > 30\,\text{GeV}$.

For Run 3, both algorithms are retrained [118], with the DeepJet algorithm used as the default. The tagger performance has been improved with respect to Run 2 as shown in Figure 4.7 (right).

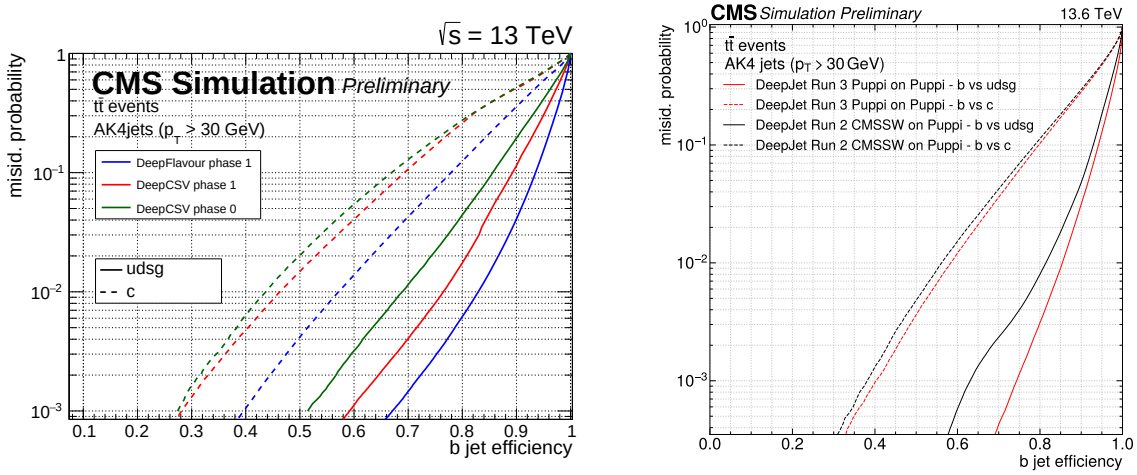


**Figure 4.7:** Performance of commonly used b-tagging algorithms at the CMS Collaboration. Shown are the misidentification rates as a function of b-tagging efficiencies for light-flavor quarks and c quarks. In Run 2 (left) the DeepFlavour (DeepJet,blue) outperforms the DeepCSV (red) algorithm. Run 3 (right) reevaluates both algorithms. The performance of DeepJet in Run 3 (red) improves with respect to Run 2 (black). Taken from Ref. [116] (left) and [118] (right).

## 4.4 Jet Calibration

The CMS Collaboration employs a factorized jet calibration [119] approach to align the four-momentum of a jet clustered from PF particles, $p^{\text{raw}}$, to the four-momentum of the particle-level jet, $p^{\text{true}}$, on average. A multiplicative correction factor $C$ is derived through a series of successive steps, to scale the four-momentum of the PF jet to obtain the calibrated jet four-momentum. Each step is tailored to mitigate specific detector effects that can influence the measurement of the four-momentum. The jet energy correction (JEC) workflow is summarized in Figure 4.8.

Additional particles that do not originate from the hard scattering process and are clustered into the jet can cause a shift in the jet energy. Energy deposits originating from pileup interactions are mitigated in the first step of the jet calibration procedure and are corrected only for CHS

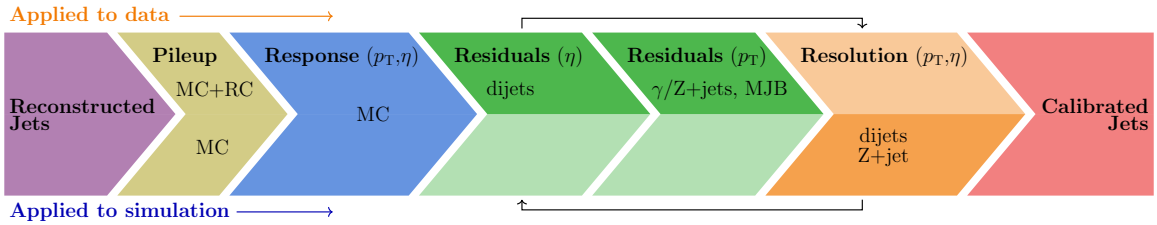


**Figure 4.8:** Workflow of the jet energy calibration used by the CMS Collaboration. The $\eta$-dependent residual corrections rely on the jet energy resolution measurement, requiring an additional iteration, indicated by the black arrows. The pileup correction is only applied to CHS jets. Adapted from Ref. [1].

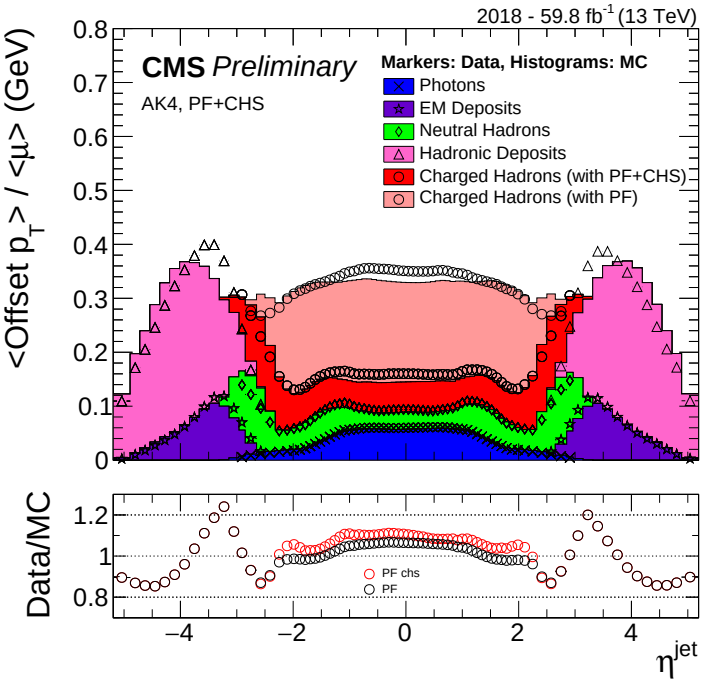


**Figure 4.9:** Average energy offset normalized by the average number of pileup interactions $\mu$ measured with the Random Cone method for data (markers) and simulations (histograms). The offset is distinguished for contributions from different types of PF candidates. Taken from Ref. [120].

jets. Afterwards, various detector effects such as non-uniformity in $\eta$, the non-linear response in $p_{\mathrm{T}}$, and biases introduced by electronic noise are corrected. Determined solely through simulations, these corrections constitute the largest part of the calibration process. Subsequently, discrepancies between data and simulations, e.g. due to imperfect detector modeling, are addressed with residual corrections. These corrections are dependent on $\eta$ and $p_{\mathrm{T}}$ to account for differences in the subdetector responses and the absolute energy scale, respectively. Finally, the JER in simulations is aligned to that observed in data by smearing the transverse momentum of the jets.

Within this thesis, the jet energy resolution scale factors (JER SFs) are measured for several data-taking periods and established techniques are thoroughly explored and further developed to prepare for harsher conditions in upcoming data taking periods. Those include the increase of pileup and additional radiation due to higher center-of-mass energies. A detailed description of the methodology is elaborated on in Chapter 6.

### 4.4.1 Pileup Offset Calibration

Contributions from pileup clustered into jets from hard scattering processes can significantly shift the measured energy. While the PUPPI algorithm mitigates the occurrence from charged and neutral particles from pileup, the CHS method only focuses on charged hadrons within tracker acceptance. To correct for pileup contributions not treated by CHS, a correction referred

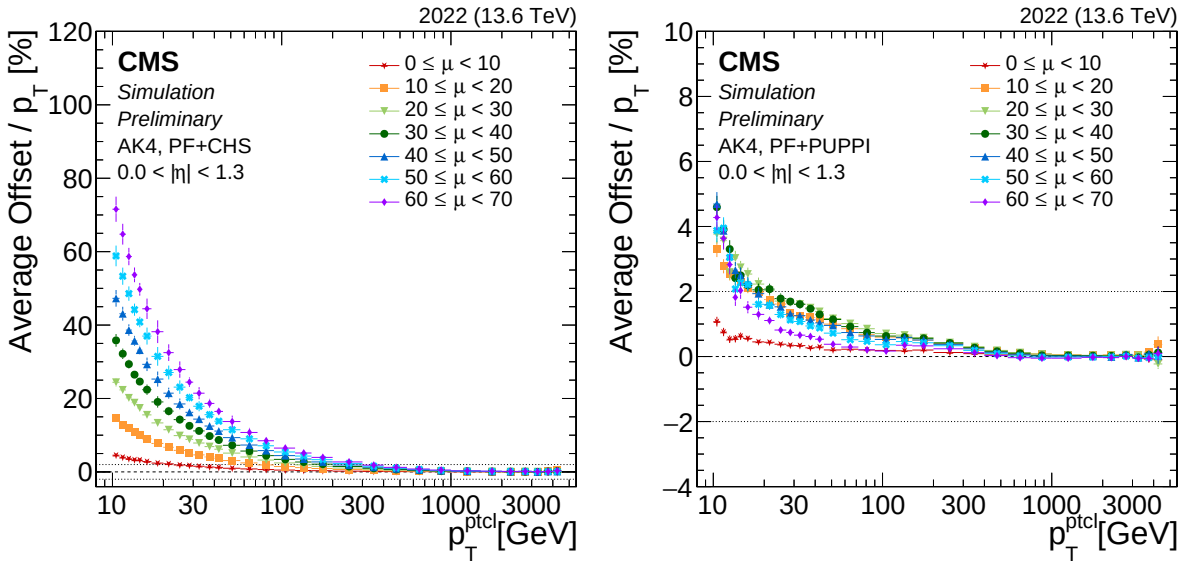


**Figure 4.10:** Average energy offset as a function of the particle-level $p_{\mathrm{T}}^{\mathrm{jet}}$ and the number of pileup interactions $\mu$ for AK4-CHS (left) and PUPPI (right) jets. Taken from Ref. [1].

to as the L1 offset correction is applied to CHS jets. A multiplicative factor $C_{\mathrm{hybrid}}$ is calculated using the *hybrid jet area method* and is defined as

$$C_{\mathrm{hybrid}} = 1 - \frac{\langle p_{\mathrm{T}}^{\mathrm{offset}} \rangle}{p_{\mathrm{T}}^{\mathrm{raw}}}. \tag{4.6}$$

Here, $\langle p_{\mathrm{T}}^{\mathrm{offset}} \rangle$ represents the average transverse momentum offset, calculated from particle-level simulations in QCD multijet events. The offset measures the average $p_{\mathrm{T}}$ difference between matched jets ($\Delta R_{\mathrm{ij}} < R/2$) with and without pileup. Figure 4.9 illustrates the average offset per particle interaction for each PF candidate. This offset can be parameterized as a function of the reconstructed transverse momentum of the jet $p_{\mathrm{T}}^{\mathrm{raw}}$, its pseudorapidity $\eta$, the effective jet area $A_j$ and the energy density $\rho$ of the event. Figure 4.10 shows the performance of AK4CHS (left) and AK4Puppi (right) jets in the barrel region ($|\eta| < 1.3$) without additional pileup corrections applied. The CHS algorithm features an average energy offset of more than 70 % for low-$p_{\mathrm{T}}$ jets, whereas the PUPPI algorithm reduces this offset to below 5 % in 2022. In the endcap region with $3.0 < |\eta| < 5.0$, the offset increases to 200 % for AK4CHS and 30 % and AK4Puppi jets. Upon applying the appropriate corrections, the energy offset for CHS jets becomes comparable to that of PUPPI jets in the barrel region and shows a lower contribution in higher $|\eta|$ regions.

Differences in data to simulation are corrected using the random cone (RC) method. Simulation-to-data scale factors are determined by utilising zero-bias data and simulations, selecting events with no hard scattering processes. Zero-bias data is collected using corresponding triggers without applying any selection criteria. In simulation, process with neutrino-only final states are generated, ensuring no signal in the detector, and combined with pileup samples. Then, PF particles are clustered with randomly-placed cones in the $\eta$-$\phi$-plane. The average energy of

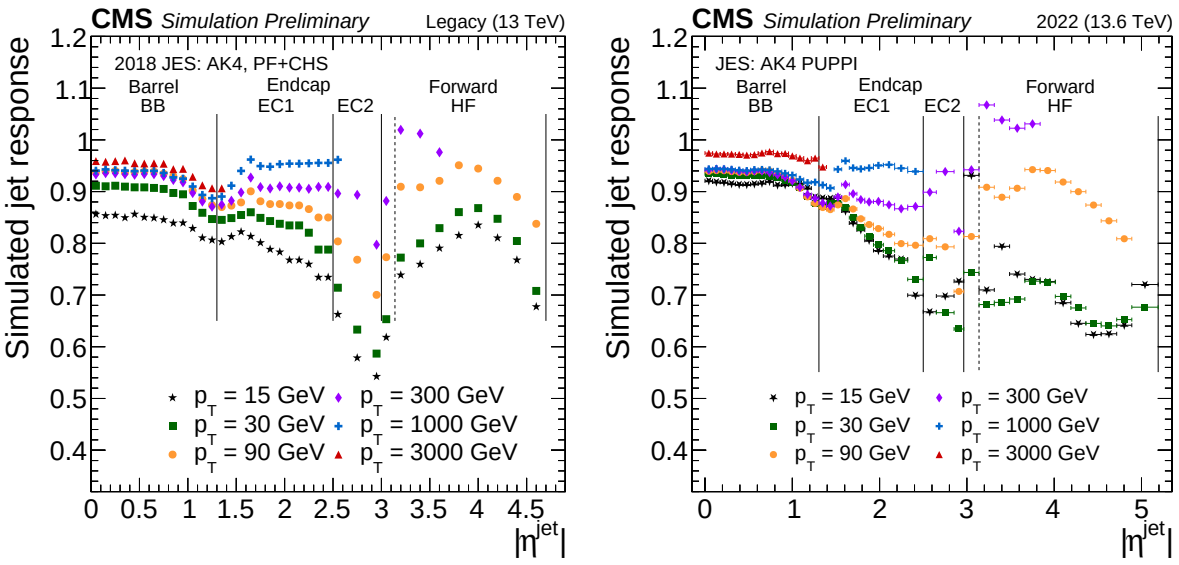


**Figure 4.11:** Simulated jet response as a function of the jet $\eta$ and $p_T$ for AK4CHS jets in 2018 (left) and AK4Puppi jets in 2022 (right). Different regions of the detector are marked by vertical gray lines, where the endcaps are shown with (EC1, $|\eta| < 2.5$) and without (EC2) tracker acceptance. Taken from Ref. [120] (left) and [1] (right).

those particles can be identified with the average offset originating from pileup contribution. The $\eta$ and $\rho$ dependent offset scale factors are then defined as

$$\frac{\langle p_T^{\text{offset}} \rangle_{\text{data}}^{\text{RC}}}{\langle p_T^{\text{offset}} \rangle_{\text{MC}}^{\text{RC}}}. \tag{4.7}$$

The differences between data and simulation in the average energy offset is shown in Figure 4.9, highlighting the distinct contributions from each PF candidate type.

### 4.4.2 Simulated Response Corrections

The second step of the JEC workflow, also referred to as L2L3Response correction, ensures that the jet energy scale (JES) of reconstructed PF jets, corrected for pileup, matches the one on particle level. Based on simulated QCD multijet events, it makes up the bulk part of the full correction chain at CMS covering the main shift in the JES . The JES is defined as the mean value of the jet response

$$R = \frac{p_T}{p_T^{\text{true}}}. \tag{4.8}$$

Here, $p_T^{\text{true}}$ is obtained from clustering particles on particle-level. These particle-level jets are matched with the closest jets clustered from PF candidates within $\Delta R_{ij} < R/2$ leading to an efficiency of $\varepsilon \approx 100\,\%$ at $p_T = 30\,\text{GeV}$. The jet response is a measure of how much the $p_T$ of jets differ on detector-level and particle-level. Hence, this correction mitigates detector effects that cause a shift in the jet four-momenta. The $\eta$ and $p_T$ dependent corrections address the

non-uniformity of the detector response and the non-linearity in $p_T$ within the full coverage of the detector. The simulation-based correction is particularly beneficial for regions of phase space that are challenging to access with data alone. This includes scenarios with low- and very high-$p_T$ jets, reaching $p_T < 15\,\text{GeV}$ and $p_T > 1000\,\text{GeV}$, respectively, as well as environments with a low ($\mu < 5$) and very high ($\mu > 40$) number of pileup interactions.
Figure 4.11 showcases the simulated jet response corrections for the years 2018 in Run 2 (left) and 2022 in Run 3 (right). The response tends to be stable in the barrel region ($|\eta| < 1.3$) with $\sim 95$ %, where the main shift of the response is due to the contribution of neutral hadrons ($\sim 15$ % of $p_T^{\text{true}}$) with a relatively low response of $\sim 0.6$ [120]. Notable variations occur outside the tracker coverage ($|\eta| > 2.5$). In this regions, the jumps for various $p_T$ values become more dominant, which is due to the transition between various subdetectors. The drop in the HF region in 2022 compared to 2018 is due to a feature of the PUPPI algorithm, which excessively removes isolated particles to reduce pileup contributions [1].

### 4.4.3 Residual Corrections

After the pileup and detector response correction, jets in simulations are well calibrated. In Run 2 and Run 3 the closure of the jet response in the barrel region ($|\eta| < 2.5$) and $30 < p_T < 2000\,\text{GeV}$ is within 0.02 %. For the transition and endcap ($2.5 < |\eta| < 5.0$) region, the closure is still below 1 %. However, there are still differences between data and simulation which lead to not perfectly calibrated jets in data. Those differences are compensated by applying residual corrections. Jet corrections derived from data cannot access the jet response directly, since particle-level information is required. Instead, corrections are derived using precisely calibrated objects as a reference. Two consecutive steps are used to measure $\eta$- and $p_T$-dependent corrections, referred to as L2Residual and L3Residual corrections, respectively.
The former utilizes dijet events, with a balanced back-to-back configuration ($\Delta\phi > 2.7$). Two established methods are used: the primary corrections are derived from the missing transverse momentum projection fraction (MPF) method, and the transverse momentum imbalance method is used as a cross-check. The MPF method consists of projecting $p_T^{\text{miss}}$ onto a reference object. That way, the response of the hadronic activity, which balances the transverse momentum of the reference object, is considered. In dijet events, it is expected that $p_T^{\text{miss}}$ primarily arises from miscalibration. The transverse momentum imbalance method corrects the measured jet response from a jet unconstrained in $\eta$ with respect to a jet in the central region ($|\eta| < 1.3$), exploiting the $p_T$ imbalance in dijet events. It is also the primary method to derive the JER SFs in this thesis and is elaborated on in more detail in Chapter 6.
The L3Residual measurement is conducted in Z+jets ($Z \rightarrow \mu\mu/ee$), $\gamma$+jets and QCD multijet events, employing both the MPF and transverse momentum imbalance method. The final correction factor is obtained from a global fit of all three processes, each of which covers a different $p_T$ range. While $Z/\gamma$+jets are particular useful for low- and mid-$p_T$ ranges jets, QCD multijet

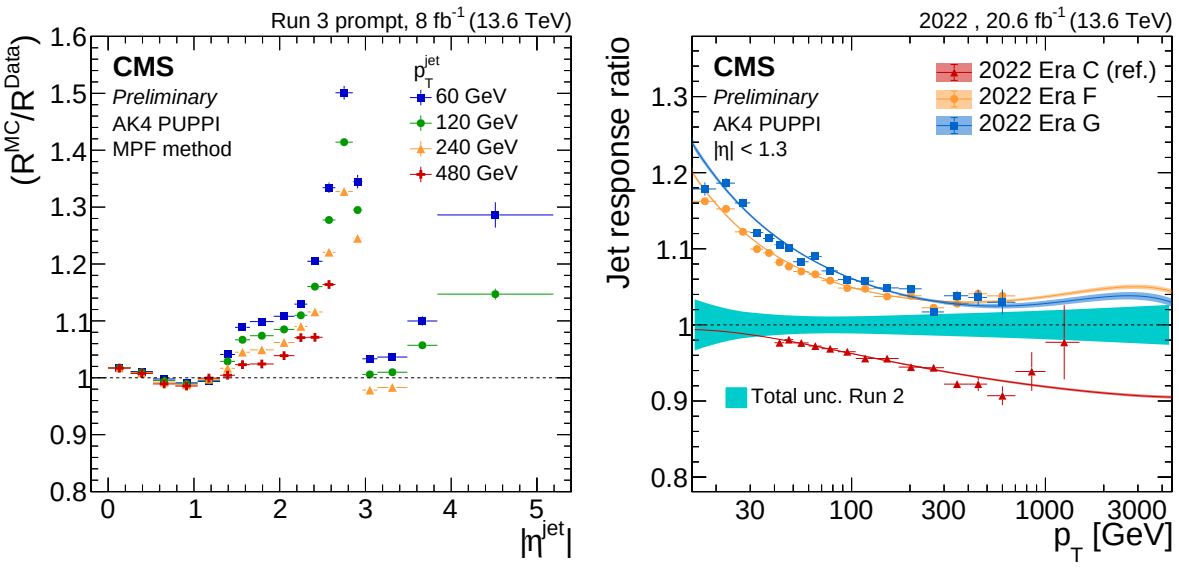


**Figure 4.12:** Data-to-simulation comparison of the jet response for year 2022 of the Run 3 data-taking period. The comparison derived from dijet events in dependence of $|\eta|$ of the jets (L2Residual, left) are shown for different $p_\mathrm{T}$ (colored markers). The $p_\mathrm{T}$-dependent comparison derived from Z+jets events (right) is compared for different eras from the year 2022. The total uncertainty from the Run 2 data-taking period is shown in blue for a comparison. Taken from Ref. [1].

events aim for high-$p_\mathrm{T}$ jets with $p_\mathrm{T} > 1000\,\mathrm{GeV}$.

Both corrections for the Run 3 data-taking period are displayed in Figure 4.12. The L2Residual corrections (left) show a similar behavior in comparison to the response corrections. While the central region is well calibrated with a difference of $\sim 2\,\%$, the transition region is not well modelled, leading to scale factors of $\sim 50\,\%$. The L3Residual corrections are highly dependent on the calibration of the HCAL, where the energy of high-$p_\mathrm{T}$ jets is predominantly deposited. On the contrary, the energy of low-$p_\mathrm{T}$ jets are mainly measured in the tracker and ECAL. The impact is seen on the right side of the Figure, where a different HB (see Figure 3.7) scale for different time periods (eras) in 2022 lead to a large shift in the jet response in data.

### 4.4.4 Additional XCone Corrections

The analysis presented in Chapter 7 primarily uses jets clustered with the XCone algorithm with a distance parameter of $R = 0.4$. These jets are corrected with the JEC derived for AK4 jets elaborated on in the previous sections. As discussed in Section 4.2.2, isolated XCone jets behave very similar to AK4 jets. However, while the XCone algorithm is able to distinguish overlapping jets, the anti-$k_\mathrm{T}$ algorithm is not. Instead it clusters all particles into one circular jet and additional crescent moon shaped jets. This difference is crucial for analyses aiming for high energetic top quark decays. The former analysis [18, 122] has introduced an additional XCone calibration procedure to account for these residual differences. The $\eta$ and $p_\mathrm{T}$-dependent correction factors are derived from simulated $\mathrm{t\bar{t}}$ events in the all-hadronic channel and applied

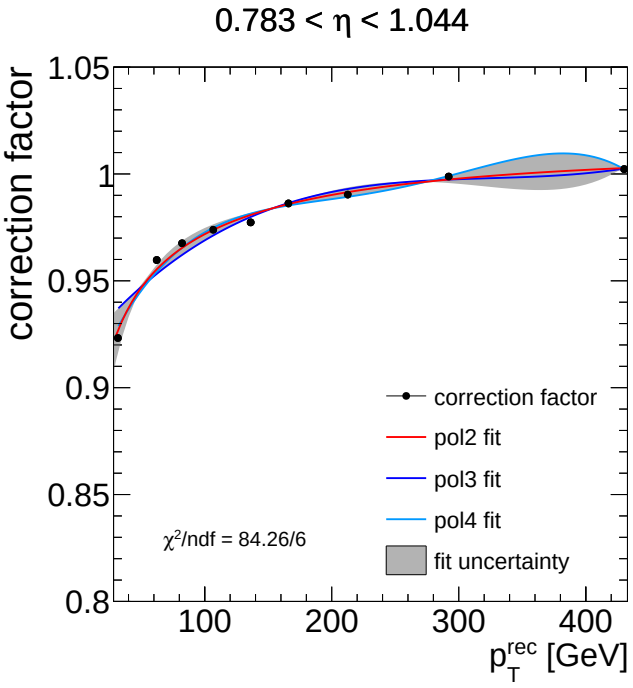


**Figure 4.13:** Derivation of the $\eta$ and $p_{\mathrm{T}}^{\mathrm{rec}}$ dependent additional XCone corrections in full hadronic $\mathrm{t\bar{t}}$ decays. The correction factors are derived for XCone jets with $R = 0.4$ corrected with AK4CHS corrections centrally provided by the CMS Collaboration. Taken from the supplementary material [121] of Ref. [18].

on top of the AK4 corrections.

The corrections are based on the jet response in Equation 4.8 for matched ($\Delta R < 0.2$) XCone jets on particle and detector level. It is calculated as the inverse of the mean value of the jet response $\langle R \rangle$ in bins of $\eta$ with respect to the reconstructed jet transverse momenta $p_{\mathrm{T}}^{\mathrm{rec}}$. The correction factor for one specific $\eta$-bin is shown in Figure 4.13. A second-order polynomial function is fitted to the measured values, to obtain a smooth function for the correction factors. Systematic uncertainties are introduced via the differences to third order and fourth order polynomial to account for the arbitrary choice of fit function.

The relative difference of the particle and detector level jets in independent simulated tW events is shown in Figure 4.14 (left). Jets on detector level are in agreement within 1 % with jets on particle level. The remaining difference is covered by the systematic uncertainties from the additional XCone corrections. The same validation procedure is performed in the $\ell$+jets channel of simulated $\mathrm{t\bar{t}}$ events and shown in Figure 4.14 (right). Here, the difference is shown for three scenarios; no JEC applied (yellow), only AK4CHS JEC applied (blue) and the combination of AK4CHS JEC and the additional XCone corrections (red). The additional XCone corrections improve the agreement in the low $p_{\mathrm{T}}$ region showing a similar result as in tW events.

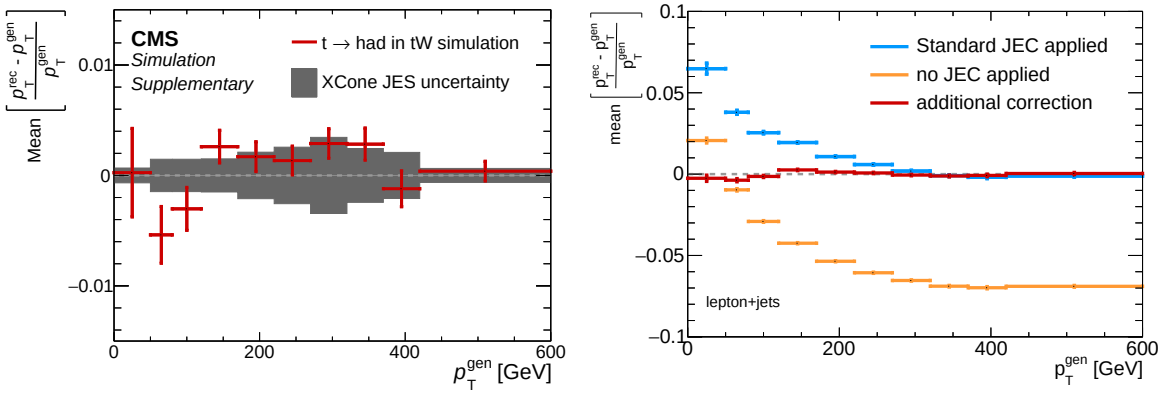


**Figure 4.14:** Relative differences of the jet $p_T$ on detector level and particle level. Shown are the validation of the additional XCone corrections in two independent samples. The differences in simulated tW samples (left) is shown with respect to the systematic uncertainties arising from the additional corrections. In the $\ell$+jets channel from simulated $t\bar{t}$ events (right), the closure with AK4CHS corrections and additional XCone corrections (red) is compared to no corrections (yellow) and only AK4CHS correction (blue) applied. Taken from the supplementary material [121] of Ref. [18].

## 4.5 Missing Transverse Momentum

The sum of the transverse momenta of the initial state particles in pp collisions vanishes. Momentum conservation requires the final state originating from this interaction also to sum up to zero. Missing transverse momentum $p_T^{miss}$ is a measure of the $p_T$ imbalance and thus of particles that do not leave signals in the detector or miscalibrations. In the scope of the SM, the only particle not interacting with the detector material is the neutrino. Nonetheless, $p_T^{miss}$ can also be induced by processes including new physics. In this thesis, the MET is either identified as the neutrino from leptonic top quark decays, or miscalibration of jets and is defined as

$$\vec{p}_T^{\,miss} = -\sum_i \vec{p}_{T,i}, \tag{4.9}$$

where $i$ runs over all PF candidates. The reconstructed $p_T^{miss,uncorr}$ depends on the correct measurement and calibration of jets. Every correction applied to an event is propagated to $p_T^{miss}$, which is then corrected by replacing the sum of all PF candidates clustered to a jet with the calibrated jet itself. The corrected $p_T^{miss}$ is thereby defined as

$$\vec{p}_T^{\,miss,corr} = -\sum_j^{n_{jets}} \vec{p}_{T,j}^{\,corr} - \sum_i^{n_{uncl.}} \vec{p}_{T,i}. \tag{4.10}$$

where the sum runs over each energy corrected jet $j$ and unclustered (uncl.) particle $i$.

# Chapter 5

# Jet Substructure at the LHC

Jets play a crucial role in high-energy physics analyses, necessitating precise calibrations for accurate results. Understanding of the jet substructure is vital for various physics observables and the identification of heavy-flavored jets. At high energies, the decay products of heavy particles are highly Lorentz-boosted featuring a small spatial separation and thus can be reconstructed within a single large-$R$ jet.
This chapter discusses the most relevant substructure variables for this thesis. The fundamental observable, the jet mass $m_{\text{jet}}$, is discussed in Section 5.1 followed by the $N$-subjettiness in Section 5.2. Grooming algorithms, which reduce contributions from soft radiation, are elaborated on in Section 5.3. Recent measurements of jet substructure variables such as the jet mass or the $N$-subjettiness are introduced in Section 5.4. This chapter is based on Ref. [123, 124, 125] if not stated otherwise.

## 5.1 Jet Mass

The jet mass is a fundamental observable in analyses of heavy particle decays. It is defined as the invariant sum of the four-momentum $p$ of all jet constituents $i$ as

$$m_{\text{jet}}^2 = \left( \sum_{\text{i}} p_{\text{i}} \right)^2 . \tag{5.1}$$

The jet mass results from a sequence of parton emissions and non-perturbative hadronization, strongly dependent on the initial parton. For jets originating from light-flavor quarks and gluons, the mass is primarily induced by the splitting in hadron showers. For the assumption of a massless parton undergoing a collinear splitting into two partons $i$ and $j$, the jet mass can be approximated as $m^2 \approx p_{\text{T,i}}\ p_{\text{T,j}}\ \Delta R_{\text{ij}}^2$ [127], with $\Delta R_{ij}$ denoting the angular distance between these two partons.
In the collinear and soft limits ($R_{ij}/p_{\text{T},k} \to 0$), the emission of additional partons is suppressed due to effects such as the running coupling of the strong interaction. The probabilities that a

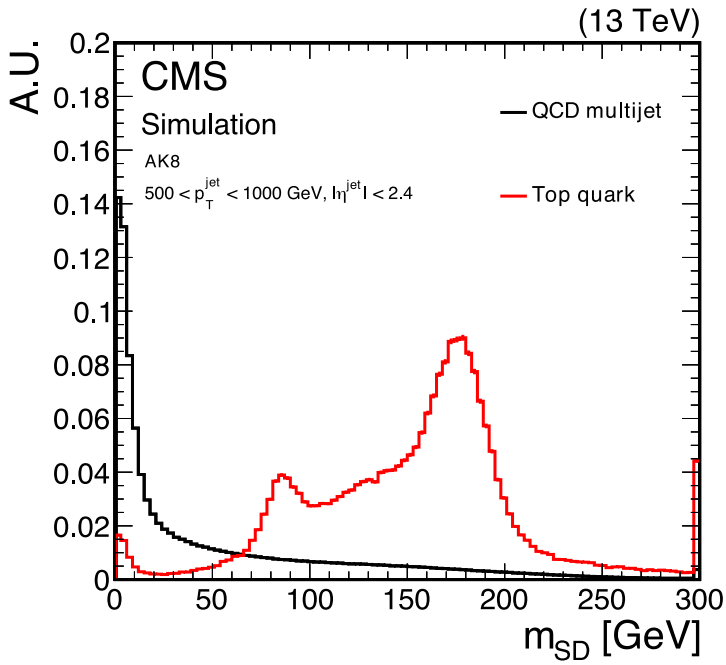


**Figure 5.1:** Normalized jet mass distribution groomed with the soft-drop algorithm for jet reconstructing the hadronic top quark decay (red) and light flavored jets (black). Jets are reconstructed with the anti-$k_T$ algorithm with $R = 0.8$ and are required to have $500 < p_T < 1000\,\text{GeV}$. Taken from Ref. [126].

gluon does not split into $q\bar{q}$ or a quark does not emits gluons are summarized in the *Sudakov form factor* [128] and depends on various parameters of the process. In the energy range where the suppression is the lowest, the so-called *Sudakov peak* [129] in the $m_{\text{jet}}$ distribution arises. The position of the peak depends linearly on the jet $p_T$. Thus, the jet mass distributions from massless partons do not peak at zero as naively expected, but instead, the peak occurs at higher values. For jets reconstructing the full decay of heavy objects, such as the top quark, the sudakov peak is less relevant due to the large mass scale of these particles. In such cases, the mass of the jets becomes sensitive to the underlying parton, allowing for a distinction between light-flavored and heavy-flavored jets. Figure 5.1 illustrates the groomed (see Section 5.3) jet mass distribution from hadronic decays of high-energetic top quarks and jets initiated by light-flavored quarks and gluons. A distinct trend is evident in both distributions, where the jet mass from hadronic top quark decays features different scenarios. Fully merged top quark decays, where all decay products are contained within one jet, result in a jet mass close to the top quark mass. When single decay products are not captured by the jet, the jet mass shifts to lower values. The peak near the W boson mass originates from jets that do not capture the b quark. Lastly, the jet mass is sensitive to additional particles from pileup, underlying event, or ISR and FSR. Additional particles clustered into the jet that do not originate from the top quark decay can shift the jet mass to higher values.

Calculating the jet mass involves many challenges due to the nature of QCD, including non-pertubative effects like hadronization. For boosted hadronic top quark decays, the jet mass

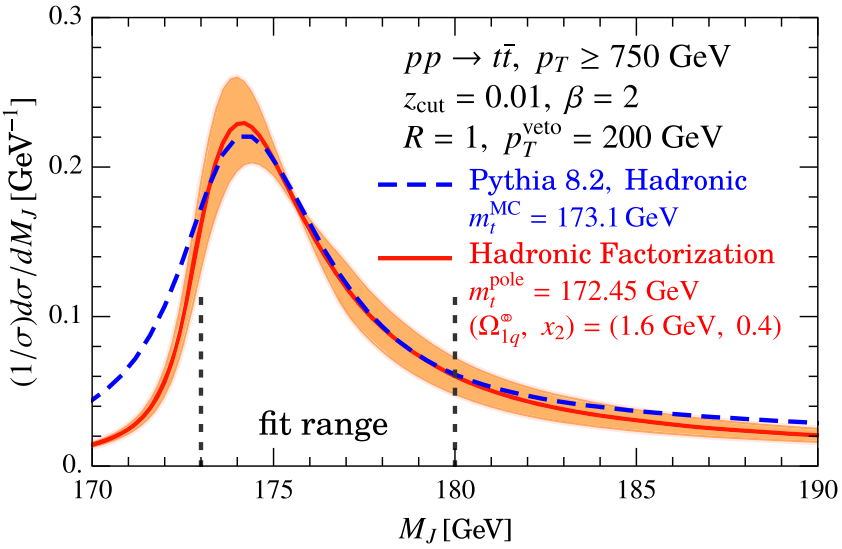


**Figure 5.2:** Differential $t\bar{t}$ production cross section as a function of the jet mass $m_{\text{jet}}$ for high-energetic hadronic top quark decays evaluated in analytic calculations from first principle (red) and from PYTHIA (blue). Taken from Ref. [16].

can be calculated from first principles using hadronization factorization within the framework of Soft-Collinear Effective Theory (SCET) [130]. This approach allows for the extraction of a well-defined top quark mass from the jet mass distribution. Moreover, direct comparisons between calculations and event generators are possible to address unanswered questions about the definition of the top quark mass, as discussed in Section 2.4.2. Such calculations are feasible due to light soft-drop grooming, which removes non-perturbative QCD effects that would further complicate the calculations.

Initial calculations were performed for $e^+e^-$ collision [131], focusing on $t\bar{t}$ events in the all-hadronic channel. These calculations apply to energy scales far above the mass scale ($Q \gg m_{\text{jet}}$). The event is separated into two hemispheres, where the jet mass is defined as the invariant mass of all particles in each hemisphere. Note, that it is vital to perform grooming procedures to remove soft and wide-angle radiation from the event. Calculations for pp collisions are more complex due to additional effects like pileup and the internal structure of the proton. For instance, the initial state comprises color-carrying particles, making the color connection between the initial and final states non-trivial. First calculations for pp collision have been introduced in Ref. [16], based on the same factorization approach as from $e^+e^-$ collisions. Here, the hadronic top quark decay must be reconstructed in one single large-$R$ jet due to higher activity in hadron colliders. Non-pertubative effects are mitigated by applying the soft drop algorithm [132] for jet grooming. The differential $t\bar{t}$ production cross section as the function of the jet mass for hadronic top quarks decays is shown in Figure 5.2. The calculations are only feasible for jets containing the full hadronic top quark decay with a $p_{\text{T}} > 750\,\text{GeV}$. Simulations generated with PYTHIA show compatibility with these calculations in the peak region.

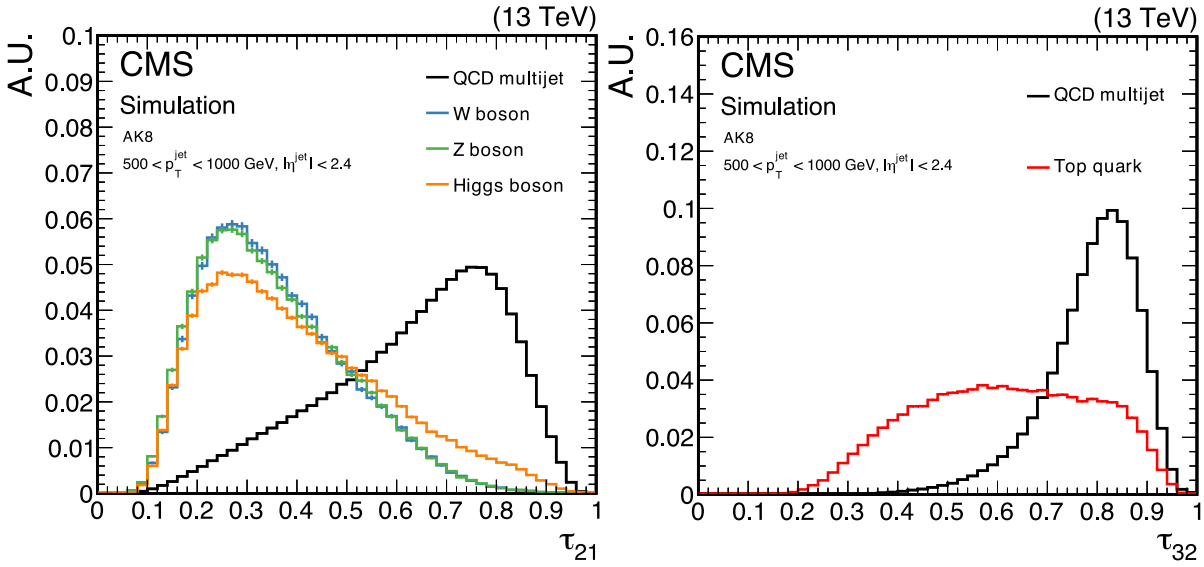


**Figure 5.3:** Normalized $N$-subjettiness ratio for different processes including QCD multijet events and heavy object decays. Two-prong decays from EW bosons can be distinguished from multijets event utilizing the $\tau_{21}$ (left) distribution. For three-prong decays, such as the top quark decay, $\tau_{32}$ (right) is taken for a distinction. Taken from Ref. [133].

## 5.2 N-subjettiness

The $N$-subjettiness is used to analyze the composition of jets by estimating how the energy is distributed within the jet. Unlike the $N$-jettiness (see Section 4.2.2) in Equation 4.3, the $N$-subjettiness only considers the jet constituents and not the particles from the entire event. The main idea is to measure how likely a jet consists of $N$ subjets. The $N$-subjettiness is defined as

$$\tau_N = \frac{1}{d_0} \sum_k p_{T,k} \min(\Delta R_{1,k}, \Delta R_{2,k}, \ldots, \Delta R_{N,k}), \tag{5.2}$$

where $p_{\mathrm{T},k}$ is the transverse momentum of the $k$-th constituent, $R_{i,k}$ is the angular distance to a subjet candidate and $d_0 = \sum_k p_{T,k} R_0$ is a normalization factor with the distance parameter $R_0$ of the original jet. The value of $\tau_N$ ranges from 0 to 1, where 0 indicates that the jet constituents perfectly align with the hypothesis of $N$ subjets. A value of $\tau_N = 1$ indicates that the energy of the jet constituents is more widely distributed within the jet.

The $N$-subjettiness allows to distinguish heavy-flavor jets from jets induced by light quarks and gluons. Although the discrimination power of the $N$-subjettiness alone is not substantial, the ratio $\tau_{\mathrm{nm}} = \tau_{\mathrm{n}}/\tau_{\mathrm{m}}$ has been shown to be effective [134]. The application of the ratio is shown in Figure 5.3, where QCD multijet events are distinguished from EW bosons (W, Z, H) with $\tau_{21}$ (left) and from jets reconstructing the full hadronic top quark decay with $\tau_{32}$ (right). The use of $\tau_{21}$ is applicable because EW bosons are expected to have a two-prong structure. In contrast, jets from light quarks and gluons are expected to resemble either an one-prong decay or two-prong decay from particle splitting, where one jet has a significantly higher $p_{\mathrm{T}}$. A similar

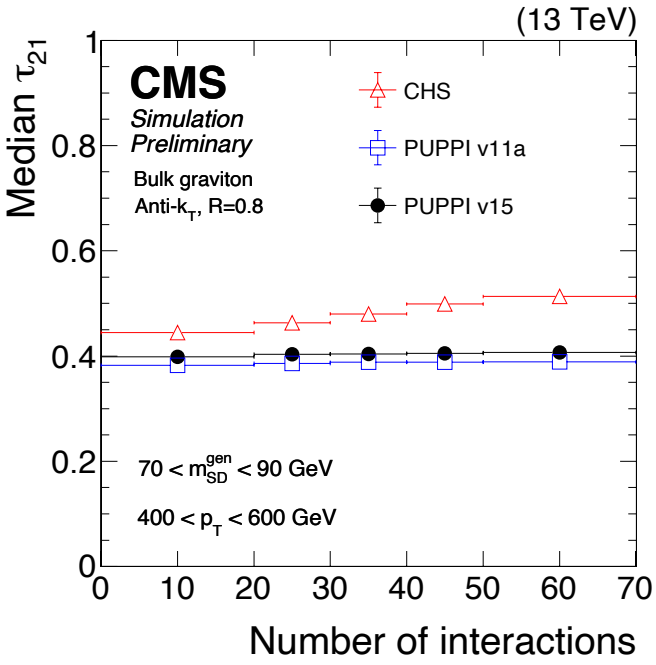


**Figure 5.4:** Median of the $N$-subjettiness ratio $\tau_{21}$ as a function of the number of the pileup interactions in an event. Compared are CHS jets (red), removing only pileup contributions from charged hadrons and different PUPPI versions (black and blue), also considering neutral hadrons. Taken from Ref. [137].

argument applies for $\tau_{32}$ and top quark decays, which feature a three-prong decay. While $\tau_{\mathrm{n}}$ is IRC safe, $\tau_{\mathrm{nm}}$ only fulfills sudakov safety [135]. Nonetheless, the ratio can be still derived from analytic calculations [126, 136], allowing for the comparisons between predictions and event generators. This allows enhancing the precision in measurements and refine the models used in simulations. However, due to the complex structure of the $N$-subjettiness, analytic calculations are limited to small jet shapes.

The $N$-subjettiness is highly sensitive to parton shower models and contributions from pileup. Additional particles clustered into the jet can redistribute the energy density, imitating structures with more prongs. Figure 5.4 illustrates the impact of pileup on the $N$-subjettiness ratio. The mean value of the $\tau_{21}$ ratio for high-$p_{\mathrm{T}}$ AK8 jets, which are expected to have a two-prong decay, is shown as a function of the number of the pileup interactions in an event, comparing different pileup mitigation techniques. For PUPPI jet, the mean $\tau_{21}$ ratio is relatively stable, whereas for CHS jets an increasing trend is evident. Although pileup can be mitigated using appropriate techniques, other phenomena also affect the energy distribution. In the scope of this thesis, the impact of FSR for boosted hadronic top quark decays is discussed in Section 7.6 investigating parton shower models in MC generators utilizing the ratio $\tau_{32}$.

## 5.3 Jet Grooming Techniques

The substructure of jets is affected by contributions from pileup, the UE, and soft radiation. Jet grooming algorithms are developed to remove soft and collinear radiation from jets, particularly large-$R$ jets, which are susceptible to these contributions. Grooming also mitigates the contributions from non-pertubative effects, facilitating theoretical prediction. With the introduction of pileup mitigation techniques like CHS and PUPPI, the pileup contribution is reduced beforehand. Commonly used jet grooming algorithms are based on reclustering large-$R$ jets. The filtering method [138] reclusters all jet constituents with a smaller filter radius $R_{\text{sub}}$ with $R_{\text{sub}} \ll R$. It retains a fixed number $N_{\text{filter}}$ of $p_{\text{T}}$-leading subjets based on the expected $N$-prong decay, which indicates the number of final state particles at LO. Typically the dominant radiation is also taken into consideration, choosing $N_{\text{filter}} = N + 1$. Contrarily, the trimming algorithm [139], commonly used by the ATLAS Collaboration, does not return a fixed number of jets. Instead, all subjets from the reclustered jet constituents with $R_{\text{sub}}$ are kept if the condition $p_{\text{T,sub}} > f_{\text{cut}}\ p_{\text{T,jet}}$ holds. Here, $p_{\text{T,sub}}$ and $p_{\text{T,jet}}$ are the transverse momenta of the subjet and the large-$R$ jet, respectively. The parameter $f_{\text{cut}}$ controls the strength of the $p_{\text{T}}$-dependent filtering. Jet pruning [140] introduces an additional angular distance condition $\Delta R_{\text{ij}} < R_{\text{prune}}$ alongside the $p_{\text{T}}$-dependent condition $\min(p_{\text{T,i}}, p_{\text{T,j}}) \geq z_{\text{prune}}\ p_{\text{T,i+j}}$, with $i$ and $j$ indicating the compared pseudojets. Pruning is applied during clustering with a dynamically defined pruning radius $R_{\text{pruning}} = m_{\text{jet}}/p_{\text{T,jet}}$, considering the mass and the transverse momenta of the original jet.

The CMS Collaboration employs the soft drop algorithm [132], which combines benefits of the aforementioned methods. It adds more degrees of freedom, addressing the angular separation and softness of two pseudojets. The soft drop algorithm reclusters the jet constituents with the CA algorithm to form an angular-ordered structure. Subsequently, the reclustered jet is separated into two pseudojets by undoing the last clustering step. The soft drop condition is defined as

$$\min(p_{\text{T},1}, p_{\text{T},2}) > z_{\text{cut}} \left( \frac{\Delta R_{12}}{R} \right)^{\beta}, \tag{5.3}$$

where $p_{\text{T,i}}$ is the transverse momentum of two pseudojets, $\Delta R_{12}$ their angular separation and $R$ the distance parameter of the jet under consideration. The parameters $z_{\text{cut}}$ and $\beta$ control the strength and angular dependency of the grooming procedure, respectively. If the condition fails, the procedure is repeated with the $p_{\text{T}}$-leading pseudojet, dropping the lower-$p_{\text{T}}$ jet until the condition holds. The value of $\beta$ depends on the phenomena under study and can take three scenarios: $\beta > 0$ suppresses wide-angle radiation but keeps collinear radiation, $\beta < 0$ lowers the restriction on wide-angle radiation and $\beta = 0$ only addresses soft radiation. At the CMS Collaboration, the default values are $z_{\text{cut}} = 0.01$ and $\beta = 0$, which are useful for measuring the jet mass of heavy-flavor jets.

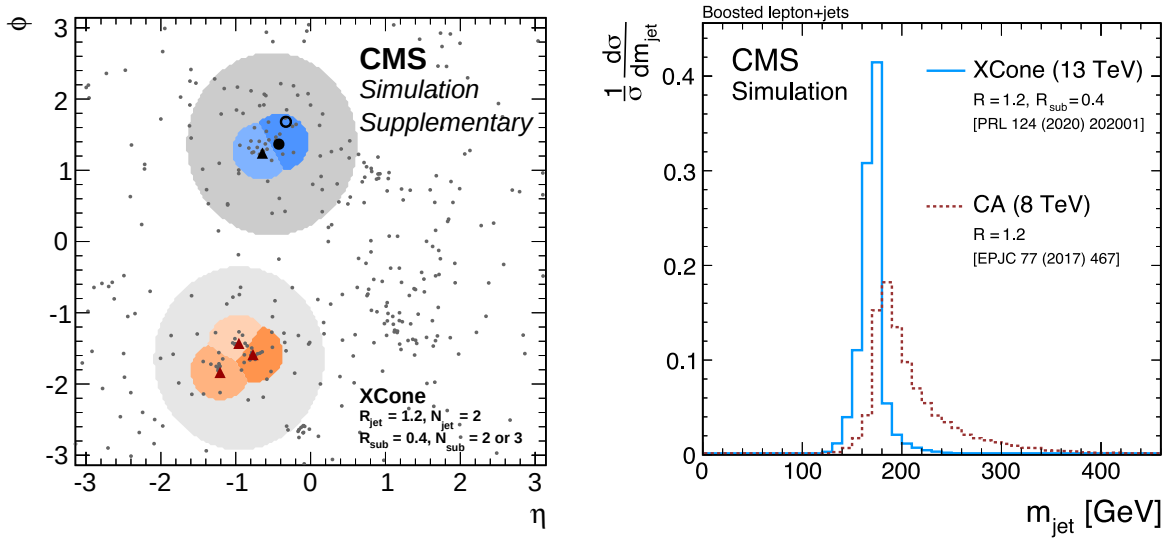


**Figure 5.5:** Jet grooming with a two-step clustering method (left) to reconstruct top quark decays with the XCone algorithm. First, one large-$R$ jet is clustered. Subsequently, the jet constituents are clustered with three smaller radius jets. The jet mass distribution (right) from the XCone clustering method (blue) is compared to ungroomed CA jets (red), aiming for high energetic top quark decays. Taken from supplementary material [121] of Ref. [18].

Another approach involves a two-step clustering procedure with the XCone jet algorithm [102], which is very similar to the filtering method. Firstly introduced in Ref. [141], a boosted $\mathrm{t\bar{t}}$ event is clustered with two large-$R$ jets, each reconstructing the full top quark decay. Constituents from each large-$R$ jet are then reclustered with three smaller XCone jets, targeting the individual decay products. This method has been excessively studied in Refs [18, 122] in the $\ell$+jets channel of high-energy $\mathrm{t\bar{t}}$ events.
Figure 5.5 (left) shows jet areas in the $\eta$-$\phi$ plane, with grey dots representing generated particles and grey (large-$R$ jets) and colored (subjets) circles indicating the jet areas. Each particle in the colored area is clustered into the jet. This method cleanly separates closely spaced jets and drops particles in the large-$R$ jet but not in the subjets, acting as a grooming algorithm. A comparison of the jet mass distribution on particle-level for the two-step clustering to ungroomed CA jets is shown in Figure 5.5 (right). The grooming improves the mass resolution by a factor of 2 from $\sim$ 14 % (CA) to $\sim$ 8 % (XCone).

## 5.4 Jet Substructure Measurements at the LHC

Jet substructure measurements in pp collisions are important for several reasons in high energy physics. They provide insights into the internal structure and evolution of jets across various $p_{\mathrm{T}}$ regions. Additionally, these measurements allow comparisons between data and theoretical models of jets, thereby providing crucial input for the modeling in event generators. Consequently, many analyses at the ATLAS and CMS Collaborations aim for substructure variables

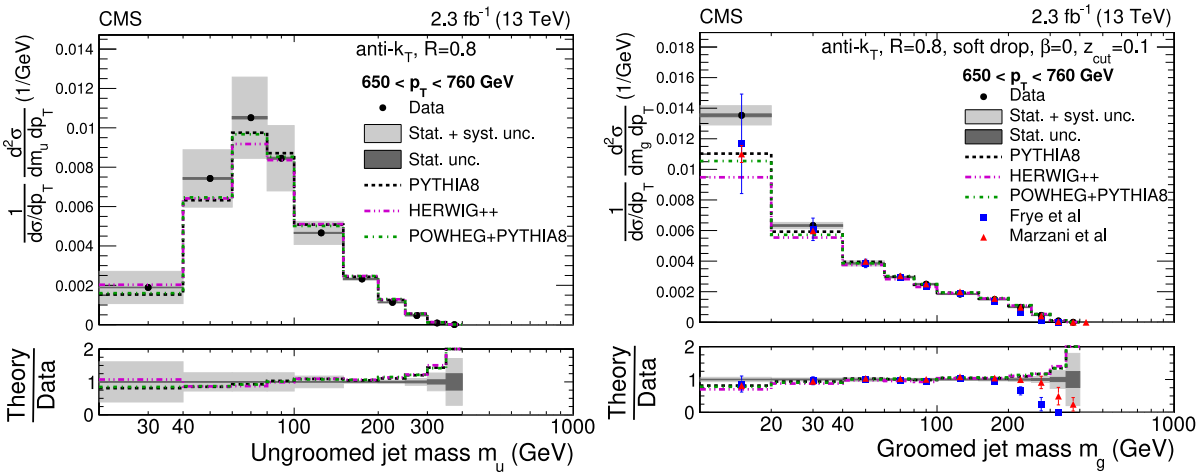


**Figure 5.6:** Measurement at the CMS detector of the normalized differential production cross section of QCD dijet events as a function of the ungroomed (left) and groomed (right) for jets clustered with the anti-$k_T$ algorithm and $R = 0.8$. Data (black markers) in both distributions are compared to several event generators (lines). The groomed jet mass is additionally compared to analytic calculations (colored markers). Taken from Ref. [142].

in numerous processes and phase spaces, such as the jet mass or the $N$-subjettiness.
The high energies at LHC allow the exploration of $p_T$ regions for jets that were inaccessible to previous particle colliders for detailed analyses. This capability facilitates detailed studies of jets, including the full decay of heavy particles.

### 5.4.1 Jet Mass Measurements

The ATLAS and CMS Collaboration measured the jet mass in light-flavored and gluons jets, as well as in decays of boosted top quarks, both providing valuable insights into the evolution and description of jets. The CMS Collaborations measured the jet mass from light flavored and gluon jets within QCD dijet events [142]. Events exhibiting a dijet topology were selected based on criteria including the number of jets, the asymmetry $A$ (see Equation 6.2), and the separation $\Delta R$ between the two $p_T$-leading jets. The measurement utilizing jets clustered with the anti-$k_T$ algorithm and a distance parameter $R = 0.8$ in a $p_T$ range of 200 GeV to 1300 GeV. The jet mass distribution at the detector level is unfolded to the particle level to obtain the multidimensional differential production cross section of QCD dijet events as a function of the jet mass and jet $p_T$. Figure 5.6 displays the cross section for the ungroomed (left) and groomed (right) jet mass in one $p_T$ bin. The distribution for the ungroomed jet mass features a sudakov peak, which scales with the $p_T$ of the jets. Performing the measurement with the groomed jet mass, employing the soft-drop algorithm, suppresses the sudakov peak and the distribution features a falling mass spectrum. The predictions derived from event generators and analytic calculations are in good agreement with the data.
The performance of the jet mass measurements can be evaluated with the jet mass response

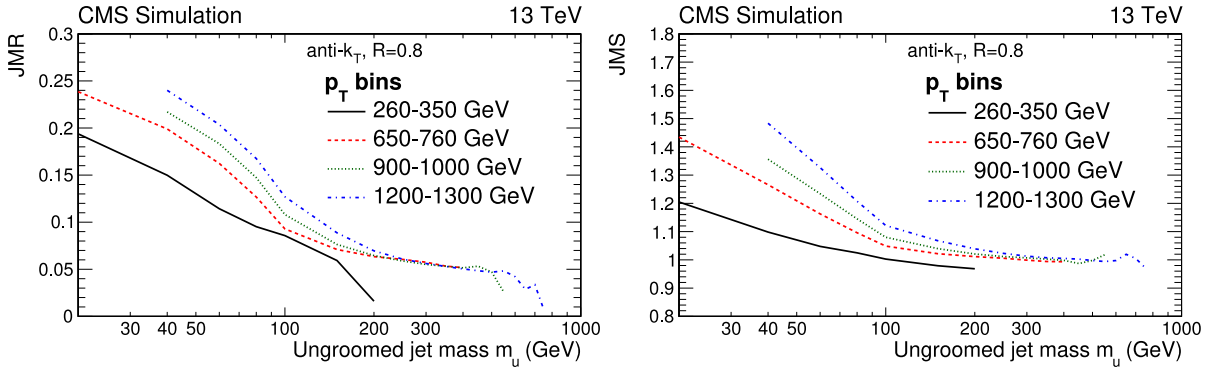


**Figure 5.7:** Measurement of the jet mass response with the CMS detector in QCD dijet events. Shown are the jet mass resolution (left) and jet mass scale (right) for several $p_{\mathrm{T}}$ ranges (colored lines). Taken from Ref. [142].

$$R_{\mathrm{mass}} = \frac{m_{\mathrm{jet}}^{\mathrm{reco}}}{m_{\mathrm{jet}}^{\mathrm{truth}}}, \tag{5.4}$$

where $m_{\mathrm{jet}}^{\mathrm{reco}}$ is the mass of the reconstructed and calibrated jet and $m_{\mathrm{jet}}^{\mathrm{truth}}$ the truth value at the particle level. Equivalent to the JES and JER (see Section 4.4), the jet mass scale (JMS) is defined as the mean of this distribution, and the jet mass resolution (JMR) as the width at one standard deviation. Figure 5.7 shows the JMR (left) and JMS (right) for the ungroomed jet masses $m_{\mathrm{u}}$ in the QCD dijet events. An increment of the JMR and JMS is observed for higher $p_{\mathrm{T}}$ ranges and smaller $m_{\mathrm{u}}$ due to higher collimation and pileup, respectively. Moreover, grooming via the soft drop algorithm strongly reduces the $p_{\mathrm{T}}$ dependency in the JMR with $\sim 10$ % for $m_{\mathrm{groomed}} = 100\,\mathrm{GeV}$.

The overall performance of the JMS and JMR highly depends on the reconstruction of particles, which differs for the ATLAS and CMS detector. At CMS, the particle reconstruction mainly relies on the PF algorithm (see Section 4.1). The reconstruction of particles at the ATLAS detector[1] focuses on the signal reconstruction in the individual subdetectors, rather then using the PF algorithm. Jet substructure observables at ATLAS are commonly derived from signals in the calorimeter, which becomes less effective for decays of boosted particles when the spatial distance of the decay products falls below the angular resolution of the detector. The angular resolution for charged particles is improved utilizing the jet mass derived from the tracker $m^{\mathrm{track}}$. In order to correct for pileup from neutral particles, the mass is corrected with the relative difference of the transverse momentum of the jet measured in the calorimeter $p_{\mathrm{T}}^{\mathrm{calo}}$ and the tracker $p_{\mathrm{T}}^{\mathrm{track}}$ summarized in the *track-assisted jet mass* [143] $m^{\mathrm{TA}}$. At the same time, $m^{\mathrm{TA}}$ substantially extend the $p_{\mathrm{T}}$ range for the jet mass calibration to $p_{\mathrm{T}}^{\mathrm{jet}} > 1000\,\mathrm{GeV}$. The mass definition can be further improved by considering more detailed information such as the energy of local clusters in the calorimeter [143]. Another method to improve the JMS and JMR is to use two comple-

[1] ATLAS uses the same subdetector types as CMS but with different technologies and configurations. A different sequence of subdetectors is used, such as placing the calorimeters outside a solenoid magnet.

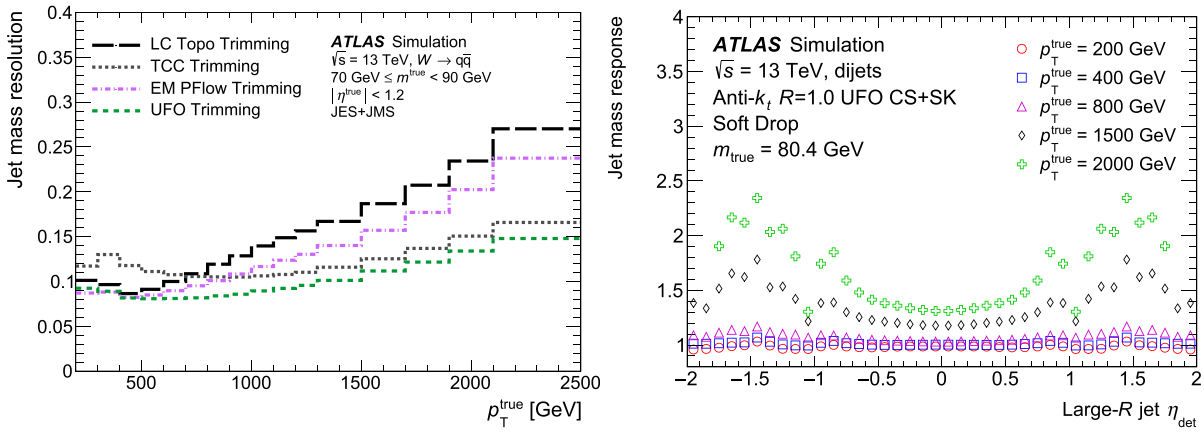


**Figure 5.8:** Measurements of the jet mass response from the ATLAS Collaboration. The JMR (left) is measured in hadronic W boson decays, where the default jet definition (topo, black) is compared to jets clustered from the newly introduced unified flow objects (UFO, green). The $\eta$-dependent JMS for jets from UFOs (right) is compared for several $p_{\mathrm{T}}$ regions from dijet events. Taken from Ref. [144].

mentary reconstruction algorithms, namely the PF algorithm and *Track-CaloClusters* (TCC). Both increase the jet mass resolution in the low- and high-$p_{\mathrm{T}}$ region, respectively, forming so-called *unified flow objects* [144] (UFOs). Those objects are then used for pileup mitigation and jet clustering algorithms. This approach further improves the JMR with up to 45 % with respect to the previous techniques. The JMR from UFOs has been obtained from the decay products of hadronic W boson decays for multiple jet definitions and is shown in Figure 5.8 (left). While a strong $p_{\mathrm{T}}$-dependency is visible for all definitions, the jets from UFOs substantially improve the JMR for $p_{\mathrm{T}} > 500\,\mathrm{GeV}$. The JMS from dijet events clustered with UFOs is shown in Figure 5.8 (right), also featuring a strong $p_{\mathrm{T}}$-dependency with an increase of the JMS up to 150 % for jets with $p_{\mathrm{T}}^{\mathrm{true}} = 2\,\mathrm{TeV}$. The results from the track-assisted mass resolution from ATLAS and the JMR at CMS derived from dijet events are very compatible.

Generally, the internal jet structure differs for jets initiated by light quarks or gluons, and jets comprising the full decay of heavy objects, such as the W boson or the top quark. Measurements of large-$R$ jets reconstructing the full hadronic top quark decay are of special interest for jet substructure measurements. These jet mass measurements do not only provide valuable input for the parton shower modeling but are also sensitive to the mass of the jet-initiating particle and thus enable an extraction of $m_{\mathrm{top}}$. Since the jet mass in hadronic top quark decays can be calculated analytically, these measurements even provide a possibility to extract $m_{\mathrm{top}}$ in a well defined mass scheme such as $m_{\mathrm{top}}^{\mathrm{pole}}$. The CMS Collaboration established first measurements [17, 18] of the jet mass in decays of boosted top quarks. In these measurements, $\mathrm{t\bar{t}}$ events in the $\ell$+jets channel ($\ell = \mu/e$) are selected, where each top quark decay is reconstructed in one large-$R$ jet. The lepton $\ell$ is used to tag the jet containing products of the leptonic top quark decay, where the other jet can be then associated with hadronic top quark decay. Boosted $\mathrm{t\bar{t}}$ events are then obtained by requiring the hadronic jet to have $p_{\mathrm{T}} > 400\,\mathrm{GeV}$. The very first measurement [17]

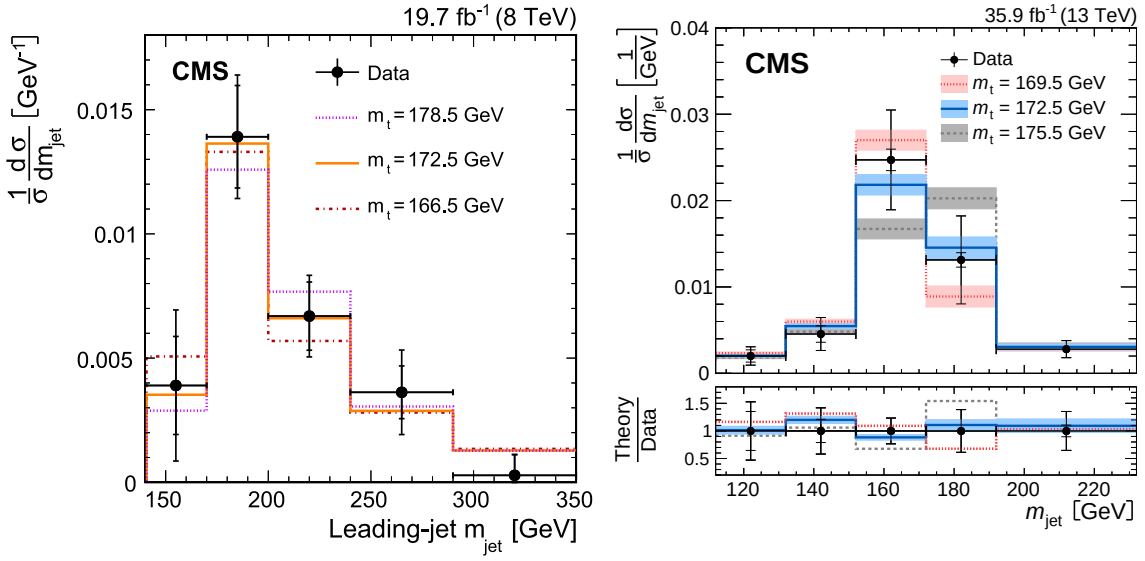


**Figure 5.9:** Normalized differential $\mathrm{t\bar{t}}$ production cross section as a function of the jet mass in hadronic decays of boosted top quarks at $\sqrt{s} = 8\,\mathrm{TeV}$ (left) and $\sqrt{s} = 13\,\mathrm{TeV}$ (right) in comparison to various top quark mass hypothesis. Taken from Ref. [17] (left) and [18] (right).

was performed with data collected at a center-of-mass energy of $\sqrt{s} = 8\,\mathrm{TeV}$. The jets were clustered with the CA algorithm and a distance parameter of $R = 1.2$. Figure 5.9 (left) shows the normalized distribution of the ungroomed jet mass in comparison to several top quark mass hypothesis from simulated templates. The top quark mass has been measured to be

$$\begin{aligned} m_t &= 170.8 \pm 6.0\,(\mathrm{stat}) \pm 2.8\,(\mathrm{syst}) \pm 4.6\,(\mathrm{model}) \pm 4.0\,(\mathrm{theo})\,\mathrm{GeV} \\ m_t &= 170.8 \pm 9.0\,\mathrm{GeV}. \end{aligned} \tag{5.5}$$

The large uncertainty arises from contributions such as the jet energy and mass scale, and the modeling of the parton showers. The dominant limitation of the measurement, however, comes from the low statistical precision. Nonetheless, this measurement provides insight into the tuning of $\mathrm{t\bar{t}}$ simulations and estimations of the jet mass scale. Here, $m_{\mathrm{top}}$ is extracted from simulations because analytic calculations of the jet mass exists only for jets with $p_{\mathrm{T}} > 750\,\mathrm{GeV}$ [16]. Such high $p_{\mathrm{T}}$ regions for jets in decays of boosted top quarks are yet not feasible for analyses at the LHC.

A next iteration of this analysis [18] substantially increased the precision of the jet mass measurement. The statistical precision is increased by using a larger dataset collected during the year 2016 from Run 2 with $\sqrt{s} = 13\,\mathrm{TeV}$. A major improvement comes from an enhanced reconstruction of the hadronic top quark decay using the two-step clustering procedure with the XCone jet algorithm, discussed in Section 5.3. The JMR of the XCone jets is illustrated in Figure 5.10 and shows changes within $\sim 1$ % over a $p_{\mathrm{T}}$ range of 400 GeV to 1500 GeV and the number of primary vertices ($N_{\mathrm{PV}}$). The robustness with respect to pileup, which scales $N_{\mathrm{PV}}$, demonstrates the effectiveness of the two-step clustering approach with the XCone algorithm to reconstruct hadronically decaying boosted top quarks.

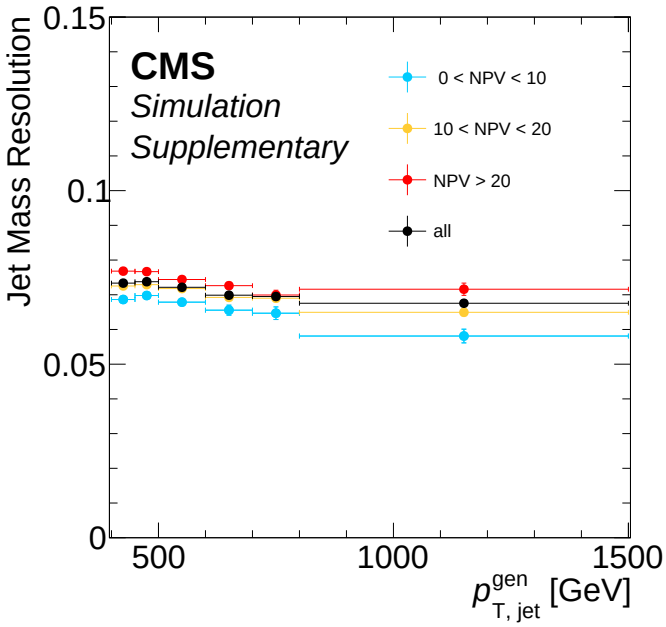


**Figure 5.10:** Jet mass resolution from jets reconstructing the hadronic decay of high-energetic top quarks as a function of the true jet $p_T$ and the number of primary vertices (NPV). Taken from supplementary material [121] of Ref. [18].

The unfolded jet mass distribution is shown in Figure 5.9 (right), which measures the top quark mass with

$$\begin{aligned} m_t &= 172.6 \pm 0.4\,(\text{stat}) \pm 1.6\,(\text{syst}) \pm 1.5\,(\text{model}) \pm 1.0\,(\text{theo})\,\text{GeV} \\ m_t &= 172.6 \pm 2.5\,\text{GeV}. \end{aligned} \tag{5.6}$$

The statistical precision has be significantly improved with respect to the first measurement. The relative bin uncertainties from the cross section is depicted in Figure 5.11 for the experimental (left) and model uncertainties (right). The dominant uncertainties arise from the JES, which comprises in the JMS, with a contribution of $\Delta m_t = 1.5\,\text{GeV}$ and the modeling of the FSR with $\Delta m_t = 1.3\,\text{GeV}$. Nonetheless, the precision has been substantially improved with respect to the first measurement. The analysis performed in the scope of this thesis aims to decouple the JMS from the JES and further improve the modeling of the FSR.

An analysis from the ATLAS Collaboration also aimed for the decay of boosted top quarks from $t\bar{t}$ events [145], reaching a phase-space for the hadronic jet with $p_T > 500\,\text{GeV}$. Two decay channels of the $t\bar{t}$ event are targeted, the $\ell$+jets and all-hadronic decay channel. While the $\ell$+jets allows to identify the hadronic top quark as discussed in the measurement from the CMS Collaboration, the all-hadronic decay channel is selected via a DNN aiming for top quarks in the final state. Based on the topology of both decay channels, different jet clustering approaches are used, aiming to reconstruct the full hadronic top quark decay. In summary, jets are clustered with the anti-$k_T$ algorithm and a distance parameter of $R = 1.0$ or the variable-$R$

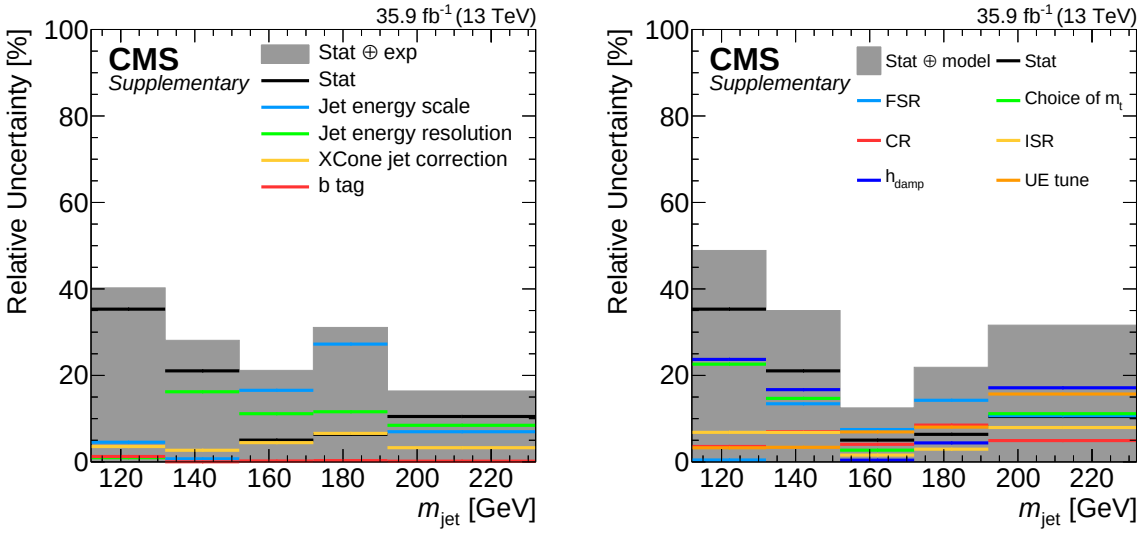


**Figure 5.11:** Relative bin uncertainties of the unfolded jet mass distribution at $\sqrt{s} = 13\,\text{TeV}$. The dominant experimental uncertainty (left) arises from the jet energy scale, while the largest model uncertainty (right) is due to the modeling of the final state radiation. Taken from supplementary material [121] of Ref. [18].

jet clustering algorithm [146] to define jets with a $p_\text{T}$-dependent jet radius. The jet mass of the $p_\text{T}$-leading large-$R$ jet in the all-hadronic channel is displayed in Figure 5.12 showing a broad peak at the top quark mass. Unlike the measurements conducted by the CMS Collaboration, the measurement from the ATLAS Collaboration does not unfold the jet mass to particle level. Instead, it focuses on unfolding several jet substructure variables, such as the $N$-subjettiness ratio $\tau_{32}$.

The calibration for the JMS is not addressed in the jet calibration procedure developed at CMS Collaboration. While a multiplicative factor corrects the jet four-momentum, the jet mass appears as an additional degree of freedom. This results in large uncertainties in analyses focusing on the jet mass in decays of boosted heavy particles as demonstrated in the $m_\text{jet}$ measurement from the CMS Collaboration [18]. As these measurements reach higher precision, calibrating the jet mass becomes essential to achieve even higher accuracy. For that reason, dedicated calibrations based on the jet mass response are required, which are usually derived in forms of simulation-to-data scale factors. The jet mass response in data can be obtained in hadronically decaying boosted heavy objects, since a clear peak in jet mass distribution is expected close to the mass of the initial particle. The decays are reconstructed with a large-$R$ jet, measured in $\text{t}\bar{\text{t}}$ events in the $\ell$+jets or all-hadronic channel.

The ATLAS Collaboration measures the residual corrections in the JMS and JMR with a simultaneous fit of simulations to data referred to as *forward folding* [147]. Further details of the jet calibration in ATLAS can be found in Ref. [148]. The $p_\text{T}$-dependent correction factors are displayed in Figure 5.13 (left), measuring a difference in the JMS up to $\sim 3$ % and for the JMR up to $\sim 30$ % including the systematic uncertainties. For the CMS Collaboration, dedicated

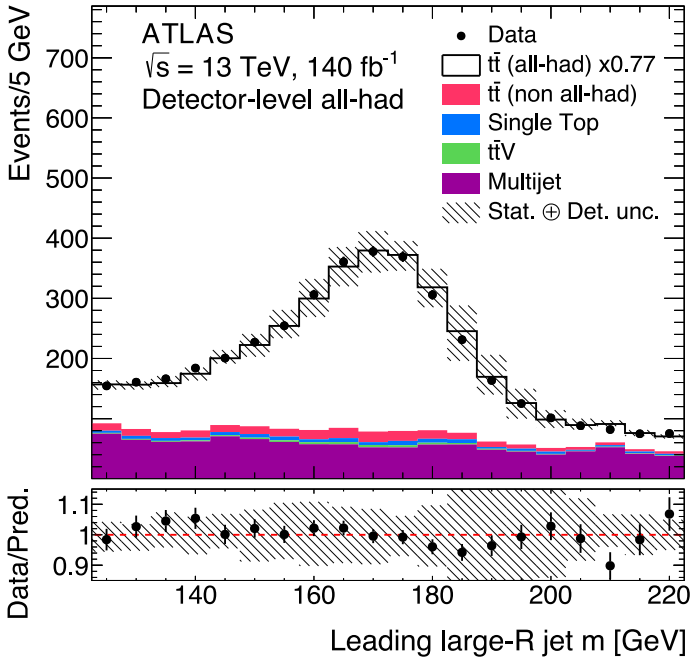


**Figure 5.12:** Jet mass distribution in hadronic decays of boosted top quarks, clustered with the anti-$k_T$ algorithm and a distance parameter of $R = 1.0$ in the $t\bar{t}$ all-hadronic channel. Taken from Ref. [145].

scale factors for the JMS have been recently measured in Ref. [149, 150]. The measurement is performed in top quark and W boson enriched samples in the $\ell$+jets channel of the $t\bar{t}$ process. Here, simulated distributions are fitted to data in three different signal regions, targeting top quark and W boson enriched regions. These regions are either selected by the jet substructure based on the $N$-subjettiness, or the ParticleNET score [151], a deep neural network (DNN) trained to distinguish boosted heavy objects from QCD events. In order to obtain the final JMS scale factors, simulated samples are fitted to data based on the soft drop jet mass for AK8 jets with $p_T > 200\,\text{GeV}$. The JMS scale factors derived for the data selected via a DNN is displayed in Figure 5.13 (right), showing a compatible result in comparison to ATLAS.

### 5.4.2 $N$-subjettiness Measurements

The aforementioned measurement by the ATLAS Collaboration in decays of highly boosted top quarks also measured the $N$-subjettiness ratio $\tau_{32}$ in jets containing the full hadronic top quark decay with $p_T > 500\,\text{GeV}$. The differential cross section as a function of $\tau_{32}$ is shown in Figure 5.14, featuring a peak at $\tau_{32} \approx 0.4$, primarily representing fully reconstructed top quark decays with a three-prong substructure. A comparison with several parton shower models indicates that the data is better described by the non-default tune of PYTHIA. This measurement exceeds the phase-space of a previous ATLAS measurement [152] of the unfolded $\tau_{32}$ distribution for jets with $p_T > 350\,\text{GeV}$, showing similar results. Measurements conducted by the CMS Collaboration of $N$-subjettiness in the $\ell$+jets channel of the $t\bar{t}$ process are detailed in Ref. [153].

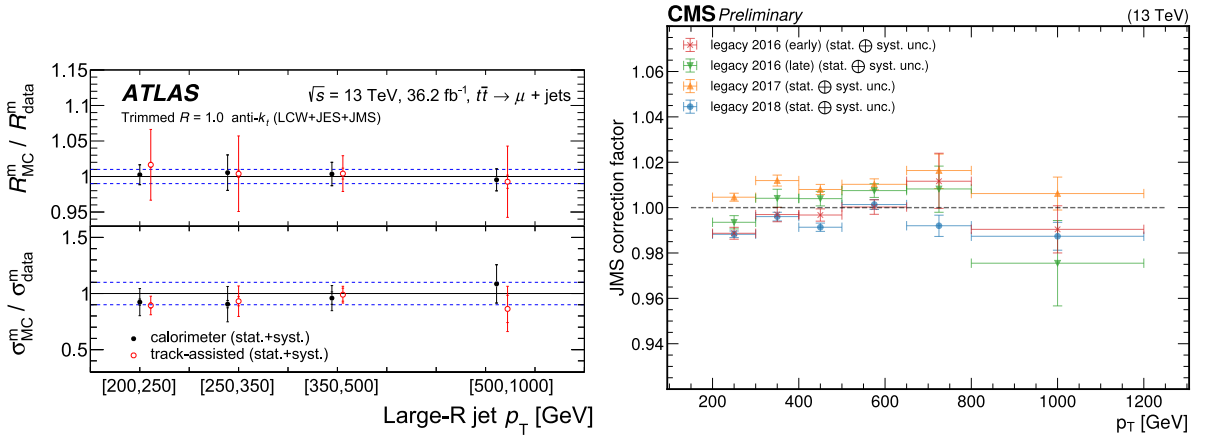


**Figure 5.13:** Measurement of data-to-simulation scale factors for corrections of the jet mass response. The ATLAS Collaboration (left) measured scale factors for the JMS and JMR simultaneously in W boson and top quark mass peak in the boosted regime in the $\ell$+jets channel of $t\bar{t}$ events. The corrections are measured for the calorimeter (black) and track-assisted (red) mass. The CMS Collaboration (right) measured the scale factors for the JMS for all years of Run 2 aiming for the same mass regions as the ATLAS Collaboration, but additionally using a W enriched samples. Taken from Ref. [148] (left) and [149] (right).

In this context, $t\bar{t}$ events at threshold production are used to measure the substructure of light-flavored jets. Figure 5.15 displays the measurement of the $N$-subjettiness ratio $\tau_{21}$ (left) and $\tau_{32}$ (right). In both cases higher values are measured, because light-flavored jets generally exhibit a one-prong substructure. While the ATLAS measurement provides the first comparison of data to simulation in $p_{\mathrm{T}}$ regions above 500 GeV, the CMS measurement aimed for a more general validation of substructure descriptions by MC simulations. Similar to the measurement from ATLAS, both results indicate that the data is best described by simulations with non-default settings for the FSR.

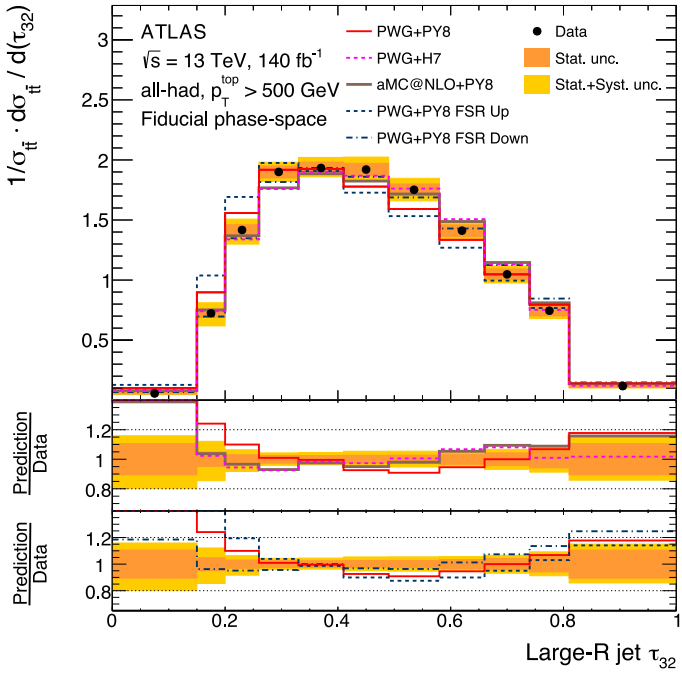


**Figure 5.14:** Measurement of $N$-subjettiness ratio $\tau_{32}$ in hadronic decays of high-energetic top quark decays by the ATLAS detector. Both top quark decays from the $t\bar{t}$ full-hadronic channel are reconstructed with one large-$R$ jet. The measurement is performed on the $p_{\mathrm{T}}$-leading jet with at least $p_{\mathrm{T}} > 500\,\mathrm{GeV}$. Data (black markers) is compared to several event generators (red, pink) and the variation of the final state modeling in PYTHIA (dark blue). Taken from Ref. [145].

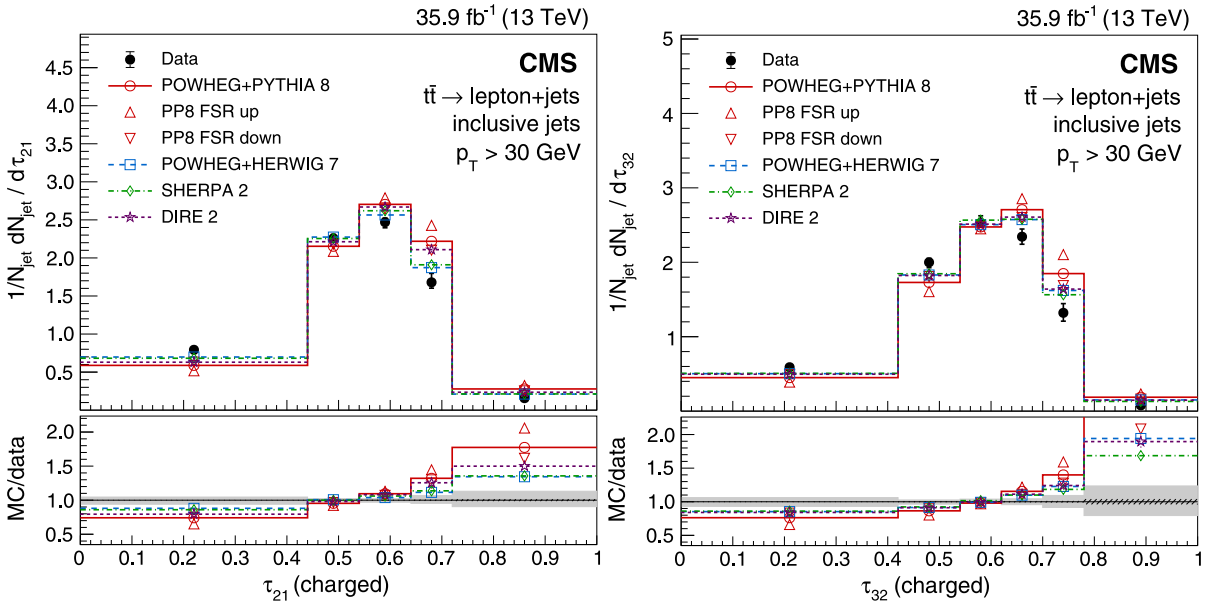


**Figure 5.15:** Measurement of $N$-subjettiness ratio $\tau_{21}$ (left) and $\tau_{32}$ (right) for light-flavored jets by CMS. The jets are selected in the $\ell$+jets channel of the $t\bar{t}$ event at threshold production. Data (black markers) is compared to several event generators (red, pink) and the variation of the final state modeling in PYTHIA (dark blue) In both cases, data (black markers) is compared to several event generators (lines) and the variation in the final state modeling in PYTHIA (triangle markers). Taken from Ref. [153].

# Chapter 6

# Jet Transverse Momentum Resolution Measurement

Jets are fundamental to high-energy physics analyses, necessitating a precise knowledge of jet properties. Key features of the jet performance are the jet energy scale and resolution. Their miscalibration can lead to a momentum imbalance in an event, resulting in a mismeasurement of missing transverse momentum. Thus, precise calibrations to ensure accurate measurements of Standard Model parameters and searches for new physics are necessary. At the CMS Collaboration, differences between the JER in simulations and data are present. These discrepancies necessitate dedicated corrections to align the JER in simulations with that observed in data, forming the final step in the jet calibration process at CMS. The methodologies employed to derive the JER in data and simulations are closely related to those used for residual corrections described in Section 4.4.

The underlying structure of the jet response and the dependency of the jet properties are discussed in Section 6.1. Here, an overview of the established techniques to derive the JER from jets without knowledge of the true jet transverse momentum is given. The data samples and simulations used for the analysis, along with the event selection to obtain dijet events, are described in Section 6.2 and 6.3, respectively. The workflow of the measurement and the experimental challenges for each step are discussed in Section 6.4. Sources of systematic uncertainties considered for the JER SFs are elaborated on in Section 6.5 followed by the results for the Run 2 and Run 3 data-taking periods in Section 6.6. Results obtained in this chapter are derived in the scope of this thesis. The application of the JER SFs at the CMS Collaboration is summarized in Section 6.7. Looking ahead to future data-taking periods with increased energies and luminosities, the possibilities of the established method are investigated and a new technique is introduced in Section 6.8. The interplay with complementary methods to derive and further improve the JER SFs is given in Section 6.9.

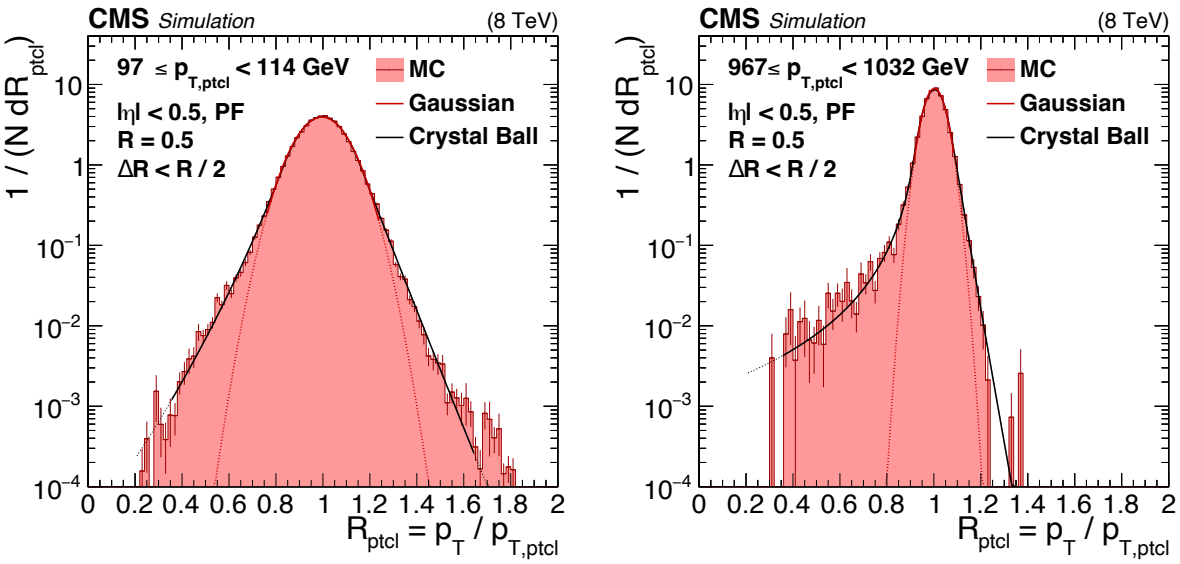


**Figure 6.1:** Jet transverse momentum ($p_\mathrm{T}$) response distribution for low-$p_\mathrm{T}$ (left) and high-$p_\mathrm{T}$ (right) jets. Reconstructed jets are matched to particle-level jets based on the angular distance $\Delta R$ in QCD multijet samples. Taken from Ref. [119].

## 6.1 Underlying Structure of the Jet Response

The jet response $R$ quantifies the accuracy with which the reconstructed transverse momentum ($p_\mathrm{T}^\mathrm{reco}$) of a jet corresponds to its particle-level transverse momentum ($p_\mathrm{T}^\mathrm{true}$) nad is defined as

$$R = \frac{p_\mathrm{T}^\mathrm{reco}}{p_\mathrm{T}^\mathrm{true}}. \tag{6.1}$$

For calibrated jets, the expected mean value of the jet response is centered around one. Figure 6.1 displays the jet response for low-$p_\mathrm{T}$ (left) and high-$p_\mathrm{T}$ (right) jets with $|\eta| < 0.5$. The mean value is referred to as JES and the width as the JER. The jet response is dependent on the jet flavor. Quark jets tend to be composed of fewer and harder particles compared to gluon jets. These particles lead to distinct response characteristics due to the non-linearity of the calorimeter response. For particle-level jets, the CMS Collaboration adopted the convention to exclude neutrinos from semi-leptonic decays of heavy hadrons from the clustering procedure, defining a response that is experimentally accessible [119]. The exclusion of neutrinos increases the compatibility in the resolution of heavy-flavor quark (c,b) jets, and light-flavor and gluon jets resulting in a similar performance. Jets used to determine the JER have been calibrated following the procedure described in Section 4.4.

The response distribution features a Gaussian core and non-Gaussian tails. The Gaussian component arises from the precision and the reconstruction capabilities of the PF algorithm, the jet clustering algorithms, and the intrinsic resolution of the subdetectors. Specifically, the tracker and the calorimeter systems show varied performance based on the $p_\mathrm{T}$ and energy of the particles. In the tracker, low-$p_\mathrm{T}$ charged particles typically are reconstructed with better resolution,

as the tracker more accurately measures hit positions and the track curvature. High-$p_T$ particles show a worse resolution due to finite hit positions and straighter tracks. Conversely, low-$p_T$ jets tend to encounter more scattering processes, introducing larger uncertainties. For the calorimeter system, the resolution dependence on the transverse momentum of particles is reversed and improves with increasing $p_T$. The resolution for low-$p_T$ jets is predominantly affected by electronic noise and pileup, whereas high-$p_T$ jets are limited by intercalibrations. These detector effects result in a energy-dependent JER. Additionally, the JER depends on the pseudorapidity $\eta$ due to the varying coverage and structural design of the subdetectors as well as the different material depths traversed. Non-Gaussian tails in the response distribution are attributed to energy mismeasurements including electronic noise, energy leakage from inactive detector regions, or particle punch-throughs. The latter describes the effect where particles only deposit a fraction of their energy due to the finite depth of the calorimeter. Symmetrical non-Gaussian tails in the low-$p_T$ regions arise from the scenario where two jets on particle-level are reconstructed as a single jet, or a single particle-level jet is reconstructed in two separated jets [119].

Accurate calibrations of the JER are essential for a variety of high-energy physics analyses, as it significantly impacts the results and their interpretations. The measurement of differential jet cross sections is particularly sensitive to the JER calibration due to migration effects in the unfolding process. These effects largely depend on the jet $p_T$. Moreover, inaccuracies in JER calibration can lead to an incorrect determination of $p_T^{miss}$, a parameter that is crucial in analyses focused on searches for new physics phenomena or targeting leptonic top quark decays. To account for these discrepancies, a smearing procedure is applied to simulated jets to align the JER with that observed in data. The jet response is not accessible in data, because the information of the true jet $p_T$ is unavailable. In order to access JER in data, it is necessary to measure quantities that are related to the jet response itself. During the Run 1 and Run 2 data-taking periods of the LHC, the CMS Collaboration primarily exploited the $p_T$ imbalance [119] (see Section 6.1.1) in dijet events to determine the JER in data and simulation. A sketch of the dijet events can be seen in Figure 6.2, where two $p_T$-leading back-to-back jets are expected. This method covers a large phase space in $p_T$ and $\eta$ with high statistical precision.

### 6.1.1 Transverse Momentum Imbalance Method

The transverse momentum imbalance method exploits the momentum conservation in hard-scattering processes. Here, the $p_T$ of the reconstructed jet under consideration is compared to the $p_T$ of a reference object. In terms of events with at least two jets, the $p_T$ imbalance is quantified by the asymmetry

$$A = \frac{p_{T,1} - p_{T,2}}{p_{T,1} + p_{T,2}}. \tag{6.2}$$

Here, $p_{T,1}$ and $p_{T,2}$ are the transverse momentum of the two $p_T$-leading jets with a random or-

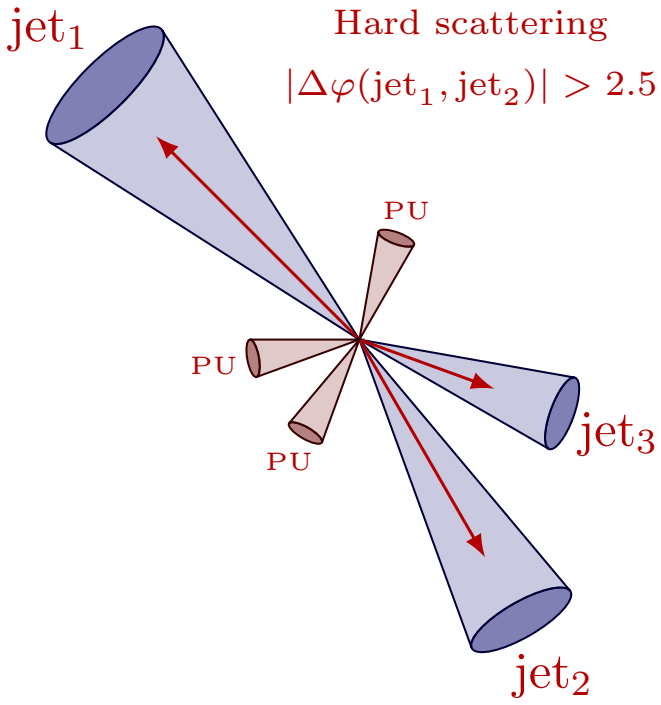


**Figure 6.2:** Illustration of QCD dijet events used for the determination of the jet transverse momentum resolution in data and simulation. The two $p_{\mathrm{T}}$-leading jets are required to be back-to-back ($|\Delta\phi| > 2.5$).

dering on event-by-event basis [154]. The choice of the ordering introduces an additional source of uncertainty in the final JER SF measurement as the asymmetry distribution can change. It has been verified that this uncertainty is well below the statistical uncertainty and is not considered in the following. However, a fixed ordering of the jets is maintained by choosing a random seed based on event-specific parameters to ensure consistent results across multiple iterations. Like the jet response, the asymmetry distribution $A$ exhibits a Gaussian core with non-Gaussian tails centered around $A = 0$. Without considering the tails, the width of the asymmetry is defined as

$$\sigma_A^2 = \left( \left| \frac{\partial A}{\partial p_{T,1}} \right| \cdot \sigma(p_{T,1}) \right)^2 + \left( \left| \frac{\partial A}{\partial p_{T,2}} \right| \cdot \sigma(p_{T,2}) \right)^2 . \tag{6.3}$$

In ideal dijet events, both jets feature the same transverse momentum at the particle level and thus are perfectly balanced. If these jets are also within the same $|\eta|$ region, it can be assumed that $\langle p_{\mathrm{T},1} \rangle \sim \langle p_{\mathrm{T},2} \rangle$ and $\sigma(p_{\mathrm{T},1}) \sim \sigma(p_{\mathrm{T},2})$. These assumptions simplify Equation 6.3, introducing the relation of the resolution of the jets' $p_{\mathrm{T}}$, denoted as $\sigma(p_{\mathrm{T}})$ and the width of the asymmetry distribution $\sigma_{\mathrm{A}}$ with

$$\sigma_{\mathrm{JER}} \equiv \frac{\sigma(p_{\mathrm{T}})}{\langle p_{\mathrm{T}} \rangle} = \sqrt{2} \cdot \sigma_A . \tag{6.4}$$

Several experiments including the CMS Collaboration [119], the ATLAS Collaboration [148]

and experiments at the Tevatron [155, 156] used this approach, which is referred to as the standard method in the following.

Requiring both jets to be located in the same $|\eta|$ region significantly constrains the number of dijet events for regions with $|\eta| > 2.0$. Furthermore, the overall $p_\mathrm{T}$ of jets decreases for higher $|\eta|$ regions and therefore such events are predominantly collected by highly prescaled triggers. A wider $\eta$ binning with respect to the central region needs to be constructed to gain sufficient statistics for the JER measurement for the high forward region. These bins come with large uncertainties and a poorer granularity in the study of different detector regions. To extend the calibration to higher $|\eta|$ values a forward extension (FE) for the transverse momentum imbalance method [154] is introduced. The extension is based on a different positioning of the jets, utilizing a well-calibrated reference jet in the barrel region ($|\eta| < 1.3$) and a probe jet not constrained in $|\eta|$. The asymmetry is adjusted accordingly and reads

$$A = \frac{p_\mathrm{T}^\mathrm{probe} - p_\mathrm{T}^\mathrm{ref}}{p_\mathrm{T}^\mathrm{probe} + p_\mathrm{T}^\mathrm{ref}}. \tag{6.5}$$

The assumption $\sigma_{p_{\mathrm{T},1}} \sim \sigma_{p_{\mathrm{T},2}}$ in Equation 6.4 does not apply anymore, because both jets are located in different $\eta$ regions. However, the introduction of a reference object with a well-known resolution $\sigma(p_\mathrm{T}^\mathrm{ref})$ allows to determine the resolution of the probe jet $\sigma(p_\mathrm{T}^\mathrm{probe})$ with

$$\sigma_\mathrm{JER} \equiv \frac{\sigma(p_\mathrm{T}^\mathrm{probe})}{\langle p_\mathrm{T}^\mathrm{probe} \rangle} = \sqrt{4 \cdot \sigma_A^2 - \left( \frac{\sigma(p_\mathrm{T}^\mathrm{ref})}{p_\mathrm{T}^\mathrm{ref}} \right)^2}. \tag{6.6}$$

The resolution of the reference jet can be estimated with the standard method.

## 6.2 Data and Simulations

The JER SFs measured in scope of this thesis use events from pp collision recorded by the CMS detector during the Run 2 and Run 3 data-taking periods at a center-of-mass energy of $\sqrt{s} = 13\,\mathrm{TeV}$ and 13.6 TeV, respectively. The corresponding integrated luminosity for each year are listed in Table 6.1. Data collected during 2016 [157], 2022 [158] and 2023 [159] are separated into two subsample each due to changed detector conditions (see Section 6.3), requiring dedicated calibrations. QCD multijet events in data are selected based on a set of triggers targeting the $p_\mathrm{T}^\mathrm{ave}$ of two jets in an event. These triggers are designed for various minimum $p_\mathrm{T}^\mathrm{ave}$ values at the HLT level. They are further categorized by the detector configuration, aiming at central jets up to $|\eta| < 2.853$ and using forward triggers otherwise. A summary of the triggers used and the corresponding $p_\mathrm{T}$ thresholds is reported in Table 6.2. Trigger thresholds are chosen such that the trigger efficiency reaches 99 %. For early 2017, no dijet triggers at the HLT level were available; instead, single-jet triggers aiming for the $p_\mathrm{T}$ of AK4 jets are used.

Simulated QCD multijet samples are generated with MADGRAPH5_aMC@NLO [47] at LO ac-

| year | 2016 | 2016 VFP | 2017 | 2018 | 2022 | 2022 EE | 2023 | 2023 BPix |
|---|---|---|---|---|---|---|---|---|
| $\mathscr{L}$ [ fb$^{-1}$ ] | 19.53 | 16.80 | 41.48 | 59.83 | 8.0 | 26.7 | 17.8 | 9.5 |

**Table 6.1:** Integrated luminosity for each year analyzed for the determination of the JER SFs. The data samples in the years 2016, 2022 and 2023 are separated into two subsample each based on changed detector conditions.

| $p_T^{\text{ave}}$ thr. | Online [GeV] | Offline [GeV] | | | | |
|---|---|---|---|---|---|---|
| | | Dijet | | | | single-jet |
| year | | 2016 | 2017 | 2018 | 2022+2023 | 2017 |
| Central | 40 | 59 | 70 | 66 | 66 | 70 |
| | 60 | 85 | 87 | 93 | 83 | 87 |
| | 80 | 104 | 111 | 118 | 108 | 111 |
| | 140 | 170 | 180 | 189 | 177 | 180 |
| | 200 | 236 | 247 | 257 | 246 | 247 |
| | 260 | 302 | 310 | 325 | 313 | 310 |
| | 320 | 370 | 373 | 391 | 378 | 373 |
| | 400 | 460 | 457 | 478 | 464 | 457 |
| | 500 | 575 | 562 | 585 | 572 | 562 |
| Forward | 60 | 86 | 73 | 93 | 79 | |
| | 80 | 110 | 93 | 116 | 99 | |
| | 100 | 132 | 113 | 142 | 122 | |
| | 160 | 204 | 176 | 210 | 194 | |
| | 220 | 279 | 239 | 279 | 273 | |
| | 300 | 373 | 318 | 379 | 365 | |

**Table 6.2:** Trigger thresholds for dijet and single-jet triggers for AK4 jets. Dijet triggers aim at the average of the two $p_{\text{T}}$-leading jets, $p_{\text{T}}^{\text{ave}}$, while single-jet triggers at the $p_{\text{T}}$ of the leading jet. The triggers are distinguished between central ($|\eta_{\text{probe}}| < 2.853$) and forward triggers ($|\eta_{\text{probe}}| < 2.853$). In this analysis, for 2017 a combination of the dijet and single-jet trigger is used in the central region.

curacy in perturbation theory for Run 2 and NLO in Run 3. The parton shower and hadronization is simulated with PYTHIA8 [53] using the CP5 tune [56]. The events are reweighted to match the expected luminosity and the number of additional pp collisions (pileup) observed in the data, assuming a total inelastic collision cross section of 69.2 mb [114]. The cross section of the inelastic pp scattering has been measured by the CMS Collaboration in Ref. [160].

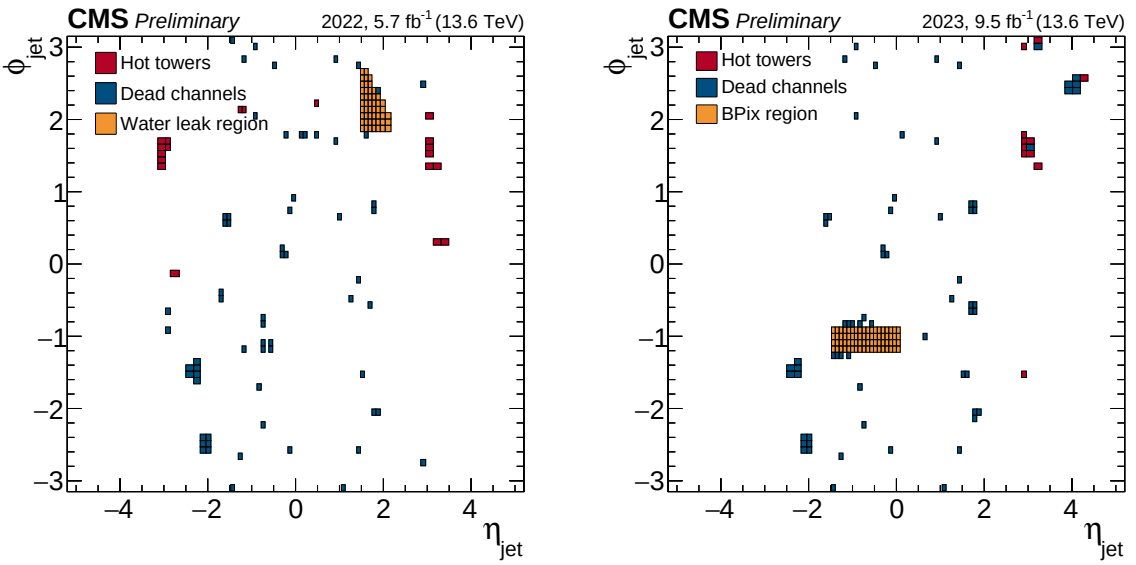


**Figure 6.3:** Malfunctioning detector regions where the measured energy is $10\sigma$ above (hot towers, red) or below (dead channels, blue) the average occupancy in the corresponding $\phi$ stripe. In 2022 (left) a water leak has been observed in the positive ECAL endcap and in 2023 (right) two consecutive layers in the barrel pixel detector became inoperable. Events with either an electron or jet in these regions are not considered for JER SFs measurement. Taken from Ref .[1] (left) and [2] (right)

## 6.3 Event Selection

The physical objects used in this analysis are reconstructed with the PF algorithm. Jets are clustered with the anti-$k_T$ algorithm with a distance parameter of $R = 0.4$. This analysis includes the CHS and PUPPI pileup mitigation techniques for Run 2 and Run 3, respectively, and are calibrated based on the procedure described in Section 4.4.

Only events with at least one well-reconstructed PV are considered. The trigger selection is applied to data but not to simulations to provide a large event yield as possible. An event is required to only activate one dijet trigger, because each trigger leads to a unique pileup profile in data. In 2017, the same condition applies for single-jet triggers. Moreover, the $p_T^{ave}$ of the two $p_T$-leading jets must be within the $p_T^{ave}$ range in which the activated trigger becomes fully efficient (see Table 6.2). Events featuring dijet topologies are selected by requiring at least two jets. Furthermore, the two $p_T$-leading jets must be back-to-back with respect to their azimuthal angle with $\Delta\phi(\text{jet1}, \text{jet2}) > 2.7$. In order to select proper reconstructed jets and reject those originating from pileup, the two leading jets must have $p_T^{jet} > 15\,\text{GeV}$, while on the particle level the requirement is set to $p_T^{jet} > 10\,\text{GeV}$. Only jets passing the tight jet ID are considered in this analysis. Additionally, the tight pileup jet ID is applied to CHS jets. Because only QCD dijet events are targeted in this analysis, events with at least one muon or electron are discarded. To be considered as a lepton, muons must pass the tight criteria of the cut based IDs [98] and electrons the non-isolated loose ID based on a BDT [99] (see sections 4.1.1 and 4.1.2). Furthermore, only muons and electrons with $p_{T,\ell} > 15\,\text{GeV}$ and $|\eta_\ell| < 2.4$ are considered to

obtain the number of leptons in an event.
A series of selection criteria based on the missing transverse momentum is applied to data and simulation. These selections aim to identify $p_{\mathrm{T}}^{\mathrm{miss}}$ arising from wrongly reconstructed events, which can be caused by detector noise or particles not originating from the bunch crossing, such as from the beam halo [77, 161]. Additionally, events affected by local malfunctioning detector regions are discarded. These regions are identified in the $\eta$-$\phi$-plane, where a cell is considered malfunctioning if its energy deviates by more than $10\,\sigma$ from the average occupancy of the corresponding $\phi$ strip. Such regions are referred to as hot towers or dead channels and are illustrated in Figure 6.3. During the various data taking years of the CMS detector, certain parts of the subdetectors occasionally malfunctioned due to the ageing of the detector or electronic failure. While radiation damage contributes to the ageing of the detector, its impact on measurements is relatively small compared to electronic failures that affect several adjacent calorimeter cells. In the data taking year 2022, a water leak in the positive endcap region of the electromagnetic calorimeter occurred [158]. This leak led to cooling limitation in the affected region and therefore has been turned off. About 7 % of the positive endcap are affected, leading to misreconstruction and mismeasurements of electrons and jets. Events are rejected if one of these objects is located in the affected region. In 2023, several modules in two layers of the barrel pixel detector became inoperable [159] and have been turned off. The affected modules in both layers overlap, resulting in a gap in the tracker hits. This gap impacts track seeds that aim for high-purity pixel-hit combinations. Figure 6.3 shows the affected area in 2022 due to the water leak (left) and the pixel issue in 2023 (right). In 2018, two endcap sectors of the HCAL were not functioning properly in the region $\eta \in [-2.96, -1.31]$ and $\phi \in [-1.57, -0.87]$. The issue led to a significant mismeasurement of the jet energy or jets can be misidentified as an electron. Additionally, events with jets in the affected area can feature a significant mismeasurement of the missing transverse momenta. Consequently. events containing electrons or jets in the region are completely rejected to avoid any biases in the event.

### 6.3.1 Treatment of Prescaled Triggers

The trigger system (see Section 3.2.6) at the CMS detector is used to reduce the amount of recorded data to meet time and memory constraints. Triggers at the CMS detector aim for various processes with different cross sections. Events with higher cross sections such as QCD multijet events are more likely to occur in comparison to processes including Higgs bosons. Thus, the rate with which a trigger accepts events is expected to be much higher in such events. Too many events, however, overwhelm the available computing resources. Prescales limit the number of events passing a certain trigger to prevent an overload of the trigger bandwidth. Only one out of $f_{\mathrm{p}}$ events passes a trigger, where $f_{\mathrm{p}}$ is the prescale factor. The prescale is adjusted to the instantaneous luminosity profile of the LHC to keep a constant rate. This adjustment can cause shifts in the recorded pileup profile since both pileup and the prescale factor scale

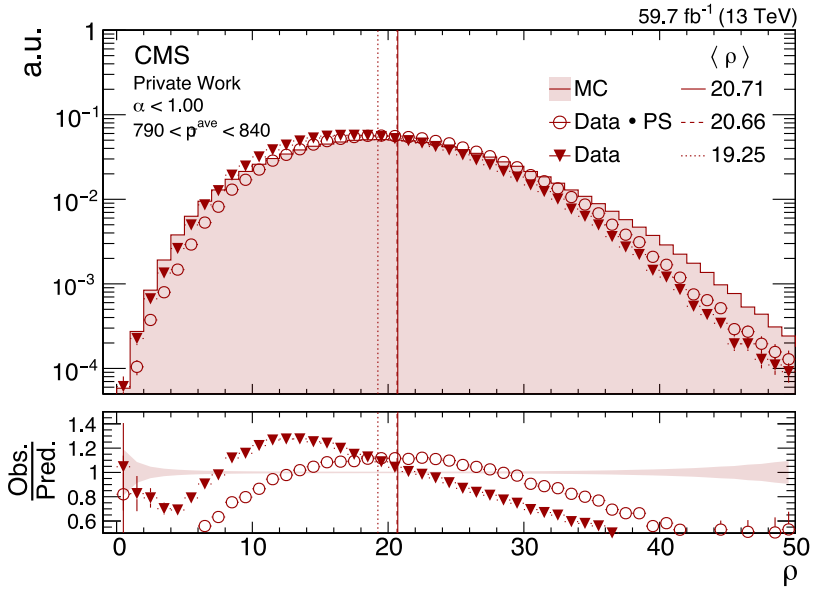


**Figure 6.4:** Median energy density $\rho$ distribution for different $p_{\mathrm{T}}^{\mathrm{ave}}$ ranges in dijet events. Shown are simulation (histogram), data with (triangle) and without (circle) the prescale factor applied. The mean of the distributions are indicated by vertical lines. The lower panel shows the ratio of data to simulations. The error bars of the markers and the error band in the lower panel respresent the statistical uncertainties.

with the instantaneous luminosity. Therefore, it is essential to account for the prescale rates to ensure that the data collected by prescaled triggers accurately represent the average pileup profile.

In this analysis, both the HLT triggers and the preceding L1 triggers, referred to as L1 seeds, are prescaled. Each L1 seed can consist of multiple triggers targeting single jets with a $p_{\mathrm{T}}$ above a certain threshold. To account for prescaling, data is weighted with the corresponding prescale factor, scaling the event yield and the statistical uncertainty. This factor is constructed via

$$f_{\mathrm{p}} = f_{\mathrm{p}}^{\mathrm{HLT}} \cdot f_{\mathrm{p}}^{\mathrm{L1min}}, \tag{6.7}$$

where $f_{\mathrm{p}}^{\mathrm{HLT}}$ is the prescale factor for the HLT trigger and $f_{\mathrm{p}}^{\mathrm{L1min}}$ for the L1 seed with the smallest prescale factor, if multiple L1 seeds are present. It is expected that the events passed to the HLT trigger are predominantly selected by the L1 trigger with the smallest prescale factor. Additionally, the trigger selection efficiency tends to decrease as the prescale factors increase.

Figure 6.4 illustrates the impact of time-dependent prescales. Shown is the distribution of the median energy deposit $\rho$, an event-based observable sensitive to pileup, in dijet events within the $|\eta| < 1.3$ region. Pileup introduces additional energy deposits in the event, causing shifts in the $\rho$ distribution. When no prescale factors are applied, a shift in the $\rho$ distribution is observed. The shifts depend on the condition under which the prescale is applied to the trigger during data taking. With prescale factor applied, the agreement between data and simulation is

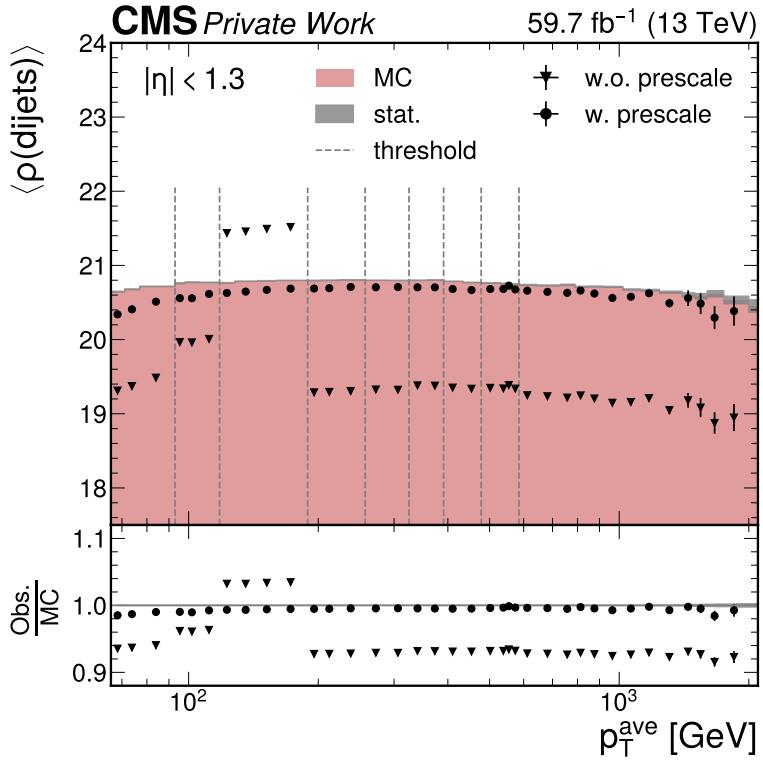


**Figure 6.5:** Mean value of the median energy density distribution in dijet events as a function of the $p_T^{ave}$ for simulations (red filled area) and data with (triangles) and without (circles) the prescale factor applied. The triggers used in different $p_T^{ave}$ ranges are indicated with the vertical gray lines. The lower panel shows the data to simulation ratio and the statistical uncertainties are indicated by the grey area.

better in comparison to no prescales applied. The width of the $\rho$ distribution is smaller than in simulation but the mean value is compatible. Simulations are reweighted to match the number of interactions per bunch crossing in data. The reweighting also aligns pileup-sensitive observables such as $\rho$ more closely. With no prescale factors applied, the pileup profile in data collected by a specific prescaled trigger is not represented by the average pileup profile anymore. Hence, simulation and data feature different pileup conditions and are not compatible. Applying the prescale factors accounts for changes in the trigger specific pileup profile, aligning the mean values in $\rho$ with these observed in simulation.

Figure 6.5 displays the mean values in $\rho$ across the entire $p_T^{ave}$ range. These mean values fluctuate in data for different trigger configurations without prescale factors applied. It is observed that data without prescaling shows a tendency towards lower $\rho$ values, indicating higher prescale factors for data-taking periods with greater pileup contributions. The distribution for the dijet trigger with a $p_T^{ave}$ threshold of 80 GeV is shifted towards higher values. For events with $p_T^{ave} \gtrsim 200$ GeV a consistent shift towards lower values is observed. After the application of the prescale factors, the overall trend in the simulations becomes more consistent with that observed in the data.

## 6.4 Scale Factor Determination

The process for deriving the JER SFs has been outlined in Section 6.1. This section delves into the specifics of the measurement and the experimental challenges encountered. The JER SFs are derived in bins of $|\eta|$ for both the standard method and the forward extension approach. In the standard method, it is required that both jets are located within the same $|\eta|$ bin. Conversely, for the FE the scale factors are determined as a function of the probe jet $|\eta|$, while the reference jet is positioned within the barrel region ($|\eta| < 1.3$). The $|\eta|$ binning is defined, such that it aligns with the underlying $|\eta|$ binning from the calorimeter cells. Several adjacent cells are merged to improve statistical precision when needed.
The asymmetry is further examined in bins defined by the average transverse momentum ($p_{\mathrm{T}}^{\mathrm{ave}}$) of the two leading jets, which is defined as

$$p_{\mathrm{T}}^{\mathrm{ave}} = \frac{p_{\mathrm{T},1} + p_{\mathrm{T},2}}{2}. \tag{6.8}$$

In general, the jet with lower $p_{\mathrm{T}}$ has a poorer resolution than higher-$p_{\mathrm{T}}$ jets, potentially degrading the overall measured response. By binning according to $p_{\mathrm{T}}^{\mathrm{ave}}$, the effect cancels out on average. The final $p_{\mathrm{T}}^{\mathrm{ave}}$ binning is aligned with the trigger thresholds, avoiding biases from combining events accepted by different trigger conditions. The granularity of the $p_{\mathrm{T}}^{\mathrm{ave}}$ binning is chosen to ensure an adequate statistical precision in each bin. It is anticipated that the statistical precision becomes insufficient in high-$p_{\mathrm{T}}$ bins for increasing $|\eta|$ ranges.

### 6.4.1 Measurement of the Asymmetry

The asymmetry distribution exhibits a Gaussian core with non-Gaussian tails. The width of the distribution is extracted from the Gaussian core of the distribution. The contribution of the non-Gaussian tails is mitigated by removing the quantiles at 1.5 % on each side. The width is then quantified using the truncated root mean square (RMS). An illustration of the asymmetry and the truncated tails is provided in Figure 6.6, which compares the asymmetry distributions for different $p_{\mathrm{T}}$ regions in both data and simulation at the reconstruction and particle levels. Notably, the distributions from data consistently show a larger width than those from simulations. In general, the width increases for lower $p_{\mathrm{T}}$ values as the resolution itself increases.

### 6.4.2 Alpha Extrapolation

In hard-scattering processes, additional jets arise from ISR and FSR, which occur more often in highly relativistic events. This radiation carries a fraction of the momentum of such processes, leading to a $p_{\mathrm{T}}$ imbalance in the dijet system. To quantify the imbalance, the additional jet activity $\alpha$ is introduced with

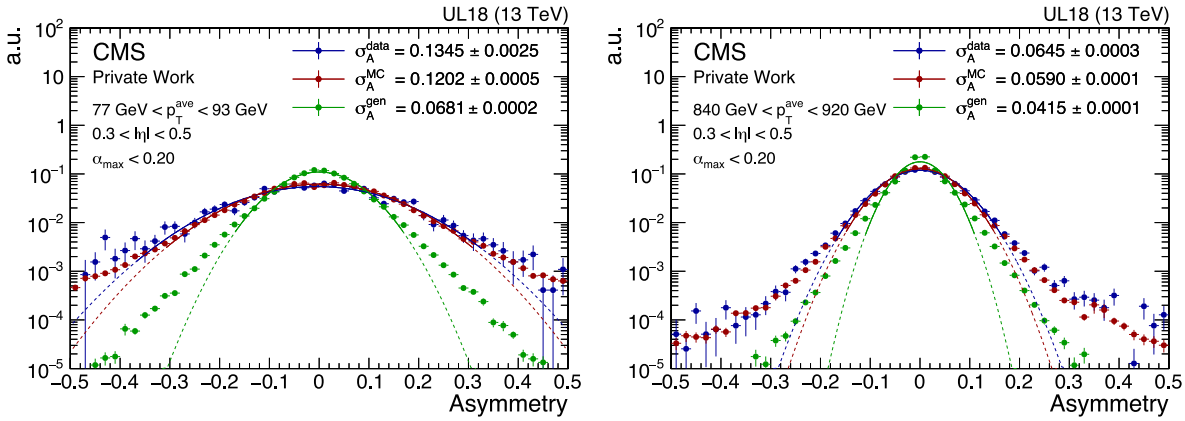


**Figure 6.6:** Normalized asymmetry distribution for data (blue), simulation (red) and for particle level (green) measured with data from 2018 at a center-of-mass energy of $\sqrt{s} = 13\,\text{TeV}$. The Gaussian fit (solid line) indicates the Gaussian core of the distribution without the areas of the truncated non-Gaussian tails (dashed lines). The width extracted as the RMS and its uncertainty is reported for all three distributions.

$$\alpha = \frac{p_\text{T}^\text{3rd jet}}{p_\text{T}^\text{ave}}. \tag{6.9}$$

Here, $p_\text{T}^\text{3rd jet}$ is the transverse momentum of the third $p_\text{T}$-leading jet and $p_\text{T}^\text{ave}$ the average of the two $p_\text{T}$-leading jets. The $p_\text{T}$ imbalance results in a broader asymmetry distribution, because the events do not exhibit a dijet topology anymore. Furthermore, the relations used in Equation 6.4 and 6.6 to determine the intrinsic resolution do not hold anymore. Consequently, the effect of additional jet activity needs to be accounted for a proper measurement of the JER. Lower ranked jets are not directly considered in this analysis, because their contribution to the $p_\text{T}$ imbalance can be neglected. The impact of the additional jet activity and the resulting limitation of the JER SF measurement is studied in detail in this thesis and further elaborated on in Section 6.8.

An extrapolation procedure is employed to evaluate the width of the asymmetry distribution as if no radiation is present with $\sigma_A(\alpha \to 0)$. The dependence of the asymmetry width on $\alpha$ is determined by measuring the asymmetry across various bins defined by the maximum value of $\alpha$ ($\alpha_\text{max}$). These bins result in inclusive intervals of $0 < \alpha < \alpha_\text{max}$ by construction, necessitating to account for bin-to-bin correlations in the extrapolation. To preserve a dijet-like event topology, a maximum threshold is set conventionally at $\alpha < 0.3$. This threshold ensures the exclusion of events with substantial additional jet activity that could distort the basic dijet configuration. In previous iterations of this analysis [119, 120, 154, 162] a linear dependence of the asymmetry width on $\alpha_\text{max}$ was assumed and parameterized as

$$\sigma_A(\alpha_\text{max}) = a + b \cdot \alpha_\text{max}. \tag{6.10}$$

Here, $a$ indicates the width of the asymmetry under the assumption of no additional radiation and $b$ the dependence of the width with increasing $\alpha_\text{max}$ thresholds. The treatment of the cor-

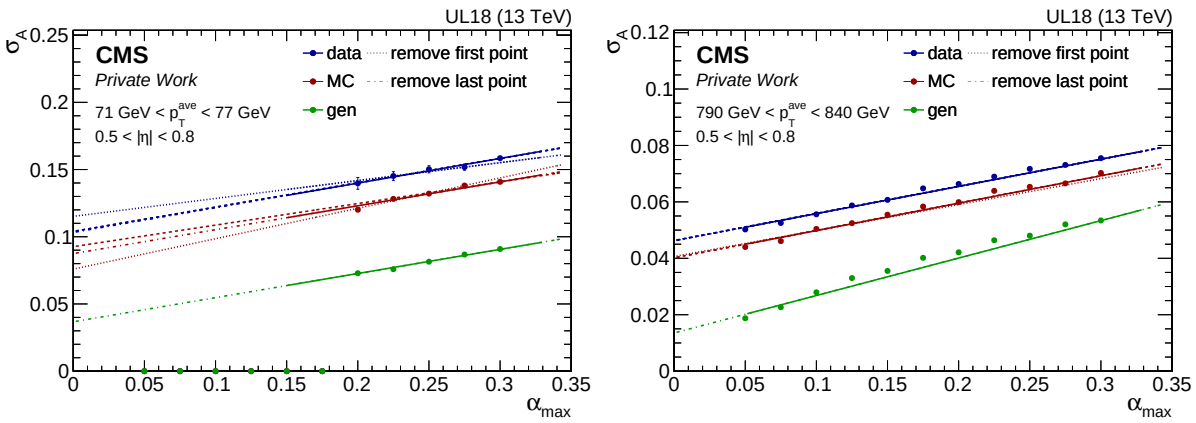


**Figure 6.7:** The width of the normalized asymmetry distribution as a function of the maximal additional jet activity for a low (left) and high (right) $p_\mathrm{T}$ ranges. The extrapolation for $\sigma_A(\alpha \to 0)$ is performed for data (blue) and simulated events at the reconstruction level (red) and particle level (green). In total, three different linear fits are used: all points are considered in the fit (solid), the first bin is removed from the fit (dotted) or the last bin (dash-dotted).

relations of the bins has been elaborated on in Ref. [163]. Only bins with adequate statistical precision are considered for the linear fit to ensure a robust description of the asymmetry distribution.

Thresholds in $\alpha_\mathrm{max}$ act as a selection criterion for dijet events based on $p_\mathrm{T}^\mathrm{ave}$. For $\alpha < 0.1$, third jets are required to have a $p_\mathrm{T}$ not exceeding 10 % of $p_\mathrm{T}^\mathrm{ave}$. This restriction particularly impacts the low-$p_\mathrm{T}$ regions, where many events are excluded due to the third jet not meeting the minimum $p_\mathrm{T}$ threshold of 15 GeV. For that reason, the statistical precision drops significantly for events with low $p_\mathrm{T}^\mathrm{ave}$ and small $\alpha_\mathrm{max}$ values. The loss in precision leads to larger fluctuations, increasing the uncertainties on $\sigma_A(\alpha \to 0)$ with a linear fit. Moreover, the event yield does not directly scale with increasing $\alpha_\mathrm{max}$ thresholds. With increasing thresholds, fewer additional events are included in the measurement, resulting in an unchanged asymmetry width for large $\alpha_\mathrm{max}$. The thresholds of $\alpha_\mathrm{max}$ at which the asymmetry width becomes constant is not precisely determined and depends on the bins in $|\eta|$, $p_\mathrm{T}^\mathrm{ave}$ and $\alpha_\mathrm{max}$. It is possible that the change to a constant trend already occurs for $\alpha_\mathrm{max} > 0.3$.

In order to account for fluctuations in the low-$p_\mathrm{T}$ region, the extrapolation is performed multiple times. First, all considered $\alpha_\mathrm{max}$ bins are included as it was done in previous iterations of the JER SFs derivation. Then, two more linear fits are performed excluding the first and last bin each. The value for $\sigma_A(\alpha \to 0)$ is obtained from the average value of the three extrapolations and denoted as $\sigma_\mathrm{var}$. The error $\delta_\mathrm{var}$ is determined from the largest deviation among the three fits from $\sigma_\mathrm{var}$. To ensure that the total uncertainty does not underestimate the uncertainty in bins where the full coverage in $\alpha_\mathrm{max}$ is well described by a linear dependence, the total uncertainty is calculated with

$$\delta_\mathrm{tot} = \sqrt{\delta_\mathrm{var}^2 + \delta_\mathrm{full}^2}. \tag{6.11}$$

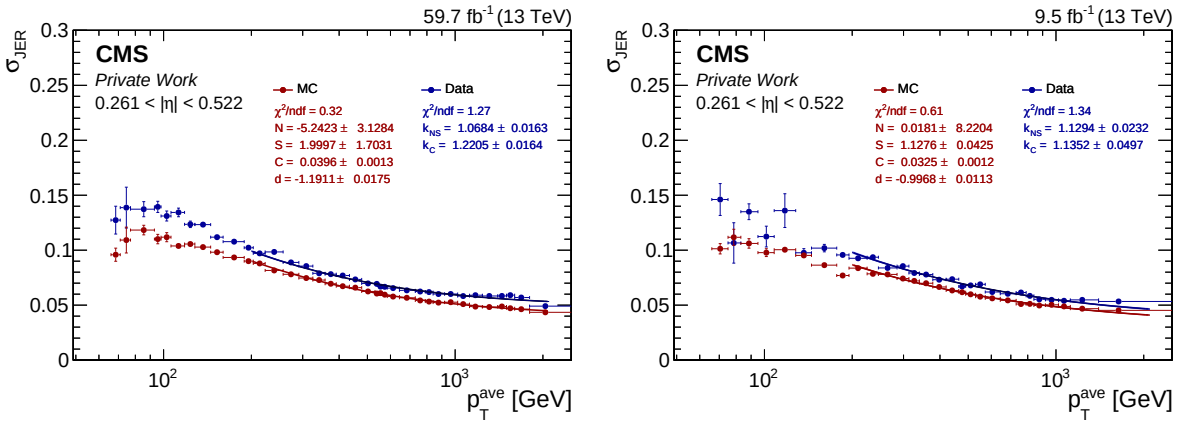


**Figure 6.8:** Jet transverse momentum resolution as a function of the $p_{\mathrm{T}}^{\mathrm{ave}}$ from QCD dijet events for the legacy calibration from 2018 (left) and the prompt reconstruction of 2023 after the BPix failure (right). The parameters from the NSC fit are given for data and simulations. Shown are the JER for a bin in the barrel region of the detector ($|\eta| < 1.3$).

Here, $\delta_{\mathrm{full}}$ indicates the uncertainty from the fit parameter $a$ from the correlated fit to all considered $\alpha_{\mathrm{max}}$ bins. Additionally, this comprehensive approach addresses both the linear and potential non-linear behavior in higher $\alpha_{\mathrm{max}}$ bins. Two example bins of the $\alpha$-extrapolation are shown in Figure 6.7 in the barrel region. In the low-$p_{\mathrm{T}}$ region (left) it can be seen that the three fits performed show different results for $\alpha \to 0$. The limited event count for lower $\alpha_{\mathrm{max}}$ thresholds and the corresponding uncertainty due to the linear assumption is better encapsulated in the approach with three fits instead of one. For higher $p_{\mathrm{T}}$ bins (right) the differences are significantly smaller and the extrapolations precision is dominated by the statistical error from the fit to the full $\alpha_{\mathrm{max}}$ range.

### 6.4.3 Particle Level Imbalance

Despite the presence of additional jet activity, $p_{\mathrm{T}}$ imbalances in dijet events can originate from several other sources. The out-of-cone effect describes the phenomenon where particles at the particle level fail to be clustered into the reconstructed jet. This effect can occur due to the creation of low-$p_{\mathrm{T}}$ particles during the fragmentation and hadronization processes, or due to particles with large angular separations. These particles remain unclustered and are not considered in the dijet topology. Conversely, particles from the underlying event or pileup that do not originate from the hard-scattering process and are not removed by pileup mitigation techniques, may also be clustered into the jet and cause additional $p_{\mathrm{T}}$ imbalance. Both phenomena lead to a broadened asymmetry distribution and are referred to as particle-level imbalance (PLI). To estimate the contributions from PLI, the asymmetry at the particle level is derived using the same methodology employed for data and simulated events at the reconstruction level, including the characterization of the Gaussian core and the $\alpha$-extrapolation. The contribution from PLI is then evaluated from the width of the asymmetry on particle level with

$$\sigma_{\mathrm{PLI}} = \sqrt{2} \cdot \sigma_A^{\mathrm{gen}}(\alpha \to 0). \tag{6.12}$$

The contribution is calculated within the same $p_{\mathrm{T}}^{\mathrm{ave}}$, $|\eta|$ and $\alpha_{\mathrm{max}}$ intervals to ensure consistency with the underlying structure of the detector-level events. It is assumed that the PLI is consistent between data and simulations, and thus the contribution is subtracted in quadrature from both widths obtains from the extrapolation $\sigma_A(\alpha \to 0)$. Hadronization and parton shower models in simulations have an impact on the PLI and are considered as an uncertainty in the measurement. Those uncertainties are further explored and discussed in Section 6.5.
Two $|\eta|$ bins for $\sigma_{\mathrm{JER}}$, after subtracting the contribution from PLI, are shown in Figure 6.8 for 2018 (left) and 2023 (right). In general, the JER in all years show a smooth trend for $p_{\mathrm{T}} > 200\,\mathrm{GeV}$ for $|\eta| < 1.3$. Changes in the trend and fluctuations for $p_{\mathrm{T}} < 200\,\mathrm{GeV}$ are further discussed in Section 6.4.5.

### 6.4.4 Data-to-Simulation Scale Factors

The data-to-simulation scale factors are determined after following the methodology outlined in the preceding sections. The scale factors are computed as the ratio of the JER measured in data ($\sigma_{\mathrm{JER}}^{\mathrm{Data}}$) and in simulations ($\sigma_{\mathrm{JER}}^{\mathrm{MC}}$), expressed as

$$s = \frac{\sigma_{\mathrm{JER}}^{\mathrm{Data}}}{\sigma_{\mathrm{JER}}^{\mathrm{MC}}}. \tag{6.13}$$

The resulting scale factors as a function of $p_{\mathrm{T}}^{\mathrm{ave}}$ in one $|\eta|$ bin are illustrated in Figure 6.9. The final $|\eta|$ dependent JER SFs are determined through a constant fit in the $p_{\mathrm{T}}$ range of 200 GeV to 1000 GeV, where a constant trend can be reasonably assumed. Any potential $p_{\mathrm{T}}^{\mathrm{ave}}$ dependencies are explored in the subsequent section.
Additionally, it has been observed that the low-$p_{\mathrm{T}}$ region for $p_{\mathrm{T}}^{\mathrm{ave}} < 150\,\mathrm{GeV}$ exhibits distinct behavior with respect to earlier measurements. Combination with the Z+jets process indicated a constant trend in the scale factors including the low-$p_{\mathrm{T}}$ region [162] for $|\eta| < 1.3$, while this measurement observes an increasing trend. Dijet events are significantly constrained in the low $p_{\mathrm{T}}$ regions due to pileup as discussed in the context of Section 6.8.1 and not directly comparable to Z+jets events. Moreover, this measurement uses the latest calibration for the Run 2 data-taking period, referred to as legacy (UL) reconstruction exhibiting a more refined overall calibration of the detector in comparison to earlier reconstruction periods. In general, the trend of the scale factors consistently exceeds unity, implying that the JER in data is indeed larger than in simulations.

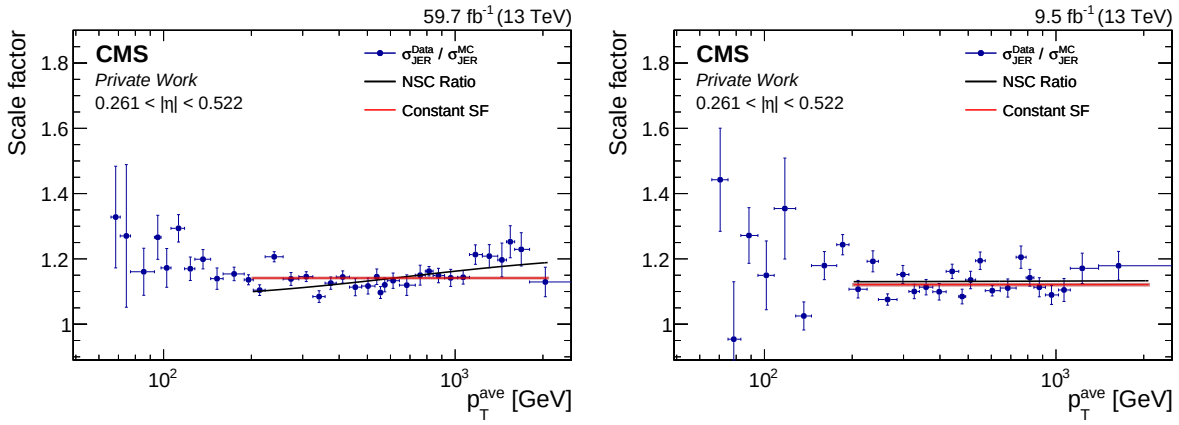


**Figure 6.9:** Data-to-simulation ratio (blue) of the JER as a function of $p_{\mathrm{T}}^{\mathrm{ave}}$ for 2018 (left) and the prompt reconstruction of 2023 after the BPix failure (right). Scale factors independent of $p_{\mathrm{T}}^{\mathrm{ave}}$ are obtained via a constant fit to the data-to-simulation ratio (red). Scale factors depending on $p_{\mathrm{T}}^{\mathrm{ave}}$ are derived from the ratio of the NSC fit to JER in the simulation and data (gray).

### 6.4.5 Transverse Momentum Dependence

In previous iterations of this analysis [119, 162], no $p_{\mathrm{T}}$ dependence for the JER SFs is observed. The JER SFs were obtained with a constant function fitted to the data-to-simulation ratio. Potential $p_{\mathrm{T}}$ dependencies were considered as an additional uncertainty arising from different trends of the JER in data and simulations.

The $p_{\mathrm{T}}$ dependence of the JER relies on the response characteristics of the subdetectors and the simulated detector response, as detailed in Section 6.1. The parametrization of the JER is motivated by the calorimeter energy resolution in Equation 3.4, referred to as NSC function, with slight modifications:

$$\frac{\sigma_{p_{\mathrm{T}}}}{p_{\mathrm{T}}}(N,S,C,d) = \sqrt{\frac{N|N|}{p_{\mathrm{T}}^2} + \frac{S^2}{p_{\mathrm{T}}^d} + C^2}. \tag{6.14}$$

Here, $N$ represents the noise term, $S$ the stochastic term and $C$ the constant term and $d$ introduces an additional degree of freedom in the stochastic term's $p_{\mathrm{T}}$ dependence. Unlike Equation 3.4, the $N$ parameter can assume negative values, which showed an overall improvement of the fit to the JER [119]. Modifications in the noise and stochastic term accommodate potential deviations in the $p_{\mathrm{T}}$ dependence when incorporating tracker information with the calorimeter. In the low $p_{\mathrm{T}}$ region the noise term dominates, while the stochastic and constant terms become significant in the mid-range and at higher $p_{\mathrm{T}}$, respectively. The $p_{\mathrm{T}}$ dependence is determined by comparing trends observed in the simulation and data. The NSC fit obtained in simulations is adapted in the data introducing the parameters $k_{NS}$ and $k_C$, which scale the noise and stochastic terms, as well as the constant term, respectively. The noise term is constrained in combination with the stochastic term due to the limited precision in the low-$p_{\mathrm{T}}$ region in dijet events. Combinations with additional processes can constrain the noise and stochastic term simultaneously in the data by introducing $k_N$ and $k_S$ separately. These combinations are further elaborated on in

Section 6.9. Measurements from dijet events are dominant in the mid $p_T$ range but also contribute to higher $p_T$ regions. When no $p_T$ dependence is present, both factors in the data, $k_{NS}$ and $k_C$, are equal, resulting in one multiplicative scale factor $k_{NSC}$ applied to all terms. However, differences in data and simulation lead to different trends in the JER, resulting in distinct $k_{NS}$ and $k_C$ parameters.
The $p_T$ dependence is only studied down to $p_T^{ave} < 200\,GeV$, as for lower $p_T$ regions dijet events are limited by contributions from pileup (see Section 6.8.1). Increasing statistical precision in the UL calibration of the Run 2 data taking period at the CMS detector and expanding the $p_T$ up to $p_T^{ave} = 2\,TeV$ revealed a $p_T$ dependence in various $|\eta|$ bins in all datasets. The $p_T$ dependence for the UL reconstruction in 2018 is shown in Figure 6.9 (left), where the NSC ratio (grey) describes the overall trend of the JER SFs down to $p_T^{ave} < 2\,TeV$. It has been verified that the lower $p_T$ threshold for the NSC fit from 150 GeV to 300 GeV does not alter the overall trend of the NSC ratio, indicating a well calibrated JER for the considered $p_T$ range of 200 GeV to 2000 GeV. For the current Run 3 data-taking period of the LHC, the calibration of the measured data is not final. Ongoing adjustments in intercalibration of the subdetectors, such as the HB scale, significantly affect the measurement in the JER SFs. Consequently, the measurement of the JER SFs in dijet events provide input for cross-checks in the condition and the performance of the detector. However, no conclusion about $p_T$-dependent JER SFs can be made, as the intercalibrations change for different reconstruction periods and different trends are observed. For instance, it has been observed that in 2022 the trend of the NSC ratio does depend on $p_T$ threshold of the NSC fit from 150 GeV to 300 GeV. Slight changes in the trend of the JER in the data down to $p_T^{ave} = 200\,GeV$ cannot be described adequately by the NSC fit. Moreover, in 2023 after the BPix failure no $p_T$ dependence for the JER SFs derived in dijets events have been observed, as depicted in Figure 6.9 (right).

## 6.5 Systematic Uncertainties

The derivation of the JER SFs is susceptible to various systematic uncertainties, each of which are detailed in this section. These uncertainties are determined by recalculating the JER SFs while varying the corresponding source of uncertainty. The resulting shifts in the JER SFs relative to their central values is then taken as the final uncertainty.

- **Pileup Reweighting**: The pileup profile in data is utilized to reweight the pileup profile in simulated events. Those distributions in simulations are calculated from the total inelastic pp scattering cross section with 69.2 mb [114, 160]. Uncertainties associated with the pileup modeling are commonly obtained at the CMS Collaboration by varying the cross section within $\pm 4.6$ %.

- **Jet Energy Scale**: All jets utilized in the analysis are corrected to the particle level. The calibration of the JES has been discussed in Section 4.4. The uncertainties arising from

this calibration are determined by scaling the jets in simulation with the up and down variations.

- **Non-Gaussian tails**: The width of the asymmetry is determined from the RMS of the Gaussian core of the distribution. Contributions from non-Gaussian tails are mitigated, by truncating 1.5 % from the distribution of each side. However, the contribution from the tails depend on the $p_{\mathrm{T}}$, $\eta$ and $\alpha$ bins leading to systematic shifts in the width measurement. To account for this dependence, a systematic uncertainty is introduced by truncating 2.5 % from each side.

- **Correction for additional jet activity**: The additional jet activity in each bin is removed by extrapolating the asymmetry width for vanishing additional jet activity. Here, a linear dependence is assumed, which is an empirical choice rather than theoretically motivated. This choice also implies that the linear dependence holds for $\alpha$ values close to the ideal dijet topology. With the current methodology and experimental setup, it is not possible to measure regions for $\alpha \to 0$ directly. A systematic uncertainty is introduced by lowering the $p_{\mathrm{T}}$ threshold for the third jets from 15 GeV to 10 GeV.

- **Particle level imbalance**: Contributions to the dijet imbalance from PLI is corrected based on the asymmetry width from particle level. This correction depends on the MC generator used for the fragmentation and hadronisation process and has been studied in Ref. [163]. The difference between HERWIG and PYTHIA resulted in a variation of 25 %. Consequently, the PLI correction factor is scaled with $\pm$25 %.

- **Prefiring**: Exposure to radiation affects the detector performance over time, particularly in regions with $|\eta| > 2.5$ due to a higher flux of ionizing particles. This leads to a transparency loss in the ECAL crystals, resulting in a time shift in the ECAL pulses. Consequently, if an event fires a L1 trigger, the event from the previous bunch crossing is considered as the interesting event, referred to as prefiring [164]. Furthermore, trigger rules prevent three consecutive L1 trigger acceptances, ultimately removing the event of interest. At the trigger level, the prefiring was uncorrected until 2018. In simulation for 2016 and 2017, prefiring is addressed by scaling down simulated events to compensate for the efficiency loss with uncertainties included incorporated through different prefire scales.

- **Initial and Final State Radiation**: The emission of radiation of initial and final state particles of the hard-scattering process is steered by the energy scale of the strong coupling $\alpha_{\mathrm{S}}(\mu)$. Variations are introduced by scaling the energy scale $\mu$ with a factor 1/2 and 2, changing the amount of emitted radiation.

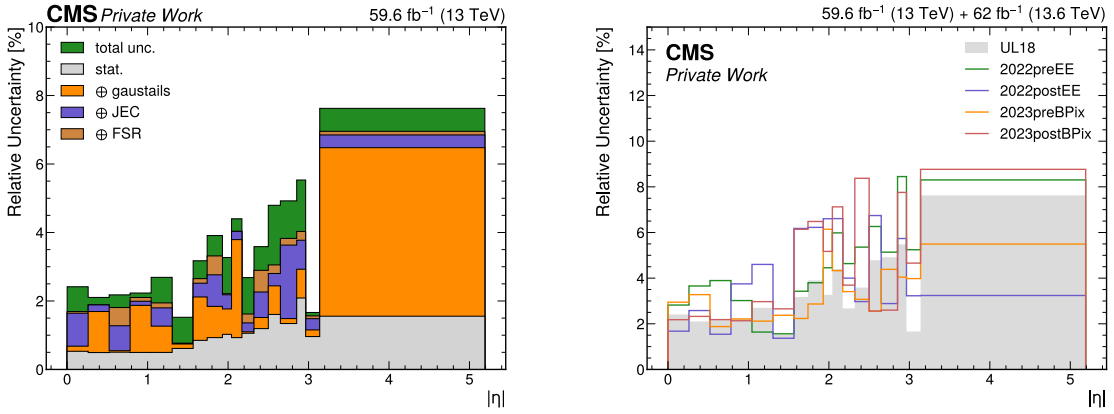


**Figure 6.10:** Relative uncertainties for the dominant sources in 2018 (left) arising from the treatment of the non-Gaussian tails (orange) and the calibration of the JES (purple). Additionally, the uncertainty arising from the modeling of the FSR (brown) is introduced in the scope of this thesis. The uncertainty from 2018 is compared to all years from the Run 3 data-taking period (right).

### 6.5.1 Total Systematic Uncertainty

The treatment of the systematic uncertainties is based on Ref. [165] and has been introduced in Ref. [154] to the JER SF measurement.
First, each source with an up ($\sigma^{\uparrow}$) and down ($\sigma^{\downarrow}$) variation, namely the pileup reweighting, PLI, JES, prefiring, ISR and FSR, is symmetrized with

$$\sigma_{\text{sys}}^{\uparrow\downarrow} = \sqrt{\left(\frac{\sigma^{\uparrow}+\sigma^{\downarrow}}{2}\right)^2 + 2\left(\frac{\sigma^{\uparrow}-\sigma^{\downarrow}}{2}\right)^2}. \tag{6.15}$$

Combining asymmetric errors results in a shift of the central value ($c_{\text{res}}^{\text{nominal}}$) with

$$c_{\text{res}}^{\text{corrected}} = c_{\text{res}}^{\text{nominal}} + \frac{\sigma^{\uparrow}-\sigma^{\downarrow}}{2} \tag{6.16}$$

Uncertainties derived from one-sided shifts, such as the non-Gaussian tails and the correction of additional jet activity, are considered symmetrical. The total uncertainty for the JER SFs are then obtained by summing all contributions from the systematic uncertainties and the statistical one in quadrature.
For years with $p_{\text{T}}$-dependent JER SFs, the total uncertainties are taken from the determination of constant JER SFs and are applied to each $p_{\text{T}}$ bin. In general, the dominant uncertainties arise from the non-Gaussian tails and the JES as illustrated in Figure 6.10 (left) for the legacy reconstruction in 2018. A comparison of the systematic uncertainties from 2018 and all years from the Run 3 data-taking period (2022 and 2023) is shown Figure 6.10 (right), yielding a similar precision across all $|\eta|$ bins.

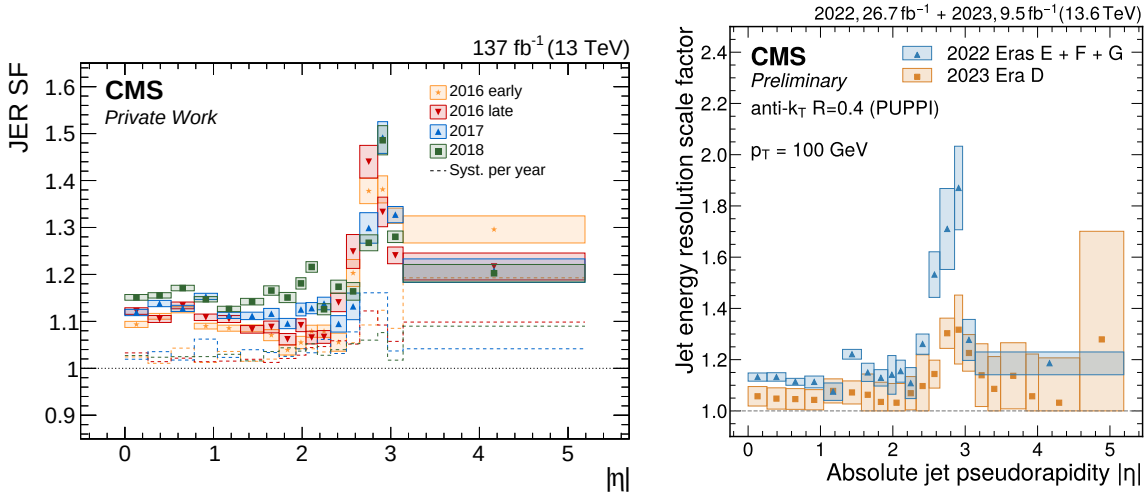


**Figure 6.11:** Jet energy resolution scale factors measured for jets clustered with the anti-$k_T$ clustering algorithm and $R = 0.4$ in dijet events. In the Run 2 data-taking period (left) the results are obtained for CHS jets in 2016 (yellow, red), 2017 (blue) and 2018 (green). For Run 3, PUPPI jets are used and the $p_T$-dependent scale factors are shown for $p_T = 100\,\text{GeV}$ in late 2022 (blue) and 2023 (yellow). The results from Run 3 are published in Ref. [2].

## 6.6 Results

The jet transverse momentum resolution scale factors from dijet events are derived for the legacy reconstruction in the data from Run 2 and the first datasets from the Run 3 data-taking period. Both correspond to an integrated luminosity of $138\,\text{fb}^{-1}$ and $62\,\text{fb}^{-1}$, respectively.

Figure 6.11 (left) shows the JER SFs from dijet events for the legacy reconstruction in the Run 2 data. JER SFs up to $\sim 15$ % in the barrel region and $\sim 50$ % in the transition region from the endcaps to the high forward region are observed. In general, the transition region is difficult to model in simulation, resulting in an significant increase in the JER SFs. Increasing JER SFs for the years by $\sim 8$ % in $|\eta| < 1.3$ indicate the ageing of the detector and have been observed in earlier iterations of this measurement [120, 154]. First calibrations in 2022 show similar results in the barrel region, while the transition region is worse with JER SFs up to $\sim 100$ %. The central values in 2023 have been derived with an extension of the MPF method in dijet events (see Section 6.8.2). Differences to the transverse momentum imbalance method derived in this work are considered as an uncertainty. Furthermore, JER SFs in 2023 are closer to unity in comparison to 2022 and the Run 2 results. The first $p_T$ dependent JER SFs in 2023 and the second reconstruction iteration for 2022 are shown in Figure 6.11 (right) for jets with $p_T = 100\,\text{GeV}$. For 2022, the JER SFs are shown for data collected after the water leak.

The results of the presented thesis for the Run 3 data-taking periods, including 2022 and 2023, have been published in Ref. [1, 2]. They are used by all CMS analyses published utilizing Run 3 data. Results for the years 2016 to 2018, will contribute to the final calibration of the Run 2 data-taking period at the CMS Collaboration and the forthcoming publication in Ref. [3].

## 6.7 Smearing Procedure in Simulation

Once the JER SFs are determined, the factor can be applied to simulated events such that the resolution matches the measured resolution in data. The correction is referred to as smearing, as the scale factors broaden the jet response in simulation. More details on the smearing procedure and its application can be found in Ref. [166]. The CMS Collaboration employs two primary approaches for the application of the JER SFs, chosen based on the specific analysis requirements. These methods are the *stochastic smearing* and the *scaling method*. However, the recommended approach is the *hybrid method*, which effectively combines both stochastic smearing and scaling techniques.

### 6.7.1 Scaling Method

The scaling method represents a fundamental approach, assuming that the reconstructed jet in simulation aligns closely with a corresponding particle level jet. This method corrects the jet transverse momentum with

$$p_{\mathrm{T}}^{\mathrm{MC,\,corr}} = p_{\mathrm{T}}^{\mathrm{MC}} + c_{\mathrm{res}}(p_{\mathrm{T}}^{\mathrm{MC}} - p_{\mathrm{T}}^{\mathrm{true}}). \tag{6.17}$$

Here, $p_{\mathrm{T}}^{\mathrm{MC}}$ denotes the transverse momentum of the unsmeared reconstructed jet in simulation and $p_{\mathrm{T}}^{\mathrm{true}}$ the transverse momentum on particle level. Successful corrections rely on the presence of a well-matched particle level jet in proximity to the reconstructed jet. Otherwise, the shift in the jet response is too large to be corrected properly. The matching criterion is defined via

$$\Delta R < \frac{R_{\mathrm{cone}}}{2} \quad \text{and} \quad \frac{|p_{\mathrm{T}}^{\mathrm{MC}} - p_{\mathrm{T}}^{\mathrm{true}}|}{p_{\mathrm{T}}^{\mathrm{MC}}} < 3\sigma_{\mathrm{JER}}^{\mathrm{MC}}, \tag{6.18}$$

where $\Delta R$ is the spatial separation of the two jets on reconstruction and particle level, and $R$ the distance parameter of the reconstructed jet. If no suitable particle level jet is matched, as is the case for pileup jets or when the reconstructed jet significantly deviates from the Gaussian approximation, the stochastic method is applied.

### 6.7.2 Stochastic Smearing

The stochastic method allows for the smearing of the jet resolution for every jet, regardless of whether it is matched to a particle level jet. Here, the $\sigma_{\mathrm{JER}}^{\mathrm{MC}}$ is convoluted with a Gaussian function with a width of $\sigma_{\mathrm{c}}$ to mimic detector effects. The width of the jet response is then defined as

$$\sigma_{\mathrm{JER}}^{\mathrm{MC,\,corr}} = \sigma_{\mathrm{JER}}^{\mathrm{MC}} \oplus \sigma_{\mathrm{c}}. \tag{6.19}$$

It is assumed that the width of the response in data also exhibits a Gaussian core and aligns with

the corrected resolution in simulation. This leads to the width of the Gaussian function of

$$\sigma_{\mathrm{c}} = \sigma_{\mathrm{JER}}^{\mathrm{MC}} \sqrt{s_{\mathrm{JER}}^2 - 1}, \tag{6.20}$$

where $s_{\mathrm{JER}}$ is the scale factor obtained previously in this chapter. Note that it is ensured in the JER SF measurement that $s_{\mathrm{JER}} \geq 1$. The correction factor applied to the transverse momentum in simulations is then defined as

$$c_{\mathrm{JER}} = 1 + \mathcal{N}(0, \sigma_{\mathrm{c}}) \sqrt{s_{\mathrm{JER}}^2 - 1}. \tag{6.21}$$

Here, a random number is sampled based on the Gaussian function with $\mathcal{N}(0, \sigma_{\mathrm{c}})$.
The scaling method is preferred over the stochastic method. First, the stochastic method only provides a factor $c_{\mathrm{JER}} > 1$, meaning that the resolution in simulation can only be broadened. Second, the procedure is irreversible unless the random factors used in the Gaussian function are stored. Lastly, the random factor can result in a different $p_{\mathrm{T}}$ imbalance within the event, leading to spurious $p_{\mathrm{T}}^{\mathrm{miss}}$.

## 6.8 Towards Larger Jet Activity

Historically, the transverse momentum imbalance method has been employed in earlier particle colliders like the Tevatron and during the Run 1 and Run 2 data-taking periods at the LHC. In pp collision, each event is confronted with pileup and additional radiation. These factors substantially limit the measurement of the JER with the transverse momentum imbalance method. Their influence becomes even more challenging with increasing luminosity and center-of-mass energies, a trend which comes inevitably with future phases of the LHC such as the HL-LHC. The impact is already evident in Run 2 and Run 3 and dedicated studies are needed to reduce their contribution. In the scope of this thesis, further investigation and refinement of the transverse momentum imbalance method are undertaken to improve its performance limitations. Additionally, an introduction of a new technique is given, which is expected to be robust with respect to pileup.

### 6.8.1 Limitations of Transverse Momentum Imbalance

The transverse momentum imbalance method faces a significant limitation due to corrections from additional jet activity. As discussed in Section 6.4.2, the requirement of $\alpha_{\mathrm{max}}$ leads to a reduction in the number of events, particularly in low-$p_{\mathrm{T}}$ regions.
Figure 6.12 illustrates the impact of $\alpha_{\mathrm{max}}$ constraints on dijet events. It shows the relative number of events for various $\alpha_{\mathrm{max}}$ thresholds as a function of $p_{\mathrm{T}}^{\mathrm{ave}}$ with respect to no constraints on the third jet ($\alpha_{\mathrm{max}}$ =1). Here, the histograms overlap as the $\alpha_{\mathrm{max}}$ bins are inclusive. The contribution of events with low $\alpha_{\mathrm{max}}$ values increases in higher $p_{\mathrm{T}}$ ranges above $p_{\mathrm{T}}^{\mathrm{jet}}$ >150 GeV.

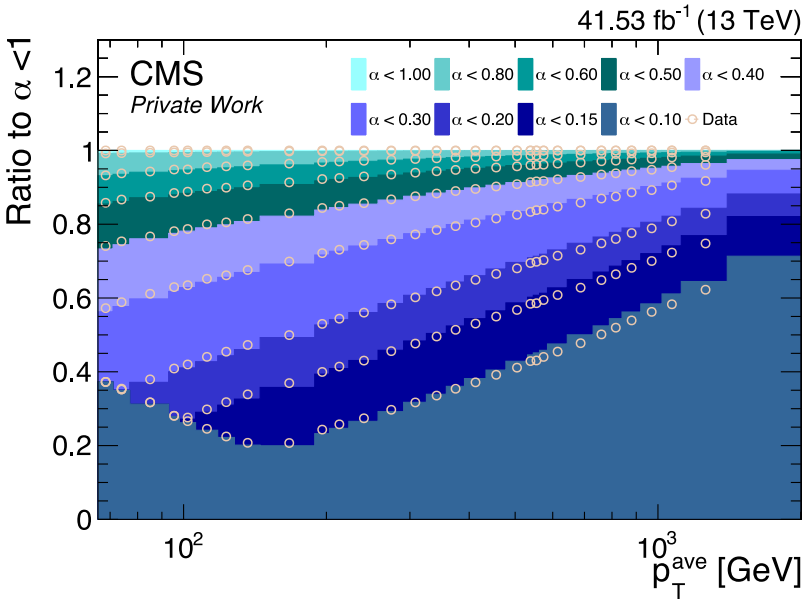


**Figure 6.12:** Relative number of events per $\alpha_{\text{max}}$ threshold compared to no constraints on the third jet ($\alpha_{\text{max}} = 1$) for each $p_{\text{T}}^{\text{ave}}$ bin. Data (circles) with a certain $\alpha_{\text{max}}$ threshold aligns with the corresponding threshold in simulation. The various $\alpha_{\text{max}}$ thresholds are inclusive, resulting in overlapping histograms.

This behavior is expected because the significance of higher-order QCD corrections is diminished with increasing $p_{\text{T}}$ for hard-scattering processes. Below $p_{\text{T}}^{\text{ave}} < 150\,\text{GeV}$, a change in the trend is observed, where the contribution from low $\alpha_{\text{max}}$ threshold increases for both data and simulation. For $\alpha_{\text{max}} < 0.1$ and $p_{\text{T}}^{\text{ave}} < 150\,\text{GeV}$, only events with a third jet below 15 GeV are considered, which falls below the $p_{\text{T}}$ thresholds considered for jets in this analysis. Contributions below this threshold arise from events with an assumed ideal dijet typology or pileup jets which feature a larger $p_{\text{T}}$ than the third jet from radiation in the dijet events. While no additional events are selected below $p_{\text{T}}^{\text{ave}} < 150\,\text{GeV}$, the contribution of $\alpha_{\text{max}} < 0.1$ rises due to the reduction of the overall event yield for higher $\alpha_{\text{max}}$ thresholds.

Another important aspect of the JER SFs derivation is the compatibility between data and simulations. As detailed in Section 6.3.1, the pileup profile in simulations is reweighted to match the average pileup profile in data. Therefore, it is essential to consider prescales in the data, such that the pileup profile in a data subset collected with prescaled triggers is represented by the average pileup profile in data. Distributions indicative to pileup levels in an event, such as the average energy density $\rho$, are sensitive to such reweighting in the simulation and data.

The mean $\rho$ value as a function of the $p_{\text{T}}^{\text{ave}}$ is shown Figure 6.13, comparing different $\alpha_{\text{max}}$ thresholds. For AK4CHS jets (left), the trend between data and simulation is consistent down to a threshold of $\alpha_{\text{max}} = 0.3$. However, deviations occur for increasing $p_{\text{T}}^{\text{ave}}$ bins with decreasing $\alpha_{\text{max}}$ thresholds. The onset of these deviations aligns with the threshold at which events are rejected if the $p_{\text{T}}$ of the third jet falls below the $p_{\text{T}}$ threshold of 15 GeV. While the mean $\rho$ values in simulations shifts towards lower values, the trend in data increases. This discrep-

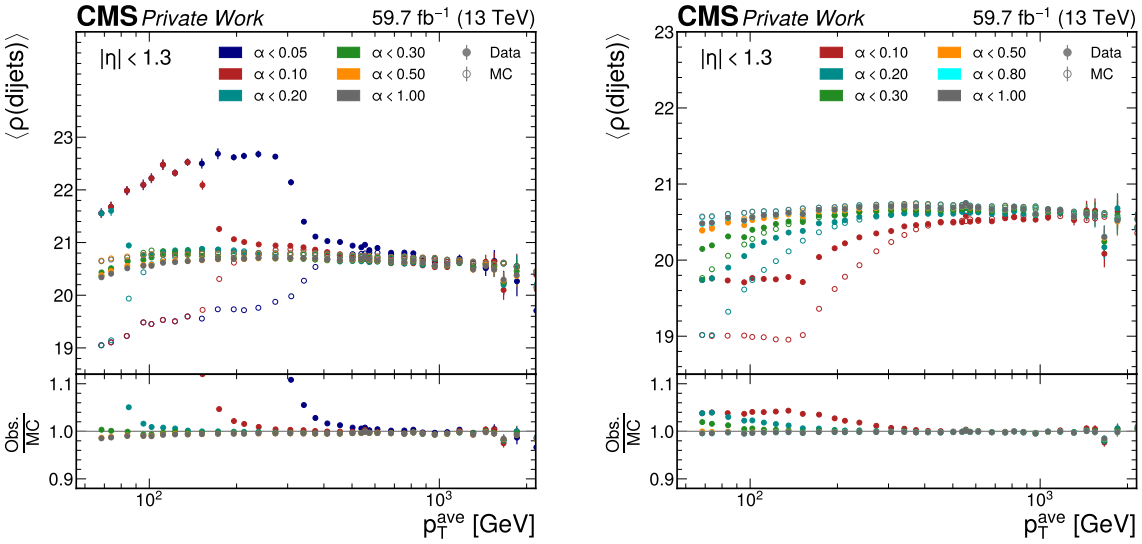


**Figure 6.13:** Mean value for the energy density $\rho$ distribution for different $\alpha_{max}$ and $p_T^{ave}$ bins in dijet events clustered with AK4CHS (left) and AK4Puppi (right) jets. Shown are simulation (open circle) and data with applied prescale factors (full circles).

ancy might be due to pileup jets that are identified as the third jet, thereby increasing the $\rho$ distribution in the data. Furthermore, if the third jet is not selected from the hard-scattering process, the $p_T$ imbalance in dijet events is wrongfully determined. Unlike in Run 2, jets in Run 3 are preferably clustered using the PUPPI algorithm. As discussed in Section 4.2, the usage of PUPPI more effectively reduces pileup contributions compared to CHS. Although L1 corrections account for pileup in CHS jets by scaling the four momentum of the entire jet rather than just the pileup contribution, discrepancies still arise. The trend for the mean $\rho$ values as a function of the $p_T^{ave}$ for PUPPI jets is illustrated in Figure 6.13 (right). Here, the trend in data aligns well with simulation for higher $\alpha_{max}$ thresholds. In contrast to AK4CHS jets, the trend in the mean $\rho$ values in data decreases for lower $\alpha_{max}$ thresholds. The decreasing trend in data occurs at lower $p_T$ ranges for the same $\alpha_{max}$ threshold relative to simulations. This earlier decline in simulations may arise from the inherent structure in simulation itself. Simulations are produced at LO with additional jet activity modeled in the parton shower, which reduces the precision of the modeling of the radiation. Consequently, simulations are more sensitive to the additional $\alpha_{max}$ thresholds, undermining the compatibility to data. The changes in the trend of $\langle\rho\rangle(p_T^{ave})$ for low-$p_T$ ranges arise from the $\alpha_{max}$ thresholds. Events in the low-$p_T$ and $\alpha$ region are not considered in this analysis, as they feature third jets below the minimum $p_T$ threshold for jets.

Section 6.4.2 discussed the linear dependence of the asymmetry width from the $\alpha_{max}$ thresholds. The challenges in the low $p_T$ region are covered using three different fits, additionally removing the first and last bin considered in the bin. However, it is not clear how the dependence changes for increasing $\alpha_{max}$ thresholds. A lower $\alpha_{max}$ reflects scenarios closely resembling ideal di-

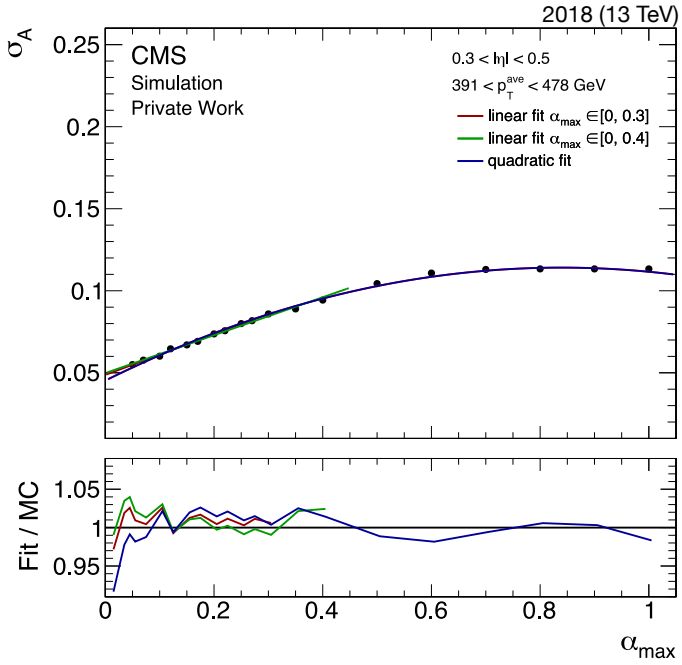


**Figure 6.14:** Width of the normalized asymmetry distribution in simulation as a function of $\alpha_{\text{max}}$. The $\alpha$ extrapolation $\sigma_A(\alpha \to 0)$ is tested using a second-degree polynomial function (blue) and a linear hypothesis up to $\alpha_{\text{max}} = 0.3$ (red) and 0.4 (green). The lower panel shows the ratio of the fit functions to the asymmetry widths.

jet events, thereby maintaining a more balanced $p_{\text{T}}$ between the two leading jets. Conversely, as $\alpha_{\text{max}}$ increases, dijet events feature higher energetic radiation relative to the to $p_{\text{T}}$ leading jets featuring a more complex event topology. Figure 6.14 illustrates the impact of increasing thresholds of $\alpha_{\text{max}}$ on the asymmetry width for the full coverage in $\alpha$. Two distinct trends are evident: a linear dependence when $\alpha_{\text{max}} \lesssim 0.5$ and a plateau for $\alpha_{\text{max}} \gtrsim 0.5$. The linear dependence for $\sigma_{\text{A}}(\alpha_{\text{max}} < 0.05)$ can only be assumed based on the empirical choice of the linear $\alpha$ extrapolation for $\alpha_{\text{max}} < 0.3$. It is not yet feasible to confirm the dependence as low $\alpha_{\text{max}}$ regions are strongly constrained based on the $p_{\text{T}}$ thresholds for jets with 15 GeV and pileup. While a reduction in the $p_{\text{T}}$ threshold for jets is possible, as it is considered in the systematic uncertainties, the reconstruction efficiency of jets decreases, and pileup remains a limiting factor. By design, the criteria for dijet selection are intended to exclude events with significant high-energy radiation, hence no further events contribute to the asymmetry distribution. As a result, the width of the asymmetry distribution remains constant since no additional events are taken into account. Furthermore, the additional event yield diminishes for increasing $\alpha_{\text{max}}$ threshold for $\alpha \gtrsim 0.2$. The transition from the linear dependence to a constant trend is not defined and dependent on the binning. Introducing three separate fits in $\sigma_A(\alpha \to 0)$ as discussed in Section. 6.4.2 accounts for the uncertainty of the changing trend. When $\sigma_A(\alpha_{\text{max}} = 0.3)$ aligns with the linear hypotheses over the full $\alpha_{\text{max}}$ range, the removal of the this point does not have an impact on the extrapolation. On the contrary, if the flattening trend already arises for $\alpha_{\text{max}} = 0.3$, the linear fit is pulled to higher values for $\sigma_A(\alpha \to 0)$, resulting in an increased

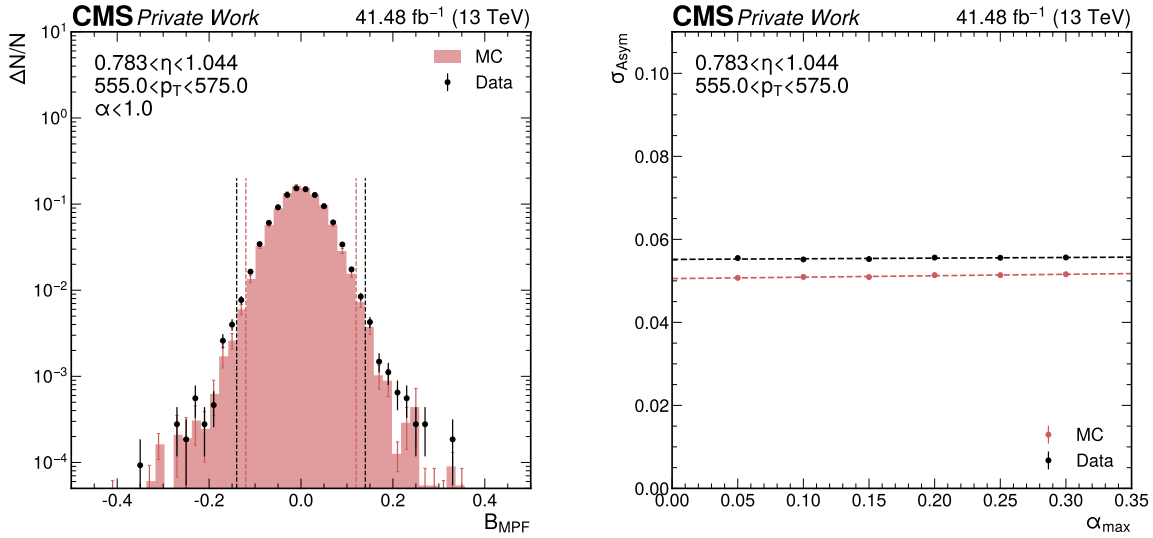


**Figure 6.15:** Response distribution from the MPF method in dijet events (left) for simulations (red histogram) and the data (black markers). The vertical lines represent the statistical uncertainty. The cutoff for the non-Gaussian tails are indicated by (dashed lines) and the width of the distribution is extracted from the truncated RMS. The width of the MPF response as a function of $\alpha_{\text{max}}$ is shown on the right. The trend in data (black) and simulations (red) is described by a linear function (dashed lines).

JER. Besides the three fits, other hypotheses have been tested to perform the $\alpha$ extrapolation including the full range, but no function described the underlying trend.
In conclusion, the transverse momentum imbalance method in dijet events comes with many challenges involving the correction for additional jet activity. Consequently, the derivation of JER SFs can be improved utilizing alternative methods which are less dependent on $\alpha$. One candidate is the MPF method, utilized for the L2Residual corrections (see Section 4.4), which already shows robustness with respect to additional jet activity. However, it is not yet explored that the MPF method also exhibits resilience to pileup effects. To address these requirements, the next section will introduce an extension to the MPF method.

### 6.8.2 Missing Transverse Momentum Projection Fraction

In the MPF method, the missing transverse momentum $p_{\text{T}}^{\text{miss}}$ is projected onto a reference object, considering the response of all hadronic activity recoiling against the reference object. For dijet events, the reference object is commonly chosen to be the reference jet in the central region of the detector with $|\eta| < 1.3$. The response distribution of the MPF method obtained from the projection is denoted as $B$ and defined as

$$B = \frac{\vec{p}_T^{\,\text{miss}} \cdot \left(\vec{p}_{\text{T}}^{\,\text{ref}} / p_{\text{T}}^{\text{ref}}\right)}{2 \cdot p_{\text{T}}^{\text{ave}}}. \tag{6.22}$$

Here, $p_{\text{T}}^{\text{ref}}$ represents the transverse momentum of the reference jet and $p_{\text{T}}^{\text{ave}}$ the average trans-

verse momentum of the two $p_{\mathrm{T}}$-leading jets in dijet events. Studies for the residual corrections have shown that the mean value of $B$ is less sensitive to $\alpha$ compared to the asymmetry distribution from the transverse momentum imbalance method [119]. The same approach is now explored for deriving the JER in data and simulations by measuring the width of $B$.
The distribution of $B$ derived in dijet events is shown in Figure 6.15 (left). A similar structure to the asymmetry distribution is evident, featuring a Gaussian core and non-Gaussian tails. Following the procedure of the transverse momentum imbalance method, the non-Gaussian tails are mitigated by removing the quantiles at 1.5 % on each side. The width then determined with the truncated RMS. In Figure 6.15 (right) the width of $B$ is shown as a function of $\alpha_{\mathrm{max}}$, where no dependence is observed. As discussed in Section 4.4, the MPF method incorporates the response of hadronic activity in the hard-scattering process. Additionally, contributions from pileup, ISR and FSR, as well as miscalibrations affect $p_{\mathrm{T}}^{\mathrm{miss}}$. Therefore, the width of the MPF response can be parameterized as

$$\sigma_B = \sigma_{\mathrm{JER}} \oplus \sigma_{\mathrm{ISR}} \oplus \sigma_{\mathrm{FSR}} \oplus \sigma_{\mathrm{pileup}}, \tag{6.23}$$

where $\sigma_{\mathrm{JER}}$ represents the JER from the reference jet, $\sigma_{\mathrm{pileup}}$ the width of the response from pileup, and $\sigma_{\mathrm{ISR/FSR}}$ the width of the response from the ISR and FSR. To isolate the measurement of $\sigma_{\mathrm{JER}}$, the widths of the responses from the other contributions must be determined separately. The MPF method can be extended by introducing an orthogonal axis relative to the reference axis. It is expected that the contribution of the reference jet to the projection of $p_{\mathrm{T}}^{\mathrm{miss}}$ onto the orthogonal axis vanishes. Thus, newly obtain response distribution $B_{\mathrm{x}}$ can be parameterized as

$$\sigma_{B_{\mathrm{x}}} = \sigma_{\mathrm{ISR}} \oplus \sigma_{\mathrm{FSR}} \oplus \sigma_{\mathrm{pileup}}. \tag{6.24}$$

By subtracting $B_x$ from $B$ in quadrature, all contributions except for $\sigma_{\mathrm{JER}}$ are canceled out, resulting in

$$\sigma_{\mathrm{JER}} = \sqrt{\sigma_B^2 - \sigma_{B_x}^2}. \tag{6.25}$$

Such relation holds in any given $p_{\mathrm{T}}$ and $|\eta|$ bin, allowing to extract a multidimensional resolution. Furthermore, this approach is expected to not rely on the correction for additional jet activity, similarly to the MPF method. Thus, the available statistics can be significantly improved. In the low $p_{\mathrm{T}}$ region, pileup becomes more dominant and thus the positioning of the reference axis is essential to effectively remove the contribution.
The extension of the MPF method is currently under development in the CMS groups at the University of Hamburg and the University of Helsinki. First results are obtained for preliminary calibrations in the Run 3 data-taking period [2] as shown in Section 6.6. Further developments in both CMS groups are ongoing. The studies performed at the University of Hamburg are predominantly conducted in the scope of another PhD project [167].

## 6.9 Complementary Methods

The transverse momentum imbalance method for dijet events is utilized for deriving the JER SFs up to the high-forward region $|\eta| < 5.2$. These events provide reliable measurements down to a threshold of $p_{\mathrm{T}}^{\mathrm{ave}} = 200\,\mathrm{GeV}$ as detailed in Section 6.8.1. Dijet events are the only final state so far that can perform JER measurements in higher $p_{\mathrm{T}}$ regions. Challenges arise from the significant reduction in the number of dijet events in low-$p_{\mathrm{T}}$ regions due to $\alpha$-extrapolation and pileup. Given that many CMS analyses focus on jets below this threshold, precise JER measurements for that $p_{\mathrm{T}}$ region become essential. Consequently, complementary methods are employed to extend the $p_{\mathrm{T}}$ range for the JER SFs determination [162].

The low-$p_{\mathrm{T}}$ region is extended using Z/$\gamma$+jets and the random cone method. For Z/$\gamma$+jets, the jet is balanced against the transverse momentum of a well-calibrated Z boson or photon $\gamma$. The Z boson decay $\mathrm{Z} \to \ell\ell$ benefits from precise calibrations due to the performance of the ECAL and muon system. The transverse momentum imbalance method for Z+jets allows for the determination of JER SFs in $p_{\mathrm{T}}$ ranges from 40 GeV up to 150 GeV. Beyond this range, event yields diminish significantly. Processes comprising $\gamma$+jets serve as a cross check for transverse momentum imbalance method of dijet events up to $|\eta| = 2.5$.

The dominant contribution in low-$p_{\mathrm{T}}$ regions to the JER measurement is described by the noise term $N$ in Equation 6.14. This term mainly encompasses the electronic noise and pileup, both of which can be estimated in simulations. Electronic noise is evaluated using samples with no interaction measured during a bunch crossing. Contributions from pileup can be constrained using the Random Cone method, as discussed in Section 4.4.1. This method involves measuring the JER for jets with and without simulated pileup. In data, the contribution from pileup and be determined with zero-biased triggers. The determination of the noise term effectively extends the range of the JER measurements to $p_{\mathrm{T}}$ regions below 40 GeV.

Continued efforts aim at improving the precision and accuracy of JER SFs with several complementary methods. Combining the measurement of the JER in QCD dijet events and Z/$\gamma$+jets, as well as using the random cone method ensures robustness across the entire jet-$p_{\mathrm{T}}$ spectrum.

# Chapter 7

# Measurement of the Jet Mass and Top Quark Mass

In this chapter the measurement of the differential $t\bar{t}$ cross section as a function of jet mass in hadronic decays of boosted top quarks is discussed. The sensitivity of the jet mass to the top quark mass allows for its extraction. Unlike top quark mass measurements at threshold production, the trajectory from the decay products of both top quark decays do not overlap. Consequently, both reconstructed top quark decays can be considered isolated from each other, providing a complementary method to measure the top quark mass. Additionally, the differential $t\bar{t}$ production cross section can be predicted from analytic calculations. Comparisons to calculations from first principle allow for the extraction of $m_{\text{top}}$ in a well-defined mass scheme, thus avoiding ambiguities in the mass definition in the event generator. However, the phase space in which these calculations are feasible is not yet accessible in the presented analysis. Consequently, the measurement extracts $m_{\text{top}}^{\text{MC}}$ until a common phase-space for the experimental and theoretical approaches is reached.

Previous iterations of this analysis demonstrated the potential to extract the top quark mass in the boosted regime. First, a precision of $\Delta m_{\text{top}} = 9.0\,\text{GeV}$ [17, 168] was achieved and increased to $\Delta m_{\text{top}} = 2.5\,\text{GeV}$ [18, 122] with a refined reconstruction approach. In the latest iteration, the precision is limited by uncertainties arising from the calibration of the jet mass scale and the modeling of FSR. Dedicated measurements are necessary to constrain these uncertainties to further improve the precision of the jet mass measurement and represent a key aspect in this thesis. The measurements presented in this chapter provide vital insights into jet substructure variables and the modeling in event generators. First studies have been conducted in Ref. [5] and have been substantially extended in this thesis to perform a measurement of the jet mass and the top quark mass.

An overall strategy to measure $m_{\text{top}}$ in the kinematic phase space of boosted top quarks and to improve the JMS and the modeling of the FSR is outlined in Section 7.1. The datasets and simulation utilized in this analysis are listed in Section 7.2 followed by the description of the event selection at both particle and detector level in Section 7.3, including the object definition and

calibration. The dedicated calibration of the jet mass scale is detailed in Section 7.4. Descriptions of the performance at the detector level are summarized in Section 7.5. Improvements in the modeling of the FSR are discussed in Section 7.6. The measurement of the differential $\mathrm{t\bar{t}}$ production cross section is elaborated on in Section 7.7. This section contains the unfolding setup up, taken from the previous measurement, the treatment of uncertainties and the final result for the differential cross section as a function of $m_{\mathrm{jet}}$. The results of this analysis have been published in Ref. [6]. Finally, studies towards an optimized event reconstruction at higher energy regimes and a new machine-learning based unfolding procedure are introduced in Section 7.9.

## 7.1 Analysis Strategy

In the boosted regime, the top quark decay products have a small spatial distance and can be reconstructed within a single jet. Consequently, both top quark decays from $\mathrm{t\bar{t}}$ events can be treated isolated and independent from each other, reducing the dependence on color connections. This characteristic is one reason that facilitates analytic calculations in the boosted regime. To achieve sensitivity of the jet mass to $m_{\mathrm{top}}$, it is essential to cluster all decay products of the hadronic top quark decay into one jet. An illustration of the reconstruction of the $\ell$+jets channel in boosted $\mathrm{t\bar{t}}$ events is shown in Figure 7.1. The jet mass is unfolded to particle level to obtain the differential $\mathrm{t\bar{t}}$ production cross section as a function of $m_{\mathrm{jet}}$, which can be used to extract $m_{\mathrm{top}}$.

In the previous measurement of the jet mass from the CMSCollaboration [6], two dominant uncertainties were identified that significantly limit the precision of the extraction of $m_{\mathrm{top}}$. These uncertainties are now constrained with dedicated measurements prior to the unfolding. The largest experimental uncertainty with $\Delta m_{\mathrm{top}} = 1.5\,\mathrm{GeV}$, arises from the calibration of the jet mass scale (JMS) due to the propagation of the JES to the jet mass. In this thesis, dedicated measurements are performed to separately evaluate the contributions of the JES and the JMS.

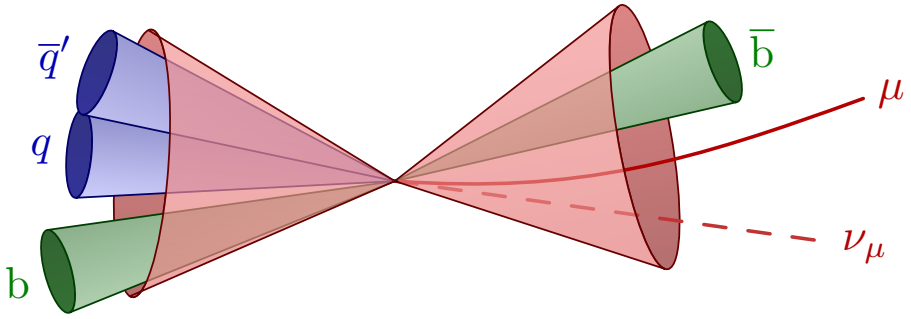


**Figure 7.1:** Sketch of the decay of boosted $\mathrm{t\bar{t}}$ events, where all decay products are reconstructed in one large-$R$ jet (red). Both decay channels feature a b jet (green). In addition, the hadronic decay comprises the light flavor quarks from the W boson decay (blue) and the leptonic decay contains the muon (solid line) and the neutrino (dashed line).

This approach ensures that the JES exclusively influences the transverse momentum ($p_T$) of the jets, while the JMS affects only the jet mass. The JMS is calibrated by exploiting the jet mass in hadronic W boson decays, which is sensitive to the JES but not to $m_{top}$. The W boson mass is reconstructed using XCone subjets identified with light flavor quarks originating from the hadronic W boson decay. The dominant model uncertainty in the previous measurement was identified with the modeling of the FSR with $\Delta m_{top} = 1.2\,\text{GeV}$. Jets reconstructing the hadronic top quark decay are particularly sensitive to additional radiation, as more energy is deposited in the jets. Therefore, the impact of the modeling of the FSR can be studied by utilising the $N$-subjettiness ratio $\tau_{32}$, which is a measure of the energy distribution within the jet. Furthermore, this measurement extends the previous measurement to the full Run 2 data-taking period including the years 2016 to 2018 at $\sqrt{s} = 13\,\text{TeV}$.

## 7.2 Data and Simulations

This analysis uses data from pp collisions at $\sqrt{s} = 13\,\text{TeV}$, recorded by the CMS detector during the Run 2 data-taking period, including the years 2016, 2017 and 2018. The recorded luminosities are $35.9\,\text{fb}^{-1}$, $41.5\,\text{fb}^{-1}$ and $59.7\,\text{fb}^{-1}$ for each respective year, culminating in a total integrated luminosity of $138\,\text{fb}^{-1}$. Data segments where the accelerator complex or detector malfunctioned are identified and excluded from the analysis.

For each year, various processes are simulated using event generators, incorporating the corresponding experimental setup. Simulations of SM processes are employed to fully characterize the data within the targeted phase space. The signal process in this measurement is the $\mathrm{t\bar{t}}$ production, which is generated at NLO using POWHEG. The total cross section is scaled to 833.9 pb, based on predictions with NNLO precision in QCD obtained from TOP++2.0 [66]. Background processes are selected based on their similarity to the final state of the $\ell$+jets channel from $\mathrm{t\bar{t}}$ events. The two largest backgrounds, single top quark production and W+jets processes, are both generated at NLO, with POWHEG used for single top quark events and MADGRAPH for W+jets. The $s$-channel of single top quark production is generated using MADGRAPH5_aMC@NLO. Additionally, MADGRAPH is used for Z+jets production at LO, normalized to the cross section obtained with NLO calculations [169]. Production of two heavy gauge bosons in the final state and QCD multijet events are generated at LO using PYTHIA. The hadronization and parton showers across all processes are also simulated using PYTHIA. Matrix element calculations in MADGRAPH are matched to parton showers using FXFX [170] for NLO and MLM [171] for LO processes.

The tuning of generators, which consists of a set of physics parameters in the simulations, is of particular interest in this analysis. Effects such as the parton shower heavily depend on these tunes, which for example comprise the strength of the effective strong coupling to steer the ISR and FSR or changes in $h_{damp}$ (see Section 2.3). In 2016, the $\mathrm{t\bar{t}}$ process is generated with the CUETP8M2T4 tune [56], while all background processes utilize the CUETP8M1 tune [172].

For 2017 and 2018, the newly introduced CP5 tune [56] is applied, incorporating modifications to the $h_{\text{damp}}$ parameter and the effective strong coupling for the ISR and FSR. Discrepancies between simulations utilizing the CP5 tune and observations in substructure variables are a key discussion point in Section 7.6.

## 7.3 Event Selection and Reconstruction

The event selection aims to suppress non-$\mathrm{t\bar{t}}$ events and select events with decays of boosted top quarks. The extraction of $m_{\text{top}}$ is performed using the differential $\mathrm{t\bar{t}}$ production cross section, which is defined on particle level. Therefore, data must be corrected for detector effects using an unfolding procedure. The kinematic region of the measurement is defined on particle level and chosen such that a similar phase space is available at the detector level. The selection criteria have been adopted from the previous iteration of this analysis as detailed in Ref.[17, 18]. The calibration of the JMS and the modeling of the FSR is performed using the same data samples and selection. Potential biases arising from the multiple use of the data samples are discussed in the corresponding sections.

### 7.3.1 Particle Level

Particle level studies are conducted exclusively in the $\ell$+jets channel of the $\mathrm{t\bar{t}}$ process. Since a single lepton $\ell$ is expected, only events containing exactly one $\ell$ are considered. The lepton is either a muon $\mu$ or an electron $e$, while the $\tau$ decay channel is treated as background. The selected lepton must fulfill $p_{\mathrm{T}} > 60\,\mathrm{GeV}$, which is motivated by the detector level selection relying on triggers targeting high-$p_{\mathrm{T}}$ muons.

Events are reconstructed using the two-step clustering procedure with XCone, detailed in Section 5.3. First, two large radius (large-$R$) jets with $R = 1.2$ are clustered to fully capture both top quark decays. Next, constituents of each jet are further clustered with three subjets and $R = 0.4$, targeting each decay product individually. The large-$R$ jet closest to the lepton is assigned to the leptonic top quark decay, while the other jet is associated with the hadronic top quark decay. The hadronic XCone jet is constructed from the invariant mass of all three subjets from the hadronic top quark decay. The final hadronic XCone jet must have $p_{\mathrm{T}} > 400\,\mathrm{GeV}$ and each subjet is required to fulfill $p_{\mathrm{T}} > 30\,\mathrm{GeV}$ and $|\eta| < 2.4$. The minimal $p_{\mathrm{T}}$ requirement ensures the selection of decays from boosted top quarks, while the $|\eta|$ criterion is driven by the tracker coverage at the detector level. Furthermore, the mass of the hadronic XCone jet must exceed the invariant mass of the combination of the leptonic XCone jet and the lepton. This condition ensures to select fully merged top quark decays and without introducing a bias on $m_{\text{jet}}$. Properly reconstructed measurements should comply with this condition since the neutrino remains undetected.

The jet assigned to the leptonic top quark decay is expected to contain only the b jet and the

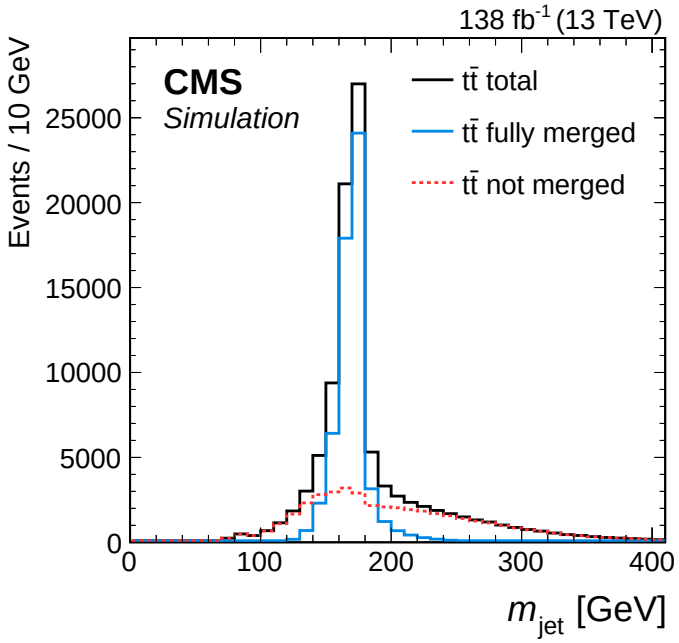


**Figure 7.2:** Jet mass distribution at the particle level after selecting hadronic top quark events. The total event yield (black) is shown for the combined dataset from the Run 2 data-taking period. The distribution is compared to scenarios of fully merged top quark decays (blue) and events not clustering all decay products(red). Published in Ref. [6].

lepton, despite being clustered with three subjets. It was confirmed that this approach does not change the measurement compared to the more natural choice of two subjets for the second jet [18]. The second jet, defined as the sum of the three subjets after removing the overlapping lepton, must have at least $p_{\mathrm{T}} = 10\,\mathrm{GeV}$ to ensure a proper reconstruction of the leptonic top quark decay.

The jet mass distribution at the particle level is illustrated in Figure 7.2. A sharp peak close to $m_{\mathrm{top}}$ is evident, predominantly featuring events in the peak region where all decay products are clustered into the jet, referred to as fully merged $\mathrm{t\bar{t}}$ events. Conversely, XCone jets not clustering all decay products of the hadronic top quark decay are called not merge $\mathrm{t\bar{t}}$ events.

### 7.3.2 Detector Level Selection

The selection at the detector level is driven by the phase space defined at the particle level. This ensures small migration into and out of the measured phase space in the unfolding procedure. Beyond selecting boosted top quark typologies from $\mathrm{t\bar{t}}$ events, the baseline selection aims to suppress non-$\mathrm{t\bar{t}}$ backgrounds.

A proper event selection and reconstruction is ensured with a low misidentification rate for leptons. Different trigger strategies are employed for the muon and electron channels in each year at the HLT level. Events containing one muon are selected using a single muon trigger with a threshold of $p_{\mathrm{T}} > 50\,\mathrm{GeV}$. In 2016, trigger for tracker muons with $p_{\mathrm{T}} > 50\,\mathrm{GeV}$ are additionally used. For the electron channel, electron and photon triggers are utilized in combination with iso-

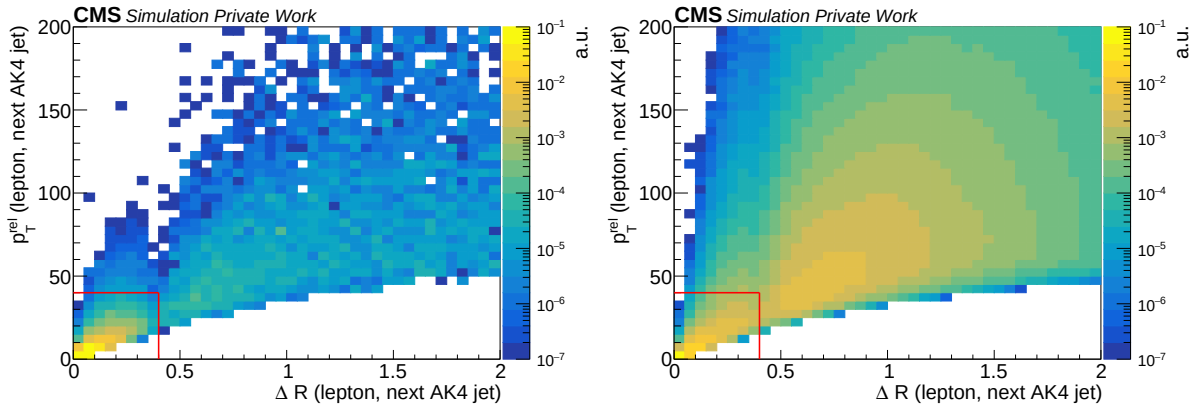


**Figure 7.3:** Event yield normalized to unit area in the $p_T^{rel}$-$\Delta R$-plane for the lepton with respect to the next AK4CHS jet for QCD (left) and $t\bar{t}$ (right) events in 2018 and the $\mu$+jets channel. The red window at lower values indicate the cut performed in the plane to reduce the QCD background.

lation criteria. Isolated electron candidates with $p_T < 120\,\text{GeV}$ are selected using triggers with thresholds of $p_T > 27$, 35, and 32 GeV for 2016, 2017, and 2018, respectively. For electrons with $p_T > 120\,\text{GeV}$, non-isolated electron triggers with $p_T > 115\,\text{GeV}$ are employed across all years. Additionally, photon triggers with $p_T > 175\,\text{GeV}$ (2016) and $p_T > 200\,\text{GeV}$ (2017 and 2018) are used to ensure high efficiencies at large electron $p_T$. Events in the simulation are weighted to match the trigger efficiency observed in the data. These weights are measured for the electron triggers in this thesis for all three years and are presented in the Appendix A.

Lepton candidates must meet specific quality criteria to be considered a lepton in this analysis. Both, muons and electrons must pass the a set of quality criteria and have $p_T > 55\,\text{GeV}$ and $|\eta| < 2.4$. The $p_T$ criterion is motivated by the trigger thresholds, ensuring selection at the trigger efficiency plateau. Electrons with $1.4 < |\eta| < 1.57$ are rejected due to the detector geometry. Events containing more than one lepton are rejected, implying that only one electron or muon is considered in the analysis. To ensure leptons originate from top quark decays and to suppress those produced within a jet, a two-dimensional isolation criterion is used. For the baseline selection a collection of AK4 jets with CHS mitigation are used. The distance between the lepton and the nearest AK4CHS jet must be $\Delta R(\ell, \text{next AK4 jet}) > 0.4$ or the relative transverse momentum $p_T^{rel}(\ell, \text{next AK4 jet}) > 40\,\text{GeV}$. The latter is defined as $p_T^{rel}(a,b) = |\vec{p}_a \times \vec{p}_b|/|\vec{p}_b|$. All AK4CHS jets with $p_T > 15\,\text{GeV}$ are considered for the two-dimensional isolation criterion. This isolation criterion effectively suppresses QCD multijet events, where muons are commonly part of hadron decays within the jet. For electrons with $p_T < 120\,\text{GeV}$, only triggers with an isolation criterion are available. Consequently, the two-dimensional isolation criteria is only applied to electrons with $p_T > 120\,\text{GeV}$. Figure 7.3 illustrates the two-dimensional cut for QCD multijet events (left) and $t\bar{t}$ events (right) in the $\mu$+jets for the year 2018, and is consistent for all three years. In QCD events, the majority of the selected events are within the limits set for the two-dimensional cut, whereas $t\bar{t}$ events are spread across the entire $p_T^{rel}$-$\Delta R$-plane. Data-to-

simulation scale factors, which are dependent on the lepton's $p_T$ and $\eta$, are applied to simulated events to adjust the efficiency of the lepton ID to that observed in the data.
The final state of the $\ell$+jets channel includes a neutrino, which cannot be detected. Therefore, a missing transverse momentum requirement of $p_T^{miss} > 50\,GeV$ is applied. This requirement suppresses contributions from Z+jets, the production of two heavy gauge boson and QCD multijet events. Two major backgrounds arise from W+jets and singly produced top quarks. While the final state of the single top quark production is similar to that of $t\bar{t}$, W+jets events are expected to lack b quarks, whereas $t\bar{t}$ events contain two. To identify b jets, the DEEPJET algorithm [117] is used. At least one AK4CHS jet must have a b-tag discriminator of 0.7221, 0.7476, or 0.7264 for the years 2016, 2017 and 2018, respectively. The efficiency in $t\bar{t}$ simulations is adjusted to match data using scale factors dependent on the jet's $\eta$, $p_T$, and b-tag score and are centrally provided by the CMS Collaboration. Adjusting the b-tagging efficiency in the simulation using these scale factors can alter the jet multiplicity and $H_T$ distribution. Although this change is small and its impact on the measurement is negligible, scale factors based on jet multiplicity are derived to restore the shapes to before b-tagging efficiency scale factors are applied. Events in 2018 with an electron or jet in $\eta < 1.3$ and $-1.57 < \phi < -0.87$ in the data are rejected due to the HCAL failure in that area (see Section 6.3). For simulations, events with electrons or jets in that region are randomly rejected based on the fraction of the affected luminosity in the data to the full dataset.
The baseline selection primarily identifies events containing the $\ell$+jets channel of the $t\bar{t}$ process. The distributions for several kinematic observables of objects used for the baseline selection are shown for the year 2016, 2017 and 2018 in Figure 7.4, 7.5, and 7.6, respectively. While all years exhibit good data to MC agreement, larger discrepancies are evident for increasing $p_T$ of the AK4 jets and $p_T^{miss}$. This trend has been observed in the previous analyses [17, 18] and originates from the modeling of the top quark $p_T$ in simulations [69]. For a phase space of the XCone jet with $p_T > 400\,GeV$, this factor is constant and accounted for in the $p_T$-differential unfolding (see Section 7.7.1).
The high purity of $t\bar{t}$ events allows for the reconstruction of the two-step clustering with the XCone algorithm at detector level. The XCone algorithm clusters all particles that are not rejected by the CHS pileup mitigation algorithm [94]. Hadronic decays of boosted top quarks are selected by only considering events where the jet assigned to the hadronic decay has $p_T > 400\,GeV$. Additionally, the subjets from the hadronic XCone jet must have $p_T > 30\,GeV$ and $|\eta| < 2.4$. Moreover, the mass of the hadronic XCone jet must exceed the invariant mass of the leptonic jet and the lepton to suppress unmerged $t\bar{t}$ events. The $p_T$ distributions for hadronic XCone jet and all its subjets are displayed in Figure 7.7, showing a good agreement between data and simulation. The JEC derived centrally by the CMS Collaboration and the additional XCone corrections (see Section 4.4) are applied to all XCone subjets.

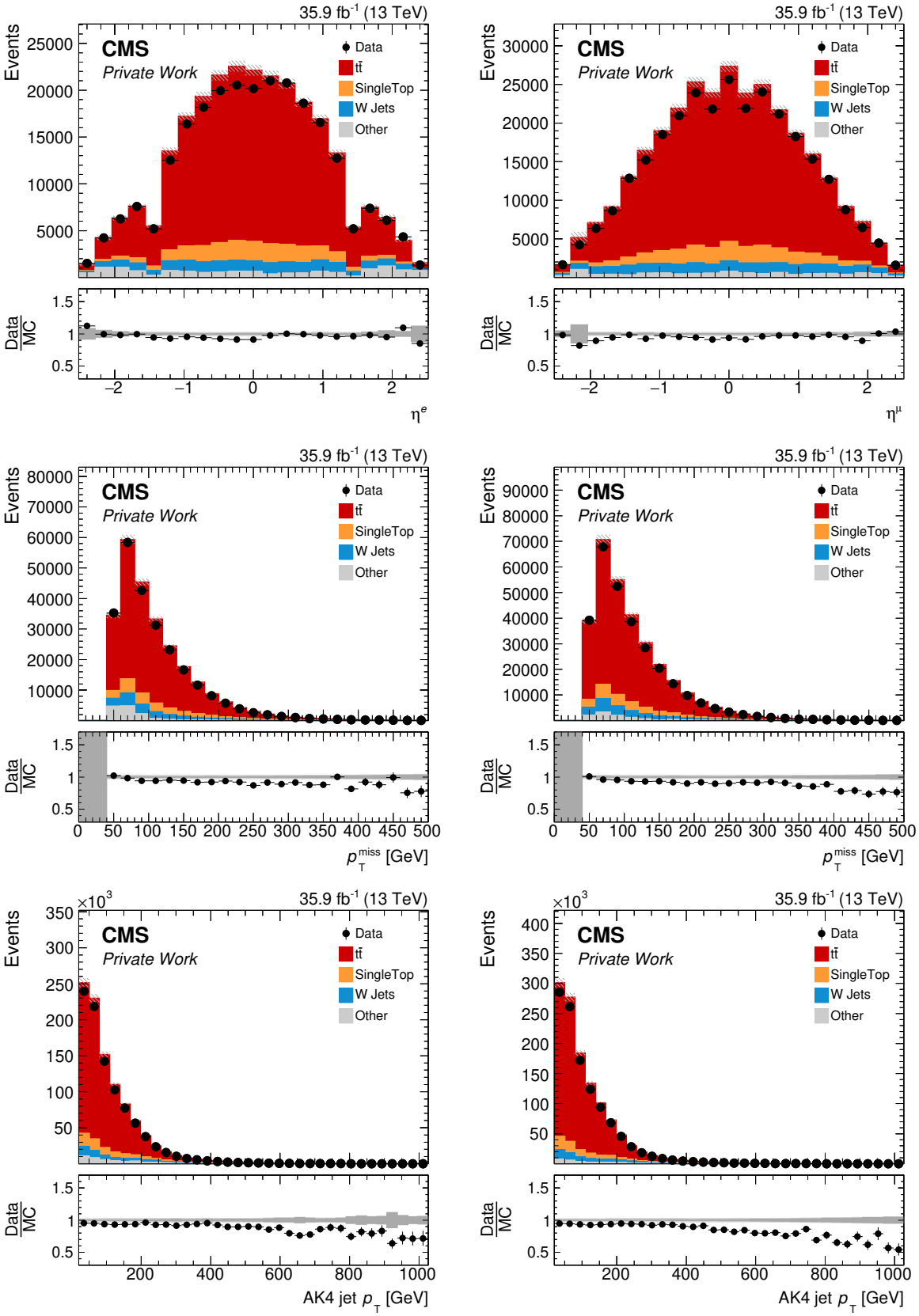


**Figure 7.4:** Distributions of the lepton $\eta$ (upper), $p_{\mathrm{T}}^{\mathrm{miss}}$ (middle) and the AK4CHS jets $p_{\mathrm{T}}$ (lower) for the $e$+jets (left) and $\mu$+jets (right) channels for 2016. Data (black) is compared to simulations in the stacked histograms with the statistical uncertainties (shaded area). The lower panel shows the data to MC agreement with the statistical uncertainties (gray).

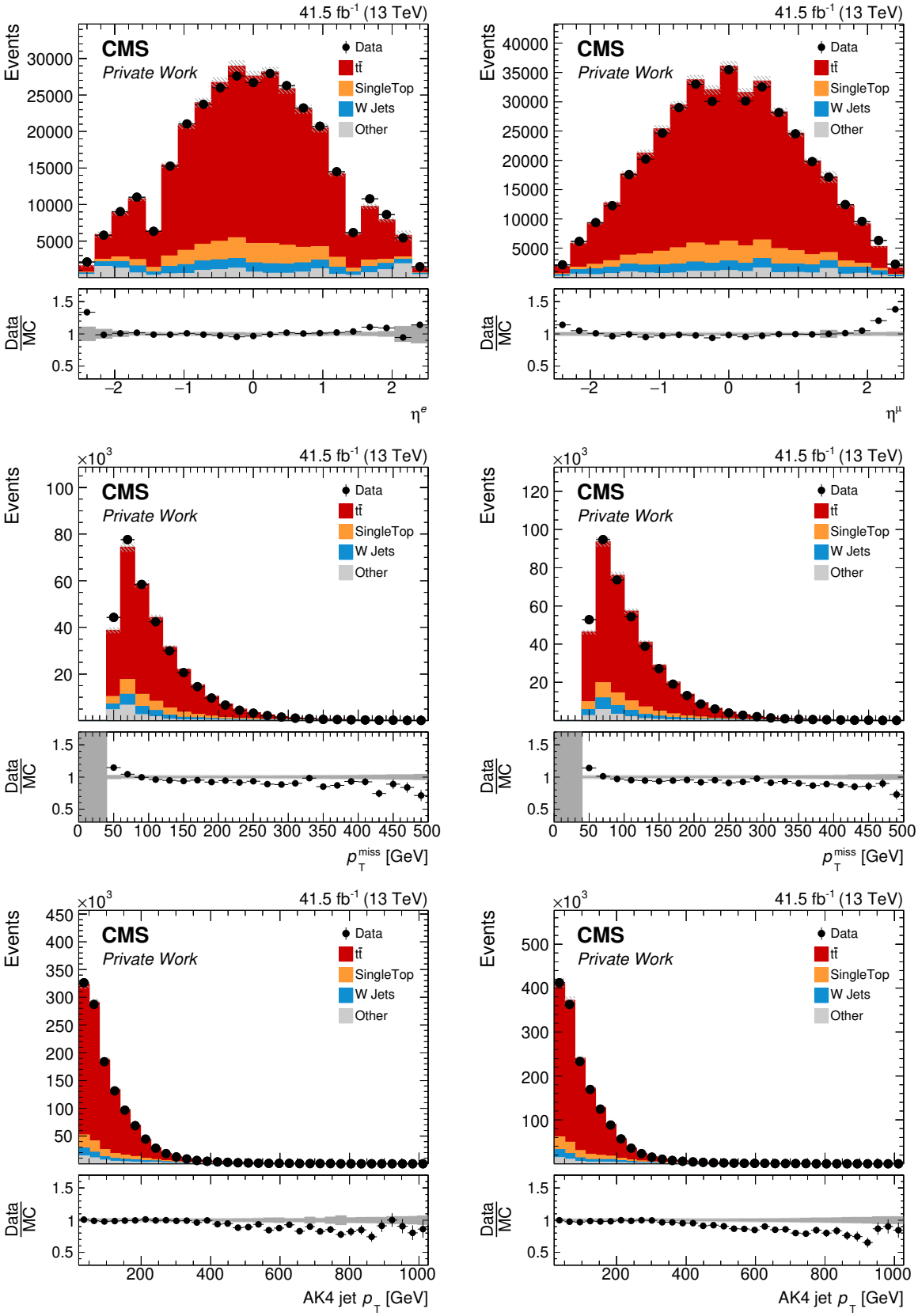


**Figure 7.5:** Distributions of the lepton $\eta$ (upper), $p_{\mathrm{T}}^{\mathrm{miss}}$ (middle) and the AK4CHS jets $p_{\mathrm{T}}$ (lower) for the $e$+jets (left) and $\mu$+jets (right) channels for 2017. Data (black) is compared to simulations in the stacked histograms with the statistical uncertainties (shaded area). The lower panel shows the data to MC agreement with the statistical uncertainties (gray).

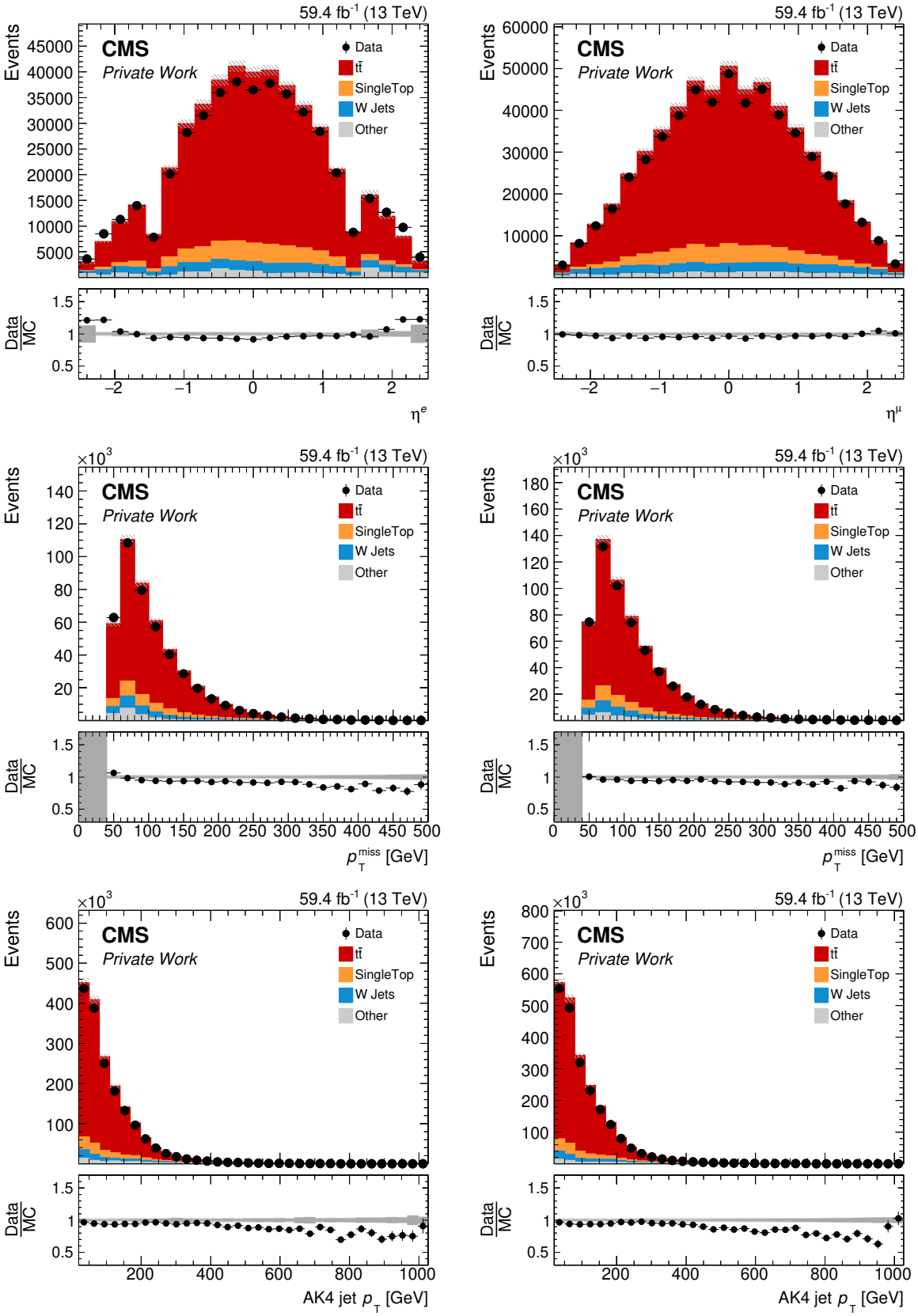


**Figure 7.6:** Distributions of the lepton $\eta$ (upper), $p_{\mathrm{T}}^{\mathrm{miss}}$ (middle) and the AK4CHS jets $p_{\mathrm{T}}$ (lower) for the $e$+jets (left) and $\mu$+jets (right) channels for 2018. Data (black) is compared to simulations in the stacked histograms with the statistical uncertainties (shaded area). The lower panel shows the data to MC agreement with the statistical uncertainties (gray).

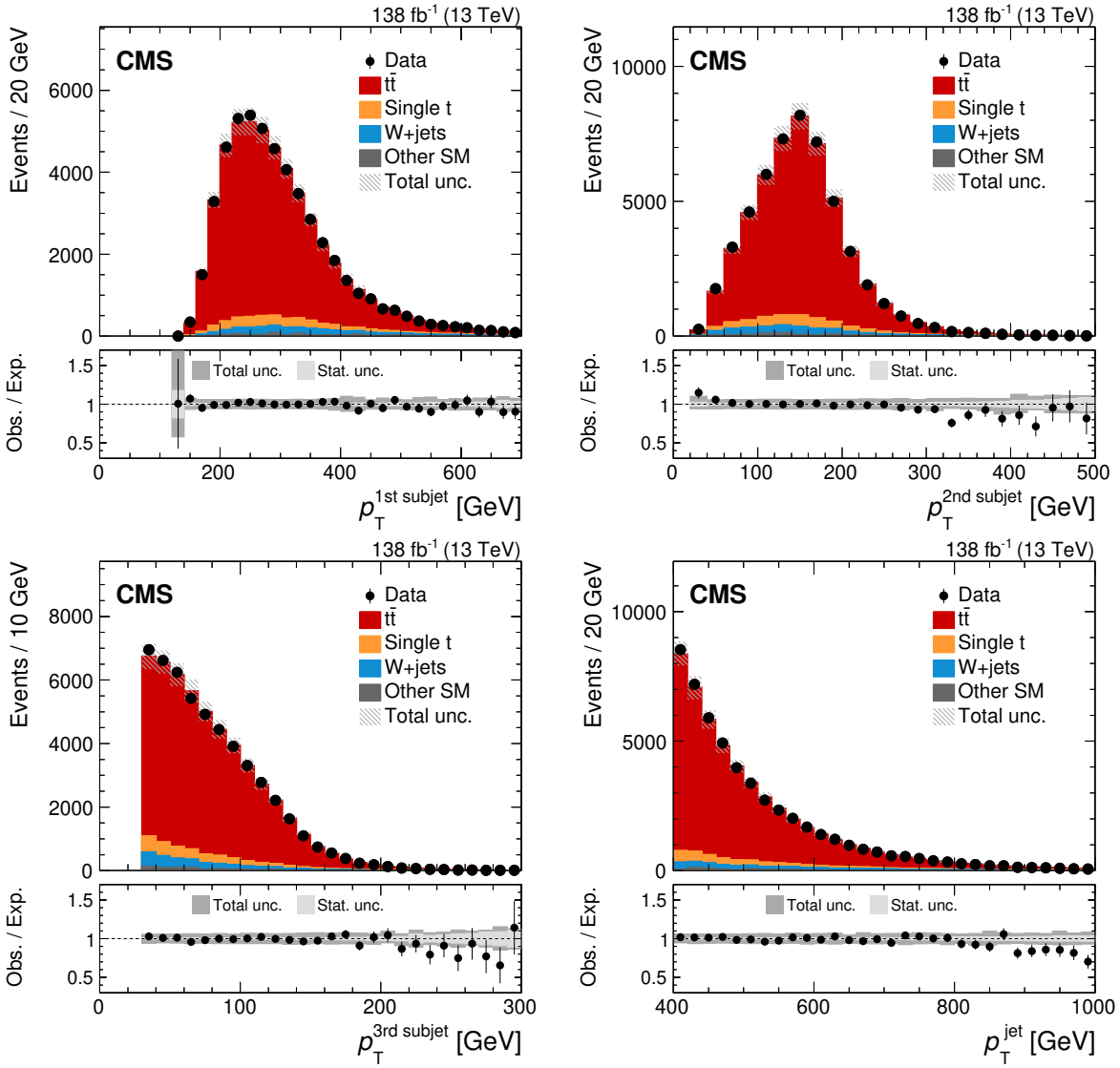


**Figure 7.7:** Distributions of the reconstructed $p_T$ of the leading (upper left), second (upper right), and third (lower left) subjet, as well as the combination of all three subjets, the hadronic XCone jet (lower right). Data (black markers) is compared to simulation in the stacked histograms, separated into the $t\bar{t}$ process (red) and the main backgrounds from single top production (yellow) and W+jets (blue) and smaller backgrounds (dark grey). The total uncertainty is represented by the shaded area. The lower panel shows the ratio of data to simulation with the statistical uncertainty (light gray) and the total uncertainty (dark grey). Published in Ref. [6].

## 7.4 Calibration of the Jet Mass Scale

The experimental precision in the previous iteration [18] of the jet mass measurement is limited by the calibration of the jet four-momentum The jet mass emerges as an additional parameter from the four momentum, and is not adequately covered in the JES calibration. These calibration are based on the jet $p_{\mathrm{T}}$ and the uncertainties were propagated to the jet mass. Consequently, embedding the JMS within the JES calibration can lead to significant uncertainties in jet mass measurement. A detailed discussion of the JMS can be found in Section 5.4.1.

As elaborated on in Section 4.4, jet corrections factors are applied to the four-momentum of the jets. The XCone subjets feature similar jet cones to anti-$k_{\mathrm{T}}$ jets and are corrected using the JEC provided by the CMS Collaboration. To account for differences between these two jet types, particularly in the treatment of nearby jets, additional residual corrections are applied on top of the JEC. Therefore, these corrections are highly correlated and calibrations of the JMS scale must consider them simultaneously. Variations in the jet corrections are invoked by the factors $f^{\mathrm{JEC}}$ and $f^{\mathrm{XCone}}$ for the JEC for AK4CHS jets and the additional XCone corrections, respectively. For the central jet corrections, $f^{\mathrm{JEC}}$ and $f^{\mathrm{XCone}}$ are set to 0 and $\pm 1$ for the variations corresponding to one standard deviation.

In this thesis, dedicated measurements of the JMS are performed using the invariant mass of the two XCone subjets containing the light flavor quarks from the hadronic W boson decay, also referred to as W jet mass. The objective is to disentangle the uncertainties affecting the JES, which only influences $p_{\mathrm{T}}^{\mathrm{jet}}$, from those impacting the JMS, which solely affect the jet mass. To achieve this, the sensitivity of the W jet mass to the jet corrections is exploited. By measuring the shifts in the W jet mass distribution for variations in the jet corrections, the value that describes the data best can be obtained. The resulting JMS factors are expressed in terms of the factors $f^{\mathrm{JEC}}$ and $f^{\mathrm{XCone}}$.

The event selection for JMS calibration is the same as for the jet mass measurement, requiring checks for potential biases and correlations as discussed later in this section. The hadronic W boson is reconstructed using two XCone subjets. In the data samples, no b-tagging algorithm is applied to jets clustered with the XCone algorithm. Therefore, XCone subjets are matched with AK4CHS jets identified as the b jet using the DEEPJET algorithm [117]. All AK4CHS jets matched to the large radius jet within $\Delta R < 1.2$ are identified. Subsequently, the XCone subjet closest to the AK4CHS jet with the highest b-tagging score is assigned to the b jet. The measurement of $m_{\mathrm{W}}$ is conducted using the invariant mass of the remaining two subjets. Data from all three years and both lepton channels are combined for this measurement.

The squared XCone jet mass can be expressed in terms of the factors $f^{\mathrm{JEC}}$ and $f^{\mathrm{XCone}}$ with

$$\begin{aligned} m_{\mathrm{jet}}^2 = \Bigg( \sum_{i=1}^{3} p_i \left( c_{\mathrm{JEC}}(p_{T,i}, \eta_i) + f^{\mathrm{JEC}} \sigma_{\mathrm{JEC}}(p_{T,i}, \eta_i) \right) \\ \times \left( c_{\mathrm{XC}}(p_{T,i}, \eta_i) + f^{\mathrm{XCone}} \sigma_{\mathrm{XC}}(p_{T,i}, \eta_i) \right) \Bigg)^2, \end{aligned} \tag{7.1}$$

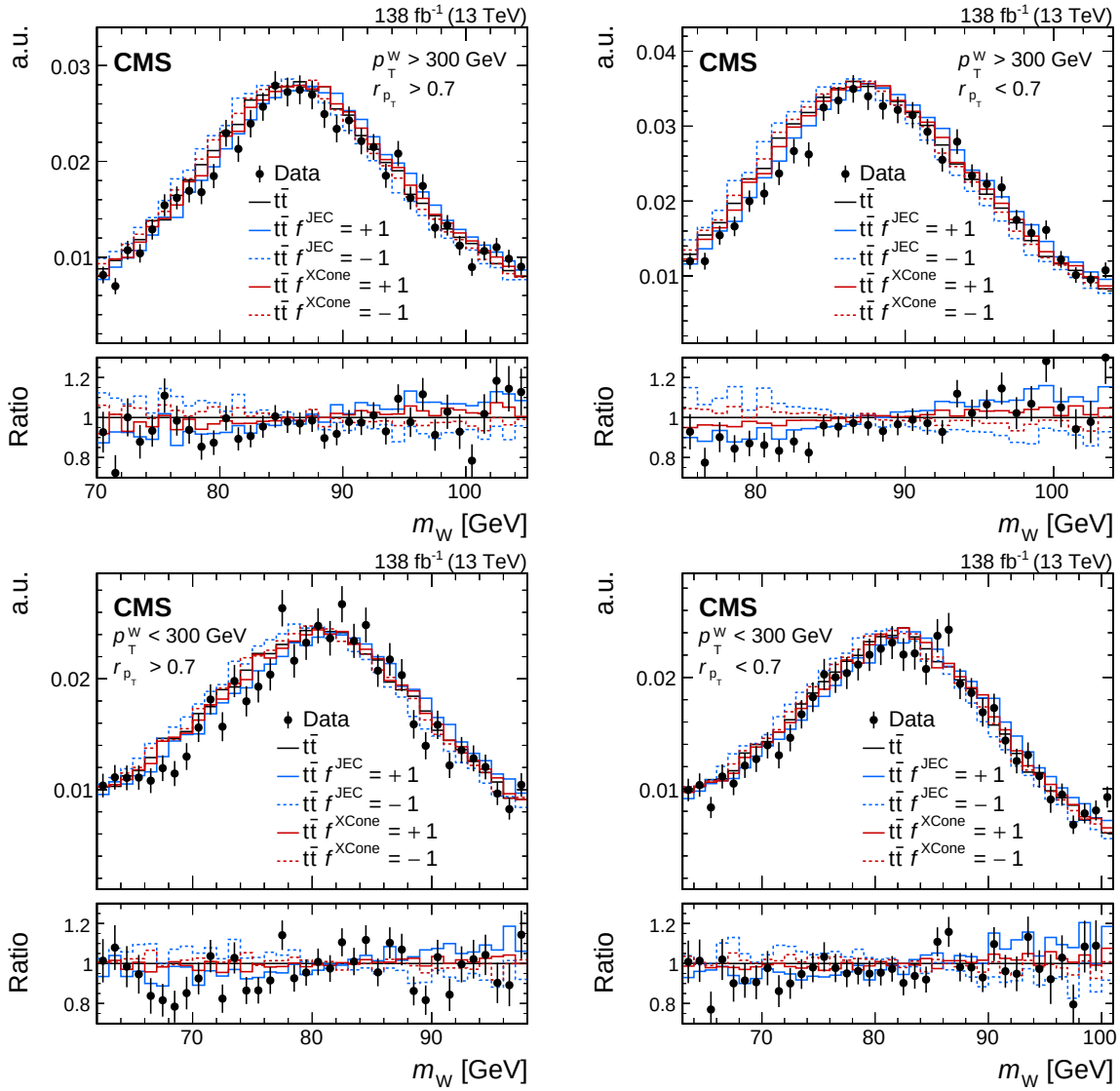


**Figure 7.8:** Reconstructed W boson mass in the four regions $p_T^W > 300\,\text{GeV}$ and $r_{p_T} > 0.7$ (upper left), $p_T^W > 300\,\text{GeV}$ and $r_{p_T} < 0.7$ (upper right), $p_T^W < 300\,\text{GeV}$ and $r_{p_T} > 0.7$ (lower left), and $p_T^W < 300\,\text{GeV}$ and $r_{p_T} < 0.7$ (lower right). Data is subtracted by the background and normalized to unit area. The normalized $t\bar{t}$ simulation additionally shows the one standard variation of the JEC and the XCone corrections. The lower panel shows the ratio of background-subtracted data and the variations in the jet corrections to the nominal $t\bar{t}$ simulation. Published in Ref.[6].

where $p_i$ is the four-momentum of the $i$-th subjet without any corrections applied, $c_{\text{JEC}}(p_{T,i}, \eta_i)$ and $c_{\text{XC}}(p_{T,i}, \eta_i)$ denote the JEC and XCone corrections, respectively, and $\sigma_{\text{JEC}}(p_{T,i}, \eta_i)$ and $\sigma_{\text{XC}}(p_{T,i}, \eta_i)$ represents the corresponding uncertainties. As stated in Equation 7.1, both correction factors and their uncertainties depend on the $p_T$ and $\eta$ of the uncorrected subjet four-momentum. The corrections $f^{\text{JEC}}$ and $f^{\text{XCone}}$ allow $m_{\text{jet}}$ to float within the one standard deviation of the JEC and the additional XCone corrections. Simultaneously, the functional form of the JEC and XCone uncertainties in $p_T$ and $\eta$ are not affected. By splitting the JES and JMS, effects are targeted that only alter the jet mass and not the $p_T$, such as splitting and merging of

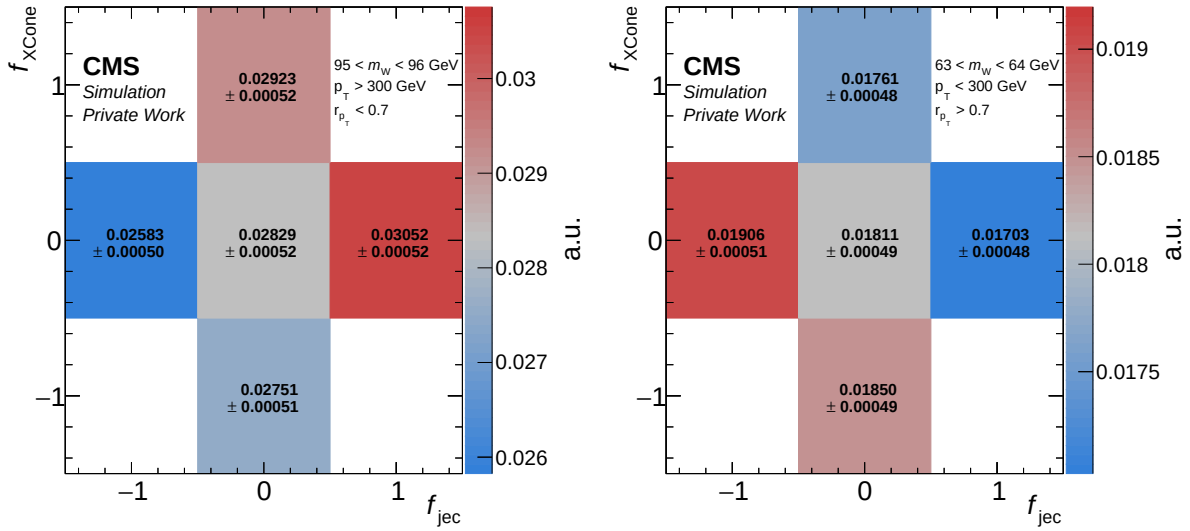


**Figure 7.9:** Two example bins of the normalized bin content of simulated $\mathrm{t\bar{t}}$ events in the $m_\mathrm{W}$ mass peak as a function of the jet correction factors $f^\mathrm{JEC}$ and $f^\mathrm{XCone}$. The nominal bin content from the nominal sample (gray) is located at $f^\mathrm{JEC} = 0$ and $f^\mathrm{XCone} = 0$ and changes of one standard deviation in the JEC and the additional XCone corrections are indicated by $+1$ (up) and $-1$ (down).

calorimeter clusters.

Variations in $f^\mathrm{JEC}$ and $f^\mathrm{XCone}$ can cancel each other out in an inclusive measurement. To maximize sensitivity and decouple variations in the XCone correction from the JEC, the measurement is divided into four regions. These regions are constructed from a two-dimensional plane of the transverse momentum of the reconstructed W boson $p_\mathrm{T}^\mathrm{W}$ and the ratio $r_{p_\mathrm{T}} = p_\mathrm{T}^{s_1}/p_\mathrm{T}^\mathrm{W}$, where $p_\mathrm{T}^{s_1}$ is the $p_\mathrm{T}$ of the leading subjet used for W boson reconstruction. The first observable, $p_\mathrm{T}^\mathrm{W}$, is associated with a maximum $p_\mathrm{T}$ threshold for the subjets, as their $p_\mathrm{T}$ cannot exceed that of the W boson, whereas the ratio is a measure for the symmetry of the subjets' $p_\mathrm{T}$. Ensuring that each bin contains approximately the same number of events, the bin boundaries are set to $p_\mathrm{T}^\mathrm{W} = 300\,\mathrm{GeV}$ and $r_{p_\mathrm{T}} = 0.7$. In the bin $p_\mathrm{T}^\mathrm{W} > 300\,\mathrm{GeV}$ and $r_{p_\mathrm{T}} < 0.7$, two symmetrical subjets with high $p_\mathrm{T}$ are reconstructed. Conversely, in the region where $p_\mathrm{T}^\mathrm{W} > 300\,\mathrm{GeV}$ and $r_{p_\mathrm{T}} > 0.7$, only one high-energy subjet contributes to $p_\mathrm{T}^\mathrm{W}$, while the other has relatively low $p_\mathrm{T}$ in comparison to the leading subjet. For $p_\mathrm{T}^\mathrm{W} < 300\,\mathrm{GeV}$ and $r_{p_\mathrm{T}} < 0.7$, two low-$p_\mathrm{T}$ subjets with approximately equal $p_\mathrm{T}$ are selected. Lastly, in the region where $p_\mathrm{T}^\mathrm{W} < 300\,\mathrm{GeV}$ and $r_{p_\mathrm{T}} > 0.7$, only one low-$p_\mathrm{T}$ subjet contributes to $p_\mathrm{T}^\mathrm{W}$, while the other has an even lower $p_\mathrm{T}$.

The effects of $c_\mathrm{JEC}$ and $c_\mathrm{XC}$, as well as $\sigma_\mathrm{JEC}$ and $\sigma_\mathrm{XC}$, differ across the four regions, allowing for the simultaneous extraction of the two factors $f^\mathrm{JEC}$ and $f^\mathrm{XCone}$. It is expected that only the peak region shows sensitivity to the variations in jet corrections. To ensure sufficient statistical precision, each bin must contain at least 100 events in the background-subtracted data to be considered. Statistical fluctuations in the tails are avoided by setting boundaries for the peak region of each W boson mass, as listed in Table. 7.1.

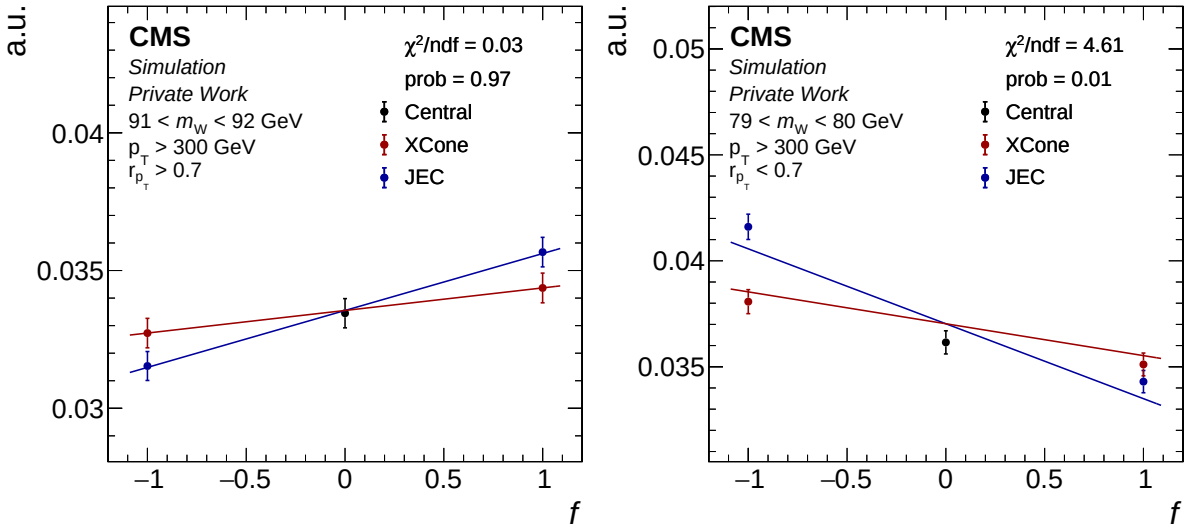


**Figure 7.10:** Projection of the two dimensional fit to the normalized bin content as a function of the variations of the jet corrections. The central value (black) indicates the nominal JEC (blue) and additional XCone corrections (red) applied, while the up and down variations are indicated by $+1$ and $-1$, respectively. Shown are two bins with a $p$-value of $> 90$ % (left) and below 5 % (right).

The tails arise from wrongful assignments of the subjets to the W boson and do not add information to the fit. In total 138 bins are considered for the JMS calibration with a bin width of 1 GeV. The calibration is performed on the distribution of background-subtracted data and $\mathrm{t\bar{t}}$ events both normalized to unit area, to only consider shape effects and not the total yield. Figure 7.8 shows the W boson distribution in all four regions in comparison to the variations of the jet corrections parameterized by $f^{\mathrm{JEC}}$ and $f^{\mathrm{XCone}}$. The down variations of both factors ($f^{\mathrm{JEC}}$ and $f^{\mathrm{XCone}} = -1$) shift the distribution to lower $m_{\mathrm{W}}$ regions, while the up variations ($f^{\mathrm{JEC}}$ and $f^{\mathrm{XCone}} = +1$) increases the mass. This behavior is expected, as the total four-momentum of the jets shifts to lower and higher values, respectively. The total shift in all four peaks ranges from $0.42 - 0.61$ GeV for $f^{\mathrm{JEC}}$ and $0.17 - 0.25$ GeV for $f^{\mathrm{XCone}}$.

The predicted dependence of the normalized bin content in simulation for the different variations in the jet corrections is obtained with a two dimensional linear fit with

$$g_i(f^{\mathrm{JEC}}, f^{\mathrm{XCone}}) = a_i + b_i f^{\mathrm{JEC}} + c_i f^{\mathrm{XCone}}. \tag{7.2}$$

Here, $a_i$, $b_i$ and $c_i$ are free parameters obtained from the fit in each of the 138 bins. The fits are performed in simulation in the $f^{\mathrm{JEC}}$-$f^{\mathrm{XCone}}$-plane illustrated in Figure 7.9 for two example $m_{\mathrm{W}}$ bins. The bin content of the nominal distribution is taken as the point at (0,0). The dependence of the normalized bin content of the jet correction variations for one standard deviation is visible. Larger sensitivity arises from variations in the JEC ($f^{\mathrm{JEC}}$), while the XCone corrections, intended as residual adjustments, show smaller changes. It has been verified that a linear fit describes the dependence of $m_{\mathrm{W}}$ on $f^{\mathrm{JEC}}$ and $f^{\mathrm{XCone}}$ sufficiently well. The goodness-of-fit is

| $p_{\mathrm{T}}^{\mathrm{W}}$ [GeV] | $r_{p_{\mathrm{T}}}$ | $m_W$ bins [GeV] |
|---|---|---|
| $> 300$ | $> 0.7$ | 70–105 |
| $> 300$ | $< 0.7$ | 75–104 |
| $< 300$ | $> 0.7$ | 62–98 |
| $< 300$ | $< 0.7$ | 63–101 |

**Table 7.1:** Mass range for the considered $m_W$ peak in each bin of $p_{\mathrm{T}}^{\mathrm{W}}$ and $r_{p_{\mathrm{T}}}$. Each bin has at least 100 events in background-subtracted data.

calculated with the incomplete gamma function as test statistic. The resulting $p$-value gives the probability that a correct model does not describe the observation by chance. For the linear prediction, four out of 138 bins feature a $p$-value of less than 5 %, indicating that the fit quality matches the expectation of statistical fluctuations only. Figure 7.10 illustrates the projection of the two-dimensional fit onto $f^{\mathrm{XCone}} = 0$ and $f^{\mathrm{JEC}} = 0$, comparing the linear hypothesis to the predictions of the jet corrections for $f^{\mathrm{JEC}}$ and $f^{\mathrm{XCone}}$, respectively. For bins with $p > 90$ % (left) the bin content is described well by the linear hypothesis. Contrarily, for one out of four bins with $p < 5$ % (right) the bin content fluctuates along the fit and the overall trend is only approximated.

The factors $f^{\mathrm{JEC}}$ and $f^{\mathrm{XCone}}$ that best describe the data are obtained by fitting simulation to data using a two-dimensional $\chi^2$ function defined as

$$\chi^2 = d^T V^{-1} d. \tag{7.3}$$

The vector $d$ is built from the differences of the prediction $g_i(f^{\mathrm{JEC}}, f^{\mathrm{XCone}})$ and the background-subtracted data in each bin $i$ of all four regions. The covariance matrix $V$ includes the statistical uncertainty in data, considering correlations from the normalisation to unit area and the uncertainties from the fits to obtain the predictions $g_i$. The latter are estimated from the statistical uncertainty of the simulated $\mathrm{t\bar{t}}$ sample. Additionally, the leading systematic uncertainties, namely the JER, modeling of the $\mathrm{t\bar{t}}$ simulation, and from the background rates are considered. Uncertainties from the modeling of the $\mathrm{t\bar{t}}$ simulation comprise the $h_{\mathrm{damp}}$ parameter, modeling of the FSR and ISR and the color reconnection model. All uncertainties are treated as fully correlated across all bins and regions. The dominant uncertainties arise from the statistical uncertainties in data, followed by the JER, while the remaining uncertainties are relatively small in comparison.

Figure 7.11 displays the resulting $\chi^2$ as a function of $f^{\mathrm{JEC}}$ and $f^{\mathrm{XCone}}$. The minimum of the $\chi^2$ function is located within the one standard deviation intervals of the JES. The global minimum has a value of $\chi^2 = 130$ with 132 degrees of freedom and the 68 % CL (95 % CL) is determined at $\chi^2 = \chi^2_{\mathrm{min}} + 2.3\,(+5.99)$. This results in the factors $f^{\mathrm{JEC}} = 0.60 \pm 0.24$ and $f^{\mathrm{XCone}} = -0.06 \pm 0.57$ with a linear correlation of $\rho = -0.66$. Compared to the one standard

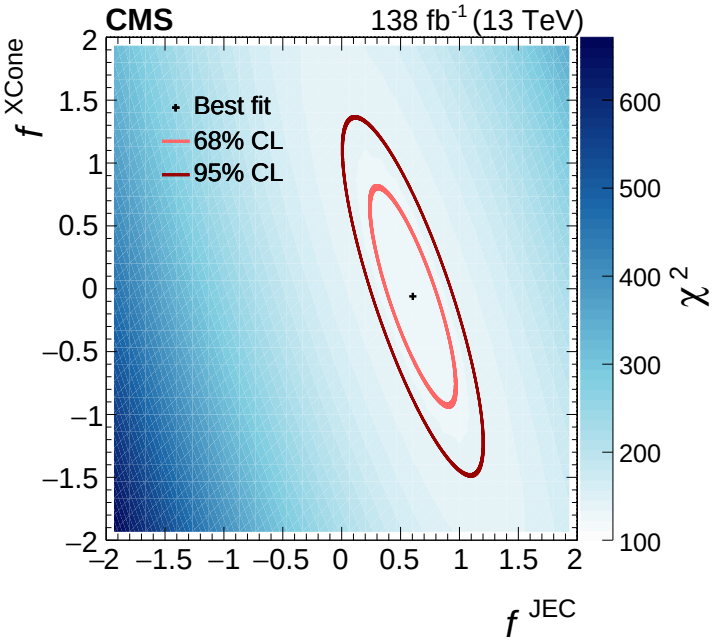


**Figure 7.11:** The two-dimensional $\chi^2$ as a function of the jet correction factors $f^{\text{JEC}}$ and $f^{\text{XCone}}$ obtained from a comparison of simulated $\mathrm{t\bar{t}}$ events to background-subtracted data in the reconstructed $m_{\text{W}}$ distribution. The minimum of the $\chi^2$ function is indicated with a black cross and the light red and dark red ellipses represent the 68 % and 95 % CL intervals, respectively. Published in Ref.[6].

deviation variation of the JES ($f^{\text{JEC}}, f^{\text{XCone}} = \pm 1$), the 68 % CL has been significantly reduced. One-dimensional uncertainties on the extracted parameters for the JMS calibrations are taken from the endpoints of the semi-minor axis of the 68 % CL. Shifts along the semi-minor axis result in the largest change in the $m_{\text{jet}}$ distribution, as both factors change in the same direction. In contrast, shifts along the semi-major axis cause changes in opposite directions, nearly canceling each other out. The extracted value pairs for ($f^{\text{JEC}}$, $f^{\text{XCone}}$) include the nominal pair (0.60, -0.06) and pairs for systematic uncertainties (0.78, 0.01) and (0.42, -0.13). These values will be referred to as the JMS correction and the JMS uncertainties, respectively.

To verify that statistical fluctuations in the simulation do not bias the result, the same measurement is performed with a bin width of 3 GeV in the $m_{\text{W}}$ distribution. The increase in the bin width reduces the number of considered bins to 47. As a result, the correlation between $f^{\text{JEC}}$ and $f^{\text{XCone}}$ is increased, which stretches the 68 % CL ellipse along the semi-major axis while maintaining a similar width. The $m_{\text{W}}$ distribution with the reduced bin size includes one bin with a $p$-value below 0.1, confirming that the linear hypothesis provides an adequate description. Additionally, the larger bin width demonstrates a similar performance compared to the 138 bins.

Originally, the bins in $p_{\text{T}}^{\text{W}}$ and $r_{p_{\text{T}}}$ were introduced to decouple both parameters. The improvement of the measurement by sorting the subjets into four regions based on their $p_{\text{T}}$ is tested by performing an inclusive measurement. The resulting 68 % CL ellipses for both measurements

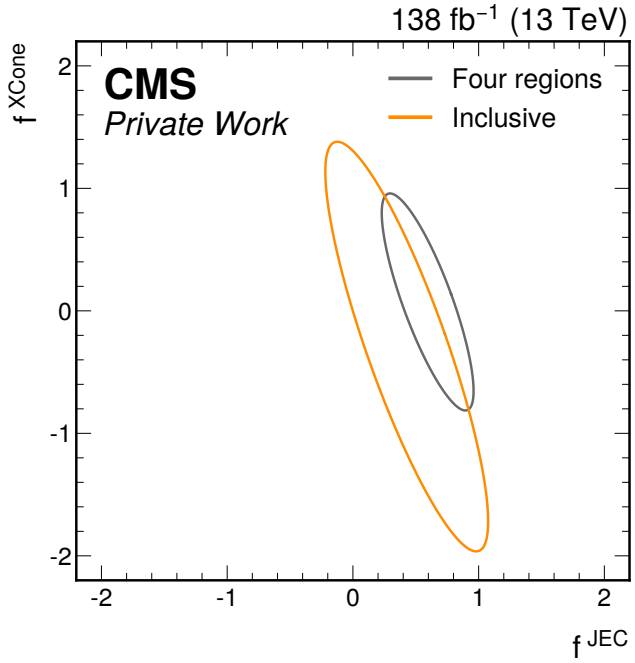


**Figure 7.12:** The 68 % CL intervals from the measurement of the JMS as a function of $f^{\text{JEC}}$ and $f^{\text{XCone}}$ from the reconstructed $m_{\text{W}}$ distribution. Shown are the 68 % CL intervals for the measurement in four regions based on the subjets $p_{\text{T}}$ (gray) and an inclusive measurement (orange) without a subdivision of the subjets.

are shown in Figure 7.12, including the measurement inclusive in the subjets' $p_{\text{T}}$ (yellow) and the separation into four bins (grey). Compatibility is observed within one standard deviation, and the four-region approach improves the precision of the JMS corrections by a factor of 1.6 compared to the inclusive measurement.

### 7.4.1 Jet Flavor Dependence

The calibration of the JMS is based on the reconstructed hadronic W decay and is therefore dominated by XCone subjets originating from light quarks. To account for differences in the detector response for different jet flavors, an additional flavor uncertainty is applied. The XCone subjet originating from the b quark is identified using the same approach as for reconstructing the hadronic W boson decay. Specifically, the XCone subjet with the smallest spatial distance to the AK4CHS jet with the highest b-tagging score, matched with the hadronic XCone jet, is assigned to the b quark. An additional flavor uncertainty, referred to as the JMS b flavor uncertainty, is considered for the b jet. This uncertainty is derived from differences in the response of b jets between PYTHIA and HERWIG, quantified in the scope of the centrally provided JEC uncertainties by the CMS Collaboration [119]. The impact on the jet mass distribution at the detector level is shown in Figure 7.13, featuring a shift of $\sim 2$ %.

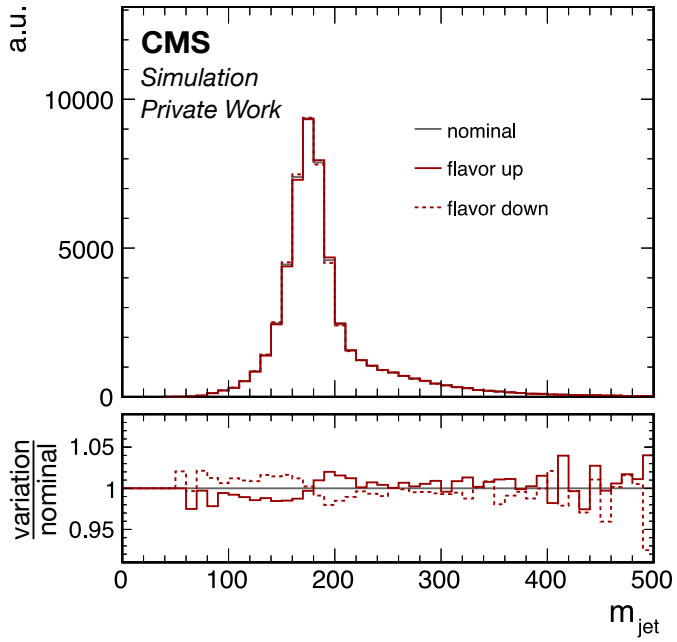


**Figure 7.13:** The jet mass distribution in simulated $\mathrm{t\bar{t}}$ events with applied JMS corrections. Shown are the central distribution (gray) and uncertainties in four-momentum of the subjet assigned to the b quark (red). The variations account for the differences in the detector response in light and heavy flavor jets and are based on the differences of the event generators in PYTHIA and HERWIG.

### 7.4.2 Testing for a bias on $m_{\mathrm{top}}$

The calibration of the JMS is performed using the same dataset as for the jet mass measurement and the modeling of the FSR. To ensure that all measurements remain uncorrelated and free from potential biases, various cross-checks are conducted. These checks verify that each observable of interest remains independent despite changes in the parameters of interest in the other measurements.

A key objective of the jet mass measurement is to measure $m_{\mathrm{top}}$. The calibration of the JMS is conducted in the reconstructed $m_{\mathrm{W}}$ mass, which is expected to be independent of $m_{\mathrm{top}}$. It has been verified that the measurement of the JMS for different $m_{\mathrm{top}}$ hypotheses does not alter the result. The extracted JMS corrections for $m_{\mathrm{top}}$ hypothesis of $m_{\mathrm{top}} = 172.5$ (central), 169.5 and 175.5 GeV are compatible within one standard deviation. Furthermore, the bin content for all jet correction variations has been compared within the statistical uncertainties. The fraction of the bin contents overlapping for two $m_{\mathrm{top}}$ hypothesis matches the expected number of compatible bins based on the 68 %, 95 % and 99 % CL intervals. Thus, a possible bias of the JMS corrections with respect to the top quark mass is excluded.

Furthermore, correlations of the JMS calibration and jet mass are tested by splitting the dataset for the measurement of the JMS calibration and jet mass. For this, the jet mass measurement (see Section 7.7.1) is conducted in five scenarios for each year:

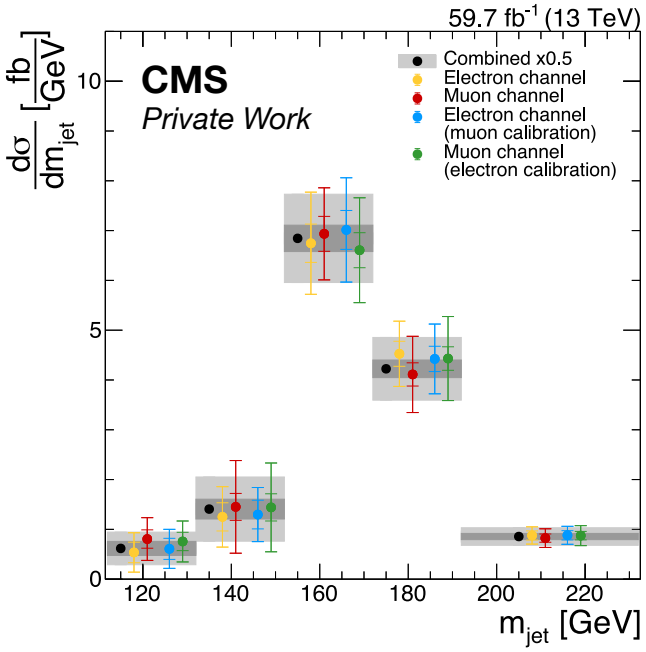


**Figure 7.14:** Differential $t\bar{t}$ production cross section as a function of the XCone jet mass for several scenarios. The JMS is either calibrated in the same channel as the jet mass measurement, namely the $e$+jets (yellow), $\mu$+jets (red) or the combined (gray) channel, or in the $e$+jets channel and applied to the $\mu$+jets channel (blue) and vice versa (green). The combined channel is scaled by a factor of 0.5 to match the same event yield.

- the calibration of the JMS and the jet mass measurement are both performed in the $e$+jets, $\mu$+jets or the combined channel, or
- the calibration of the JMS is performed in the $e$+jets ($\mu$+jets) channel and the jet mass measurement in the $\mu$+jets ($e$+jets) channel.

The differential $t\bar{t}$ production cross section as the function of jet mass is compared for each scenario in Figure 7.14. To obtain the same normalization, the combined measurement is scaled with a factor of 0.5. Only statistical uncertainties and those connected to the JES, JER and JMS are included. All distribution perfectly agree within their statistical uncertainties. Additionally, the $m_{\text{top}}$ extraction is performed for $t\bar{t}$ simulations with $m_{\text{top}} = 171.5\,\text{GeV}$ and $173.5\,\text{GeV}$ as pseudo data and compared between the five scenarios as depicted in Figure 7.15. No trend is evident for the extraction of $m_{\text{top}}$ in the different subsets in the data and all values agree well within one standard deviation.

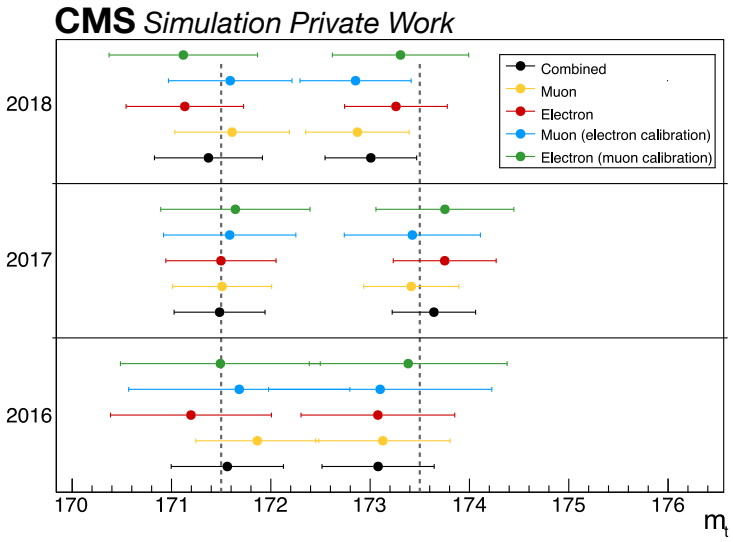


**Figure 7.15:** Extraction of $m_{\text{top}}$ from the differential $\mathrm{t\bar{t}}$ production cross section as a function of the XCone jet mass for all scenarios in the years 2016, 2017 and 2018. Simulated samples with a $m_{\text{top}}$ hypothesis of 171.5 GeV and 173.5 GeV are used as pseudo data. The JMS is either calibrated in the same channel as the jet mass measurement, namely the $e$+jets (yellow), $\mu$+jets (red) or the combined (gray) channel, or in the $e$+jets channel and applied to the $\mu$+jets channel (blue) and vice versa (green).

## 7.5 Performance at Detector Level

After applying the newly measured JMS calibration, the JES affects only the $p_{\text{T}}$ of the jets, while the JMS affects only the jet mass. The reconstructed $m_{\text{W}}$ mass distribution, shown in Figure 7.16 (left) after applying the JMS corrections, reveals a clear peak at the $m_{\text{W}}$ mass with good agreement between simulation and data across the full mass range. The jet mass distribution used for the unfolding procedure and the subsequent measurement of the top quark mass is displayed in Figure 7.16 (right), featuring a clear peak close to the top quark mass.

Figure 7.17 (left) presents the mean values of the reconstructed W boson and $m_{\text{jet}}$ as a function of the number of primary vertices $N_{\text{PV}}$. The jet mass for the reconstructed top quark and W boson decay exceeds the simulated $m_{\text{top}}$ and $m_{\text{W}}$ by 4 GeV and 2 GeV, respectively. This shift to higher mass values is attributed to pileup and the UE. An increasing trend in both mean values with higher $N_{\text{PV}}$ is evident, especially for the jet mass comprising the top quark decay. However, the slope increases by a maximum of 2 GeV for the top quark jet mass, indicating that the XCone reconstruction and calibration effectively mitigate most pileup contributions. The mean values in data are well described by the simulation.

Figure 7.17 (right) shows the JMR as a function of the true jet $p_{\text{T}}$ and $N_{\text{PV}}$. The JMR is derived from the width parameter of the Gaussian function fitted to the distribution of $m_{\text{jet}}^{\text{rec}}/m_{\text{jet}}^{\text{gen}}$, where $m_{\text{jet}}^{\text{rec}}$ is the mass of the calibrated reconstructed jet and $m_{\text{jet}}^{\text{gen}}$ is the jet mass at the particle level. For the inclusive measurement in $N_{\text{PV}}$, the JMR ranges within 7-8 % up to $p_{\text{T}} = 1500\,\text{GeV}$ and improves for higher jet $p_{\text{T}}$. The JMR is 6-7 % for low $N_{\text{PV}}$ events and increases by approxi-

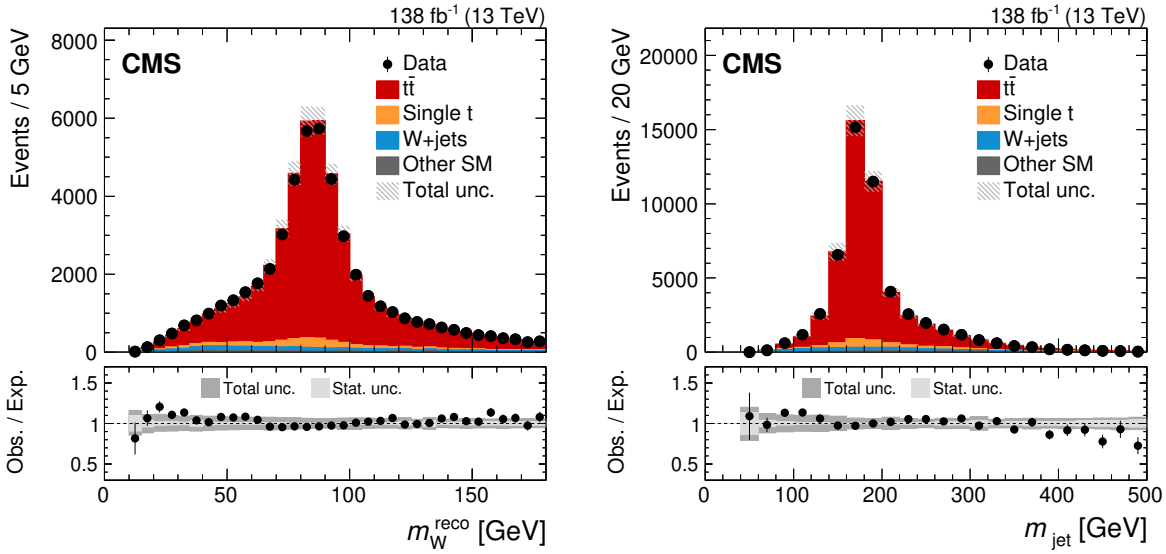


**Figure 7.16:** Jet mass distribution of the reconstructed hadronic W boson (left) and top quark (right) decays. Both are reconstructed based on the two-step clustering approach with the XCone jet algorithm in $\mathrm{t\bar{t}}$ events. Data (black markers) is shown with the statistical uncertainties. Simulation (filled histograms) are shown with the total uncertainties (shaded area). The ratio of data to simulation in the bottom panel shows the contribution from both, the statistical (light gray) and systematic (dark gray) uncertainty separated. Published in Ref. [6].

mately 1 % for events with $N_{\mathrm{PV}} > 20$. An overall increase of the JMR by approximately 0.5 % is observed compared to the previous iteration (see Figure 5.10). This shift is negligible considering that two additional datasets are utilized with an approximately four times larger event yield.

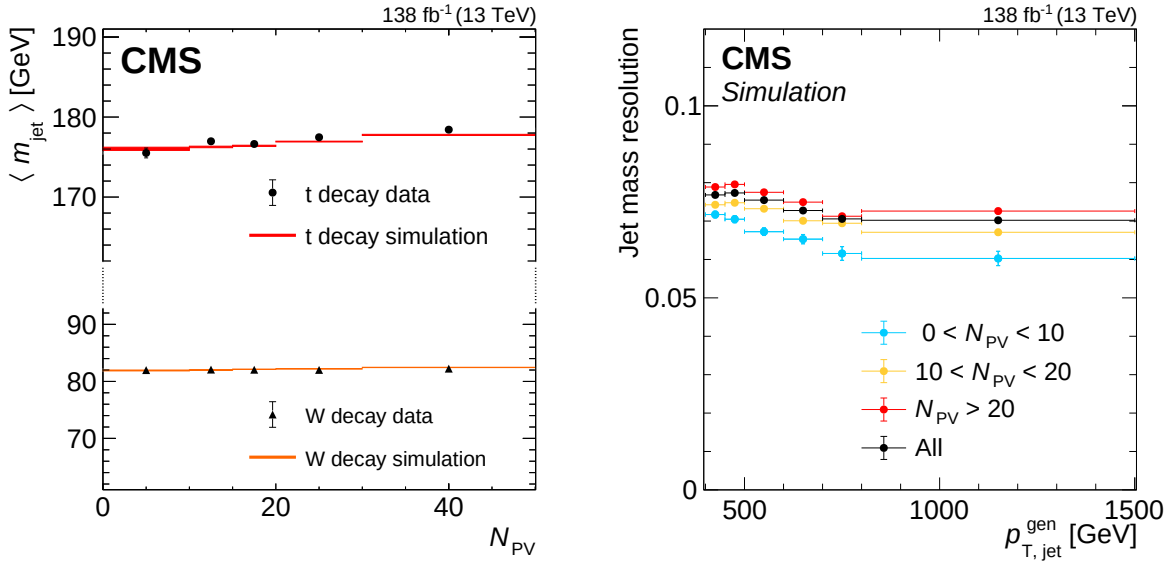


**Figure 7.17:** The mean value for the $m_{\text{jet}}$ distribution for the hadronic top quark and W boson decay, as a function of the number of primary vertices $N_{\text{PV}}$ (left). Data (black markers) are compared to simulated $\text{t}\bar{\text{t}}$ events (filled bands) including the statistical uncertainties represented by the vertical lines and the width of the band. The jet mass resolution (right) for the XCone jet is shown for simulation as function of the $p_{\text{T}}$ on particle level and for different $N_{\text{PV}}$ intervals (colors). The statistical uncertainty is indicated by the vertical error bars. Published in Ref. [6].

## 7.6 Modeling of the Final State Radiation

The modeling of the FSR represents the largest model uncertainty in the previous measurement of the jet mass at $\sqrt{s} = 13\,\text{TeV}$ [18] with $\Delta m_{\text{top}} = 1.2\,\text{GeV}$. In simulation, the renormalization scale $\mu$ affects the definition of the strong coupling constant for the FSR modeling, denoted as $\alpha_{\text{S}}^{\text{FSR}}(\mu^2)$. The strength of the strong coupling steers the amount of the FSR in a process, which adds more particles to the jet and thereby contributes to jet mass. To control the amount of FSR, the energy scale is varied by a factor $f_{\text{FSR}}$. The previous analysis estimated the uncertainty on the FSR with factors of 0.5 and 2 in the FSR simulation. Consequently, the effective strong coupling is varied from $\alpha_{\text{S}}^{\text{FSR}}(m_{\text{Z}}^2) = 0.1365$ for the central value to 0.1556 and 0.1217 for the up and down variation, respectively. It is assumed that the variation of the FSR energy scale of the CUETP8M2T4 tune with a factor of $f_{\text{FSR}} = 0.5$ and 2 overestimates the uncertainty. For 2017 and 2018, the CP5 tune is employed with $\alpha_{\text{S}}^{\text{FSR}}(m_{\text{Z}}^2) = 0.118$. Uncertainties can be measured with a broader range of variations with $f_{\text{FSR}} \in \{1/4, 1/2, 1/\sqrt{2}, \sqrt{2}, 2, 4\}$. It is known that the default set of parameters for the tune does not adequately describe jet substructure observables in data, and larger values of FSR scale are preferred [56]. To constrain these uncertainties and to remedy the non-fitting default parameters in samples utilizing the CP5 tune, the modeling of the FSR is studied more closely to determine the value of $\alpha_{\text{S}}^{\text{FSR}}(m_{\text{Z}}^2)$ that describes the data best. To effectively capture variations in the renormalization scale $\mu$ and the resulting amount of FSR, a sensitive variable is required. The $N$-subjettiness ratio $\tau_{32} = \tau_3/\tau_2$ is selected for this purpose. This ratio is particularly suitable at identifying changes in the internal jet structure

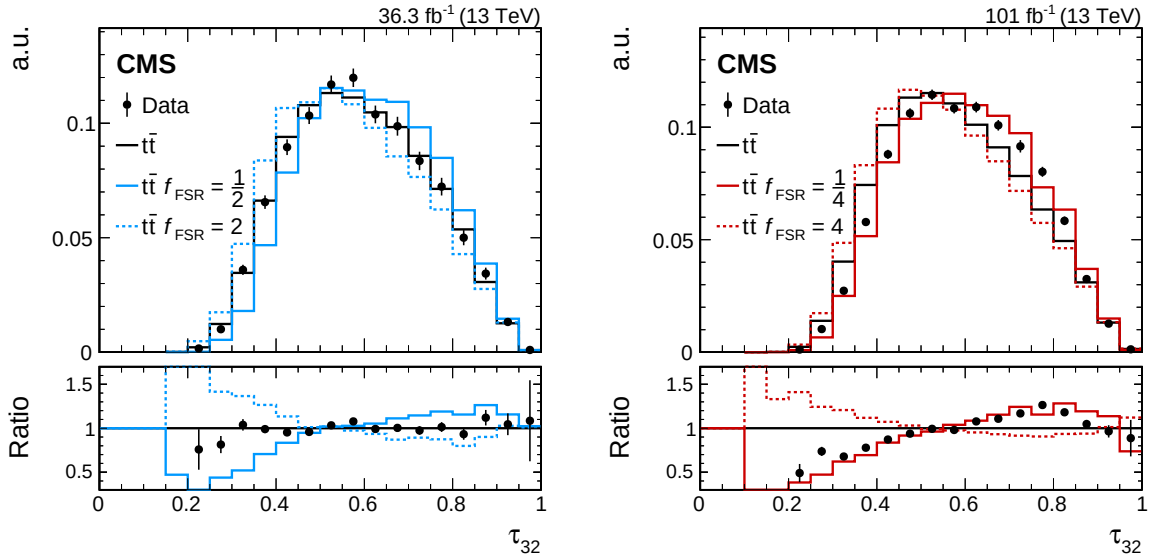


**Figure 7.18:** The normalized $\tau_{32}$ distributions measured in AK8CHS jets in hadronic decays of boosted top quarks. A mass requirement of $m_{\text{jet}} > 140\,\text{GeV}$ ensures fully merged decays. Background-subtracted data is compared to $\text{t}\bar{\text{t}}$ simulation in 2016 (left) with the CUETP8M2T4 tune and in the combined dataset of 2017 and 2018 (right) with the CP5 tune. The lower panel shows the ratio of data and the variations to the nominal $\text{t}\bar{\text{t}}$ samples with $f_{\text{FSR}} = 1$. Published in Ref. [6].

caused by additional radiation. As extra radiation is incorporated into the jet, it alters the prong structure, making $\tau_{32}$ a reliable indicator for distinguishing between three-prong decays and those with fewer and higher prongs. This sensitivity to additional radiation makes $\tau_{32}$ an optimal observable for determining the $f_{\text{FSR}}$ value that best aligns with the observed data. Given the three-prong structure of hadronic top quark decays, the ratio $\tau_{43}$ might seem a more natural choice, as it incorporates the four-prong structure when including additional radiation within the XCone jet. Featuring a narrow peak at $\langle\tau_{43}\rangle \approx 0.9$, $\tau_{43}$ does not distinguish the different prong structures as effectively as $\tau_{32}$.

The datasets from 2017 and 2018, both employing the CP5 tune, are combined for this measurement and referred to as the CP5 dataset. For 2016, the variations in $f_{\text{FSR}}$ remain consistent with those used in previous analyses and read $f_{\text{FSR}} \in \{1/2, 1, 2\}$. For the CP5 dataset, the full range of variations is explored. Only shape effects are considered studying the differences in the normalized distributions. The same selection criteria used for the JMS calibration and the jet mass measurement are applied here. The $\tau_{32}$ distribution is measured using AK8CHS jets, which are more sensitive to the amount of FSR compared to XCone jets obtained with the two-step clustering, as they are ungroomed. Additionally, the jet size of AK8 jets is comparable to that of XCone jets constructed from three subjets. To identify AK8 jets that encompass the hadronic decay of boosted top quarks, these jets are matched with XCone jets within $\Delta R < 0.8$. In cases where multiple AK8 jets satisfy this criterion, the jet with the highest $p_{\text{T}}$ is selected. A mass requirement of $m_{\text{jet}} > 140\,\text{GeV}$ is imposed to ensure the clustering of all particles from the hadronic top quark decay into the jet. Figure 7.18 displays the $N$-subjettiness ratio $\tau_{32}$ in

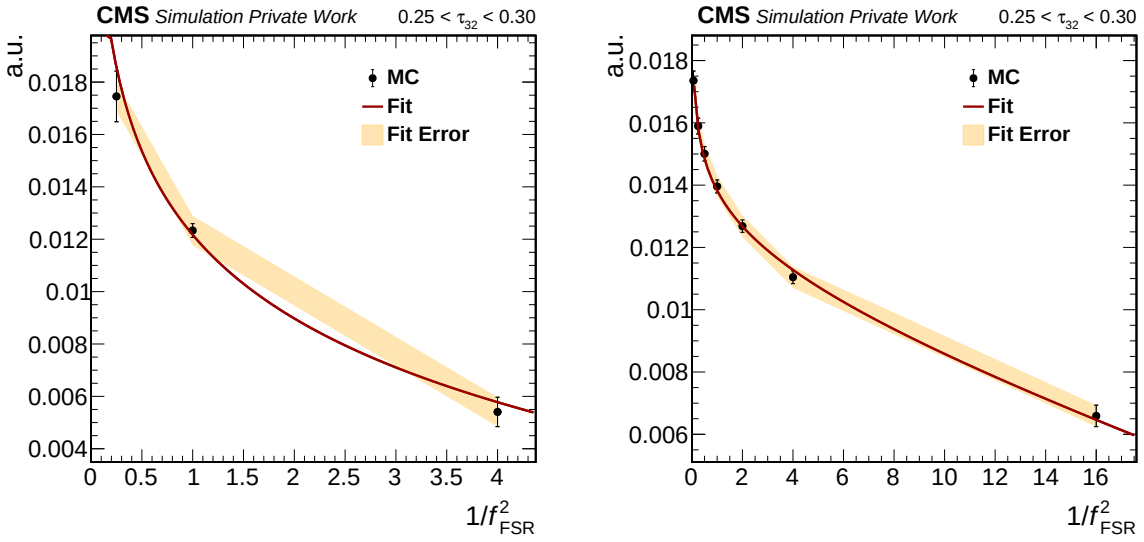


**Figure 7.19:** The normalized bin content of the $\tau_{32}$ distribution in one example bin obtained from AK8CHS jets as a function of $1/f_{\mathrm{FSR}}^2$. The observations in simulation (black marker) are described by a logarithmic fit (red). The uncertainty on the fit is obtained from the largest statistical uncertainty from any point.

dependence of $f_{\mathrm{FSR}}$ for 2016 (left) and the CP5 dataset (right). Lower values of $f_{\mathrm{FSR}}$ correspond to higher $\tau_{32}$ values, while higher $f_{\mathrm{FSR}}$ values result in a lower average $\tau_{32}$ value. This trend is consistent with the expectations, as decreasing $f_{\mathrm{FSR}}$ increases $\alpha_{\mathrm{S}}^{\mathrm{FSR}}$, leading to more radiation. Conversely, minimal radiation in top quark decays does not alter the three-prong structure resulting in lower average $\tau_{32}$ value.

The factor $f_{\mathrm{FSR}}$ that is most compatible with the data is determined by minimizing the $\chi^2$ function, equivalent to that in Equation 7.3. The vector of the differences is constructed by background-subtracted data and the prediction $g_i(f_{\mathrm{FSR}})$ in each bin $i$ of the $\tau_{32}$ distribution with

$$g_i(f_{\mathrm{FSR}}) = a_i + b_i \log f_{\mathrm{FSR}}^{-2} + c_i f_{\mathrm{FSR}}^{-2}. \tag{7.4}$$

Here, $a_i$, $b_i$ and $c_i$ free parameters from the fit. In the 2016 data sample the quadratic $c_i$ term is omitted, as only three points are available. The prediction is inspired by the logarithmic dependence of $\alpha_{\mathrm{S}}^{\mathrm{FSR}}$ on variations of the squared energy scale with $\alpha_{\mathrm{S}}^{\mathrm{FSR}}((f_{\mathrm{FSR}} \cdot \mu)^2)$. Two example fits are illustrated in Figure 7.19 for 2016 (left) and the CP5 dataset (right). The logarithmic prediction $g_i(f_{\mathrm{FSR}})$ describes simulation well within one standard deviation.

The covariance matrix in the $\chi^2$ calculation contains the statistical uncertainties from the data, including the correlation from the normalization, the fit uncertainty, jet calibration uncertainties, and uncertainties in the modeling of the $\mathrm{t\bar{t}}$ process. The fit uncertainty is conservatively estimated by the largest statistical uncertainty in simulation from any point, represented as black markers in Figure 7.19. This choice stems from the low statistical precision in simulation from the variation with $f_{\mathrm{FSR}} = 4$, originating from a large spread of weights. Uncertainties from

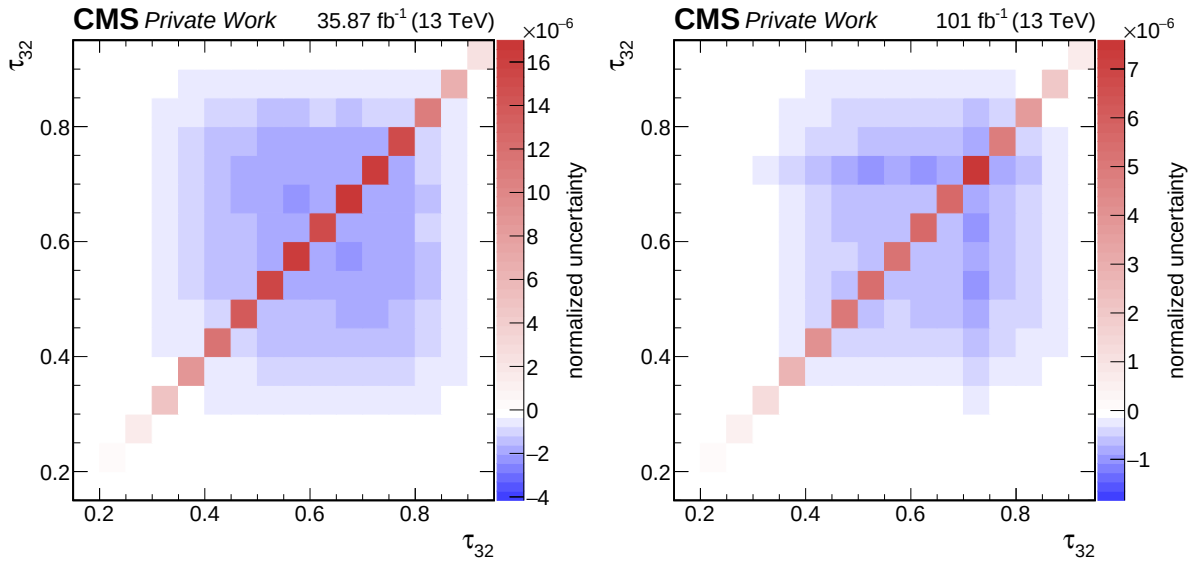


**Figure 7.20:** Covariance matrix representing the statistical uncertainty in data for the normalized $\tau_{32}$ distribution in AK8 jets reconstructing the hadronic decay of boosted top quarks in 2016 (left) and the combination of 2017 and 2018 (right). The red and blue bins denote correlated and anti-correlated bins, respectively. The primary contribution to the $f_{\mathrm{FSR}}$ uncertainty arises from the statistical precision in the data.

the jet calibration encompass the JEC, additional XCone corrections and the newly determined JMS. It has been verified that the jet calibrations affect the event yield but do not alter the shape of the $\tau_{32}$ distribution. These changes fall within the statistical uncertainties, excluding any biases to the JMS measurement. For the model uncertainties the UE tune, $h_{\mathrm{damp}}$ and the modeling of the ISR are considered.

The dominant uncertainty arises from the statistical precision of the data. The covariance matrices are illustrated in Figure 7.20 for 2016 (left) and the CP5 dataset (right). The anti-correlation between different bins is evident, as an increase in one bin content necessitates a decrease in another.

Figure 7.21 illustrates the $\chi^2$ function for 2016 (left) and the CP5 dataset (right). Best-fit values are obtained from $\chi^2_{\mathrm{min}}$, with uncertainties corresponding to one standard deviation taken at $\chi^2 = \chi^2_{\mathrm{min}} + 1$. The values are $f_{\mathrm{FSR}} = 0.97 \pm 0.07$ for 2016 and $f_{\mathrm{FSR}} = 0.33 \pm 0.02$ for the CP5 dataset. For 2016, the best-fit value indicates that data are adequately described by the default CUETP8M2T4 tune. In contrast, the value for the CP5 dataset shows that higher FSR energy scales describe data better in comparison to the initial set of parameters. However, in both measurements, the uncertainty has been significantly reduced with respect to the previous range of $f_{\mathrm{FSR}} = 0.5$ and 2 used for the corresponding one standard deviation.

The $f_{\mathrm{FSR}}$ values can be translated to values of $\alpha_{\mathrm{S}}^{\mathrm{FSR}}(m_{\mathrm{Z}}^2)$ using the five active flavors on the four-loop evolution of $\alpha_{\mathrm{S}}$ [173]. The best-fit values yield $\alpha_{\mathrm{S}}^{\mathrm{FSR}}(m_{\mathrm{Z}}^2) = 0.1373^{+0.0017}_{-0.0018}$ for 2016 and $\alpha_{\mathrm{S}}^{\mathrm{FSR}}(m_{\mathrm{Z}}^2) = 0.1416^{+0.0018}_{-0.0019}$ for the CP5 dataset. These values do not represent a direct measurement of $\alpha_{\mathrm{S}}^{\mathrm{FSR}}$, which requires a more sophisticated treatment of theory uncertainties. However,

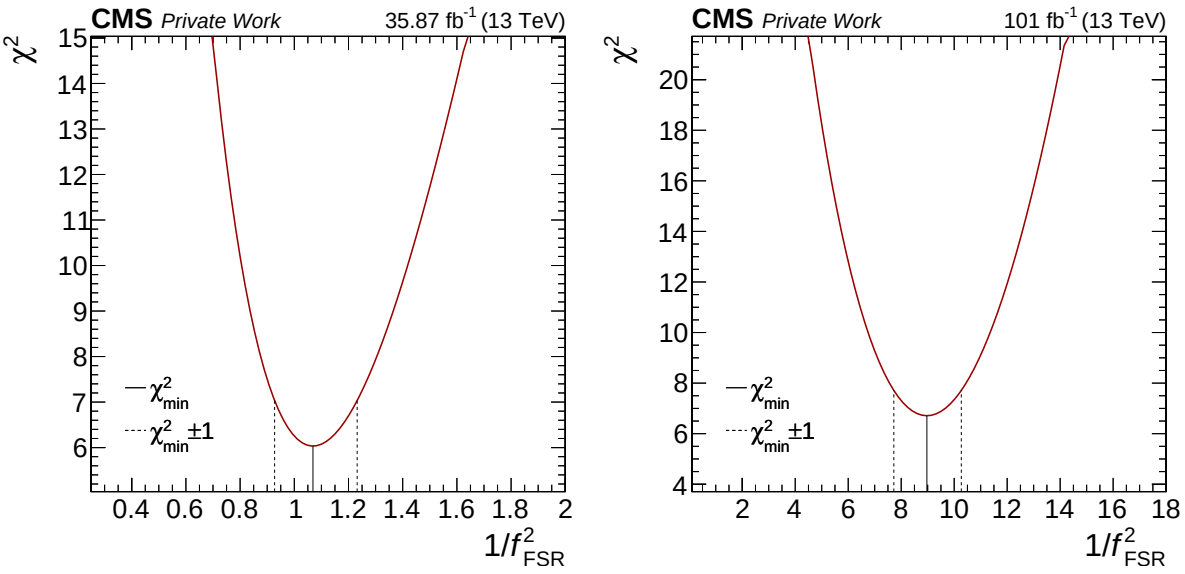


**Figure 7.21:** The $\chi^2$ for the extraction of $f_{\mathrm{FSR}}$ from the $\tau_{32}$ distribution from AK8 jets clustering the full hadronic top quark decay. Simulation in 2016 (left) utilize the CUETP8M2T4 tune and for those from 2017 and 2018 the CP5 tune from PYTHIA each. The value describing data best is extracted from the minimum $\chi^2_{\mathrm{min}}$ (solid line) and the uncertainty corresponding to one standard deviation at $\chi^2 = \chi^2_{\mathrm{min}} + 1$ (dashed lines).

they can be used to calibrate the tunes in $\mathrm{t\bar{t}}$ samples generated with POWHEG +PYTHIA. The proximity and compatibility of these values compared to the initial $\alpha_{\mathrm{S}}^{\mathrm{FSR}}(m_{\mathrm{Z}}^2)$ values for the CUETP8M2T4 and CP5 tunes illustrate the effectiveness of the calibration. Moreover, the results for 2016 are compatible with those for the combination of 2017 and 2018, which inherit dominant statistical uncertainties stemming from the large spread of weights used in the samples for $f_{\mathrm{FSR}} = 4$. It has been verified that adjusting the simulation with $f_{\mathrm{FSR}} = 0.33$ describes the data equally well or better for all relevant distributions in this measurement.

### 7.6.1 Stability against $m_{\mathrm{jet}}$ and $p_{\mathrm{T}}^{\mathrm{jet}}$

The same event selection is used as for the JMS calibration, the jet mass measurement and the extraction of the top quark mass. Any potential biases need to be excluded to ensure a proper measurement of the FSR modeling without any correlations to other parameters of interest in this analysis. Shape-shifting effects of the $\tau_{32}$ distribution for variations in the jet corrections have been ruled out by comparing the normalized distributions. The compatibility with different $m_{\mathrm{top}}$ hypotheses has been tested using the same approach. While larger fluctuations in the $\tau_{32}$ distribution are evident due to the limited statistical precision of the $m_{\mathrm{top}}$ samples, and several bins deviate from the nominal value of $m_{\mathrm{top}} = 172.5\,\mathrm{GeV}$, no consistent trend is observed. Furthermore, to support the hypothesis that $\tau_{32}$ is not correlated to the jet mass measurement in decays of boosted top quarks, the $f_{\mathrm{FSR}}$ extraction has been performed for several bins of $m_{\mathrm{jet}}$ from the AK8 jets. These are summarized in Figure 7.22 (left) showing the extracted $f_{\mathrm{FSR}}$ value for 2016 and the CP5 dataset in dependence of the $m_{\mathrm{jet}}$ bins. For all bins up to $m_{\mathrm{jet}} = 200\,\mathrm{GeV}$,

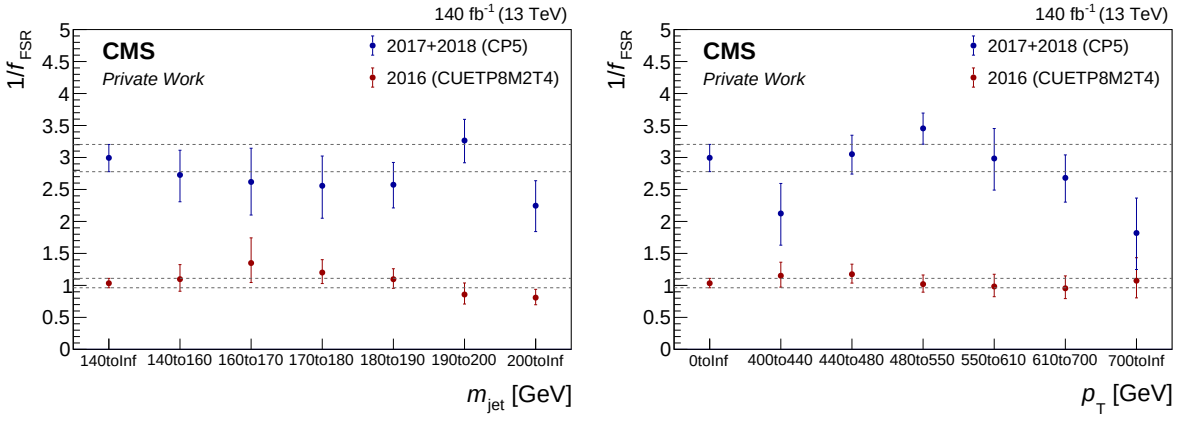


**Figure 7.22:** The dependence of the extracted $f_{\mathrm{FSR}}$ value describing data best in bins of $m_{\mathrm{jet}}$ (left) and $p_{\mathrm{T}}^{\mathrm{jet}}$ (right) of the AK8 jet. Shown are the extractions for 2016 (red) with the CUETP8M2T4 tune and the combination of 2017 and 2018 (blue) utilizing the CP5 tune. The values extracted from the inclusive bins is indicated by the dashed lines.

the measured $f_{\mathrm{FSR}}$ to describe data best are compatible to the inclusive mass range. Only for the last mass bin with $m_{\mathrm{jet}} > 200\,\mathrm{GeV}$ a deviation in both years is visible, which is expected based on the fraction of overlapping extracted $f_{\mathrm{FSR}}$ factors within the 68 % CL intervals. Generally, the hypothesis that the $\tau_{32}$ is independent of $m_{\mathrm{jet}}$ is confirmed within the uncertainties.
The modeling of the FSR is complex and depends on several factors. In order to confirm that the uncertainty is well described by the factors extracted from changes in the $N$-subjettiness distribution, $f^{\mathrm{FSR}}$ is extracted for various bins in $p_{\mathrm{T}}^{\mathrm{jet}}$ of the selected AK8 jets. The amount of FSR in one process depends on $p_{\mathrm{T}}^{\mathrm{jet}}$ and therefore these studies allow to check for any biases in the measurement performed in the previous sections. Figure 7.22 (right) shows the comparison between the extracted $f^{\mathrm{FSR}}$ values in the inclusive measurement and from the various $p_{\mathrm{T}}^{\mathrm{jet}}$ bins. In both datasets, from 2016 and CP5, no trend is visible and most values are compatible within one standard deviation. For high $p_{\mathrm{T}}$ and $m_{\mathrm{jet}}$, more unmerged events are selected which impact the $f_{\mathrm{FSR}}$ measurement. The same applies for the $p_{\mathrm{T}}$ region close to the $p_{\mathrm{T}}$ threshold of the XCone jet to select boosted top quark events. AK8 jets are much smaller and do not capture the hadronic decays of boosted top quarks as efficient as the two-step clustering procedure with the XCone jet algorithm and thus selects more unmerged $\mathrm{t\bar{t}}$ events.

## 7.7 Differential Cross Section Measurement

Cross section measurements are performed at the particle level, requiring corrections for detector effects and pileup in data. This correction process, known as unfolding, adjusts the data from detector level to particle level. The unfolding setup used in this analysis is based on TUnfold [174] and is optimized in the previous measurement [18]. An overview of the unfolding setup is given in Section 7.7.1, where a detailed description and the motivation for the chosen parameters can be found in Ref. [18, 122]. The treatment of the different uncertainty sources

is described in Section 7.7.2, and the incorporation of the newly obtained FSR factor into the unfolding procedure is discussed. The results for the differential $\mathrm{t\bar{t}}$ production cross section are summarized in Section 7.7.3.

### 7.7.1 Unfolding

The TUNFOLD framework provides a regularized and multidimensional unfolding method. The core concept is to build a matrix $A$ that captures the migration from a particle-level bin $x_i$ to a detector-level bin $y_i$. Generally, the inverse of $A$ describes the reverse migration. The unfolding process minimizes the Lagrangian $\mathscr{L}$, which comprises three component with

$$\mathscr{L} = \mathscr{L}_1 + \mathscr{L}_2 + \mathscr{L}_3 \tag{7.5}$$

The first term represents the least squares with

$$\mathscr{L}_1 = (\vec{y} - A\vec{x})^T V_{yy}^{-1} (\vec{y} - A\vec{x}), \tag{7.6}$$

where $\vec{x}$ is the unfolded result, $\vec{y}$ the detector level distribution, $V$ is the covariance matrix constructed from $\vec{y}$ and $A$ is the migration matrix. Differences between particle and detector level necessitate careful treatments when inverting $A$. Variations at the particle level may be less pronounced at the detector level due to the finite detector resolution than vice versa and small variations in data can lead to large variations on particle level. Regularization addresses this issue by mitigating fluctuations in the data due to finite statistical precision. The second term, which includes regularization, is defined as

$$\mathscr{L}_2 = \tau^2 (\vec{x} - f_b \vec{x}_0)^T L^T L (\vec{x} - f_b \vec{x}_0), \tag{7.7}$$

where $\tau$ is the regularization strength, which mitigates deviations of the unfolded results from $f_b \vec{x}_0$. In this analysis $f_b$ is set to the ratio of event yields in simulation used to determine $A$ and the distribution being unfolded, accounting for normalization differences. The regularization strength is chosen by minimizing the global correlation coefficient [175]. The matrix $L$ determines the regularization condition, where this analysis uses the curvature mode. The third term $\mathscr{L}_3$ represents an area constraint enforcing a normalization of $\vec{x}$, but is not used in this analysis.

The migration matrix in this analysis is constructed from simulated $\mathrm{t\bar{t}}$ samples generated with POWHEG, using $m_{\mathrm{top}} = 172.5\,\mathrm{GeV}$. To capture events migrating into and out of the fiducial region, various sideband regions are constructed by lowering selection requirements. These sidebands represent orthogonal phase spaces. The minimum $p_{\mathrm{T}}$ threshold for the XCone jet is set to $350 < p_{\mathrm{T}} < 400\,\mathrm{GeV}$, the lepton $p_{\mathrm{T}}$ is lowered to $55 < p_{\mathrm{T}}^{\ell} < 60\,\mathrm{GeV}$, at least one XCone subjet must have $10 < p_{\mathrm{T}} < 30\,\mathrm{GeV}$, the invariant mass of the XCone jet must be less than the invariant mass of the lepton jet, and one AK4 jet must pass a less stringent b-tagging

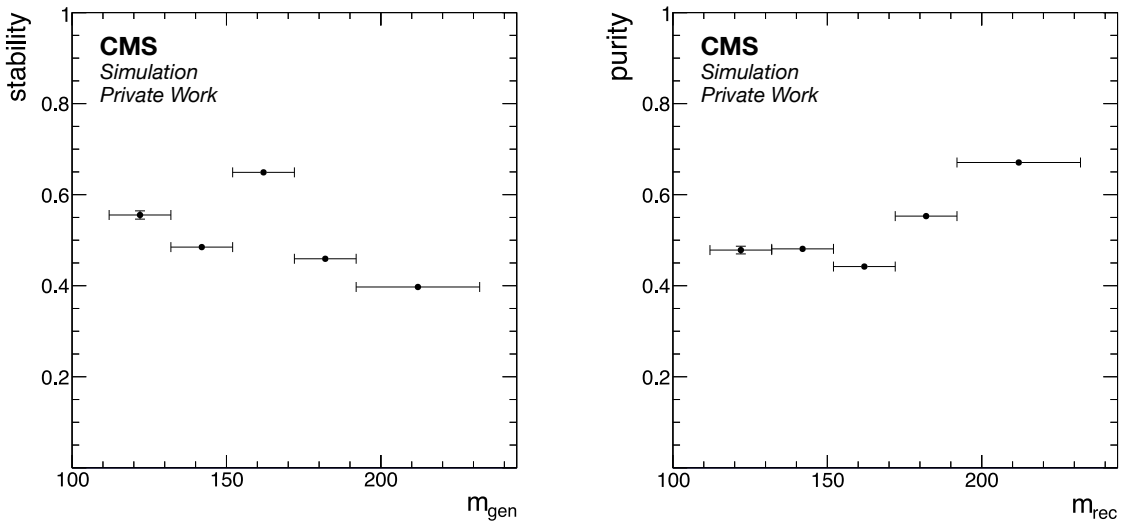


**Figure 7.23:** Stability (left) and purity (right) of the unfolding setup for the combined channels in 2018. Results for 2016 and 2017 show a similar performance.

requirement but not the criteria from the measurement phase space. At the particle level, similar sidebands are defined, except for the b-tagging requirement, as it is applicable solely at the detector level. These sidebands ensure that most migrations into and out of the fiducial region are within the unfolding setup and not solely estimated from simulations.

All phase spaces based on $p_{\mathrm{T}}^{\mathrm{jet}}$ and $m_{\mathrm{jet}}$ are further subdivided into a finer binning to enhance the unfolding procedure and achieve high granularity. These bins are optimized to obtain the highest precision for model uncertainties from $\mathrm{t\bar{t}}$ simulations and in the extraction of $m_{\mathrm{top}}$. Bins of $p_{\mathrm{T}}$ at the detector level increase sensitivity to $p_{\mathrm{T}}$-dependent effects and are combined after the unfolding. At the detector level, the $m_{\mathrm{jet}}$ binning is selected to ensure that each bin contains sufficient events. For the particle level, the bin width is chosen such that they include twice the jet mass resolution. A resolution of 6 % in the mass peak with 172 GeV corresponds to a bin width of about 20 GeV. The bin edges of $m_{\mathrm{jet}} \in [112, 132, 152, 172, 192, 232]$ GeV are selected to ensure a linear dependence of the bin content as a function of $m_{\mathrm{top}}$ from different simulated templates. They are further subdivided into four bins during the unfolding with $\Delta m_{\mathrm{jet}} = 10\,\mathrm{GeV}$ to increase the sensitivity. To avoid large bin-to-bin correlations, these bins are merged afterwards. Overflow and underflow bins do not add sensitivity to the measurement but are considered for proper normalization.

The performance of the unfolding setup and the migration between the particle and detector levels are evaluated with the purity and stability. Purity is defined as the fraction of events that are generated in the same bin as they are reconstructed. Conversely, the stability is the fraction of events that are reconstructed in the same bin as they are generated. Both metrics are shown for 2018 in Figure 7.23 as a function of $m_{\mathrm{jet}}$, with stability on the left and purity on the right. The performance in 2016 and 2017 is very similar and exceeds 40 % in each bin. Only the the stability in 2018 is slightly under 40 %, due to the low statistical precision in that bin.

In total, the migration matrix comprises 200 bins at the detector level and 72 bins at the particle level. Background contributions are estimated using simulation and subtracted from data prior to the unfolding. Afterwards, the data are corrected for the newly calibrated FSR scale. All variations of the FSR parameter are unfolded, and the bin content is interpolated at the best fit value. The correction for data is derived from the expected shift in the bin content in the simulation, resulting in a shift below 5 %. Only in 2018 the first bin is shifted by 40 %, which can be explained by the low statistical precision in this bin. All three years are unfolded individually to check for potential biases originating from different tunes. Considering the calibration of the FSR scale, these are well in agreement within one standard deviation. The same holds true for the separate unfolding of the $e$+jets and $\mu$+jets channels. For the final measurement, all data and simulated samples are combined prior to the unfolding.

### 7.7.2 Uncertainties

Several factors impact the resulting measurement of the unfolded $m_{\text{jet}}$ distribution. These effects include statistical uncertainties as well as systematic uncertainties related to the experimental setup or the modeling of the $\mathrm{t\bar{t}}$ process. Generally, the impact of each source on the five output bins after the unfolding is used to estimate each uncertainty source. However, in the scope of this section, the changes in the two peak bins $m_{\text{top}} \in [152, 172, 192]$ GeV are considered as a reference, if not stated otherwise, as those bins show the greatest sensitivity to $m_{\text{top}}$. For each uncertainty, a covariance matrix is constructed, capturing the changes in the distribution and the bin-to-bin correlations. In total, four types of uncertainties are identified: statistical, experimental, model, and theory uncertainties. Systematic uncertainties are derived only from simulated $\mathrm{t\bar{t}}$ events unless the uncertainty is directly related to a background process.

#### Statistical Uncertainties

Statistical uncertainties arise from the finite statistical precision in data. These uncertainties are propagated through the unfolding setup using Gaussian error propagation, taking into account the bin-to-bin correlations from normalization and from the unfolding. In the previous measurement [18], these uncertainties were up to 7 % in the peak bins of the unfolded distribution. By including 2017 and 2018, the size of the collected data increased by a factor of four, improving the peak bin uncertainty to approximately 3 % and reducing the first mass bin uncertainty from 36 % to 16 %.

#### Experimental Uncertainties

Experimental uncertainties arise from the calibration of physical objects in the detector. These uncertainties are estimated by constructing a new migration matrix, varying the correction factors by one standard deviation at the detector level. The resulting shift in the migration matrix,

relative to the nominal one, leads to a shift in the bins of the unfolded $m_{\text{jet}}$ distribution. For each variation, the average shift is determined by considering the positive and negative variations in each bin. The variation of one parameter with the largest total shift is used to derive the bin-to-bin correlations, which are conservatively estimated with a correlation coefficient of $\rho = \pm 1$.

For the JMS, the one standard deviation is obtained from the semi-minor axis where $f^{\text{JEC}}$ and $f^{\text{XCone}}$ are varied in the same direction. While the JMS is derived for light-flavor quarks, the JMS flavor uncertainty accounts for the difference in the detector response for different jet flavors. This uncertainty, estimated from response differences in PYTHIA and HERWIG, is applied to the subjets matched with AK4 b-tagged jets. The JES and JER are also applied to AK4CHS jets to properly calculate the $p_{\text{T}}^{\text{miss}}$ and XCone subjets for any selection criterion. XCone subjets are further corrected with the additional XCone corrections to account for the differences to AK4 jets. Furthermore, uncertainties arise from aligning the pileup profile in simulation to match that in the data, and from the instantaneous luminosity, which is varied by 1.2 %, 2.3 %, 2.5 % or 1.6 % for 2016, 2017, 2018 or the combined dataset, respectively [176, 177, 178]. Moreover, uncertainties in prefiring weight in simulation are accounted for, as well as scale factors applied for the trigger and lepton identification for each selected lepton. Backgrounds are estimated from simulation and subtracted from data prior to the unfolding. The statistical uncertainties in these samples are significantly smaller compared to the uncertainties in the cross sections of the corresponding processes. These uncertainties are 19 % and 23 % for the two dominant background processes, W+jets and single top quark production, respectively, and 100 % for other SM processes. The statistical uncertainties in the simulation, are considered as part of the experimental uncertainties.

A summary of the experimental uncertainties is shown in Figure 7.24 for the unfolded distribution before (left) and after (right) normalization to the fiducial cross section. Each relevant experimental uncertainty source is displayed in comparison to the statistical and total experimental uncertainties. The latter is derived by adding all contributions and the statistical uncertainty for each bin in quadrature. In the previous measurement, the largest experimental uncertainty was the JES, which contributed 12 % and 31 % in the peak bins when propagated to the JMS. By introducing a dedicated JMS calibration and treating the JMS and JES separately, their contributions are now 5 % and 4-7 % in the peak bins, respectively. The JMS flavor reaches approximately 4 %. This reduction is achieved since the JMS only affects the jet mass, while the JES impacts only the $p_{\text{T}}^{\text{jet}}$. The current largest experimental uncertainty arises from the JER, contributing 6-7 %. Other contributions are below the statistical uncertainties including the additional XCone corrections, the reweighing of the pileup profile and the statistical uncertainties in simulations. Uncertainties arising from instantaneous luminosity, the scale factors for the trigger and lepton identification, and the corrections to account for prefiring are found to be negligible.

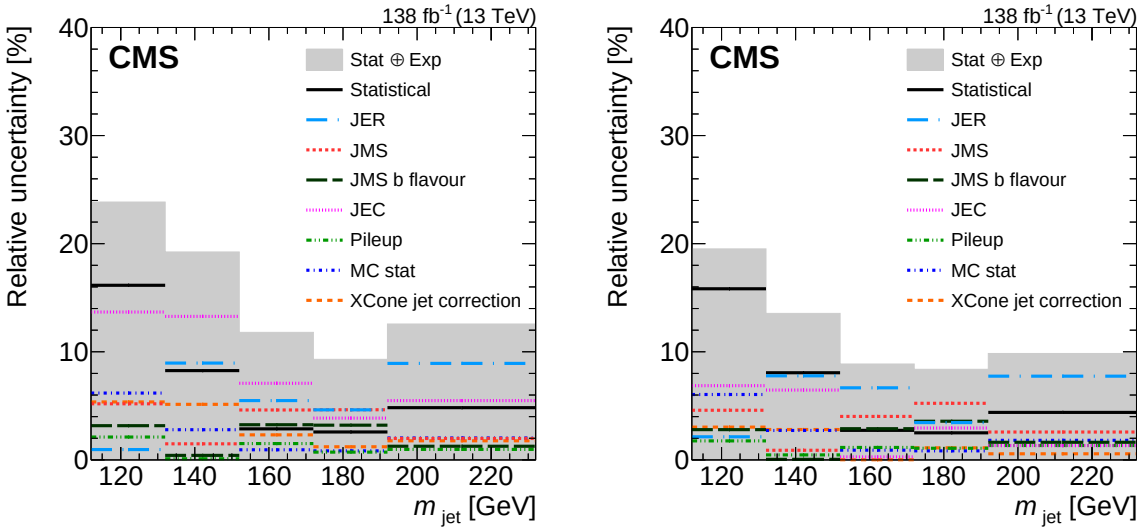


**Figure 7.24:** Relative experimental uncertainties for the differential $t\bar{t}$ production cross section as a function of $m_{\text{jet}}$ before (left) and after (right) normalizing to the fiducial cross section. Several contributions (colored lines) are shown in comparison to the statistical uncertainties (black line) and total uncertainty, evaluated from all experimental uncertainties and the statistical uncertainty (grey area). Published in Ref. [6].

## Model and Theory Uncertainties

Data are unfolded with a migration matrix constructed from $t\bar{t}$ simulations generated with POWHEG. Model uncertainties address the model parameters in these simulations that might not accurately represent the data, potentially leading to a bias in the unfolded distribution. To quantify these uncertainties, the $m_{\text{jet}}$ distributions obtained from variations of the model parameters are unfolded using the nominal migration matrix. Differences between the unfolded distribution and the particle level distribution from the corresponding variation are then considered as uncertainties. The variation of one parameter that leads to the largest shift in the mean value of the $m_{\text{jet}}$ distribution is used to define the uncertainty. This approach implies that statistical fluctuations in the varied simulation are absorbed into the model uncertainties. In low statistics samples, this can lead to an overestimation of the model dependence. Similar to the treatment of experimental uncertainties, a covariance matrix is constructed for each variation, including bin-to-bin correlations. It has been verified in the previous measurement that constructing a new migration matrix for each variation, similar to the approach used for experimental uncertainties, yields compatible results.

Model parameter uncertainties include variations in the PDFs, choice of $m_{\text{top}}$, scales, different MC generators, and particle showers including the ISR and FSR. For scale variations, the factorization scale $\mu_{\text{F}}$ and the renormalization scale $\mu_{\text{R}}$ are each varied by a factor of 2, resulting in six total variations: both $\mu_{\text{F}}$ and $\mu_{\text{R}}$ up (down), $\mu_{\text{F}}$ central with $\mu_{\text{R}}$ up (down), and $\mu_{\text{F}}$ up (down) with $\mu_{\text{R}}$ central. The largest uncertainty arises when both scales are varied in the same direction, and is further considered in this analysis. For the uncertainties from the PDF, 100 replicas

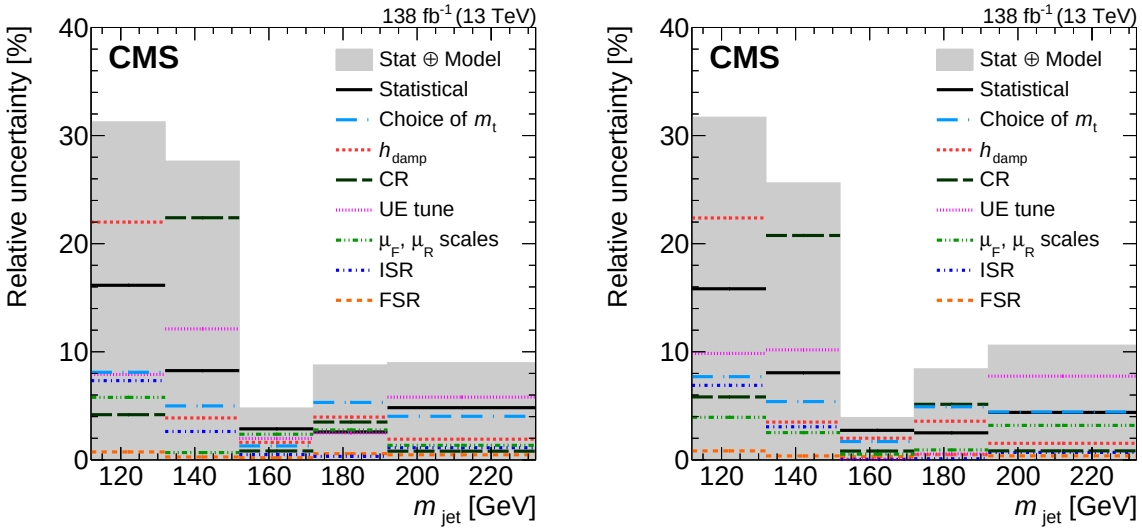


**Figure 7.25:** Relative model uncertainties for the differential cross section as a function of $m_{\text{jet}}$ before (left) and after (right) normalizing to the fiducial cross section. Several contributions (colored lines) are shown in comparison to the statistical uncertainties (black line) and total uncertainty, evaluated from all model uncertainties and the statistical uncertainty (grey area). Published in Ref. [6].

of the NNPDF [179] set are unfolded, and the one with the largest shift is taken. Although this is a conservative estimation, it remains negligible in this analysis. The matching of the matrix element and the parton showers is controlled with the parameter $h_{\text{damp}} = 1.58^{+0.66}_{-0.59}$ [56], which is varied within its uncertainties. For color reconnection (CR), three models are utilized: the gluon-move scheme [180], the QCD-inspired scheme [181], and the MPI-based scheme [182]. The uncertainty from the underlying event (UE) is small due to the two-step clustering approach, which acts as a grooming algorithm. The ISR scale is varied by a factor of 2 for both tunes, the CUETP8M2T4 and CP5 [56]. The specific treatment of the choice of $m_{\text{top}}$ and the FSR scale is detailed below.

A summary of the most relevant model uncertainties is displayed in Figure 7.25 for the relative uncertainties of the unfolded distribution before (left) and after (right) the normalisation to the fiducial cross section. The largest uncertainty arises from the choice of $m_{\text{top}}$ with 1-5 % and the choice of the model of the color reconnection with 1-4 %. Both uncertainties are affected by a low statistical precision in the available samples, which is expected to contribute significantly to these uncertainties.

The modeling of b fragmentation has a negligible impact because the entire decay is clustered into one jet. To estimate the corresponding uncertainty, the $p_{\text{T}}$ spectrum of the b quark is significantly reweighted. This exaggerated effect on the b quark $p_{\text{T}}$ results in a negligible bias in the unfolded distribution, translating to an uncertainty of 0.08 GeV. As the modeling of b fragmentatio is highly overestimated, the uncertainty is not included in this measurement. Additionally, the invisible fraction of semileptonic b hadron decays was studied and found to

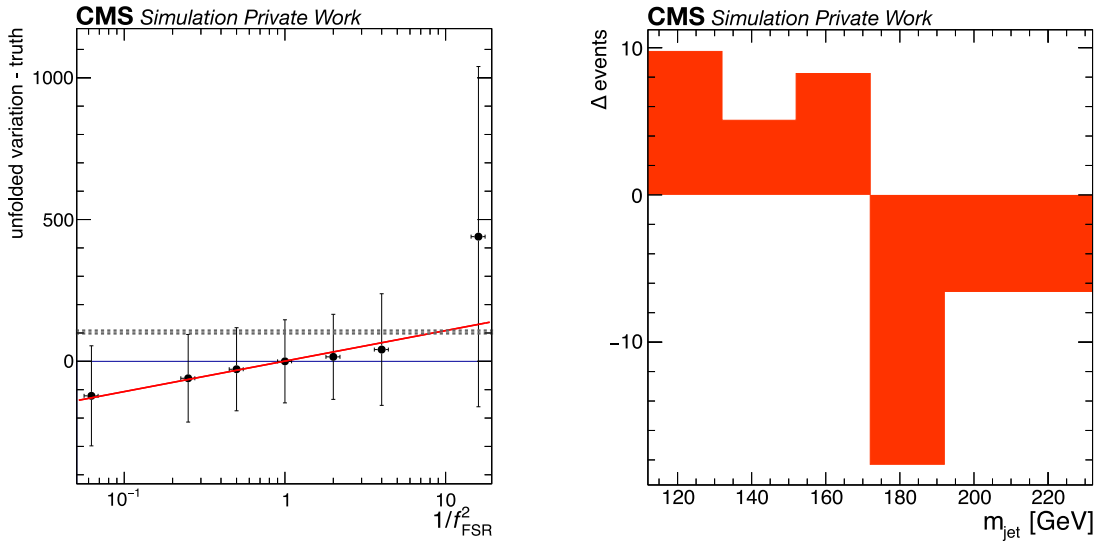


**Figure 7.26:** Differences of the event yield in one bin ($132 < mjet < 152\,\text{GeV}$) of the unfolded $m_{\text{jet}}$ distribution as a function of $f_{\text{FSR}}$ relative to the particle level prediction (left). The differences are fit with a logarithmic function (red line). The difference corresponding to the uncertainties of the best fit value of $f_{\text{FSR}} = 0.33$ are displayed with dashed lines. The event yield differences for each $m_{\text{jet}}$ bin, evaluated at the best fit value and the one standard deviation is shown on the right. Shown are simulations from 2018 utilizing the CP5 tune.

be negligible as well.

The evaluation of uncertainties from the choice of $m_{\text{top}}$ and the FSR scale is handled differently compared to the sources described above. In both cases, the differences between the unfolded variation and the truth in each bin $i$ are described as a function of the varied parameters, $m_{\text{top}}$ and $1/f^2_{\text{FSR}}$. For the FSR scale, the variations of $f_{\text{FSR}}$ correspond to the up and down variations of $f_{\text{FSR}}$ and $1/f_{\text{FSR}}$, respectively. Variation in the unfolded distribution for the bin $132 < m_{\text{jet}} < 152\,\text{GeV}$ as a function of $1/f^2_{\text{FSR}}$ are displayed in Figure 7.26 (left). Each marker is associated with one variation in $f_{\text{FSR}}$ and corresponds to the respective difference of the event yield in that particular bin to the nominal value of $f_{\text{FSR}} = 1$. The dependence of the difference in the event yield is described using a logarithmic hypothesis based on Equation 7.4. The differences in the bin content are better described by omitting quadratic term. The differences are evaluated at the best-fit values determined in Section 7.6 and the one standard deviation (dashed lines). Figure 7.26 (right) shows the difference for each bin of the unfolded $m_{\text{jet}}$ distribution considered for the extraction of $m_{\text{top}}$. In the previous measurement, the largest model uncertainty was the modeling of the FSR, which contributed 8-15 % in the peak bins. With the dedicated calibration in Section 7.6, the uncertainty is reduced to below 2 % in both bins and considered to be negligible.

For the choice of $m_{\text{top}}$, a linear function is fitted to the differences of the five values $m_{\text{top}} \in [169.5, 171.5, 172.5, 173.5, 175.5]$ GeV relative to the nominal value with $m_{\text{top}} = 172.5\,\text{GeV}$. The uncertainties are evaluated from the fit values at $\Delta m_{\text{top}} = \pm 1\,\text{GeV}$ from the nominal value.

This range is found to describe the data best, and the absolute uncertainty in each bin is taken as the average of both directions. A new covariance matrix is then constructed from these uncertainty values. The correlation between the bins is derived from the $m_{\text{top}}$ variation that causes the largest shift in the $m_{\text{jet}}$ distribution. It has been verified that the correlations from different $m_{\text{top}}$ variations do not significantly affect the results.
Theory uncertainties address uncertainties in the particle-level prediction due to variations of modeling parameters. The same set of parameters used for the model uncertainties, namely the scales $\mu_{\text{F}}/\mu_{\text{R}}$, ISR, FSR, CR, UE tune, and $h_{\text{damp}}$, are taken into account here, except for the choice of $m_{\text{top}}$. The FSR variation is taken from the provided variation for the one standard deviation with $f_{\text{FSR}} = 0.5$ and 2, and is not calibrated separately as for the model uncertainties. Each variation is compared to the POWHEG simulation at the particle level, used to construct the migration matrix, referred to as POWHEG truth. For each source, the variation with the largest shift in the mean of the $m_{\text{jet}}$ distribution with respect to the POWHEG truth is considered for the uncertainties. The covariance matrix is constructed from the differences in each bin of the largest variation and POWHEG truth.

### 7.7.3 Results

Prior to the unfolding, data from all years, as well as the $e$+jets and $\mu$+jets channels, are combined. Additionally, each year and channel is unfolded separately to ensure no biases are present. The resulting differential $\mathrm{t\bar{t}}$ production cross section as a function of the jet mass in the fiducial region is displayed in Figure 7.27 for each year individually and for the combined dataset. Data are compared to simulation from POWHEG, which shows theoretical uncertainties. In 2016 (upper left), the uncertainty is larger than in 2017 (upper right) and 2018 (lower left), due to the different tunes used in these years. The large uncertainty indicates that the variation of the FSR scale by a factor of 2 in the tune CUETP8M2T4 overestimates the uncertainty, as it decreases for the data samples with the tune CP5. For the combined dataset (lower right) the precision of the total theoretical uncertainty is similar to 2017 and 2018.
The $\mathrm{t\bar{t}}$ production cross section in the fiducial region in the mass range $112 < m_{\text{jet}} < 240\,\text{GeV}$ is determined with

$$\begin{aligned} \sigma^{2016} &= 599.36 \pm 13.59\,(\text{stat}) \pm 48.15\,(\text{exp}) \pm 18.72\,(\text{model})\ \text{fb} \\ \sigma^{2016}_{\text{MC}} &= 693.74 \pm 107.83\,\text{fb} \end{aligned} \tag{7.8}$$

for 2016,

$$\begin{aligned} \sigma^{2017} &= 599.40 \pm 13.71\,(\text{stat}) \pm 42.73\,(\text{exp}) \pm 25.72\,(\text{model})\ \text{fb} \\ \sigma^{2017}_{\text{MC}} &= 695.87 \pm 56.90\,\text{fb} \end{aligned} \tag{7.9}$$

for 2017, and

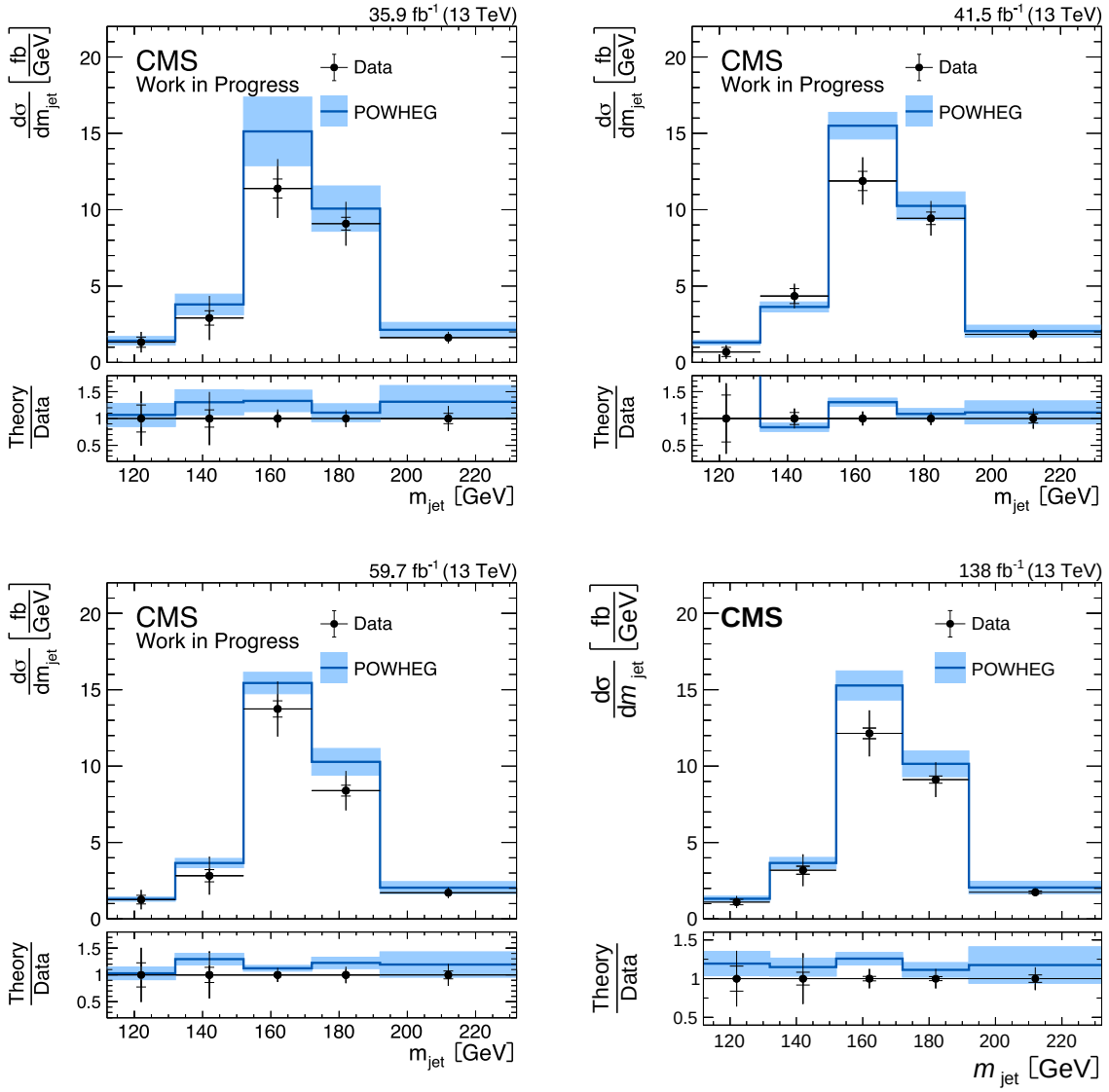


**Figure 7.27:** Differential $\mathrm{t\bar{t}}$ production cross section as a function of $m_{\mathrm{jet}}$ for 2016 (upper left), 2017 (upper right), 2018 (lower left) and the combined dataset of all three years (lower right). Data (black markers) is compared to predictions of the $\mathrm{t\bar{t}}$ production with POWHEG. The total uncertainties are represented by vertical bars and the statistical uncertainties by short vertical bars. The theoretical uncertainties in simulation are indicated by the filled areas (light blue). The lower panel shows the ratio of the predictions to data. The distribution for the combination of all three years is published in Ref. [6].

$$\begin{aligned}\sigma^{2018} &= 590.39 \pm 11.33\,(\mathrm{stat}) \pm 56.22\,(\mathrm{exp}) \pm 21.03\,(\mathrm{model})\ \mathrm{fb} \\ \sigma^{2018}_{\mathrm{MC}} &= 695.06 \pm 53.15\,\mathrm{fb}\end{aligned} \tag{7.10}$$

for 2018.

The overall uncertainties for each year are calculated by combining the respective covariance matrices, which includes the statistical, the experimental, and the model uncertainties. All values obtained in data agree within one standard deviation with the predictions in simulations.

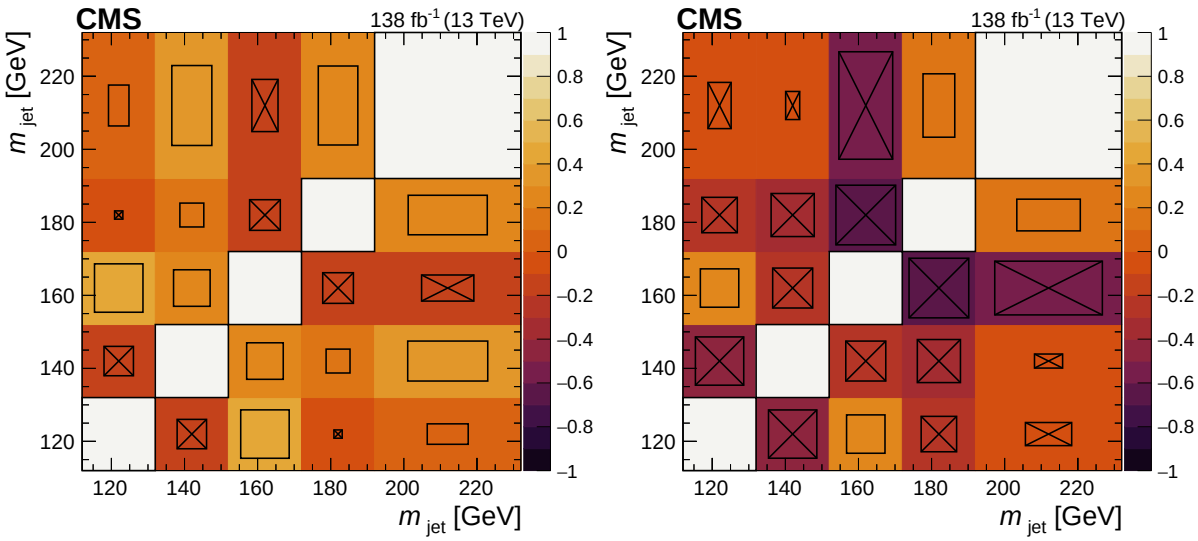


**Figure 7.28:** The covariance matrix for the unfolded $m_{\text{jet}}$ distribution before (left) and after (right) the normalization to the total cross section. Shown are the negative (boxes with crosses) and positive (empty boxes) correlations. Published in Ref. [6].

The total covariance matrix for the combination of all three years is illustrated in Figure 7.28 before (left) and after (right) the normalization to the total cross section Here, all sources of statistical, experimental, and model uncertainties are included.

## 7.8 Top Quark Mass Measurement

The top quark mass $m_{\text{top}}$ is extracted from the normalized unfolded differential $\mathrm{t\bar{t}}$ production cross section. In principle, one would like to compare this distribution to analytic calculations. However, these do not exist yet for the phase space of the measurement presented here. Therefore, for the time being, the extraction is performed by only comparing the measured cross section to the prediction from POWHEG. The extraction of $m_{\text{top}}$ is performed by comparing the normalized $\mathrm{t\bar{t}}$ production cross section to different $m_{\text{top}}$ hypotheses with $m_{\text{top}} \in [169.5, 171.5, 172.5, 173.5, 175.5]$ GeV. The linear template fit framework [183] is used to extract $m_{\text{top}}$. It analytically solves the parameter estimation problem by exploiting the linear dependence of the bins of the unfolded distribution as a function of $m_{\text{top}}$. Furthermore, the contributions of uncertainties to the measurement of $m_{\text{top}}$ can be extracted individually.
To verify that the mass can be extracted without any biases in the data, the mass is extracted from simulations using different $m_{\text{top}}$ hypotheses as pseudo data. This extraction process includes the full set of uncertainties. All $m_{\text{top}}$ extractions are compared to their true values, as shown in Figure 7.29. Ideally, the measured value should match the $m_{\text{top}}$ hypothesis in the simulation, denoted as $m_{\text{top}}^{\text{measured}} = m_{\text{top}}^{\text{true}}$. The extraction of all mass points is found to be compatible within one standard deviation of the ideal measurement. To further test for the absence of systematic shifts, a linear fit is performed across all measured mass values, and is compatible with the ideal

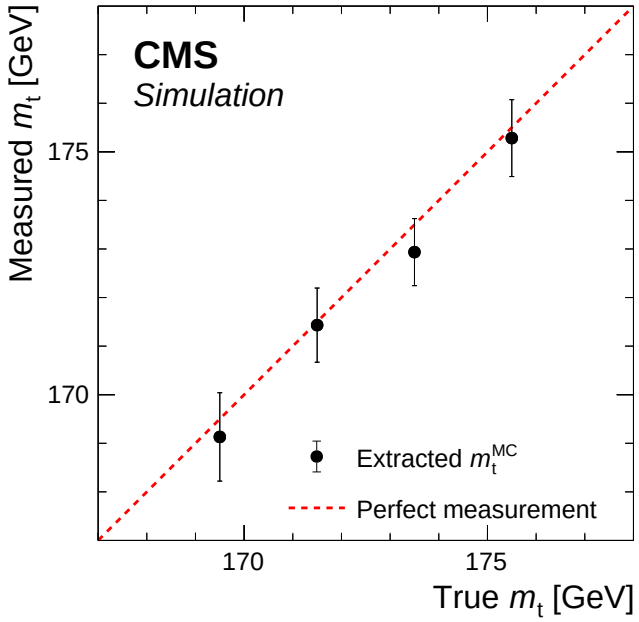


**Figure 7.29:** Top quark mass extraction using simulated $t\bar{t}$ samples with the $m_{top}$ hypothesis 169.5 GeV, 171.5 GeV, 173.5 GeV and 175.5 GeV as pseudo data. The perfect measurement where the measured value is equal to the true top quark mass in simulation is indicated by the red line. Published in Ref. [6].

measurement within the statistical uncertainties.

For the top quark mass measurement, data for all three years as well as the $e$+jets and $\mu$+jets channel are combined prior to the unfolding. As illustrated for the normalized unfolded $m_{jet}$ distribution in Figure 7.30, the bins in the peak regions are most sensitive to $m_{top}$. It has been verified that the mass measurements from different years yield similar results. The template fit for the $m_{top}$ extraction in the data is shown in Figure 7.31 and yields

$$\begin{aligned} m_{top} &= 173.06 \pm 0.24\,(\text{stat}) \pm 0.61\,(\text{exp}) \pm 0.47\,(\text{model}) \pm 0.23\,(\text{theo})\ \text{GeV} \\ &= 173.06 \pm 0.84\ \text{GeV}. \end{aligned} \tag{7.11}$$

In comparison to the previous analysis using 2016 data which achieved a precision 2.5 GeV on $m_{top}$, the precision has been improved by a factor of three. The individual uncertainties are listed in Table 7.2. The combination of the full Run 2 dataset has reduced the statistical uncertainty by a factor of 2. The dominant experimental uncertainties are now the JER with $\Delta m_{top}(\text{JER}) = 0.4\,\text{GeV}$ and the JMS and its corresponding flavor uncertainty, each contributing $\Delta m_{top}(\text{JMS}) = 0.27\,\text{GeV}$. Previously, the uncertainty from the JES resulted in $\Delta m_{top}^{\text{prev.}}(\text{JES}) = 1.5\,\text{GeV}$, but separating this source into the JMS, JMS flavor and JES has reduced the total uncertainty by a factor of three to $\Delta m_{top}(\text{JES+JMS+JMS flavor}) = 0.4\,\text{GeV}$. The most significant model uncertainty now arises from the choice of $m_{top}$ with $\Delta m_{top} = 0.4\,\text{GeV}$ followed by the CR model and the $h_{damp}$ with $\Delta m_{top} = 0.19\,\text{GeV}$ each. It is assumed that for choice

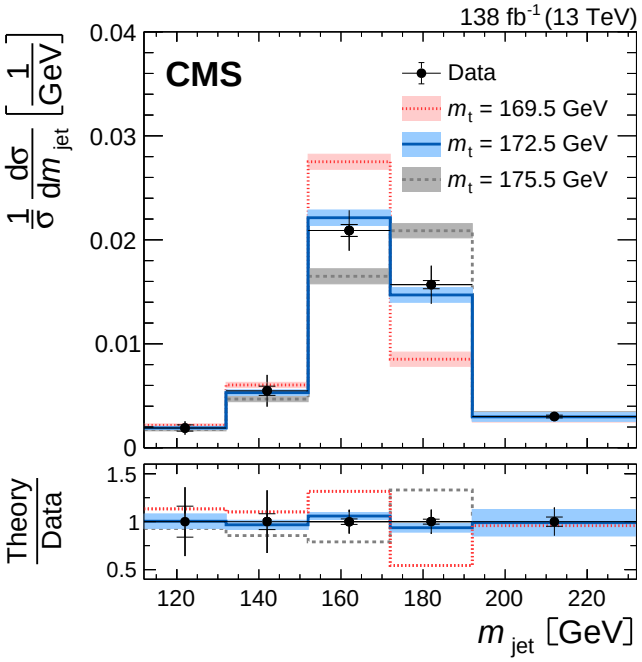


**Figure 7.30:** Normalized differential $\mathrm{t\bar{t}}$ production cross section for the years for the full Run 2 dataset. Data (black markers) is compared to simulation generated with POWHEG with the $m_{\mathrm{top}}$ hypothesis $m_{\mathrm{top}} = 169.5\,\mathrm{GeV}$ (red), $172.5\,\mathrm{GeV}$ (blue) and $175.5\,\mathrm{GeV}$ (gray). Statistical uncertainties are represented by the horizontal line on the error bars and the total uncertainty by the vertical line. Simulations are shown with theory uncertainties only. The lower panel shows the ratio of the $m_{\mathrm{top}}$ predictions to data. Published in Ref. [6].

of $m_{\mathrm{top}}$ and CR is significantly altered by the low statistical precision of the samples themselves. The sensitivity of the unfolding setup to $m_{\mathrm{top}}$ is further discussed in Section 7.9.

The improvement of the top quark mass measurement compared to previous measurements [17, 18] is shown in Figure 7.32. Major advancements in event reconstruction and the refined unfolding setup have led to a significant reduction in all uncertainty categories compared to the $\sqrt{s} = 8\,\mathrm{TeV}$ analysis. Additionally, the larger dataset compared to 2016 only has substantially increased the statistical precision in the boosted regime. The dedicated calibration of the JMS and the refined modeling of the FSR have contributed to a further enhancement of this measurement. With an uncertainty below 1 GeV, this measurement from boosted top quark production now achieves a precision comparable to the most accurate $m_{\mathrm{top}}$ measurements at threshold production.

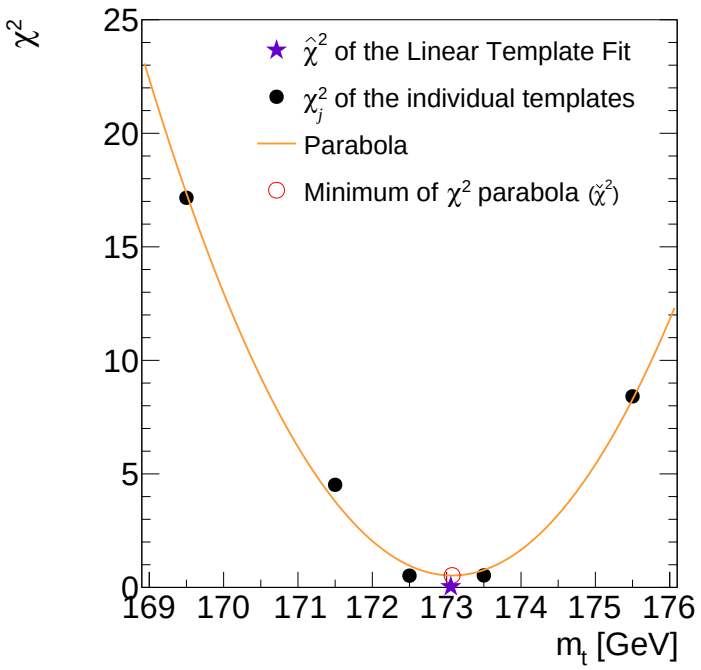


**Figure 7.31:** Extraction of the top quark mass from the normalized unfolded $m_{\text{jet}}$ distribution. A second order polynomial function (yellow) is fitted to the $\chi^2$ values for various $m_{\text{top}}$ hypothesis (black markers). The minimum of the $\chi^2$ function is indicated by the red circle. The setup is adapted from Ref. [183].

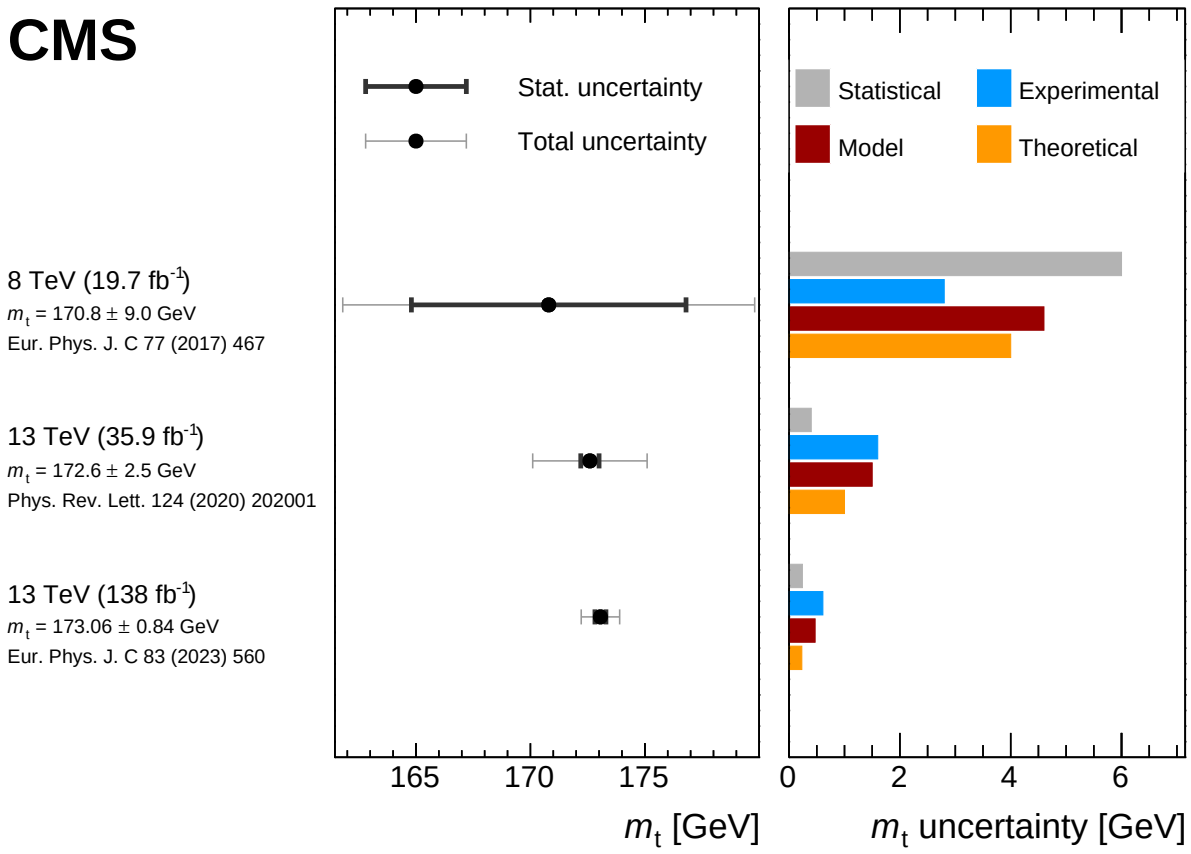


**Figure 7.32:** Comparison of the $m_{\text{top}}$ extractions from jet mass measurements in hadronic decays of boosted top quarks. Shown are the results of the measurements from $\sqrt{s} = 8\,\text{TeV}$ [17], at 13 TeV for 2016 [18] and the analysis presented in this thesis with the full data-taking period of Run 2 [6]. The left panel shows the measured $m_{\text{top}}$ value with the statistical (thick bars) and total (thin bars) uncertainties. The right panel shows the contribution from the each uncertainty group, namely the statistical (gray), experimental (blue), model (red), and theory (yellow) uncertainties. Taken from Ref. [69].

| **Source** | **Uncertainty** [ GeV] |
|---|---|
| Jet energy resolution | 0.38 |
| Jet mass scale | 0.37 |
| Jet mass scale b flavor | 0.26 |
| MC stat | 0.09 |
| Pileup | 0.08 |
| Jet energy scale | 0.07 |
| Additional XCone corrections | 0.01 |
| Backgrounds | 0.01 |
| **Experimental total** | 0.61 |
| | |
| Choice of $m_{\text{top}}$ | 0.41 |
| Colour reconnection | 0.17 |
| $h_{\text{damp}}$ | 0.09 |
| Underlying event tune | 0.09 |
| $\mu_{\text{F}}$, $\mu_{\text{R}}$ scales | 0.08 |
| ISR | 0.02 |
| FSR | 0.02 |
| **Model total** | 0.47 |
| | |
| Underlying event tune | 0.13 |
| FSR | 0.11 |
| $\mu_{\text{F}}$, $\mu_{\text{R}}$ scales | 0.10 |
| Colour reconnection | 0.09 |
| $h_{\text{damp}}$ | 0.04 |
| ISR | 0.04 |
| **Theory total** | 0.23 |
| | |
| **Statistical** | 0.24 |
| **Total** | 0.84 |

**Table 7.2:** Uncertainties in the extraction of $m_{\text{top}}$ from the normalized differential $\mathrm{t\bar{t}}$ production cross section. Shown are the total uncertainties and each contribution. The single contributions are further grouped into experimental, model, theory, and statistical uncertainties. Uncertainties below 0.01 GeV are not listed, namely the choice of the PDF, b-tagging, the luminosity measurement, and the lepton triggers and identification.

## 7.9 Advancing Measurement Techniques

The measurement of the JMS and the calibration of the FSR modeling have provided valuable input for the jet mass measurement in decays of boosted top quarks. The precision in the top quark mass achieved in these studies is compatible with that of top quark mass measurements at threshold production. One of the main objectives, however, is to extract $m_{\text{top}}$ in a well-defined mass scheme rather than relying on simulations and parton shower modeling. Although analytic calculations exist for the differential $\mathrm{t\bar{t}}$ cross section as a function of $m_{\text{jet}}$, the relevant phase space for hadronic jets with $p_{\text{T}} > 750\,\text{GeV}$ remains inaccessible for measurements at the LHC. Several challenges for the comparison to calculations have been identified: the small statistical precision after selecting jets with $p_{\text{T}} > 750\,\text{GeV}$ as required in existing calculations, the reduced effectiveness of the two-step clustering approach, and the broad binning in $m_{\text{jet}}$ which is limited by the $m_{\text{jet}}$ resolution due to the unfolding setup.

The expected integrated luminosity to achieve the same statistical precision as during the full Run 2 data-taking period with $138\,\text{fb}^{-1}$ for $p_{\text{T}} > 400\,\text{GeV}$ is evaluated for jets with a $p_{\text{T}}$ exceeding 750 GeV in Ref. [69]. As discussed in Section 3.1, the expected event yield is proportional to the integrated luminosity and scales with the production cross section of the process of interest. Thus, the required luminosity to obtain the same number of events as in the Run 2 measurement with $138\,\text{fb}^{-1}$ of data for a given $p_{\text{T}}$ threshold can be predicted by studying the jet $p_{\text{T}}$ distribution (see Figure 7.7, lower right). Figure 7.33 shows the $p_{\text{T}}$ threshold that would result in a similar statistical precision as in the Run 2 measurement as a function of the integrated luminosity. Although the center-of-mass energy and with it the $\mathrm{t\bar{t}}$ production cross section will slightly increase for Run 3, the same conditions as in Run 2 are assumed for simplicity. On the other hand, it was observed in Ref. [184] that the current event reconstruction becomes less efficient at very high $p_{\text{T}}$ such that the projection might be optimistic. With the simple projection it was found that in order to achieve the same statistical precision for $p_{\text{T}} > 750\,\text{GeV}$, an integrated luminosity of about $3000\,\text{fb}^{-1}$, which is planned to be collected after the HL-LHC data-taking period, is required. An improved reconstruction and selection of high energetic $\mathrm{t\bar{t}}$ events can increase the available statistics at higher $p_{\text{T}}$ thresholds, potentially allowing for the extraction of $m_{\text{top}}$ before the HL-LHC data-taking period.

The following sections present a reconstruction approach for higher energies and a new unfolding method. The reconstruction approach is explored in the context of a Master's thesis [11], supervised by the author of this PhD project. Additionally, the new unfolding approach was developed as part of other PhD projects [12, 13], with the author of this thesis pre-processing the simulated samples and contributed to the conceptional work. The results will be published in Ref. [14].

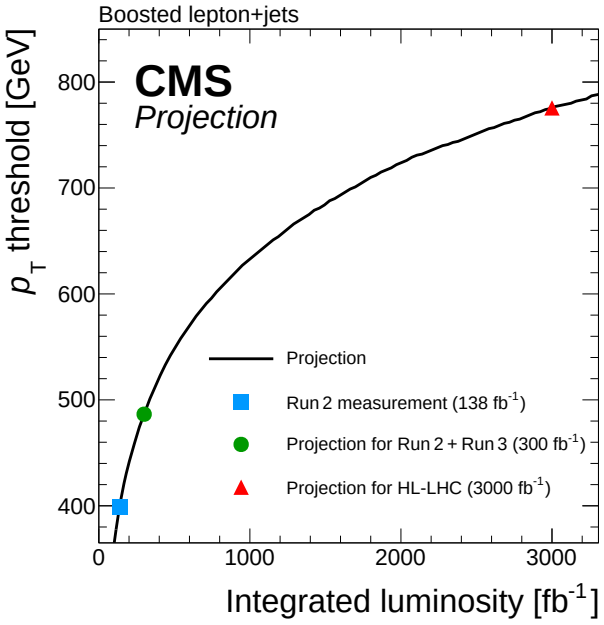


**Figure 7.33:** Projection of the statistical precision for the $p_T$ thresholds as a function of the integrated luminosity. achieved in this analysis with the full Run 2 data. The integrated luminosity for the current analysis is marked in blue (square), the threshold for the combination of Run 2 and Run 3 in green (circle) and the projection for the HL-LHC in red (triangle). For the full range of the integrated luminosity, the same conditions as for the CMS detector in Run 2 are assumed. Taken from Ref. [69].

### 7.9.1 Optimizing the High-$p_T$ Reconstruction

The two-step clustering approach for reconstructing $t\bar{t}$ events using the XCone algorithm efficiently captures the full top quark decay, as demonstrated in Section 7.3.1. However, at higher jet $p_T$, the effectiveness of the clustering procedure diminishes. For higher $p_T$ thresholds of the XCone jet, the contribution from high-energetic radiation increases. Consequently, the XCone algorithm does not properly reconstruct the full $t\bar{t}$ process. For instance, the jet initiated by a high-energetic gluon can be clustered instead of the hadronic top quark decay. Additionally, if the gluon jet and the b jet have a small spatial distance, they might be clustered into one jet, excluding the decay products of the W boson. These configurations result in misidentification of the hadronic top quark decays and incorrectly selected decays of boosted top quarks, leading to a significant tail in the $m_{jet}$ distribution. Once the decay products are not fully clustered into the XCone jets, their information is lost for further analyses. A proposed solution, as detailed in Ref. [184], involves clustering three large-$R$ jets instead of two jets for the two-step clustering procedure. This approach allows for the clustering of both top quark decays with high $p_T$ thresholds, despite the impact of jets from high-energetic gluons on the reconstruction. The main challenge is to correctly identify the jet corresponding to the hadronic top quark decay, as explored in Ref.[11]. These studies are conducted with $t\bar{t}$ simulations from 2018 with the same baseline selection discussed in Section 7.3. The $t\bar{t}$ events are clustered using three large-$R$ jets

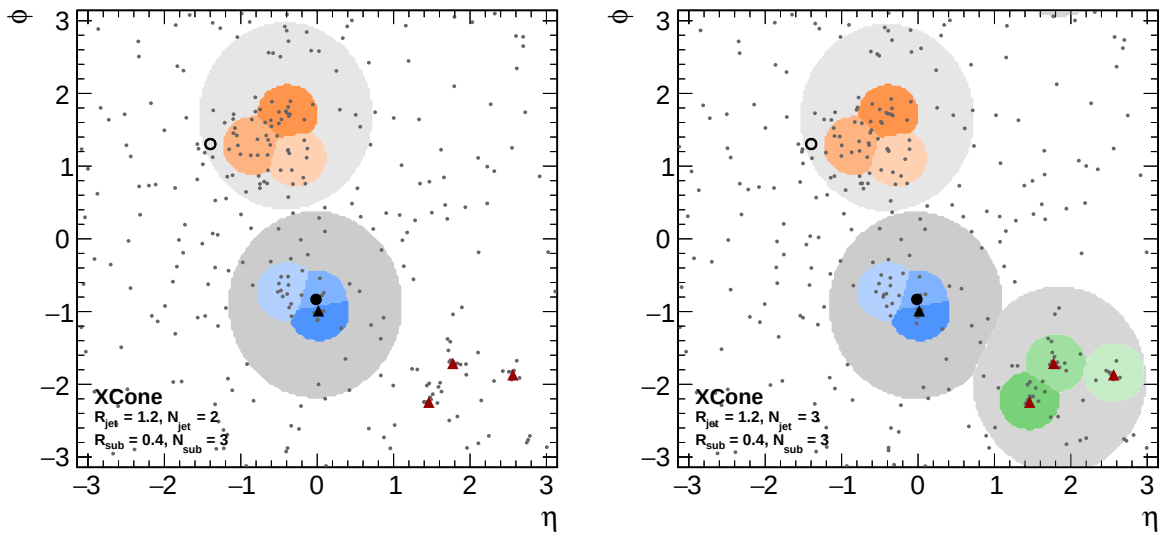


**Figure 7.34:** Event display for an $t\bar{t}$ event reconstructed with the two-step clustering approach with the XCone algorithm for two (left) and three (right) large-$R$ jets. The decay products from the hadronic top quark decay (red triangles) are reconstructed utilizing three large-$R$ jets. Shown in communication with Ref. [11].

with $R = 1.2$, each subdivided into three more subjets with $R = 0.4$.

Figure 7.34 shows an event display for an $t\bar{t}$ event reconstructed with two (left) and three (right) large-$R$ XCone jets. The decay products originating from the hadronic top quark decay (red triangles) are only reconstructed using a third large-$R$ jet. While the jet with the smallest angular distance $\Delta R$ to the lepton can be assigned to the leptonic top quark decay, several configurations for the hadronic top quark decay are possible. The hadronic top quark decay products can be reconstructed separately in both jets not assigned to the leptonic decay, featuring a small spatial distance, or in a single jet. Reconstructions in two overlapping large-$R$ XCone jets result in a total number of six subjets, which cannot be directly assigned to the decay products. The invariant mass of all six subjets generally significantly exceeds $m_{\text{top}}$. However, less than 10 % of the selected events feature a reconstruction of the hadronic top quark decay in two adjacent XCone jets and thus are discarded in the following. In case of two well-separated jets not assigned to the lepton, the jet with the largest $p_{\text{T}}$ is assigned to the hadronic top quark decay. For $p_{\text{T}} > 400\,\text{GeV}$, this approach lead to similar results as for the clustering with two jets, although it is still possible that not the full hadronic top quark decay is reconstructed. In $p_{\text{T}}$ regions above 750 GeV, high energetic radiation can still lead to misidentified hadronic top quark decays. First identification approaches using jet substructure variables, such as the $N$-subjettiness, show an improved identification of hadronic top quark decays compared to the identification based on the jet $p_{\text{T}}$ or the clustering with two large-$R$ jets.

The studies presented in this section illustrate that the reconstruction of high-energy $t\bar{t}$ events can be improved by clustering three large-$R$ XCone jets instead of two. Identification of the hadronic top quark decay from the jets not assigned to the lepton can be conducted using jet

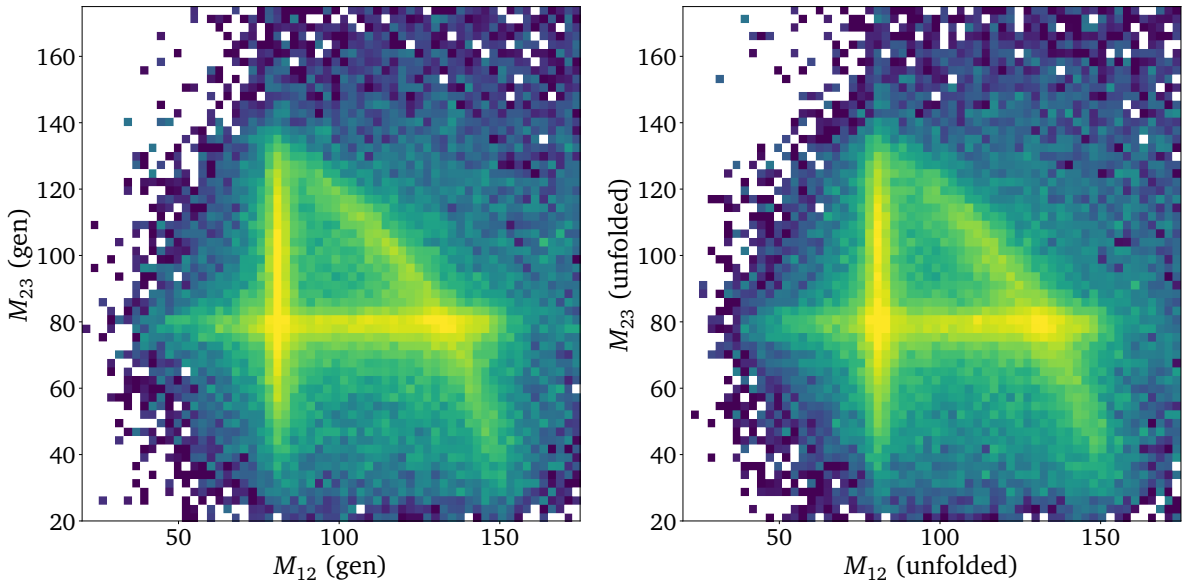


**Figure 7.35:** Correlation of the invariant jet mass from the two $p_{\mathrm{T}}$-leading subjets (1 and 2) and the two sub-leading subjets (2 and 3) from the XCone jet at the particle level (left) and after the event-based unfolding (right). High-density regions are indicated in yellow, while areas with fewer events are shown in dark blue. Taken from Ref. [14].

substructure variables. A detailed understanding of the dynamics of the three-jet clustering can lead to a potential jet mass measurement for $p_{\mathrm{T}} > 750\,\mathrm{GeV}$ with similar precision to that obtained for the two-jet clustering in the region of $p_{\mathrm{T}} > 400\,\mathrm{GeV}$. Moreover, a $p_{\mathrm{T}}$ dependent radius for the subjets during the jet clustering could improve the reconstruction of individual decay products, as the parton showers become more collimated for higher $p_{\mathrm{T}}$ ranges.

### 7.9.2 Event-Based Unfolding

The unfolding setup used in this analysis is based on the TUnfold framework [174]. Such frameworks are restricted to handling a small number of observables. However, the unfolded jet mass distribution is limited by the dependence of the unfolding setup on several model parameters in simulation, where the largest bias is introduced from the choice of $m_{\mathrm{top}}$. Consequently, the dominant limitation in the extraction of the top quark mass arises from this bias. Therefore, a new unfolding method based on machine learning (ML) is explored to reduce these dependencies. ML provides the possibility to perform an unbinned unfolding and to consider multiple kinematic observables simultaneously.

In this section, the unfolding setup is introduced using the generative network Conditional Flow Matching (CFM) [185]. The CFM is based on a diffusion process capable of handling the unfolding on event-to-event basis. A detailed description of the developed network is given in Ref.[14]. The observables of interest are several kinematic features of the subjets, including the mass $m_i$ (monojet mass), the transverse momentum $p_{\mathrm{T},i}$ and the pseudorapidity $\eta_i$ for the $i$-th subjet, as well as the invariant mass $M_{ik}$ (dijet mass) of two subjets $i$ and $k$. Unfolding the top

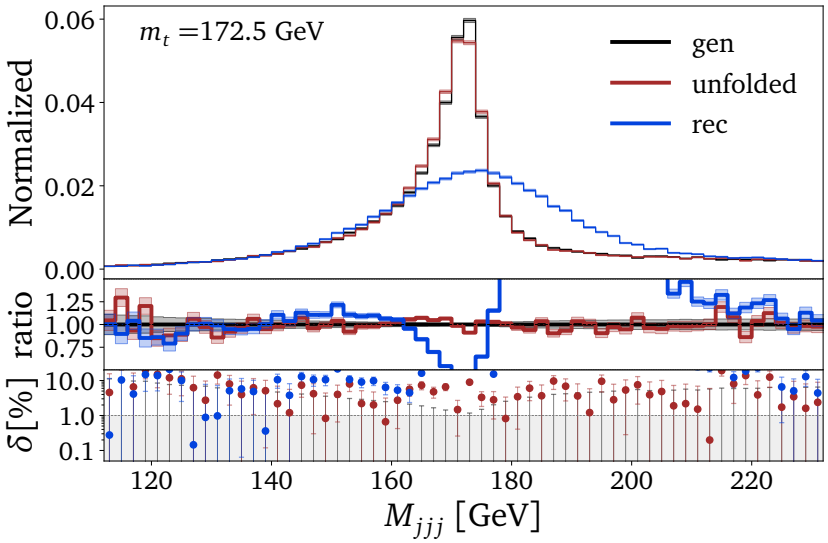


**Figure 7.36:** The jet mass distribution from the combination of all three subjets obtain from $t\bar{t}$ simulations with $m_{\text{top}} = 172.5\,\text{GeV}$ using a four dimensional parametrization. Shown are the distribution on reconstruction level (red), particle level (black) and the unfolded distribution (red). The panel in the middle shows the ratio to particle level, while the lower panel represents the relative statistical uncertainty. Taken from Ref. [14].

quark decay presents many challenges, as the top quark mass itself and the W boson mass $m_{\text{W}}$ are dominant features learned by the network over the full set of input features.

Initial approaches involve utilizing a four-dimensional parameterization, including the sum of the squared monojet mass of all three subjets $M_{ijk}$ (trijet mass), and from any combination for the three dijet masses $M_{ik}$. Correlations among the input features are captured by the conditional generative networks. Figure 7.35 shows the correlation of the invariant mass from the first two $p_{\text{T}}$-leading subjets and the second and third $p_{\text{T}}$-leading subjets at the particle level (left) and the unfolded events (right). When two subjets reconstruct the W boson, they are independent of the remaining one, resulting in three distinct trends. Both the particle level and unfolded distributions are compatible, indicating that the network accurately captures these correlations. At the intersection points of each line, it is not feasible to identify the two subjets originating from the W boson decay based on their masses. Figure 7.36 compares the unfolded distribution to the particle and reconstruction levels. The unfolded distribution aligns well with the particle level for the trijet mass, and has also been verified for the dijet masses and each subjet individually. However, a bias towards the top quark mass parameter in the simulation used for training is observed. If a network trained with a sample at $m_{\text{top}} = 172.5\,\text{GeV}$ is applied to templates with different $m_{\text{top}}$ hypotheses used as pseudo data, the unfolded distribution closely resembles that of the training mass. One major challenge is that a sharp peak of the trijet mass at the generator level results in a much broader peak at the reconstruction level induced by detector effects. This dependence is also evident in a network trained on six input features, comprising the dijet masses and the masses of the individual subjets.

The constraint on $m_{\text{top}}$ can be reduced by using multiple samples with different $m_{\text{top}}$ hypotheses

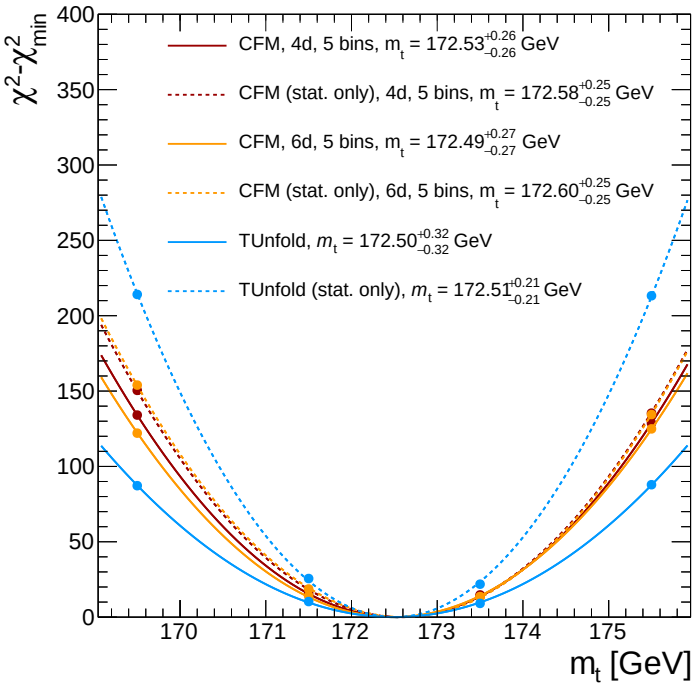


**Figure 7.37:** Extraction of the top quark mass by minimizing the $\chi^2$, only considering the statistical uncertainties (dotted lines) and additionally the choice of $m_{\text{top}}$ (solid lines). Shown are the unfolding setup with TUnfold (blue) and generative network CFM using a four (red) and six (yellow) dimensional paramatrization. Taken from Ref. [14].

to mitigate the training bias. Additionally, a global estimate for $m_{\text{top}}$ is introduced based on the mean value of the trijet mass $M_{ijk}$ at the reconstruction level in each training batch, which is expected to approximate the $m_{\text{top}}$ parameter in simulations. The dependence on the choice of $m_{\text{top}}$ is illustrated in Figure 7.37, showing the extraction procedure for $m_{\text{top}}$ from the previous TUnfold setup and the current CFM network. In this comparison, the CFM network, based on a four and six dimensional parameterization, utilizes the same $m_{\text{jet}}$ binning as in the TUnfold setup. The statistical uncertainty for the CFM network is larger, as indicated by the increased width of the $\chi^2$ function, but the impact of the choice of $m_{\text{top}}$ is significantly smaller. This improvement reduces the influence of the $m_{\text{top}}$ choice from a leading uncertainty to a negligible contribution.

After understanding the main dynamics of the unfolding with a generative network, a more comprehensive set of twelve input features is employed using a CFM with a transformer architecture as first described in Ref. [186]. An additional cut on the azimuthal angle difference between the two $p_{\text{T}}$-leading subjets $\Delta\phi_{ij} > 0.1$, is applied to improve the network's performance, as it struggles with low differences in $\Delta\phi$. The final result of the unfolded distribution shows compatibility with the particle level within a few percent, with a greater deviation observed compared to lower-dimensional parameterizations. This behavior is expected, as the precision of a network generally decreases with higher dimensional input.

Nonetheless, these studies provide valuable insights into multidimensional event-based unfolding, which is capable of reducing the dependence of a fixed number of output bins and the

dependence on the choice of $m_{\text{top}}$ in simulations. This approach enhances the overall accuracy and reliability of the unfolding process by incorporating a broader range of kinematic features.

# Chapter 8

# Summary

At the LHC, a thorough understanding of jets is essential for precision measurements of standard model (SM) parameters and searches for new physics. The top quark is of particular interest for precision measurements of SM parameters. Its properties, such as its mass, are key parameters in the electroweak sector and precise measurements give insights into the dynamics of particle physics. In this thesis, two analyses are presented, one aiming for the calibration of jets and the other for the measurement of the jet mass in hadronic decays of boosted top quarks.

First, the determination of the jet energy resolution scale factors (JER SF) is presented. These scale factors are applied to simulated jets in order to match the JER observed in data. The calibration is conducted in QCD dijet events using the transverse momentum ($p_{\mathrm{T}}$) imbalance method. The JER SFs are derived for the final calibration of the data collected during the data-taking period Run 2 of the LHC in 2016, 2017, and 2018 with an integrated luminosity of $35.9\,\mathrm{fb}^{-1}$, $41.5\,\mathrm{fb}^{-1}$, and $59.7\,\mathrm{fb}^{-1}$, respectively. Additionally, the first JER SFs for the Run 3 data-taking period were measured for data collected in 2022 and 2023 corresponding to $34.7\,\mathrm{fb}^{-1}$ and $27.3\,\mathrm{fb}^{-1}$, respectively. The measurement of the JER in the newest data-taking period Run 3 provided valuable information on the collected data and the current conditions of the detector. The uncertainties are compatible to those of the Run 2 JER SFs, indicating a similar precision in the calibrations of the data samples. Furthermore, the $p_{\mathrm{T}}$ range was extended up to 2 TeV revealing $p_{\mathrm{T}}$ dependent JER SFs. In the scope of this thesis, the limitations of the transverse momentum imbalance method were studied, which heavily relies on the correction for additional jet activity in QCD dijet events. It has been shown that the JER SFs determination is only valid down to a jet $p_{\mathrm{T}}$ of 200 GeV. The correction for the additional jet activity significantly reduces the event yield for QCD dijet events. Furthermore, jets originating from pileup reduce the compatibility of data to simulation for low-$p_{\mathrm{T}}$ jets, as pileup jets can be misidentified with the third jet from QCD dijet events. Contributions from pileup will become even more dominant for increasingly instantaneous luminosity. A new strategy for the additional jet activity was introduced to correct for a non-ideal dijet topology. Lastly, a first insight in the determination of the JER SFs with an extension of the missing transverse mo-

mentum projection fraction (MPF) method was elaborated on in this thesis. This method is less dependent on the additional jet activity in QCD dijet events. Moreover, it is expected to be robust against contribution from pileup and thus allows for the measurement of the JER SFs for jets with $p_{\mathrm{T}} < 200\,\mathrm{GeV}$. The extension of the MPF method is subject to future iterations of the determination of the JER SFs at the CMS detector.
In the second analysis, the differential $\mathrm{t\bar{t}}$ production cross section as a function of the jet mass is measured using the $\ell$+jets decay channel in boosted $\mathrm{t\bar{t}}$ events. The leptonic decay serves as a tag for $\mathrm{t\bar{t}}$ events, while the jet mass measurement is performed on the jet reconstructing the full hadronic top quark decay with $p_{\mathrm{T}} > 400\,\mathrm{GeV}$. This analysis reduces two dominant uncertainties identified in a previous measurement with data collected in 2016: the calibration of the jet mass scale (JMS) and the modeling of final state radiation (FSR). The analyzed data in this analysis correspond to an integrated luminosity of $138\,\mathrm{fb}^{-1}$ and has been collected during the Run 2 data-taking period of the LHC. The JMS is measured independently from the jet energy scale (JES) by reconstructing the hadronic W boson decay from subjets of the hadronic XCone jet. Initially, the JES contributed an uncertainty to the extraction of top quark mass $m_{\mathrm{top}}$ with $\Delta m_{\mathrm{top}} = 1.5\,\mathrm{GeV}$. With the new measurement incorporating the JMS and the JES, the uncertainty is reduced to $\Delta m_{\mathrm{top}} = 0.4\,\mathrm{GeV}$. The modeling of the FSR is refined by measuring the $N$-subjettiness ratio $\tau_{32}$. It was found that the variations in CUETP8M2T4 drastically overestimate the one standard deviation uncertainties. Moreover, the central value used in CP5 does not accurately describe the data, indicating a preference for higher FSR energy scales. After the calibration of the FSR scale, the effective strength of the strong coupling $\alpha_{\mathrm{S}}^{\mathrm{FSR}}$ of both tunes are compatible with each other. As a result, the uncertainty arising from the modeling of the FSR were drastically reduced, becoming a negligible uncertainty in the jet mass measurement. The top quark mass $m_{\mathrm{top}}$ was measured using simulated templates with $m_{\mathrm{top}} = 173.06 \pm 0.84\,\mathrm{GeV}$, achieving a precision that is now compatible with measurements at threshold production. The performed calibrations in this thesis provide valuable information for event generators and enhances our understanding of the jet substructure in hadronic decays of boosted top quarks. Now, the largest experimental and model uncertainties are the JER and the choice of $m_{\mathrm{top}}$, respectively. The former is expected to be minimized with a newer and more precise set of calibrations, while the latter is reduced using a new event-based unfolding technique. Furthermore, a refined reconstruction of the $\mathrm{t\bar{t}}$ process at high energies is explored, clustering three large-$R$ jets with the XCone algorithm. These studies set the foundation for an improved jet mass measurement in higher $p_{\mathrm{T}}$ regions to enable the extraction of $m_{\mathrm{top}}$ from theory calculations. It is further planned to perform the extraction of $m_{\mathrm{top}}$ in dependence of the jet $p_{\mathrm{T}}$. To that end, $m_{\mathrm{top}}^{\mathrm{MC}}$ can be extracted from the unfolded distribution in bins of the jet $p_{\mathrm{T}}$. Future iterations of this analysis will explore the event-based unfolding setup utilizing machine learning to reduce model uncertainties by unfolding the top quark decay kinematics in much higher dimensions. The full potential of the measurement can be achieved by including all of these improvements to reach a phase space accessible in analytic calculations.

# Appendix A

# Electron Trigger Scale Factors

The electron trigger scale factors are measured using the orthogonal dataset method, which utilizes two uncorrelated triggers. For this purpose, the dilepton channel is used, where one top quark decay includes a muon and the other one an electron. The muon trigger acts as a tag, and the efficiency of the electron trigger path is measured by dividing event yields before and after applying the electron trigger path. The scale factors for the efficiency in simulations are then obtained with the ratio of the efficiency in data to that in simulations with $\varepsilon_{\text{data}}/\varepsilon_{\text{MC}}$. All triggers and IDs are identical to the lepton definitions and baseline selection presented in Section 7.3. The only difference is the requirement of exactly one electron and one muon.
The scale factors are derived in three bins for the electron $p_{\text{T}}^{e}$ with $p_{\text{T}}^{e} < 120\,\text{GeV}$, $120 < p_{\text{T}}^{e} < 200\,\text{GeV}$, and $p_{\text{T}}^{e} > 200\,\text{GeV}$, as well as ten bins for $|\eta^{e}| \in [0.0, 0.8, 1.444, 1.566, 2.0, 2.5]$. The $p_{\text{T}}^{e}$ binning is motivated by the electron IDs and the isolation criteria, while the $\eta$ binning accounts for the detector geometry and the gap in the ECAL at $|\eta^{e}| \in [1.444, 1.566]$, where electrons can not be reconstructed properly. Figure A.2, A.3 and A.4 show the efficiencies (left) and data-to-simulation scale factors (right) for the years 2016, 2017 and 2018, respectively. The applied method to derive the electron trigger scale factors requires both trigger to be uncorrelated. The correlation can be calculated with $\alpha = (\varepsilon_{\mu} \cdot \varepsilon_{e})/\varepsilon_{\mu,e}$. Here, the subscripts indicate the efficiency of the corresponding triggers. For $\alpha = 1$, both triggers are fully uncorrelated, as they select two orthogonal data samples. First, the baseline selection is performed without any triggers applied. Then, the efficiency for the muon and electron triggers is measured separately with $\varepsilon_{\mu}$ and $\varepsilon_{e}$, respectively. The combination of both triggers is taken from the aforementioned measurement. The value of $\alpha$ is close to unity within the order of $\mathcal{O}(10^{-3})$, proving that both triggers can be treated as uncorrelated.
A closure test is performed by repeating the measurement with applied scale factors to simulation. Figure A.5 shows the the measurement of the scale factors as a function of the electron $p_{\text{T}}$ (left) and $\eta$ (right). While the scale factors are derived as a function of the electron $\eta$ and in bins of the electron $p_{\text{T}}$, the closure test is performed inclusively in the electron $p_{\text{T}}$. A closure uncertainty of 2 % is applied to account for the differences to unity in the region of $p_{\text{T}}^{e} < 200\,\text{GeV}$ and $|\eta| > 2$. Note, that the lepton trigger uncertainties are negligible in this measurement.

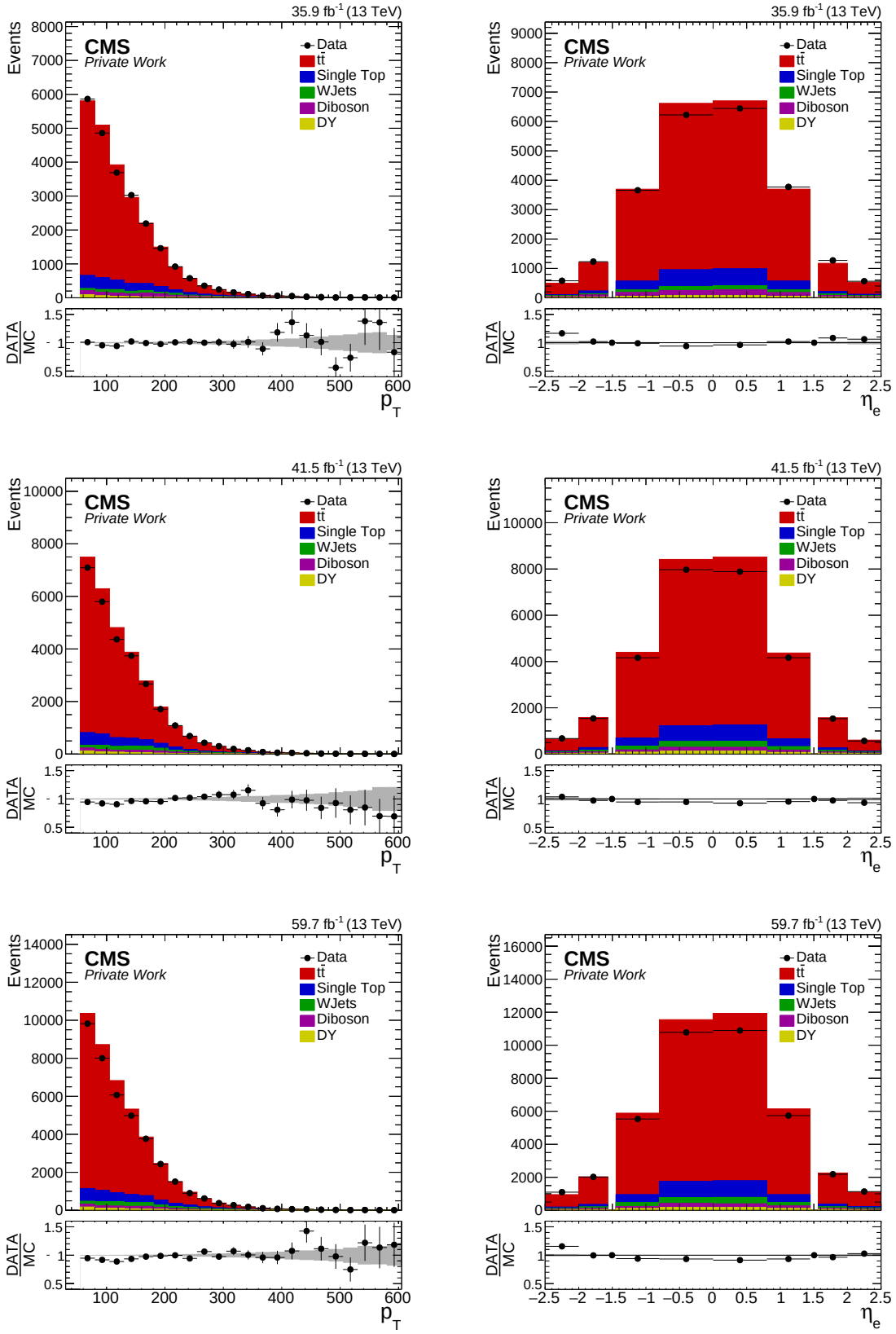


**Figure A.1:** Distribution of the electron $p_{\mathrm{T}}^{e}$ (left) and $\eta^{e}$ (right) after passing the single muon and electron trigger for the $\mathrm{t\bar{t}}$ dilepton decay channel in the years 2016 (upper), 2017 (center) and 2018 (lower). The lower panel shows data-to-simulation ratio with the statistical uncertainties (grey area, vertical lines)

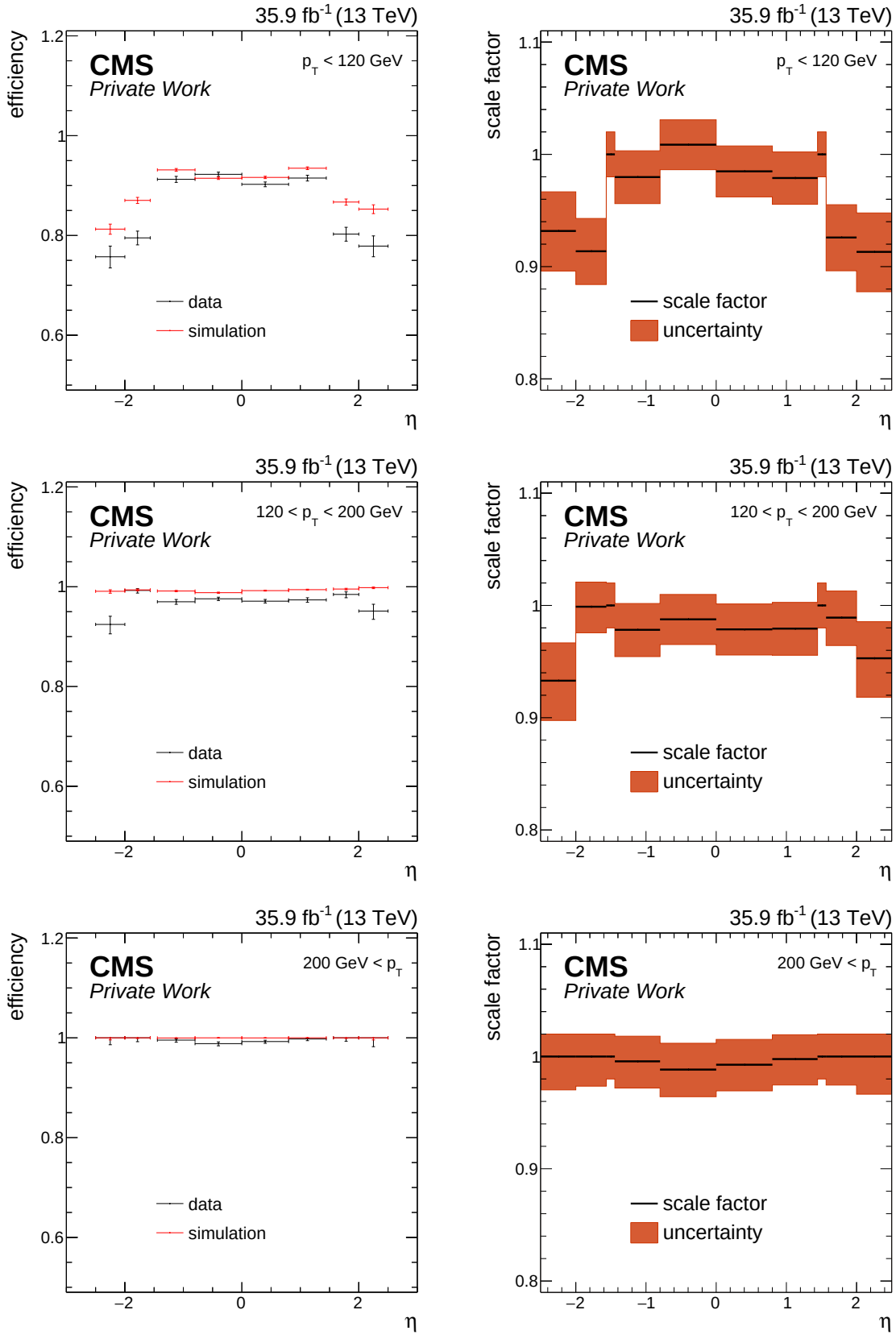


**Figure A.2:** Efficiencies for single electron triggers in 2016 in data and simulation (left) and the simulation-to-data scale factors (right) measured for electrons with $p_{\mathrm{T}}^{e} < 120\,\mathrm{GeV}$ (upper), $120 < p_{\mathrm{T}}^{e} < 200\,\mathrm{GeV}$ (center) and $p_{\mathrm{T}}^{e} > 200\,\mathrm{GeV}$ (lower).

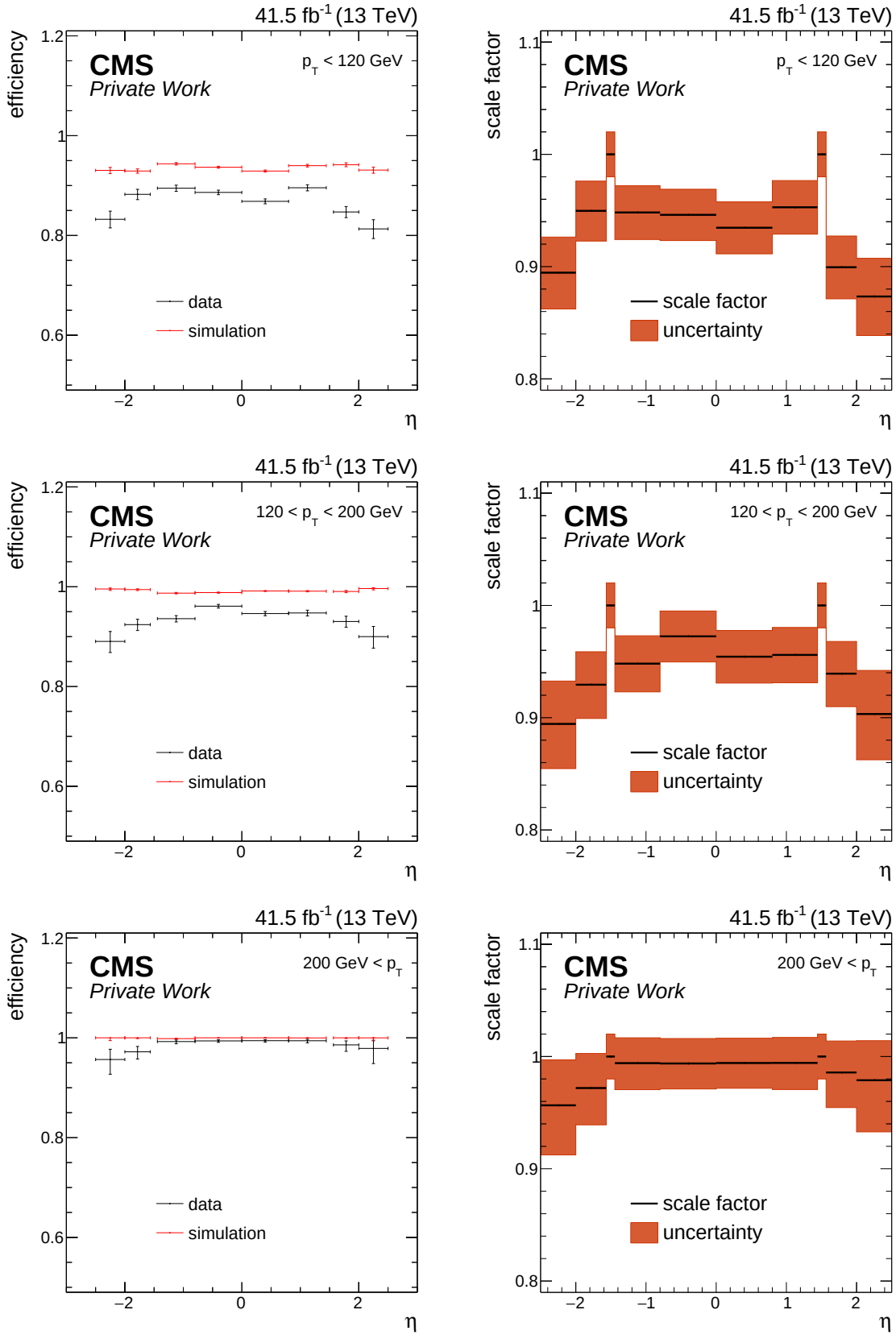


**Figure A.3:** Efficiencies for single electron triggers in 2017 in data and simulation (left) and the simulation-to-data scale factors (right) measured for electrons with $p_{\mathrm{T}}^{e} < 120\,\mathrm{GeV}$ (upper), $120 < p_{\mathrm{T}}^{e} < 200\,\mathrm{GeV}$ (center) and $p_{\mathrm{T}}^{e} > 200\,\mathrm{GeV}$ (lower).

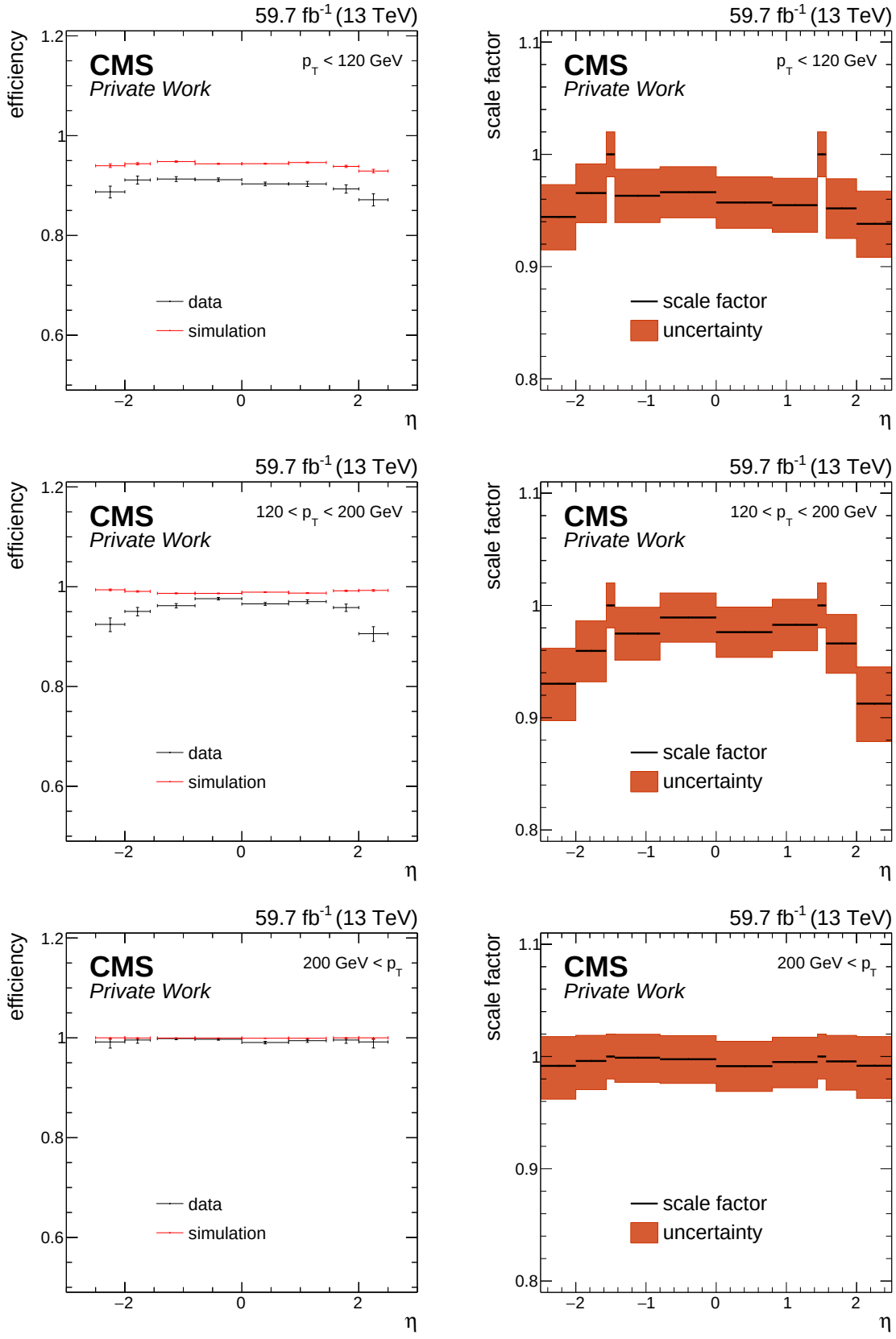


**Figure A.4:** Efficiencies for single electron triggers in 2018 in data and simulation (left) and the simulation-to-data scale factors (right) measured for electrons with $p_{\mathrm{T}}^{e} < 120\,\mathrm{GeV}$ (upper), $120 < p_{\mathrm{T}}^{e} < 200\,\mathrm{GeV}$ (center) and $p_{\mathrm{T}}^{e} > 200\,\mathrm{GeV}$ (lower).

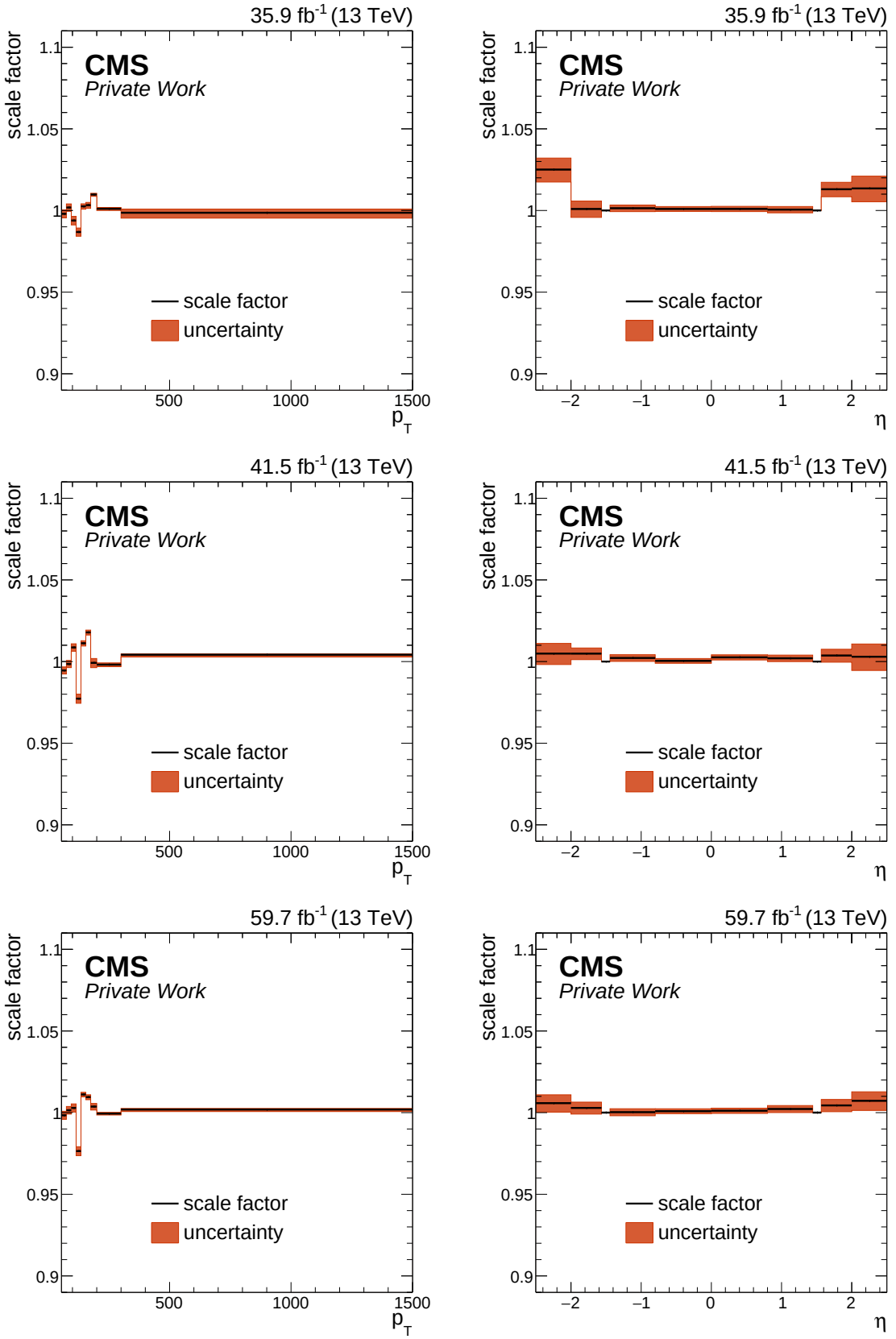


**Figure A.5:** Closure test of the scale factor measurement in 2016 (upper), 2017 (center) and 2018 (lower). The scale factors are applied as a function of the electron $p_{\mathrm{T}}^{e}$ (left) and $\eta$ (right).

# Bibliography


[1] CMS Collaboration, *Jet Energy Scale and Resolution Measurements Using Prompt Run 3 Data Collected by CMS in the Last Months of 2022 at 13.6 TeV*, Technical Report CMS-DP-2023-045, CERN, Geneva, 2023.

[2] CMS Collaboration, *Jet Energy Scale and Resolution Measurements Using Run 3 Data Collected by CMS in 2022 and 2023 at 13.6 TeV*, Technical Report CMS-DP-2024-039, CERN, Geneva, 2024.

[3] CMS Collaboration, *Jet calibration in the leagcy reconstruction in Run 2*, Publication in prepation.

[4] The ColumnFlow team, *columnflow*, `https://github.com/columnflow/columnflow`, release v0.2.4.

[5] A. Paasch, *Towards an Improved Precision of Jet Mass Measurements in Decays of Boosted Top Quarks*, Master's thesis, Universität Hamburg, 2020.

[6] CMS Collaboration, *Measurement of the differential* $\mathrm{t\bar{t}}$ *production cross section as a function of the jet mass and extraction of the top quark mass in hadronic decays of boosted top quarks*, *The European Physical Journal C* 83 (2023), no. 7, 560, doi: 10.1140/epjc/s10052-023-11587-8.

[7] D. Schwarz and A. Paasch, *Measurement of the jet mass distribution of boosted top quarks and the top quark mass with CMS*, *PoS* EPS-HEP2023 (2024) 327, doi: 10.22323/1.449.0327.

[8] A. Paasch, *Measurement of the top mass with boosted jets*, in proceedings of QCD@LHC 2022, Orsay, France.

[9] A. Paasch, *Measurement of the jet mass distribution of boosted top quarks and the top quark mass with CMS*, in proceedings of 14th International Workshop on Boosted Object Phenomenology, Reconstruction, Measurements and Searches in HEP (BOOST).

[10] A. Paasch, *Measurements of the top-quark mass from boosted jets at CMS*, in proceedings of 42nd International Conference on High Energy Physics (ICHEP).

[11] N. Goebels, *in preparation*, Master's thesis, Universität Hannover.

[12] S. Palacios, *in preparation*, PhD thesis, Ruprecht Karls Universität Heidelberg.

[13] L. Favaro, *in preparation*, PhD thesis, Ruprecht Karls Universität Heidelberg.

[14] T. Plehn, L. Favaro, S. Palacios et al., *How to Unfold Top Decays*, Publication in preparation.

[15] OpenAI, *ChatGPT: A large language model trained by OpenAI*, https://www.openai.com/chatgpt, Version GPT-4o, last accessed: 16.08.2024.

[16] A. H. Hoang, S. Mantry, A. Pathak et al., *Extracting a short distance top mass with light grooming*, *Phys. Rev. D* 100 (2019) 074021, doi: 10.1103/PhysRevD.100.074021, arXiv:1708.02586.

[17] CMS Collaboration, *Measurement of the jet mass in highly boosted* $\mathrm{t\bar{t}}$ *events from pp collisions at* $\sqrt{s} = 8$ *TeV*, *Eur. Phys. J.* C77 (2017), no. 7, 467, doi: 10.1140/epjc/s10052-017-5030-3, arXiv:1703.06330.

[18] CMS Collaboration, *Measurement of the jet mass distribution and top quark mass in hadronic decays of boosted top quarks in pp collisions at* $\sqrt{s} = 13$ *TeV*, *Phys. Rev. Lett.* 124 (2020) 202001, doi: 10.1103/PhysRevLett.124.202001, arXiv:1911.03800.

[19] M. E. Peskin and D. V. Schroeder, *An Introduction to quantum field theory*, Addison-Wesley, 1995.

[20] T. Lancaster and S. J. Blundell, *Quantum Field Theory for the Gifted Amateur*, Oxford University Press, 2014.

[21] S. Weinberg, *The Quantum Theory of Fields*, Cambridge University Press, 1995.

[22] M. Thomson, *Modern particle physics*, Cambridge University Press, 2013.

[23] C. Burgard, *Standard model of physics*, `https://texample.net/tikz/examples/model-physics/`, last accessed: 10.03.2024.

[24] Super-Kamiokande Collaboration, *Evidence for oscillation of atmospheric neutrinos*, *Phys. Rev. Lett.* 81 (1998) 1562–1567, doi: 10.1103/PhysRevLett.81.1562, `arXiv:hep-ex/9807003`.

[25] SNO Collaboration, *Measurement of the rate of $\nu_e + d \to p + p + e^-$ interactions produced by $^8B$ solar neutrinos at the Sudbury Neutrino Observatory*, *Phys. Rev. Lett.* 87 (2001) 071301, doi: 10.1103/PhysRevLett.87.071301, `arXiv:nucl-ex/0106015`.

[26] ATLAS Collaboration, *Observation of a new particle in the search for the Standard Model Higgs boson with the ATLAS detector at the LHC*, *Phys. Lett.* B716 (2012) 1–29, doi: 10.1016/j.physletb.2012.08.020, `arXiv:1207.7214`.

[27] CMS Collaboration, *Observation of a New Boson at a Mass of 125 GeV with the CMS Experiment at the LHC*, *Phys. Lett.* B716 (2012) 30–61, doi: 10.1016/j.physletb.2012.08.021, `arXiv:1207.7235`.

[28] L. Morel, Z. Yao, P. Cladé et al., *Determination of the fine-structure constant with an accuracy of 81 parts per trillion*, *Nature* 588 (2020), no. 7836, 61–65, doi: 10.1038/s41586-020-2964-7.

[29] H. Burkhardt and B. Pietrzyk, *Recent BES measurements and the hadronic contribution to the QED vacuum polarization*, *Phys. Rev. D* 84 (2011) 037502, doi: 10.1103/PhysRevD.84.037502.

[30] Particle Data Group, R. L. Workman, et al., *Review of Particle Physics*, *Progress of Theoretical and Experimental Physics* 2022 (2022), no. 8, 083C01, doi: 10.1093/ptep/ptac097.

[31] C. S. Wu, E. Ambler, R. W. Hayward et al., *Experimental Test of Parity Conservation in Beta Decay*, *Phys. Rev.* 105 (1957) 1413–1415, doi: 10.1103/PhysRev.105.1413.

[32] J. Ellis, M. K. Gaillard, and D. V. Nanopoulos, *A Historical Profile of the Higgs Boson. An Updated Historical Profile of the Higgs Boson*, doi: 10.1142/9789814733519_0014.

[33] J. F. Donoghue, *Introduction to the Effective Field Theory Description of Gravity*, 1995, arXiv:gr-qc/9512024.

[34] D. Clowe, M. Bradač, A. H. Gonzalez et al., *A Direct Empirical Proof of the Existence of Dark Matter*, *The Astrophysical Journal* 648 (2006), no. 2, L109, doi: 10.1086/508162.

[35] The Muon $g-2$ Collaboration, *Measurement of the Positive Muon Anomalous Magnetic Moment to 0.20 ppm*, *Phys. Rev. Lett.* 131 (2023) 161802, doi: 10.1103/PhysRevLett.131.161802.

[36] LHCb Collaboration, *Addendum: Test of lepton universality in beauty-quark decays*, *Nature Physics* 19 (2023), no. 10, 1517–1517, doi: 10.1038/s41567-023-02095-3.

[37] B. Capdevila, A. Crivellin, S. Descotes-Genon et al., *Patterns of New Physics in $b \to s\ell^+\ell^-$ transitions in the light of recent data*, *Journal of High Energy Physics* 2018 (2018), no. 1, 93, doi: 10.1007/JHEP01(2018)093.

[38] CDF Collaboration, *High-precision measurement of the W boson mass with the CDF II detector*, *Science* 376 (2022), no. 6589, 170–176, doi: 10.1126/science.abk1781.

[39] T. Markkanen, A. Rajantie, and S. Stopyra, *Cosmological Aspects of Higgs Vacuum Metastability*, *Frontiers in Astronomy and Space Sciences* 5 (2018) doi: 10.3389/fspas.2018.00040.

[40] A. Grinbaum, *Which fine-tuning arguments are fine?*, *Found. Phys.* 42 (2012) 615–631, doi: 10.1007/s10701-012-9629-9.

[41] G. Altarelli and G. Parisi, *Asymptotic freedom in parton language*, *Nuclear Physics B* 126 (1977), no. 2, 298–318, doi: 10.1016/0550-3213(77)90384-4.

[42] Y. L. Dokshitzer, *Calculation of the Structure Functions for Deep Inelastic Scattering and e+ e- Annihilation by Perturbation Theory in Quantum Chromodynamics.*, *Sov. Phys. JETP* 46 (1977) 641–653.

[43] S. Bailey, T. Cridge, L. A. Harland-Lang et al., *Parton distributions from LHC, HERA, Tevatron and fixed target data: MSHT20 PDFs*, *The European Physical Journal C* 81 (2021), no. 4, 341, doi: 10.1140/epjc/s10052-021-09057-0.

[44] J. C. Collins, D. E. Soper, and G. F. Sterman, *Factorization of Hard Processes in QCD*, *Adv. Ser. Direct. High Energy Phys.* 5 (1989) 1–91, doi: 10.1142/9789814503266_0001, arXiv:hep-ph/0409313.

[45] J. C. Collins and D. E. Soper, *The Theorems of Perturbative QCD*, *Annual Review of Nuclear and Particle Science* 37 (1987), no. Volume 37, 383–409, doi: 10.1146/annurev.ns.37.120187.002123.

[46] CMS Collaboration, *CMS Standard Model summary plots*, https://twiki.cern.ch/twiki/bin/view/CMSPublic/PhysicsResultsCombined, last accessed: 07.03.2024.

[47] J. Alwall, R. Frederix, S. Frixione et al., *The automated computation of tree-level and next-to-leading order differential cross sections, and their matching to parton shower simulations*, *JHEP* 07 (2014) 079, doi: 10.1007/JHEP07(2014)079, arXiv:1405.0301.

[48] S. Frixione and B. R. Webber, *Matching NLO QCD computations and parton shower simulations*, *JHEP* 06 (2002) 029, doi: 10.1088/1126-6708/2002/06/029, arXiv:hep-ph/0204244.

[49] P. Nason, *A new method for combining NLO QCD with shower Monte Carlo algorithms*, *JHEP* 11 (2004) 040, doi: 10.1088/1126-6708/2004/11/040, arXiv:hep-ph/0409146.

[50] S. Frixione, P. Nason, and C. Oleari, *Matching NLO QCD computations with Parton Shower simulations: the POWHEG method*, *JHEP* 11 (2007) 070, doi: 10.1088/1126-6708/2007/11/070, arXiv:0709.2092.

[51] S. Alioli, P. Nason, C. Oleari et al., *A general framework for implementing NLO calculations in shower Monte Carlo programs: the POWHEG BOX*, *JHEP* 06 (2010) 043, doi: 10.1007/JHEP06(2010)043, arXiv:1002.2581.

[52] S. Frixione, P. Nason, and G. Ridolfi, *A Positive-weight next-to-leading-order Monte Carlo for heavy flavour hadroproduction*, *JHEP* 09 (2007) 126, doi: 10.1088/1126-6708/2007/09/126, arXiv:0707.3088.

[53] T. Sjöstrand, S. Ask, et al., *An Introduction to PYTHIA 8.2*, *Comput. Phys. Commun.* 191 (2015) 159, doi: 10.1016/j.cpc.2015.01.024, arXiv:1410.3012.

[54] G. Corcella, I. G. Knowles, G. Marchesini et al., *HERWIG 6: An event generator for hadron emission reactions with interfering gluons (including supersymmetric processes)*, *JHEP* 01 (2001) 010, doi: 10.1088/1126-6708/2001/01/010, arXiv:hep-ph/0011363.

[55] J. Bellm and L. Gellersen, *High dimensional parameter tuning for event generators*, *Eur. Phys. J. C* (2019) doi: 10.1140/epjc/s10052-019-7579-5, arXiv:1908.10811.

[56] CMS Collaboration, *Extraction and validation of a new set of CMS PYTHIA8 tunes from underlying-event measurements*, *Eur. Phys. J. C* 80 (2020) 4, doi: 10.1140/epjc/s10052-019-7499-4, arXiv:1903.12179.

[57] GEANT4 Collaboration, *Geant4—A simulation toolkit*, *Nucl. Instrum. Meth. A* 506 (2003) 250, doi: 10.1016/S0168-9002(03)01368-8.

[58] J. Allison et al., *Geant4 developments and applications*, *IEEE Trans. Nucl. Sci.* 53 (2006) 270, doi: 10.1109/TNS.2006.869826.

[59] CDF Collaboration, *Observation of Top Quark Production in $\bar{p}p$ Collisions with the Collider Detector at Fermilab*, *Phys. Rev. Lett.* 74 (1995), no. 14, 2626–2631, doi: 10.1103/PhysRevLett.74.2626, arXiv:hep-ex/9503002.

[60] DØ Collaboration, *Observation of the Top Quark*, *Phys. Rev. Lett.* 74 (1995), no. 14, 2632–2637, doi: 10.1103/PhysRevLett.74.2632, arXiv:hep-ex/9503003.

[61] ATLAS Collaboration, *Measurement of the top-quark mass using a leptonic invariant mass in pp collisions at $\sqrt{s}$ = 13 TeV with the ATLAS detector*, *Journal of High Energy Physics* 2023 (2023), no. 6, 19.

[62] CMS Collaboration, *Measurement of the top quark mass using a profile likelihood approach with the lepton + jets final states in proton–proton collisions at $\sqrt{s}$ = 13 TeV*, *The European Physical Journal C* 83 (2023), no. 10, 963.

[63] J. Ellis, *TikZ-Feynman: Feynman diagrams with TikZ*, *Comput. Phys. Commun.* 210 (2017) 103–123, doi: 10.1016/j.cpc.2016.08.019, arXiv:1601.05437.

[64] CMS Collaboration, *Measurement of differential $\mathrm{t\bar{t}}$ production cross sections in the full kinematic range using* lepton + *jets events from proton-proton collisions at $\sqrt{s}$ = 13 TeV*, *Phys. Rev. D* 104 (2021) 092013, doi: 10.1103/PhysRevD.104.092013.

[65] S. Catani, S. Devoto, M. Grazzini et al., *Top-quark pair production at the LHC: fully differential QCD predictions at NNLO*, *Journal of High Energy Physics* 2019 (2019), no. 7, 100, doi: 10.1007/JHEP07(2019)100.

[66] M. Czakon and A. Mitov, *Top++: A Program for the Calculation of the Top-Pair Cross-Section at Hadron Colliders*, *Comput. Phys. Commun.* 185 (2014) 2930, doi: 10.1016/j.cpc.2014.06.021, arXiv:1112.5675.

[67] LEP Collaboration, *Electroweak parameters of the Z0 resonance and the standard model*, *Physics Letters B* 276 (1992), no. 1, 247–253, doi: 10.1016/0370-2693(92)90572-L.

[68] Gfitter Group Collaboration, *The global electroweak fit at NNLO and prospects for the LHC and ILC*, *Eur. Phys. J.* C74 (2014) 3046, doi: 10.1140/epjc/s10052-014-3046-5, arXiv:1407.3792.

[69] CMS Collaboration, *Review of top quark mass measurements in CMS*, Technical Report CMS-TOP-23-003, CERN, Geneva, 2024, to be submitted to Physics Reports.

[70] CMS Collaboration, *Running of the top quark mass from proton-proton collisions at* $\sqrt{s}$ *= 13TeV*, *Physics Letters B* 803 (2020) 135263, doi: 10.1016/j.physletb.2020.135263.

[71] A. H. Hoang and I. W. Stewart, *Top Mass Measurements from Jets and the Tevatron Top-Quark Mass*, *Nucl. Phys. Proc. Suppl.* 185 (2008) 220–226, doi: 10.1016/j.nuclphysbps.2008.10.028, arXiv:0808.0222.

[72] A. H. Hoang, *What is the Top Quark Mass?*, *Annual Review of Nuclear and Particle Science* 70 (4, 2020) 225–255, doi: 10.1146/annurev-nucl-101918-023530, arXiv:2004.12915.

[73] ATLAS Collaboration, *A precise interpretation for the top quark mass parameter in ATLAS Monte Carlo simulation*, ATL-PHYS-PUB-2021-034, CERN, Geneva, 2021.

[74] LHC Top Physics Working Group, *LHCTopWG Summary Plots*, https://twiki.cern.ch/twiki/bin/view/LHCPhysics/LHCTopWGSummaryPlots, 2023, Topic revision r94 28.01.2024.

[75] L. Evans and P. Bryant, *LHC Machine*, *Journal of Instrumentation* 3 (2008), no. 08, S08001, doi: 10.1088/1748-0221/3/08/S08001.

[76] ATLAS Collaboration, *The ATLAS Experiment at the CERN Large Hadron Collider*, *JINST* 3 (2008) S08003, doi: 10.1088/1748-0221/3/08/S08003.

[77] CMS Collaboration, *The CMS experiment at the CERN LHC*, *JINST* 3 (2008) S08004, doi: 10.1088/1748-0221/3/08/S08004.

[78] ALICE Collaboration, *The ALICE experiment at the CERN LHC*, *JINST* 3 (2008) S08002, doi: 10.1088/1748-0221/3/08/S08002.

[79] LHCb Collaboration, *The LHCb Detector at the LHC*, *JINST* 3 (2008) S08005, doi: 10.1088/1748-0221/3/08/S08005.

[80] E. Mobs, *The CERN accelerator complex - 2019. Complexe des accélérateurs du CERN - 2019*, `https://cds.cern.ch/record/2684277`, 2019.

[81] M. Vretenar, J. Vollaire, R. Scrivens et al., *Linac4 design report*, volume 6 of *CERN Yellow Reports: Monographs*, CERN, Geneva, 2020.

[82] O. Aberle, I. Béjar Alonso, et al., *High-Luminosity Large Hadron Collider (HL-LHC): Technical design report*, CERN Yellow Reports: Monographs, CERN, Geneva, 2020.

[83] CERN, *LS3 schedule change*, `https://hilumilhc.web.cern.ch/article/ls3-schedule-change`, last accessed: 22.02.2024.

[84] CMS Collaboration, *CMS Physics: Technical Design Report Volume 1: Detector Performance and Software*, Technical Report CMS-TDR-8-1, CERN, Geneva, 2006.

[85] T. Sakuma and T. McCauley, *Detector and Event Visualization with SketchUp at the CMS Experiment*, *J. Phys. Conf. Ser.* 513 (2014) 022032, doi: 10.1088/1742-6596/513/2/022032, `arXiv:1311.4942`.

[86] CMS Collaboration, *Description and performance of track and primary-vertex reconstruction with the CMS tracker*, *JINST* 9 (2014), no. 10, P10009, doi: 10.1088/1748-0221/9/10/P10009, `arXiv:1405.6569`.

[87] CMS Collaboration, *The CMS Phase-1 pixel detector upgrade*, *Journal of Instrumentation* 16 (2021), no. 02, P02027, doi: 10.1088/1748-0221/16/02/P02027.

[88] CMS Collaboration, *The CMS electromagnetic calorimeter project: Technical Design Report*, Technical Report CMS-TDR-4, CERN, Geneva, 1997.

[89] CMS, ECAL/HCAL Collaboration, *The CMS barrel calorimeter response to particle beams from 2-GeV/c to 350-GeV/c*, *Eur. Phys. J.* C60 (2009) 359–373, doi: 10.1140/epjc/s10052-009-0959-5.

[90] C. Battilana, *Upgrades of the CMS muon detectors: from Run 3 towards HL-LHC*, *PoS* EPS-HEP2019 (2020) 156, doi: 10.22323/1.364.0156.

[91] CMS Collaboration, *The performance of the CMS muon detector in proton-proton collisions at $\sqrt{s}$ = 7 TeV at the LHC*, *Journal of Instrumentation* 8 (2013), no. 11, P11002, doi: 10.1088/1748-0221/8/11/P11002.

[92] CMS Collaboration, *The TriDAS Project - Technical Design Report, Volume 1: The Trigger Systems*, Technical Report CMS-TDR-6-1, CERN, Geneva, 2000.

[93] CMS Collaboration, S. Cittolin, A. Rácz, and P. Sphicas, *CMS The TriDAS Project: Technical Design Report, Volume 2: Data Acquisition and High-Level Trigger. CMS trigger and data-acquisition project*, Technical Report CMS-TDR-6, CERN, Geneva, 2002.

[94] CMS Collaboration, *Particle-flow reconstruction and global event description with the CMS detector*, *JINST* 12 (2017) P10003, doi: 10.1088/1748-0221/12/10/P10003, arXiv:1706.04965.

[95] W. Adam, B. Mangano, T. Speer et al., *Track Reconstruction in the CMS tracker*, Technical Report CMS-NOTE-2006-041, CERN, Geneva, 2006.

[96] D. Barney, *CMS Detector Slice*, http://cds.cern.ch/record/2120661, 2016, last accessed: 22.03.2024.

[97] CMS Collaboration, *Performance of photon reconstruction and identification with the CMS detector in proton-proton collisions at $\sqrt{s}$ = 8 TeV*, *Journal of Instrumentation* 10 (2015), no. 08, P08010, doi: 10.1088/1748-0221/10/08/P08010.

[98] CMS Collaboration, *Performance of the CMS muon detector and muon reconstruction with proton-proton collisions at $\sqrt{s}$ = 13 TeV*, *JINST* 13 (2018) P06015, doi: 10.1088/1748-0221/13/06/P06015, arXiv:1804.04528.

[99] CMS Collaboration, *Electron and photon reconstruction and identification with the CMS experiment at the CERN LHC*, *JINST* 16 (2021) P05014, doi: 10.1088/1748-0221/16/05/P05014, arXiv:2012.06888.

[100] A. Hocker, P. Speckmayer, et al., *TMVA - Toolkit for Multivariate Data Analysis with ROOT: Users guide. TMVA - Toolkit for Multivariate Data Analysis*, Technical Report CERN-OPEN-2007-007, CERN, Geneva, 2007, TMVA-v4 Users Guide: 135 pages, 19 figures, numerous code examples and references.

[101] M. Cacciari, G. P. Salam, and G. Soyez, *The anti-$k_T$ jet clustering algorithm*, *JHEP* 04 (2008) 063, doi: 10.1088/1126-6708/2008/04/063, arXiv:0802.1189.

[102] I. W. Stewart, F. J. Tackmann, J. Thaler et al., *XCone: N-jettiness as an Exclusive Cone Jet Algorithm*, *JHEP* 11 (2015) 072, doi: 10.1007/JHEP11(2015)072, arXiv:1508.01516.

[103] M. Cacciari, G. P. Salam, and G. Soyez, *FastJet user manual*, *Eur. Phys. J. C* 72 (2012) 1896, doi: 10.1140/epjc/s10052-012-1896-2, arXiv:1111.6097.

[104] Y. L. Dokshitzer, G. D. Leder, S. Moretti et al., *Better jet clustering algorithms*, *JHEP* 08 (1997) 001, doi: 10.1088/1126-6708/1997/08/001, arXiv:hep-ph/9707323.

[105] M. Wobisch and T. Wengler, *Hadronization corrections to jet cross-sections in deep inelastic scattering*, in *Workshop on Monte Carlo Generators for HERA Physics (Plenary Starting Meeting)*, pp. 270–279. 4, 1998. arXiv:hep-ph/9907280.

[106] S. Catani, Y. L. Dokshitzer, M. Seymour et al., *Longitudinally invariant $k_T$ clustering algorithms for hadron hadron collisions*, *Nucl. Phys. B* 406 (1993) 187–224, doi: 10.1016/0550-3213(93)90166-M.

[107] S. D. Ellis and D. E. Soper, *Successive combination jet algorithm for hadron collisions*, *Phys. Rev. D* 48 (1993) 3160–3166, doi: 10.1103/PhysRevD.48.3160, arXiv:hep-ph/9305266.

[108] I. W. Stewart, F. J. Tackmann, and W. J. Waalewijn, *N-Jettiness: An Inclusive Event Shape to Veto Jets*, *Phys. Rev. Lett.* 105 (2010) 092002, doi: 10.1103/PhysRevLett.105.092002, arXiv:1004.2489.

[109] CMS Collaboration, CMS Collaboration, *Public CMS Luminosity Information*, `https://twiki.cern.ch/twiki/bin/view/CMSPublic/LumiPublicResults`, Topic revision r198 11.04.2024.

[110] CMS Collaboration, *Pileup Removal Algorithms*, Technical Report CMS-PAS-JME-14-001, CERN, Geneva, 2014.

[111] D. Bertolini, P. Harris, M. Low et al., *Pileup per particle identification*, *Journal of High Energy Physics* 2014 (2014), no. 10, 59, doi: 10.1007/JHEP10(2014)059.

[112] CMS Collaboration, *Pileup Jet Identification*, Technical Report CMS-PAS-JME-13-005, CERN, Geneva, 2013.

[113] CMS Collaboration, *Pileup-per-particle identification: optimisation for Run 2 Legacy and beyond*, Technical Report CMS-DP-2021-001, CERN, Geneva, 2021.

[114] CMS Collaboration, *Pileup mitigation at CMS in 13 TeV data*, *Journal of Instrumentation* 15 (2020), no. 09, P09018, doi: 10.1088/1748-0221/15/09/P09018.

[115] CMS Collaboration, *Identification of heavy-flavour jets with the CMS detector in pp collisions at 13 TeV*, *JINST* 13 (2018) P05011, doi: 10.1088/1748-0221/13/05/P05011, `arXiv:1712.07158`.

[116] CMS Collaboration, *Performance of b tagging algorithms in proton-proton collisions at 13 TeV with Phase 1 CMS detector*, Technical Report CMS-DP-2018-033, CERN, Geneva, 2018.

[117] E. Bols, J. Kieseler, M. Verzetti et al., *Jet flavour classification using DeepJet*, *Journal of Instrumentation* 15 (2020), no. 12, P12012, doi: 10.1088/1748-0221/15/12/P12012.

[118] CMS Collaboration, *A first look at early 2022 proton-proton collisions at $\sqrt{s}$ = 13.6 TeV for heavy-flavor jet tagging*, Technical Report CMS-DP-2023-012, CERN, Geneva, 2023.

[119] CMS Collaboration, *Jet energy scale and resolution in the CMS experiment in pp collisions at 8 TeV*, *Journal of Instrumentation* 12 (2017), no. 02, P02014, doi: 10.1088/1748-0221/12/02/P02014.

[120] CMS Collaboration, *Jet energy scale and resolution measurement with Run 2 Legacy Data Collected by CMS at 13 TeV*, Technical Report CMS-DP-2021-033, CERN, Geneva, 2021.

[121] CMS Collaboration, *Supplementary Material of CMS-TOP-19-005*, `http://cms-results.web.cern.ch/cms-results/public-results/publications/TOP-19-005/index.html`.

[122] D. Schwarz, *Measurements of jet mass, top quark mass and top tagging efficiencies in decays of boosted top quarks at CMS*, PhD thesis, Universität Hamburg, 2020.

[123] R. Kogler, *Advances in Jet Substructure at the LHC: Algorithms, Measurements and Searches for New Physical Phenomena*, volume 284, Springer, 2021.

[124] M. S. Simone Marzani, Gregory Soyez, *Looking Inside Jets*, volume 958, Springer, 2019.

[125] A. J. Larkoski, I. Moult, and B. Nachman, *Jet substructure at the Large Hadron Collider: A review of recent advances in theory and machine learning*, *Physics Reports* 841 (2020) 1–63, doi: 10.1016/j.physrep.2019.11.001.

[126] D. Napoletano and G. Soyez, *Computing N-subjettiness for boosted jets*, *Journal of High Energy Physics* 2018 (2018), no. 12, 31, doi: 10.1007/JHEP12(2018)031.

[127] G. P. Salam, *Towards jetography*, *The European Physical Journal C* 67 (2010), no. 3, 637–686, doi: 10.1140/epjc/s10052-010-1314-6.

[128] V. V. Sudakov, *Vertex parts at very high-energies in quantum electrodynamics*, *Sov. Phys. JETP* 3 (1956) 65–71.

[129] M. Dasgupta, A. Fregoso, S. Marzani et al., *Towards an understanding of jet substructure*, *Journal of High Energy Physics* 2013 (2013), no. 9, 29, doi: 10.1007/JHEP09(2013)029.

[130] C. W. Bauer, D. Pirjol, and I. W. Stewart, *Soft-collinear factorization in effective field theory*, *Phys. Rev. D* 65 (2002) 054022, doi: 10.1103/PhysRevD.65.054022, `arXiv:hep-ph/0109045`.

[131] S. Fleming, A. H. Hoang, S. Mantry et al., *Jets from massive unstable particles: Top-mass determination*, *Phys. Rev.* D77 (2008) 074010, doi: 10.1103/PhysRevD.77.074010, arXiv:hep-ph/0703207.

[132] A. J. Larkoski, S. Marzani, G. Soyez et al., *Soft Drop*, *JHEP* 05 (2014) 146, doi: 10.1007/JHEP05(2014)146, arXiv:1402.2657.

[133] CMS Collaboration, *Identification of heavy, energetic, hadronically decaying particles using machine-learning techniques*, *Journal of Instrumentation* 15 (2020), no. 06, P06005, doi: 10.1088/1748-0221/15/06/P06005.

[134] J. Thaler and K. Van Tilburg, *Identifying Boosted Objects with N-subjettiness*, *JHEP* 03 (2011) 015, doi: 10.1007/JHEP03(2011)015, arXiv:1011.2268.

[135] A. J. Larkoski, S. Marzani, and J. Thaler, *Sudakov safety in perturbative QCD*, *Phys. Rev. D* 91 (2015) 111501, doi: 10.1103/PhysRevD.91.111501.

[136] G. P. Salam, L. Schunk, and G. Soyez, *Dichroic subjettiness ratios to distinguish colour flows in boosted boson tagging*, *Journal of High Energy Physics* 2017 (2017), no. 3, 22, doi: 10.1007/JHEP03(2017)022.

[137] CMS Collaboration, *Pileup-per-particle identification: optimisation for Run 2 Legacy and beyond*, Technical Report CMS-DP-2021-001, CERN, Geneva, 2021.

[138] J. M. Butterworth, A. R. Davison, M. Rubin et al., *Jet Substructure as a New Higgs-Search Channel at the Large Hadron Collider*, *Phys. Rev. Lett.* 100 (2008) 242001, doi: 10.1103/PhysRevLett.100.242001.

[139] D. Krohn, J. Thaler, and L.-T. Wang, *Jet trimming*, *Journal of High Energy Physics* 2010 (2010), no. 2, 84, doi: 10.1007/JHEP02(2010)084.

[140] S. D. Ellis, C. K. Vermilion, and J. R. Walsh, *Techniques for improved heavy particle searches with jet substructure*, *Phys. Rev. D* 80 (2009) 051501, doi: 10.1103/PhysRevD.80.051501.

[141] J. Thaler and T. F. Wilkason, *Resolving Boosted Jets with XCone*, *JHEP* 12 (2015) 051, doi: 10.1007/JHEP12(2015)051, arXiv:1508.01518.

[142] CMS Collaboration, *Measurements of the differential jet cross section as a function of the jet mass in dijet events from proton-proton collisions at* $\sqrt{s} = 13$ *TeV*, *JHEP* 11 (2018) 113, doi: 10.1007/JHEP11(2018)113, arXiv:1807.05974.

[143] ATLAS Collaboration, *Track assisted techniques for jet substructure*, ATL-PHYS-PUB-2018-012, CERN, Geneva, 2018.

[144] ATLAS Collaboration, *Optimisation of large-radius jet reconstruction for the ATLAS detector in 13 TeV proton–proton collisions*, *European Physical Journal C* 81 (2021), no. 4, doi: 10.1140/epjc/s10052-021-09054-3.

[145] ATLAS Collaboration Collaboration, *Measurement of jet substructure in boosted* $t\bar{t}$ *events with the ATLAS detector using* 140 $\text{fb}^{-1}$ *of 13 TeV pp collisions*, *Phys. Rev. D* 109 (Jun, 2024) 112016, doi: 10.1103/PhysRevD.109.112016.

[146] D. Krohn, J. Thaler, and L.-T. Wang, *Jets with Variable R*, *JHEP* 06 (2009) 059, doi: 10.1088/1126-6708/2009/06/059, arXiv:0903.0392.

[147] ATLAS Collaboration, *Measurement of large radius jet mass reconstruction performance at* $\sqrt{s} = 8$ *TeV using the ATLAS detector*, ATLAS-CONF-2016-008, CERN, Geneva, 2016.

[148] ATLAS Collaboration, *In situ calibration of large-radius jet energy and mass in 13 TeV proton–proton collisions with the ATLAS detector*, *Eur. Phys. J. C* 79 (2019), no. 2, 135, doi: 10.1140/epjc/s10052-019-6632-8.

[149] CMS Collaboration, *Calibration of the Jet Mass Scale using boosted W bosons and top quarks*, Technical Report CMS-DP-2023-044, CERN, Geneva, 2023.

[150] S. Albrecht, *Measurement of jet mass distributions of boosted W bosons*, PhD thesis, Universität Hamburg, 2023.

[151] CMS Collaboration, *Jet algorithms performance in 13 TeV data*, Technical Report CMS-PAS-JME-16-003, CERN, Geneva, 2017.

[152] ATLAS Collaboration, *Measurement of jet-substructure observables in top quark, W boson and light jet production in proton-proton collisions at* $\sqrt{s}$ *= 13 TeV with the ATLAS detector*, *Journal of High Energy Physics* 2019 (2019), no. 8, 33, doi: 10.1007/JHEP08(2019)033.

[153] CMS Collaboration, *Measurement of jet substructure observables in* $\mathrm{t\bar{t}}$ *events from proton-proton collisions at* $\sqrt{s} = 13TeV$, *Phys. Rev. D* 98 (2018), no. 9, 092014, doi: 10.1103/PhysRevD.98.092014, arXiv:1808.07340.

[154] A. Malara, *Calibration of the jet transverse momentum resolution and search for heavy resonances decaying into a Z and a Higgs boson with the CMS experiment*, PhD thesis, Universität Hamburg, 2021.

[155] DØ Collaboration, *High-*$p_T$ *jets in* $\overline{p}p$ *collisions at* $\sqrt{s} = 630$ *and 1800 GeV*, *Phys. Rev. D* 64 (2001) 032003, doi: 10.1103/PhysRevD.64.032003.

[156] DØ Collaboration, *Measurement of the inclusive jet cross section in* $p\overline{p}$ *collisions at* $\sqrt{s}$=1.96 TeV, *Phys. Rev. D* 85 (2012) 052006, doi: 10.1103/PhysRevD.85.052006.

[157] CMS Collaboration, *Simulation of the Silicon Strip Tracker pre-amplifier in early 2016 data*, Technical Report CMS-DP-2020-045, CERN, Geneva, 2020.

[158] CMS Collaboration, CMS Collaboration, *Problems and solutions: the ECAL leak story*, https://cmsexperiment.web.cern.ch/index.php/news/problems-and-solutions-ecal-leak-story, 2024, last accessed: 31.07.2024.

[159] CMS Collaboration, *Performance of Muon Reconstruction in the CMS High Level Trigger using pp Collision data at* $\sqrt{s}$ *= 13.6 TeV in 2023*, Technical Report CMS-DP-2024-005, CERN, Geneva, 2024.

[160] CMS Collaboration, *Measurement of the inelastic proton-proton cross section at* $\sqrt{s} = 13$ *TeV*, *Journal of High Energy Physics* 2018 (Jul, 2018) 161, doi: 10.1007/JHEP07(2018)161.

[161] S. Orfanelli, A. Dabrowski, M. Giunta et al., *A novel Beam Halo Monitor for the CMS experiment at the LHC*, *Journal of Instrumentation* 10 (nov, 2015) P11011, doi: 10.1088/1748-0221/10/11/P11011.

[162] CMS Collaboration, *Jet energy scale and resolution performance with 13 TeV data collected by CMS in 2016-2018*, Technical Report CMS-DP-2020-019, CERN, Geneva, 2020.

[163] K. Goebel, *Probing supersymmetry based on precise jet measurementsat the CMS experiment*, PhD thesis, Universität Hamburg, 2015.

[164] CMS Collaboration, *Performance of the CMS Level-1 trigger in proton-proton collisions at $\sqrt{s}$ = 13 TeV*, *Journal of Instrumentation* 15 (2020), no. 10, P10017, doi: 10.1088/1748-0221/15/10/P10017.

[165] R. Barlow, *Asymmetric errors*, *eConf* C030908 (2003) WEMT002, arXiv:physics/0401042.

[166] M. Schroeder, *Quality of Jet Measurements and Impact on a Search for New Physics at CMS*, PhD thesis, Universität Hamburg, 2012.

[167] Y. Fischer, *in preparation*, PhD thesis, Universität Hamburg.

[168] T. Dreyer, *First measurement of the jet mass in events with highly boosted top quarks and studies with top tagging at CMS*, PhD thesis, Universität Hamburg, 2019.

[169] Y. Li and F. Petriello, *Combining QCD and electroweak corrections to dilepton production in the framework of the FEWZ simulation code*, *Phys. Rev. D* 86 (2012) 094034, doi: 10.1103/PhysRevD.86.094034.

[170] R. Frederix and S. Frixione, *Merging meets matching in MC@NLO*, *Journal of High Energy Physics* 2012 (2012), no. 12, 61, doi: 10.1007/JHEP12(2012)061.

[171] J. Alwall, S. Höche, F. Krauss et al., *Comparative study of various algorithms for the merging of parton showers and matrix elements in hadronic collisions*, *The European Physical Journal C* 53 (2008), no. 3, 473–500, doi: 10.1140/epjc/s10052-007-0490-5.

[172] CMS Collaboration, *Event generator tunes obtained from underlying event and multiparton scattering measurements*, *Eur. Phys. J. C* 76 (2016) 155, doi: 10.1140/epjc/s10052-016-3988-x, arXiv:1512.00815.

[173] F. Herren and M. Steinhauser, *Version 3 of RunDec and CRunDec*, *Computer Physics Communications* 224 (2018) 333–345, doi: 10.1016/j.cpc.2017.11.014.

[174] S. Schmitt, *TUnfold: an algorithm for correcting migration effects in high energy physics*, *JINST* 7 (2012) T10003, doi: 10.1088/1748-0221/7/10/T10003, arXiv:1205.6201.

[175] S. Schmitt, *Data Unfolding Methods in High Energy Physics*, *EPJ Web Conf.* 137 (2017) 11008, doi: 10.1051/epjconf/201713711008, arXiv:1611.01927.

[176] CMS Collaboration, *Precision luminosity measurement in proton–proton collisions at $\sqrt{s}$ = 13 TeV in 2015 and 2016 at CMS*, *The European Physical Journal C* 81 (2021), no. 9, 800, doi: 10.1140/epjc/s10052-021-09538-2.

[177] CMS Collaboration, *CMS luminosity measurement for the 2017 data-taking period at $\sqrt{s} = 13$ TeV*, Technical Report CMS-PAS-LUM-17-004, CERN, Geneva, 2018.

[178] CMS Collaboration, *CMS luminosity measurement for the 2018 data-taking period at $\sqrt{s} = 13TeV$*, Technical Report CMS-PAS-LUM-18-002, CERN, Geneva, 2019.

[179] NNPDF Collaboration, *Parton distributions for the LHC Run II*, *JHEP* 04 (2015) 040, doi: 10.1007/JHEP04(2015)040, arXiv:1410.8849.

[180] S. Argyropoulos and T. Sjöstrand, *Effects of color reconnection on $\mathrm{t\bar{t}}$ final states at the LHC*, *Journal of High Energy Physics* 2014 (2014), no. 11, 43, doi: 10.1007/JHEP11(2014)043.

[181] J. R. Christiansen and P. Z. Skands, *String formation beyond leading colour*, *Journal of High Energy Physics* 2015 (2015), no. 8, 3, doi: 10.1007/JHEP08(2015)003.

[182] T. Sjöstrand and M. van Zijl, *A multiple-interaction model for the event structure in hadron collisions*, *Phys. Rev. D* 36 (1987) 2019–2041, doi: 10.1103/PhysRevD.36.2019.

[183] D. Britzger, *The Linear Template Fit*, *The European Physical Journal C* 82 (2022), no. 8, 731, doi: 10.1140/epjc/s10052-022-10581-w.

[184] A. Paasch, *Improving the Jet Mass Reconstruction in Highly Boosted Top Quark Decays*, Bachelor's thesis, Universität Hamburg 2018.

[185] A. Butter, N. Huetsch, S. Palacios Schweitzer et al., *Jet Diffusion versus JetGPT – Modern Networks for the LHC*, 2023, arXiv:2305.10475.

[186] T. Heimel, N. Huetsch, R. Winterhalder et al., *Precision-Machine Learning for the Matrix Element Method*, 2023, arXiv:2310.07752.

# Danksagung

Hiermit möchte ich mich bei Allen bedanken, die mich auf dem Weg zu dieser Arbeit begleitet haben. Zunächst möchte ich mich ausdrücklich bei Johannes Haller bedanken, der mir die Gelegenheit gegeben hat, meine wissenschaftliche Arbeiten seit meinem Bachelor in seiner Gruppe durchzuführen. Du hast mir die Möglichkeit geboten, die volle Bandbreite wissenschaftlicher Erfahrungen zu sammeln, indem ich mich auf vielen Konferenzen mit internationalen Kollegen austauschen konnte. Zudem standest du in allen Bereichen immer als Ansprechpartner zur Verfügung und hast mich in vielen Aspekten unterstützt. Der gleiche Dank gilt Roman Kogler, der mich im selben Zeitraum betreut und motiviert hat. Du hattest immer ein offenes Ohr und durch deine gute Laune haben sich viele Probleme von alleine gelöst. Des Weiteren möchte ich mich bei euch beiden für die Gutachterrolle für diese Arbeit bedanken.
Zudem möchte ich mich bei Gudrid Moortgat-Pick, Christian Schwanenberger und meinem Prüfungvorsitzenden Jochen Liske für die Teilnahme an meiner Prüfungskommision bedanken.
Ebenfalls möchte ich mich bei Matthias Schröder für das Korrekturlesen meiner vollständigen Arbeit bedanken. Du hast dir zusätzlich immer wieder die Zeit genommen meine Projekte mit voranzubringen und mit dir konnte man über alle möglichen Themen sprechen. Ob über dir Arbeit oder private Angelegenheiten, du hattest immer einen passenden Ratschlag.
Ein besonderer Dank gilt Dennis Schwarz, der mich seit meiner Bachelorarbeit betreut hat. Du warst immer für Fragen zur Physik, zum Programmieren oder einfach über alltägliche Dinge verfügbar. Danke, dass du dir die Zeit genommen hast um diese Arbeit (fast) vollständig zu lesen und zu kommentieren. Es hat mir immer wieder sehr viel Freude bereitet mit dir an gemeinsamen Projekten zu arbeiten.
Ein besonderer Dank gilt auch Andrea Malara für die Betreuung der Jet Kalibrierungen. Durch dich habe ich nicht nur eine Leidenschaft für Jets entwickelt, sondern auch eine Menge über das Programmieren gelernt. Wann immer es nötig war hast du mich neu motiviert und vorangebracht. *Un ringraziamento speciale va anche al dottor Andrea Malara per la supervisione delle calibrazioni dei jet. Grazie a te, non solo ho sviluppato una passione per i jet, ma ho anche imparato molto sulla programmazione. Ogni volta che è stato necessario, mi hai motivato e spinto ad andare avanti.*
Das Gleiche gilt für Daniel Savoiu, der gemeinsam mit mir die Jet Korrekturen in der Gruppe geleitet hat. Durch die gemeinsame Arbeit habe ich eine Menge über das Programmieren und das Organisieren von gemeinsamen Projekten gelernt.
Meinem langjährigen Büronachbarn seit meiner Masterarbeit, Finn Labe, möchte ich für die vielen hilfreichen und angenehmen Diskussionen und Momente danken. Ob innerhalb des Büros oder weit außerhalb der Arbeit beim Geocaching, mit dir war eine gute Zeit immer gewiss.
Ein weiterer Danke geht an Sofia Palacios, Luigi Favaro und Tilmann Plehn für das gemein-

same spannende Unfolding Projekt und die Möglichkeit die Messung bei euch in Heidelberg vorzustellen.
Ein besonderer Dank geht auch an die (ehemaligen) Gruppenmitglieder und Kollegen, die die Arbeitsumgebung sehr angenehm gestaltet haben und mit ihrer Expertise immer weiterhelfen konnten. Mein Dank gilt Matteo Bonanomi und Ksenia De Leo für die vielen Italienischstunden. *Grazie al dottor Matteo Bonanomi e a Ksenia De Leo per le numerose lezioni di italiano.* Danke auch an Daniel Hundhausen für die gemeinsame Zeit auf der CSC in Krakau und den vielen Konferenzen, die wir zusammen erlebt haben. Ich danke Alexander Grohsjean für die Unterstützung bei der Erzeugung der MC-Samples, Mathis Frahm für die Hilfe mit columnflow, und Steffen Albrecht für die ständige Bereitschaft, mir bei meinen Frameworkproblemen zu helfen. Ein weiterer Dank geht an Arthur Lobanov, Arne Reimers und Anna Benecke, die meine Fragen stets bereitwillig beantwortet haben. Schließlich danke ich Henrik Jabusch, Christopher Matthies und Yannick Fischer für ein sehr angenehmes Arbeitsklima und viele lustige Momente.
Ein besonderer Dank geht an meine Familie und Freunde, die mich mein gesamtes Studium unterstützt haben. Vorallem möchte ich meiner Frau Mareike danken, die mich die gesamte Zeit über tatkräftig und mit viel Geduld unterstützt hat.